



Advances in proton MR spectroscopy for quantifying pain associated metabolic changes in the human brain

DISSERTATION

zur Erlangung des akademischen Grades
Doktoringenieur (Dr.-Ing.)

vorgelegt der Fakultät für Informatik und Automatisierungstechnik
der Technischen Universität Ilmenau

von Dipl.-Ing. Alexander Gussew
geboren am 13. Juni 1979 in Perm, Russische Föderation

Tag der Einreichung: 14. Februar 2011

Tag der wissenschaftlichen Aussprache: 11. Juli 2011

Gutachter:

1. Apl. Prof. Dr.-Ing. habil. Andreas Keller
2. Prof. Dr. rer. nat. med. habil. Jürgen R. Reichenbach
3. Univ. Prof. Dr. Ewald Moser

urn:nbn:de:gbv:ilm1-2011000210

Zusammenfassung

Die vorliegende Arbeit beschreibt die Anwendung der Protonenmagnetresonanzspektroskopie (^1H -MRS) zum nicht invasiven Nachweis von schmerzinduzierten Änderungen des erregenden Neurotransmitters Glutamat sowie anderer Metaboliten im menschlichen Gehirn. Diese Informationen könnten zu einem tieferen Verständnis der biochemischen Prozesse während der zerebralen Schmerzverarbeitung beitragen. Nach einer kurzen Einführung in die Problematik der Schmerzforschung sowie in die Grundlagen der MRS-Technik wird eine im Rahmen dieser Arbeit implementierte Methode zur Berechnung absoluter Metabolitenkonzentrationen unter Berücksichtigung der heterogenen Gewebeszusammensetzung im spektroskopischen Volumen beschrieben. Der Vorteil dieses Verfahrens in Bezug auf die Verbesserung der Quantifizierungsgenauigkeit wird anhand von Ergebnissen spektroskopischer Messungen in einem Phantom sowie in Gehirnen gesunder Probanden belegt. Der zweite Teil befasst sich mit der Implementierung einer Technik zur reizgetriggerten Akquisition von MR Spektren, welche eine Abtastung verschiedener Stimulationszustände mit einer zeitlichen Auflösung von wenigen Sekunden zulässt und somit die Detektion dynamischer Änderungen von Metaboliten im Gehirn ermöglicht. Durch die Anwendung dieser Methode bei Messungen an gesunden Probanden konnten Änderungen im Glutamatstoffwechsel infolge einer Stimulation mit kurzen akuten Schmerzreizen nachgewiesen werden. Im dritten Teil der Arbeit wird schließlich eine an gesunden Probanden und Patienten mit chronischen Schmerzen durchgeführte Studie vorgestellt, innerhalb derer die Auswirkungen der Schmerzchronifizierung auf den Metabolismus in schmerzverarbeitenden kortikalen Regionen untersucht wurden. Die Ergebnisse dieser Studie belegen die Hypothese, dass chronischer Schmerz mit Veränderungen im Neurotransmitterstoffwechsel sowie mit degenerativen Prozessen auf zellulärer Ebene einhergeht. Zusammenfassend lässt sich sagen, dass es mit der ^1H -MRS möglich ist, schmerzinduzierte Änderungen der Metaboliten im menschlichen Gehirn unter Verwendung von klinischen Standardverfahren zu quantifizieren. Dies wiederum eröffnet ein breites Feld für weitere Untersuchungen, welche zur Erforschung der zerebralen Schmerzverarbeitung sowie zur Verbesserung der Spezifität diagnostischer Verfahren bei chronischen Schmerzen beitragen könnten.

Abstract

In this work non-invasive *in vivo* detection of excitatory neurotransmitter glutamate and other cortical metabolites and their changes in the presence of acute and chronic pain was performed in the human brain with proton magnetic resonance spectroscopy (^1H -MRS). This information can be used to better understand biochemical processes of cerebral pain processing. Following introductory material, the first part of this thesis describes the implemented method for post-processing of MR spectroscopic data to estimate absolute concentrations of the brain metabolites by considering the heterogeneous tissue composition in the spectroscopic voxel. Phantom and *in vivo* brain studies demonstrated the advantage of this method by reduced inter-individual variation of calculated metabolic concentrations as well as enhanced quantitation accuracy. The second part of this work presents the implemented method for the stimulus triggered data sampling permitting the acquisition of *in vivo* ^1H -MR spectra with a time resolution of few seconds. It was shown that this method enables detection of changes of the neurotransmitter glutamate induced by short acute pain stimuli. Considering these data, it was possible to characterise changes of the glutamatergic neurotransmission associated with the sensation of the acute pain. The third part describes *in vivo* measurements on chronic pain patients and healthy controls aiming to evaluate the changes of several brain metabolites in the different cerebral pain processing regions associated with chronic pain. Patients revealed decreased concentrations of the metabolic cell density markers and neurotransmitters indicating the degenerative processes as well as neurotransmitter dysfunctions, respectively. Results of this thesis indicate that pain induced metabolic changes in the human brain are traceable with the ^1H -MRS by using experimental environment as it is used in clinical routine. This offers a broad spectrum of further applications aiming to explore the cerebral pain processing as well as to improve the specificity of the diagnostic assessment of the chronic pain disease.

Abbreviations

α_x	Relative water content in tissue X
\vec{B}_0	Main static magnetic field
$\vec{B}_1(t)$	Time variant excitation magnetic field
BOLD	Blood Oxygen Level Dependent contrast
BW	Sampling bandwidth
CHESS	CHEmical Shift Selective water suppression
CLBP	Chronic low back pain
CRLB	Cramer-Rao-Lower-Bound
CSF	Cerebrospinal fluid or liquor
CSI	Chemical shift imaging
Cr	Creatine
C_x	Concentration of substance X
EC	Eddy Current
FID	Free Induction Decay
fMRS	Functional Magnetic Resonance Spectroscopy
FWHM	Full Width at Half Maximum
f_x	Relative volume fraction of tissue X in the MRS voxel
GABA	γ -aminobutyric acid
Glu	Glutamate
Gln	Glutamine
Glx	Sum of glutamate and glutamine
GM	Grey matter
G_x, G_y, G_z	Magnitudes of linear magnetic field gradients
h	Planck constant
I_x	Signal intensity of substance X
J	Scalar coupling constant
\vec{L}	Intrinsic angular momentum
LCModel	Linear Combination Model
mI	<i>Myo</i> -Inositol
MM	Macromolecule
MRI	Magnetic Resonance Imaging
MRS	Magnetic Resonance Spectroscopy
MP-RAGE	Magnetization Prepared Rapid Gradient Echo

\vec{M}_{xy}	Transverse macroscopic magnetisation
\vec{M}_z	Longitudinal macroscopic magnetisation
NAA	N-acetyl-aspartate
NAS	Number of averaged single acquisitions
NMR	Nuclear Magnetic Resonance
N_{samp}	Number of sampled time course points
PRESS	Point RESolved Spectroscopy
R_x	Relaxation related signal attenuation for substance X
SD	Standard deviation
SNR	Signal to noise ratio
SVD	Singular Value Decomposition
SVS	Single Voxel Spectroscopy
T_1	Time constant of longitudinal relaxation
T_2	Time constant of transverse relaxation
TA	Acquisition time
tCho	total choline (phosphorylcholine + glycerophosphorylcholine)
TE	Echo time
TR	Repetition time
TTL	Transistor Transistor Logic
$u(t)$	Time signal
$U(\omega)$	Frequency spectrum
VAS	Visual-Analogue pain Scale
VoI	Volume of Interest
Vox	Voxel
w_k	Channel weighting factor
WM	White matter
γ	Gyromagnetic ratio
δ	Chemical shift
φ	Signal phase
$\vec{\mu}$	Nuclear magnetic moment
$\vec{\omega}_0$	Larmor frequency

Contents

1	Introduction	1
1.1	Historical development of anatomical imaging	1
1.2	Magnetic resonance spectroscopy (MRS)	2
1.3	<i>In vivo</i> MR spectroscopic investigation of pain related metabolic changes in the brain	4
1.4	Objectives of the thesis	6
2	NMR Basics	9
2.1	Physical principles of Nuclear Magnetic Resonance (NMR)	9
2.1.1	Nuclear spin and magnetic moment	9
2.1.2	Macroscopic magnetisation	11
2.1.3	Resonance	12
2.1.4	Relaxation	13
2.1.5	NMR signal detection	16
2.2	Magnetic resonance imaging (MRI)	18
2.2.1	Slice selection	19
2.2.2	Frequency encoding	19
2.2.3	Phase encoding	19
2.2.4	Two dimensional spatial encoding	20
2.3	Magnetic resonance spectroscopy (MRS)	22
2.3.1	Identification of chemical compounds	23
2.3.1.1	Chemical shift and peak intensity	23
2.3.1.2	Spin-spin coupling and peak splitting	24
2.3.2	<i>In vivo</i> MRS	27
2.3.2.1	Localisation of target volume	27
2.3.2.2	Preparation of <i>in vivo</i> MRS examination	30
2.3.3	Absolute quantitation of MR spectra	33
2.3.3.1	Importance and method description	33
2.3.3.2	External and internal referencing	34
2.3.3.3	Data pre-processing	35
3	Absolute quantitation of brain metabolites	41
3.1	Introduction	41

3.1.1	Theoretical aspects	41
3.1.2	Determination of the tissue volume fractions in the brain	44
3.2	Combined processing of MRI and MRS data	47
3.2.1	Description of the data processing stream	47
3.2.2	Tissue segmentation of brain MRI data	47
3.2.3	Co-alignment of MRI and MRS data	50
3.3	Experimental validation	52
3.3.1	General experimental conditions	53
3.3.2	Post-processing of MR spectra	53
3.3.3	<i>In vitro</i> study	54
3.3.3.1	Description of phantom	54
3.3.3.2	Performed measurements	55
3.3.4	<i>In vivo</i> study	57
3.3.4.1	Performed measurements	58
3.3.4.2	Post processing of MRI and MRS data	58
3.3.4.3	Statistical data evaluation	59
3.4	Results	59
3.4.1	<i>In vitro</i> study	59
3.4.2	<i>In vivo</i> study	61
3.5	Discussion	63
3.5.1	<i>In vitro</i> study	65
3.5.2	<i>In vivo</i> study	67
4	<i>In vivo</i> functional ¹H-MRS	71
4.1	Introduction	71
4.1.1	Functional neuroimaging	71
4.1.2	Functional MR spectroscopy (fMRS)	72
4.1.2.1	<i>In vivo</i> ¹³ C-fMRS	72
4.1.2.2	<i>In vivo</i> ¹ H-fMRS	73
4.2	Time resolved fMRS experiments during pain stimulation	75
4.2.1	Application of painful heat stimuli	75
4.2.2	Spectroscopic data sampling	76
4.2.3	Reconstruction of MR spectra	78
4.2.4	Weighted linear combination of multi-channel MRS data	82
4.3	<i>In vivo</i> examinations on healthy volunteers	87
4.3.1	Subject population	87
4.3.2	Adjustment of stimulus temperature	88
4.3.3	Acquisition of MRI and MRS data	88
4.3.4	Calculation of absolute metabolic concentrations	89
4.4	Results of <i>in vivo</i> ¹ H-fMRS study	89

4.4.1	Evaluation of subjectively perceived pain intensity	89
4.4.2	Evaluation of spectroscopic data quality	90
4.4.3	Evaluation of pain related metabolite level changes	90
4.5	Discussion	94
4.5.1	Technical aspects of implemented method	94
4.5.2	Detection of heat pain associated glutamate changes	96
5	<i>In vivo</i> brain ¹H-MRS at chronic pain	99
5.1	Introduction	99
5.2	Material and Methods	99
5.2.1	Patient population	99
5.2.2	MR imaging and ¹ H-MR spectroscopy	100
5.2.3	Quantitation of ¹ H-MRS data	101
5.2.4	Evaluation of structural MRI data	101
5.2.5	Statistical analysis	101
5.3	Results	102
5.3.1	Spectroscopic data quality	102
5.3.2	CLBP related metabolic changes	102
5.3.3	CLBP related morphological changes	107
5.4	Discussion	109
6	Conclusions and Outlook	115
	Bibliography	126
	List of Figures	128
	List of Tables	129
	Appendix	131
A.1	Look-up table for brain tissue class labeling of MRI data	131

1 Introduction

1.1 Historical development of anatomical imaging

Since thousands of years humans have been dealing with the exploration of the anatomical structure of the human body, but also with the exploration of the physiological processes taking place in biological tissue. On the one hand, they recognised that all diseases are associated with damage of tissue. On the other hand, they also believed that exploring their own body can provide a deeper understanding of complex phenomena, like emotions or self-perception, which also play an important role in the occurrence or healing of diseases. Around 300 B.C., the Greek physicians Herophilos and Erasistratus performed the first anatomical research based on dissections of human cadavers and obtained a more informed view of the human body than was previously available [Staden, 1989]. For example, these ancient scientists distinguished between arteries and veins, described the function of the heart as a mechanical pump and identified the physiological meaning of brain ventricles. Dissection remained the only method for gaining knowledge about human anatomy until the end of the 19th century, when the first X-ray image, depicting a human hand (see Fig. 1.1 left), was taken by Wilhelm Conrad Röntgen [Röntgen, 1895]. Only a few years later, X-rays were routinely used for medical purposes. Since then, the X-ray technology has undergone tremendous development, and today it is used for example in computed tomography (CT) to acquire three-dimensional images of the human body with excellent contrast (see Fig. 1.1 right) [Kalender, 2006].

Alternative imaging techniques, which do not utilize the potentially dangerous ionizing radiation of X-rays, are also in widespread use. The most prevalent of these is *Magnetic Resonance Imaging* (MRI) with its advantage of excellent contrast between soft tissues (i.e., grey and white matter in the brain, cerebral spinal fluid in ventricles, muscles and fat). The development of MRI dates back to the pioneering research efforts of Felix Bloch and Edward Purcell, who discovered the *Nuclear Magnetic Resonance* (NMR) phenomenon in 1946 [Bloch et al., 1946; Purcell et al., 1946]. This phenomenon arises from the interaction of magnetic moments of atomic nuclei with static magnetic fields and *radio frequency* (rf) radiation in the range of several tens of MHz. The spatial mapping of NMR signals in a thin slice of a sample is made possible by using magnetic field gradients, which vary the resonance frequencies of atomic nuclei as a function of position [Lauterbur, 1973; Mansfield and Grannell, 1973]. The most abundant isotope in biological tissue that gives rise to an NMR signal is hydrogen (¹H). Therefore, almost all clinical MRI appli-

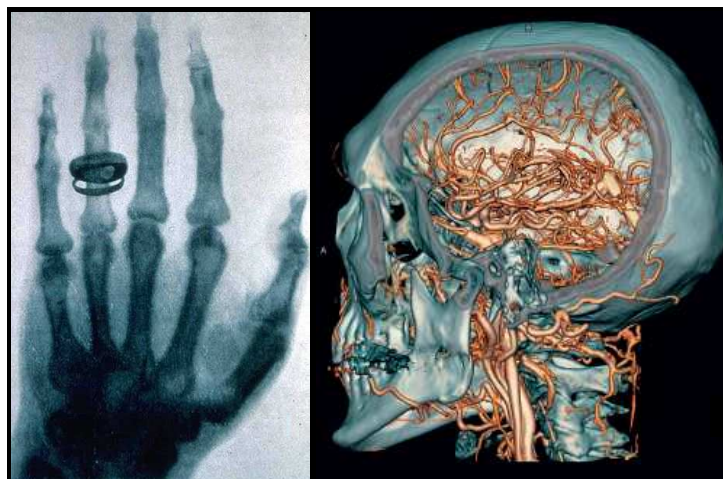


Figure 1.1: An X-Ray image of a human hand (a) acquired by W.C. Röntgen in 1896 and a high resolution reconstruction of 3D CT data from human head bones and cortical vessels (b) Images (a) and (b) were adapted from <http://de.wikipedia.org/wiki/Röntgen> and http://www.medical.siemens.com/siemens/en_INT/gg_ct_FBAs/files/somatomworld/somatom_sessions/SOMATOM_Sessions_19.pdf, respectively).

cations are based on the detection of ^1H -NMR signals. The fact that these signals are sensitive to physiological properties, like nuclei density, diffusion, molecular mobility and magnetic susceptibility, makes MRI a very versatile modality, which can be used to obtain information about a large number of different anatomical and physiological parameters, which are varying between different types of biological tissue (see Fig. 1.2). Thus, MRI is ideally suited to detect morphological and pathological changes (e.g. tumours), which are associated with changes of MR relevant properties.

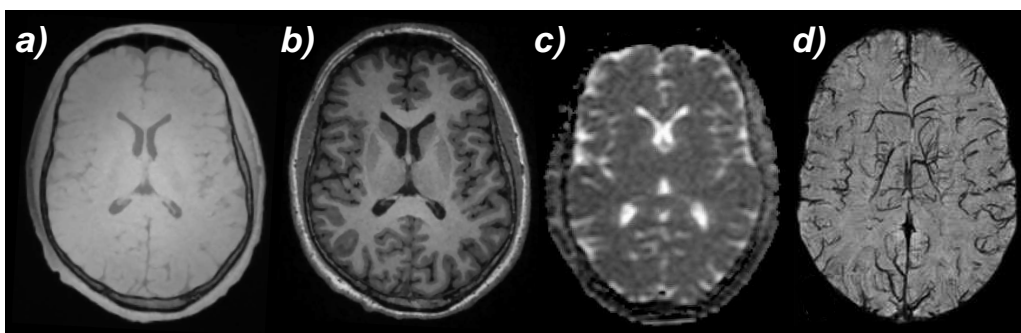


Figure 1.2: Different MRI contrasts of the transverse brain slice: (a) hydrogen density based contrast, (b) T_1 relaxation based contrast [Güllmar, 2008], (c) particle diffusion based contrast [Hiepe, 2009] and (d) magnetic susceptibility based contrast [Deistung et al., 2008].

1.2 Magnetic resonance spectroscopy (MRS)

In contrast to the morphological information extracted by MRI, *Magnetic Resonance Spectroscopy* (MRS) allows non-invasive detection of biochemical substances (metabolites)

directly in the living tissue (see Fig. 1.3).

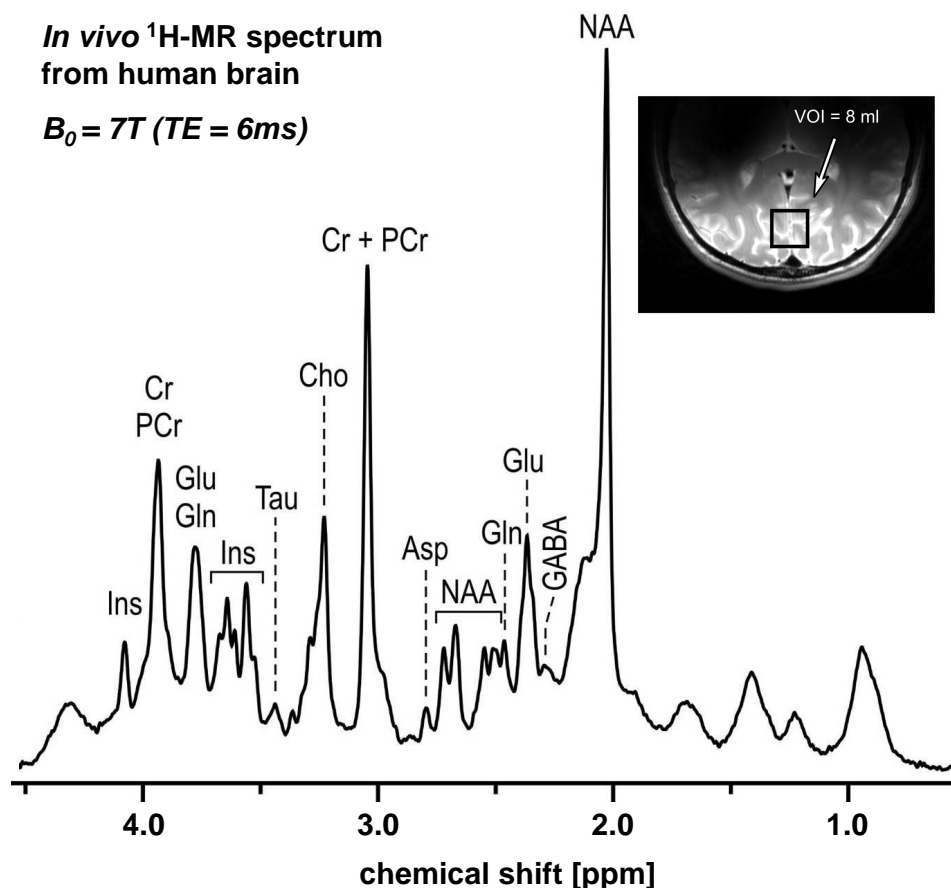


Figure 1.3: *In vivo* ^1H -MR spectrum from the occipital cortex of a healthy volunteer ($B_0 = 7\text{T}$; STEAM based single voxel spectroscopy; $TE = 6\text{ms}$). Abbreviations of detectable metabolites: NAA: N-Acetyl-Aspartate; GABA: γ -aminobutyric acid; Glu: glutamate; Gln: glutamine; Asp: aspartate; Cr: creatine; PCr: phosphocreatine; Cho: choline; Tau: taurine; Ins: myo-inositol. [Tkáč and Gruetter, 2005]

The appearance of metabolite resonances in different frequency ranges in an MR spectrum is due to the fact that resonance frequencies are affected by the electronic environment of an atomic nucleus within a molecule [Dickinson, 1950; Proctor and Yu, 1950]. Similar to MRI, clinical *in vivo* applications of MRS are mostly based on the detection of signals from hydrogen nuclei (^1H). With human whole-body MR scanners operating at static magnetic fields of 1-7 T, *in vivo* ^1H -MRS is sensitive enough to detect low-molecular weight metabolites with tissue concentrations typically larger than 1 mmol/l (e.g., choline, creatine, lactate or amino-acids). The concentrations in tissue may change in pathological cases, since these metabolites are involved in different processes, like cell membrane metabolism (choline), energy metabolism in cell mitochondria (creatine), intercellular transmission of action potentials between neurons (amino acids glutamate and GABA) and metabolism of specific cell types (N-acetyl-aspartate in neurons and myo-Inositol in astroglial cells) [Govindaraju et al., 2000]. Due to this additional information, MRS rep-

resents a powerful clinical tool, which can be used in combination with other imaging modalities, like MRI, CT or *Positron Emission Tomography* (PET) to increase specificity of diagnostic assessment. Applying MRS can contribute to early detection of diseases, since metabolic alterations frequently occur prior to the manifestation of morphological changes. Today, ^1H -MRS is usually applied for diagnosis and therapy monitoring of cancer, multiple sclerosis, Alzheimer disease, metabolic diseases, hypoxic tissue damage or inflammatory processes [Burtscher and Holtås, 2001; Heyne et al., 2006; Mountford et al., 2010]. With recent advances it has become possible to extract metabolic markers related to the occurrence and progress of psychiatric disorders, such as schizophrenia or depression [Mason and Krystal, 2006; Rzanny et al., 2003; Smesny et al., 2007]. In a study on brains of pig cadavers, Banaschak et al. [2005] demonstrated the possibility to determine the *post mortem* interval by analysing time courses of metabolic changes occurring after death over several weeks. Besides measuring ^1H compounds, MRS is also able to measure the signals of phosphorous nuclei (^{31}P) in molecules and, thus allows to explore the energy metabolism *in vivo* by detecting metabolites like *Adenosine Triphosphate* (ATP), *Phosphocreatine* (PCr) or *inorganic phosphate* (Pi). This feature, for instance, can be utilised to detect changes in energy metabolism of muscles during exercise and to use this information for the diagnosis of muscle fatigue or injuries [Rzanny et al., 2006].

1.3 *In vivo* MR spectroscopic investigation of pain related metabolic changes in the brain

One rather exciting ongoing direction in clinical research is to explore and investigate processes that are underlying the perception of pain. Due to its protective function with respect to human survival, pain perception represents an important physiological sense. However, if acute pain turns to chronic pain its original relevance for maintaining health is lost, and quality of life may decline dramatically for the affected person. In many cases, chronic pain also triggers depression, anxiety states or other mental disorders [Tracey and Bushnell, 2009]. One of the rife forms of chronic pain disease in Western industrial countries is *chronic low back pain* (CLBP) [Andersson, 1999], which is associated with high direct and indirect costs for healthcare systems due to potential invalidity and lifelong therapy [Dagenais et al., 2008]. One particularly critical point is the lack of precise knowledge about the origins and causes of CLBP. In fact, the real challenge is to distinguish spinal pathology from non-specific low back pain [Rubinstein and van Tulder, 2008]. In Western Europe only 10 % of CLBP cases can be ascribed to defined pathological disorders. For the remaining 90 % of patients the disease is characterised as *non-specific chronic low back pain* (nCLBP) [Krismer and Tulder., 2007]. Consequently, therapeutic approaches are also non-specific and therefore often less efficient. Improved understanding of the pathological origins underlying the manifestation of chronic pain may thus help to

develop specific preventive or therapeutic methods for managing chronic pain disease [Borsook et al., 2007].

One frequently discussed hypothesis why pain turns from an acute to a chronic state assumes hypersensitisation and reorganisation of neuronal networks in the central nervous system (CNS) [Borsook et al., 2007; Brooks and Tracey, 2005; Tracey and Bushnell, 2009]. Due to the hypersensitisation peripheral stimuli, which are normally perceived as non-painful, induce massive pain sensation. Recent results of modern functional neuroimaging methods, like *functional magnetic resonance imaging* (fMRI) or PET, have already revealed new insights into the functional and spatial aspects of cerebral pain processing in humans [Apkarian et al., 2005; Peyron et al., 2000]. The so-called '*Pain Matrix*' comprises brain areas such as insular cortex, cingulate cortex, medial prefrontal cortex, thalamus and amygdala [Borsook et al., 2007]. It has been shown that chronic pain leads to structural changes (degeneration) in these areas. However, the question about the origins of these changes still remains open. Recent spectroscopic studies described altered neurotransmitter metabolism in the brain of chronic pain patients [Harris et al., 2009; Mountford et al., 2010; Prescott et al., 2009; Siddall et al., 2006; Stanwell et al., 2010] as well as cellular degenerative processes reflecting structural changes [Fukui et al., 2006; Grachev et al., 2002; Pattany et al., 2002]. Therefore, the MRS may be crucial to understand the biochemical origins of chronic pain associated changes in the brain.

Hypersensitisation of cerebral regions that processing pain may be assumed to be reflected in disordered neuronal activations. However, measuring changes of blood oxygenation by fMRI or detecting altered glucose consumption by PET only reflects changes of global neuronal activity without a direct link to the underlying metabolic processes. Unlike these techniques, ^1H -MR spectroscopy makes it possible to selectively detect excitatory or inhibitory neurotransmitters in the brain, such as glutamate (Glu), γ -aminobutyric acid (GABA) or intermediate neurotransmission products, like glutamine (Gln). In chronic pain disease, it potentially may help to ascertain, whether the mentioned neuronal hypersensitisation is related to disordered excitatory or inhibitory neurotransmission.

Currently, describing neurotransmission events by means of *in vivo* ^1H -MR spectroscopy is limited by the low temporal resolution of data acquisition, which typically lasts at least several minutes. Consequently, in a functional experiment, i.e., in an experiment aiming to relate metabolic levels to neuronal states, the determined neurotransmitter levels reflect steady state conditions rather than event related changes. Therefore, there is a clear need to increase temporal resolution to enable functional investigations of pain associated neurotransmitter changes.

The accuracy of determining concentrations of neurotransmitters Glu, Gln or GABA *in vivo* is limited by their complex spectral multiplet structure and spectral overlap with other signals having similar chemical shifts (see Fig. 1.4). Nevertheless, due to its relatively high concentration in the brain (ca. 8–10 mmol/l), Glu can be reliably quantified by using conventional ^1H -MRS techniques, even at 3 T on clinical whole body MR scanners [Gussew

et al., 2008; Schubert et al., 2004]. The low cortical levels of Gln (2–4 mmol/l) and GABA (1 – 20 mmol/l) [Govindaraju et al., 2000] require improved detection sensitivity, which can, for instance, be achieved with higher magnetic fields (> 3 T) [Tkáč and Gruetter, 2005] or by applying modified MR spectroscopic techniques, such as spectral editing [Rothman et al., 1984].

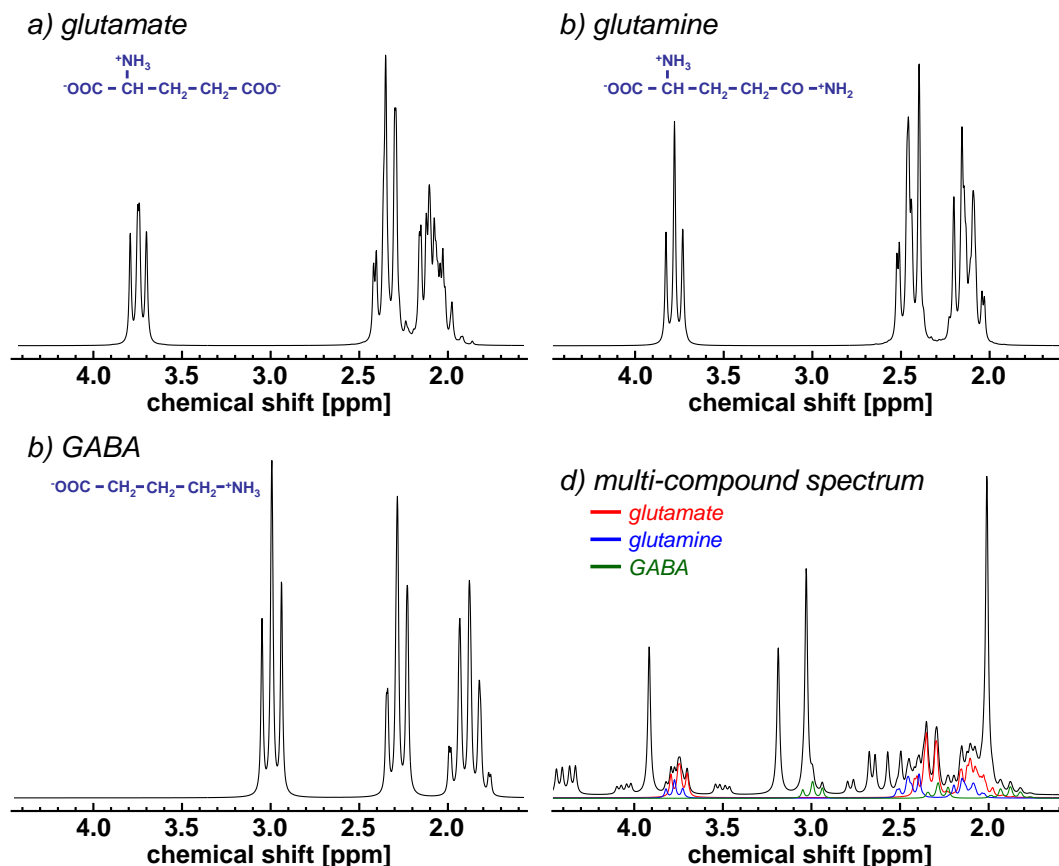


Figure 1.4: Simulated ^1H -MR spectra of glutamate (a), glutamine (b), GABA (c) show their complex spectral multiplet structures. In a multi-compound spectrum (d) the direct identification of Glu (red), Gln (blue) and GABA (green) is limited by spectral overlap with other signals (here NAA, Cr, Cho) having similar chemical shifts as well as by their low intensities due to the low cortical concentrations. ^1H -MR spectra were simulated for $B_0 = 3\text{ T}$ and $TE = 0\text{ ms}$ by using NMR Scope tool included in the jMRUI 4.0 package (<http://www.mrui.uab.es/mrui/>).

1.4 Objectives of the thesis

Against this background, the main objective of the present thesis was to investigate possibilities of detecting pain associated neurotransmitter changes in the human brain.

Specifically, an experimental method was implemented for time resolved sampling of spectroscopic data during pain stimulation (see Chap. 4). It was hypothesised that pain perception due to short acute pain stimuli causes an enhanced glutamatergic neurotrans-

mission in corresponding brain areas. To prove this hypothesis, *in vivo* experiments were performed in healthy volunteers.

The second aim was to investigate whether metabolic changes exist in the brain of patients suffering from chronic pain (see Chap. 5). Assuming elevated Glu release during pain perception (as it should be verified in the healthy volunteer study in Chap. 4), it was hypothesised that chronic pain should lead to excitotoxic neuronal damage due to prolonged enhanced glutamatergic activity [Mark et al., 2001]. This, in turn, should be reflected in morphological changes as well as in decreased concentrations of cerebral metabolic cell density markers (NAA, mI).

The thesis contains four major parts. The first part (chapter 2) covers techniques of *in vivo* proton MR spectroscopy. Starting from basic principles of magnetic resonance imaging and magnetic resonance spectroscopy, this chapter focuses on localised data acquisition and quantitation of ^1H -MR spectra in tissue.

The second part (chapter 3) describes the post-processing of MRS and MRI brain data to determine absolute metabolite concentrations from brain ^1H -MR spectra while taking into account the heterogeneous tissue composition in spectroscopic voxels. The experimental part of this chapter covers the results of two studies, which were performed with a multi-compartment phantom with aqueous metabolite solutions (*in vitro* study) and with healthy volunteers (*in vivo* study), respectively, to evaluate the accuracy of metabolite quantitation with the implemented method.

The third part (chapter 4) describes the implemented experimental approach for time-resolved detection of pain associated glutamate changes. This chapter also summarises the results of experiments, performed in healthy volunteers during application of short heat pain stimuli.

Finally, the fourth part (chapter 5) presents the results of clinical ^1H -MR spectroscopic measurements on healthy controls and patient with chronic low back pain to evaluate metabolic changes associated with chronic pain disease.

2 Basics of MR imaging and MR spectroscopy

2.1 Physical principles of Nuclear Magnetic Resonance (NMR)

2.1.1 Nuclear spin and magnetic moment

The fundamental principle of all nuclear magnetic resonance (NMR) techniques is based on the interaction of elementary nuclear particles (nucleons), like protons, neutrons and electrons, with externally applied magnetic fields. Besides their rest mass and electrical charge nucleons exhibit another fundamental property - the intrinsic angular momentum or spin (\vec{L}). According to quantum mechanics, the magnitude of nuclear angular momentum is always restricted to discrete values [de Graaf, 2007]:

$$|\vec{L}| = \frac{h}{2\pi} \cdot \sqrt{I(I+1)} \quad (2.1)$$

$$h = 6.62 \cdot 10^{-34} \text{ J} \cdot \text{s}$$

$$I = \text{spin quantum number}; I = 0, \frac{1}{2}, 1, \frac{3}{2}, \dots$$

If there exists a preferred spin direction, for example due to the presence of an external magnetic field, the orientation of \vec{L} is specified by a second spin quantum number m with $2I+1$ different values ($-I, -I+1, \dots, I-1, I$). For example, in protons or neutrons with $I = 1/2$, the z -component of \vec{L} , i.e., the component parallel to the magnetic field pointing along the z -axis in a 3D coordinate system, can only take two orientations (assuming the magnetic field pointing along the z -axis in a 3D coordinate system), characterised by $m = -1/2$ and $m = 1/2$:

$$\vec{L}_z = \frac{h}{2\pi} \cdot m \cdot \vec{e}_z. \quad (2.2)$$

Atomic nuclei consist of protons and neutrons. Thus, their nuclear spin is composed of the spins of all nuclear particles (nucleons). Depending on the number of protons and neutrons in the nucleus, the nuclear spin quantum number may be equal to zero (the numbers of protons and neutrons are both even), half integral (for isotopes with odd mass numbers) or integral (the numbers of protons and neutrons are both odd). In general, only nuclei with non-zero spin in the ground state are relevant for NMR, since only these nuclei have a net nuclear magnetic moment $\vec{\mu}$, which interacts with external

magnetic fields. The relationship between the nuclear angular momentum and the nuclear magnetic moment is given by:

$$\vec{\mu} = \gamma \cdot \vec{L}, \quad (2.3)$$

The gyromagnetic ratio γ is the proportionality constant of this relationship and is characteristic for each isotope (see Tab. 2.1).

Table 2.1: List of selected isotopes with their spins, characteristic values of the gyromagnetic ratio (γ in $MHz \cdot T^{-1}$), corresponding magnitudes of the Larmor-frequency $\vec{\omega}_0$ (at $|\vec{B}_0| = 3$ Tesla in MHz) and natural abundance. The table is adapted from [de Graaf, 2007].

Isotope	I	γ [MHz/T]	ω_0 at 3T [MHz]	Natural abundance [%]
^1H	1/2	42.02	126.1	99.985
^{13}C	1/2	10.57	31.7	1.108
^{31}P	1/2	17.03	51.1	100.000
^{23}Na	3/2	11.12	33.4	100.000

Due to its relation with the nuclear angular momentum (see Eq. 2.3), $\vec{\mu}$ is also characterised by discrete orientations in the presence of an external magnetic field:

$$\vec{\mu}_z = \gamma \cdot \vec{L}_z = \gamma \cdot \frac{h}{2\pi} \cdot m \cdot \vec{e}_z \quad (2.4)$$

When exposed to an external magnetic field \vec{B}_0 , spins experience a torque \vec{T} due to the interaction between \vec{B}_0 and $\vec{\mu}$, which is given by:

$$\vec{T} = \vec{\mu} \times \vec{B}_0 \quad (2.5)$$

Since $\vec{\mu}$ is associated with an angular momentum \vec{L} , the magnetic moment is unable to follow the field directly. Rather the torque induces a rate of change of the angular momentum that, by considering Eq. 2.3, can be written:

$$\vec{T} = \frac{d\vec{L}}{dt} = \frac{1}{\gamma} \cdot \frac{d\vec{\mu}}{dt} \quad (2.6)$$

Combining Eqs. 2.5 and 2.7 gives:

$$\frac{d\vec{\mu}}{dt} = \gamma \cdot [\vec{\mu} \times \vec{B}_0] \quad (2.7)$$

Since the magnitude of $\vec{\mu}$ remains constant, the torque induced change of $\vec{\mu}$ means that the nuclear magnetic moment periodically changes its orientation relative to \vec{B}_0 , i.e., it rotates (or precesses) around the \vec{B}_0 axis with an angular frequency $\vec{\omega}_0$ (so-called *Larmor*

frequency):

$$\begin{aligned} \frac{d\vec{\mu}}{dt} &= \vec{\mu} \times \vec{\omega}_0 \\ \text{with } \vec{\omega}_0 &= -\gamma \cdot \vec{B}_0 \end{aligned} \quad (2.8)$$

The magnitude of the Larmor frequency depends on the magnitude of the applied \vec{B}_0 field and is also specific for different nuclei (see the Tab. 2.1). The sign of the gyromagnetic ratio γ defines the sense of the spin precession around the applied field. Most nuclei have positive γ implying the negative sign of the Larmor frequency and therefore the precession is in the clockwise direction [Levitt, 2008].

The potential energy E due to the interaction between $\vec{\mu}$ and \vec{B}_0 , is given by:

$$E = -|\vec{\mu}_z| \cdot |\vec{B}_0| \quad (2.9)$$

By considering the discrete orientations of $\vec{\mu}_z$ (see Eq. 2.4), spins with $I = 1/2$ (e.g. hydrogen nuclei ^1H) can occupy two discrete energy levels, E_1 or E_2 , which are corresponding to parallel and anti-parallel orientations of $\vec{\mu}_z$ relative to \vec{B}_0 , respectively:

$$\begin{aligned} E_1 &= -\frac{h}{2\pi} \cdot \frac{1}{2} \cdot \gamma \cdot |\vec{B}_0| & \text{for } m = +\frac{1}{2} \\ E_2 &= +\frac{h}{2\pi} \cdot \frac{1}{2} \cdot \gamma \cdot |\vec{B}_0| & \text{for } m = -\frac{1}{2} \end{aligned} \quad (2.10)$$

The difference between E_1 and E_2 depends on the strength of the \vec{B}_0 field:

$$\Delta E = E_2 - E_1 = \frac{h}{2\pi} \cdot \gamma \cdot |\vec{B}_0| = \frac{h}{2\pi} \cdot |\vec{\omega}_0| \quad (2.11)$$

2.1.2 Macroscopic magnetisation

Since observable macroscopic *Nuclear Magnetic Resonance* (NMR) phenomena result from the interaction of a large number of nuclei with \vec{B}_0 , one adequate description of these phenomena is not to consider the behaviour of individual nuclei, but rather to describe the behavior collectively of a macroscopic magnetisation resulting from the nuclear magnetic moments of all participating nuclei. For hydrogen nuclei (^1H), the two allowed orientations of $\vec{\mu}_z$ imply that two spin populations with different energies will exist in the presence of \vec{B}_0 . In thermodynamic equilibrium, the ratio between the number of parallel spins (N_\uparrow , lower energy level E_1) and anti-parallel spins (N_\downarrow , higher energy level E_2) is given by the Boltzmann distribution:

$$\frac{N_\uparrow}{N_\downarrow} = \exp\left(\frac{\Delta E}{k \cdot T}\right) = \exp\left(\frac{h \cdot \gamma \cdot |\vec{B}_0|}{2\pi \cdot k \cdot T}\right), \quad (2.12)$$

where k is the Boltzmann constant ($k = 1.38066 \cdot 10^{-23}$ J/K) and T the absolute temperature in Kelvin. For example, for a 1 mm^3 large sample of water placed in a 3 Tesla

magnetic field at 37° ($= 310.15\text{ K}$), the relative thermal equilibrium excess of parallel hydrogen nuclei is only 0.002%. However, since 1 mm^3 water contains approximately $6.7 \cdot 10^{22}$ hydrogen nuclei, there are $13.3 \cdot 10^{17}$ more parallel than anti-parallel hydrogen spins in this volume. This difference gives rise to the static macroscopic magnetisation \vec{M}_0 , which has only a longitudinal non-zero component \vec{M}_z in thermodynamic equilibrium state (\vec{M}_z : longitudinal macroscopic magnetisation parallel to \vec{B}_0). In contrast, there is no transverse macroscopic magnetisation component (\vec{M}_{xy}) in thermodynamic equilibrium due to the uniform distribution of the individual phase angles of the precessing spins (phase incoherence).

Since the magnitude of measured NMR signals is proportional to the magnitude of \vec{M}_z , high values of \vec{M}_z are crucial for all NMR experiments. However, in biological samples or *in vivo* tissue, the possibilities for $|\vec{M}_z|$ enhancement are restricted to an increase of \vec{B}_0 strength, because temperature can not be changed, i.e. lowered (see Eq. 2.12).

2.1.3 Resonance

In order to detect the induced macroscopic magnetisation, a transverse magnetisation component is necessary, which rotates with angular frequency $\vec{\omega}_0$ (see Eq. 2.8) in the transverse XY plane ($\vec{M}_{xy} \perp \vec{B}_0$). Formation of transverse magnetisation \vec{M}_{xy} requires phase coherence of precessing spins. This can be achieved by an additional, oscillating magnetic field $\vec{B}_1(t)$ oriented transverse to the main magnetic field \vec{B}_0 , whose $\vec{\omega}_{rf}$ matches the Larmor-frequency of the spins (i.e., it fulfills the resonance condition):

$$\vec{B}_1(t) = |\vec{B}_1| \cdot [\cos(\omega_{rf} \cdot t) \cdot \vec{e}_x + \sin(\omega_{rf} \cdot t) \cdot \vec{e}_y + 0 \cdot \vec{e}_z] \quad (2.13)$$

From a macroscopic point of view, \vec{B}_1 causes a torque, which turns the \vec{M} vector away from the \vec{B}_0 axis. The motion of the magnetisation vector under the influence of the $\vec{B}_1(t)$ field at resonance is illustrated in Fig. 2.1a. The mathematical description of the temporal behaviour of \vec{M} is given by the Bloch equations [Bloch et al., 1946]:

$$\frac{d\vec{M}}{dt} = \gamma \cdot [\vec{M}(t) \times \vec{B}_1(t)] \quad (2.14)$$

In order to simplify the description of the \vec{M} evolution during \vec{B}_1 excitation, the stationary laboratory frame of reference $[x, y, z]^T$ is replaced by a rotating frame of reference $[x', y', z']^T$, whose x' and y' axes rotate with the Larmor frequency around the z' -axis ($z'=z$):

$$\begin{bmatrix} x' \\ y' \\ z' \end{bmatrix} = \begin{bmatrix} \cos(\omega_0 \cdot t) & -\sin(\omega_0 \cdot t) & 0 \\ \sin(\omega_0 \cdot t) & \cos(\omega_0 \cdot t) & 0 \\ 0 & 0 & 1 \end{bmatrix} \cdot \begin{bmatrix} x \\ y \\ z \end{bmatrix} = \begin{bmatrix} x \cdot \cos(\omega_0 \cdot t) - y \cdot \sin(\omega_0 \cdot t) \\ x \cdot \sin(\omega_0 \cdot t) + y \cdot \cos(\omega_0 \cdot t) \\ z \end{bmatrix} \quad (2.15)$$

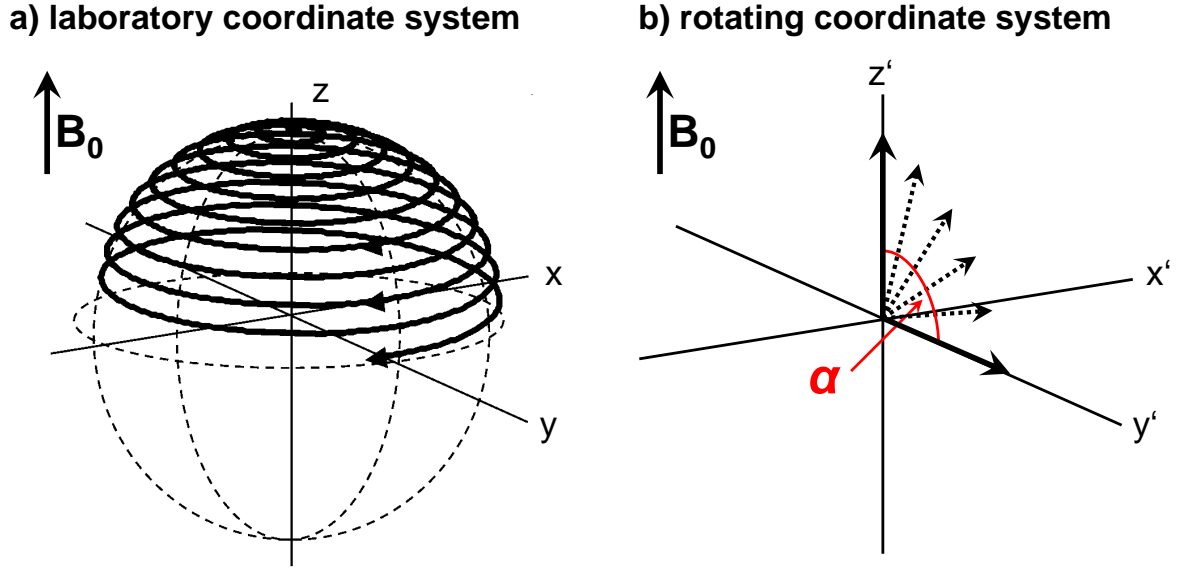


Figure 2.1: Visualisation of the trajectory of the magnetisation vector \vec{M} during the \vec{B}_1 rf excitation in the stationary laboratory (a) and rotating (b) frame of reference. The flip angle α depends linearly on the \vec{B}_1 pulse magnitude as well as on the duration of the \vec{B}_1 excitation. Subplot a) is adapted from de Graaf [2007].

As shown in Fig. 2.1b, the \vec{B}_1 induced orientational change of \vec{M} is characterised by a flip angle α with respect to the z' -axis, which depends on the \vec{B}_1 pulse magnitude and duration Δt :

$$\alpha = \gamma \cdot |\vec{B}_1| \cdot \Delta t \quad (2.16)$$

In the special case of a 90° \vec{B}_1 pulse (rf pulse), the \vec{M} vector is tilted completely into the transverse plane and the magnitude of generated transverse magnetisation \vec{M}_{xy} equals the \vec{M}_z magnitude in the thermal equilibrium state. In the case of a 180° rf pulse, \vec{M} is inverted and points along the $-z$ -axis.

2.1.4 Relaxation

Relaxation describes the return of magnetization to thermal equilibrium after the $\vec{B}_1(t)$ perturbation has been applied. As this return is usually approximately exponential, the dynamical behaviour of the magnetisation can be characterized by an exponential time constant. In fact, two relaxation processes take place simultaneously, which are characterised by time constants T_1 and T_2 : the recovery of the longitudinal magnetisation \vec{M}_z (see Fig. 2.2a) and the decay of the transverse magnetisation \vec{M}_{xy} (see Fig. 2.2b):

$$|\vec{M}_z(t)| = |\vec{M}_z(0)| \cdot \left(1 - e^{-\frac{t}{T_1}}\right) \quad (2.17)$$

$$|\vec{M}_{xy}(t)| = |\vec{M}_{xy}(0)| \cdot e^{-\frac{t}{T_2}} \quad (2.18)$$

T_1 relaxation is a process, in which energy from the spin system is transferred to the surrounding 'lattice' (which can be a solid or a liquid). T_2 or 'spin-spin' relaxation is the irreversible loss of phase coherence among the precessing spins, which is mainly caused by fluctuating microscopic magnetic fields.

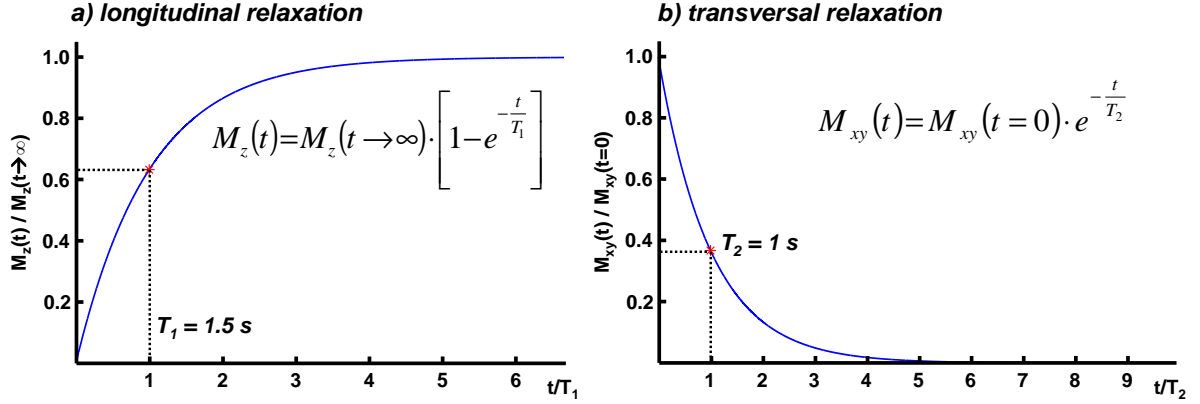


Figure 2.2: Relaxation processes following perturbation of the magnetisation with an \vec{B}_1 rf pulse: (a) exponential T_1 dependent recovery of longitudinal magnetisation \vec{M}_z and (b) exponential T_2 dependent decay of transverse magnetisation \vec{M}_{xy} . Time courses are based on simulated data.

One effect, which is associated with T_1 relaxation, is the so-called saturation of \vec{M}_z magnitude, following a series of successively performed excitations. Assuming an infinitely short T_1 (instantaneous relaxation), the longitudinal magnetisation prior to the first excitation and all following excitations would be the same. However, a finite T_1 relaxation constant induces successive reduction of the available longitudinal magnetisation depending on the time interval between the excitations (so-called *repetition time* TR):

$$|\vec{M}_z(TR)| = |\vec{M}_z(0)| \cdot \left(1 - e^{-\frac{TR}{T_1}}\right) \quad (2.19)$$

The T_2 relaxation appears as an exponential decay of \vec{M}_{xy} magnitude towards zero (thermal equilibrium). Besides the microscopic 'spin-spin' relaxation (time constant T_2), the phase coherence loss is usually accelerated by macroscopic B_0 inhomogeneities in the sample. Both, microscopic and field inhomogeneity related transverse relaxations occur simultaneously with specific time constants T_2 and $T_{2, \text{inhom}}$, respectively. The effective transverse relaxation is then characterised by the time constant T_2^* :

$$\frac{1}{T_2^*} = \frac{1}{T_2} + \frac{1}{T_{2, \text{inhom}}} \quad (2.20)$$

Typically, the time constant $T_{2, \text{inhom}}$ is substantially smaller compared to T_2 and usually dominates the transverse magnetisation loss. However, contrary to the stochastic, irreversible T_2 relaxation, the field inhomogeneity is assumed to be constant in time and

thus static. This implies that the $T_{2, \text{inhom}}$ related phase coherence loss can be reversed by applying the so-called spin echo (*SE*) method (see Fig. 2.3), which was first described in 1950 by Erwin Hahn [Hahn, 1950]. This method is based on a 90° rf excitation followed by magnetisation refocusing with a 180° rf pulse after half the echo time TE . Application of the refocusing pulse reverses the \vec{B}_0 inhomogeneity related phase shifts between spin ensembles. Therefore, after the 180° rf pulse, differently located spins start to rephase and finally generate a macroscopic transverse magnetisation (spin echo) at the time point TE . Compared to the initial \vec{M}_{xy} magnitude immediately after the 90° rf excitation, the spin echo's \vec{M}_{xy} magnitude is attenuated according to the irreversible loss of spin phase coherence due to pure T_2 relaxation:

$$|\vec{M}_{xy}(TE)| = |\vec{M}_{xy}(0)| \cdot e^{-\frac{TE}{T_2}} \quad (2.21)$$

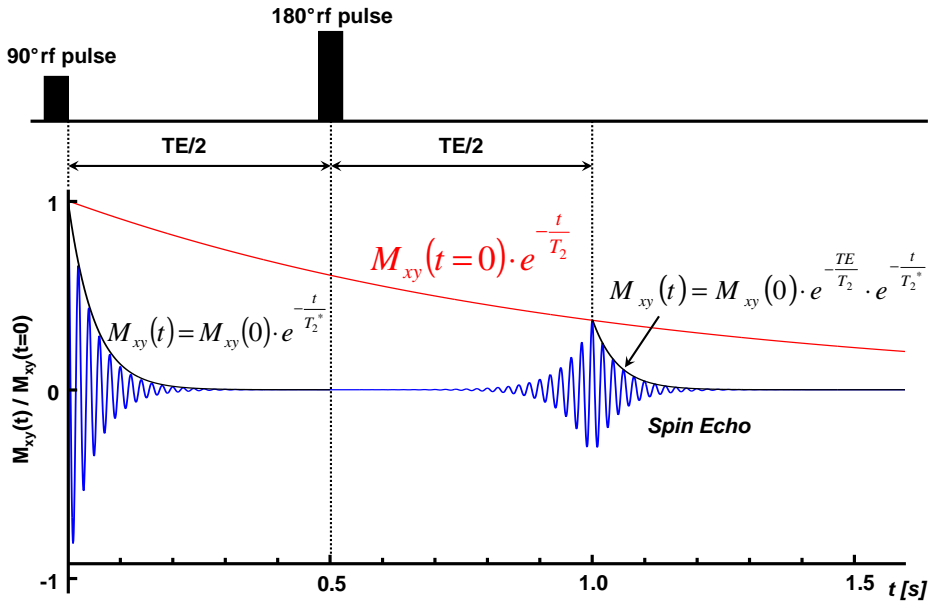


Figure 2.3: A simple spin-echo experiment consists of a 90° rf excitation followed by magnetisation inversion after $TE/2$ by means of a 180° rf pulse. After the 90° excitation the \vec{M}_{xy} magnetisation essentially decays with T_2^* due to \vec{B}_0 magnetic field inhomogeneities. An 180° rf refocusing pulse inverts the phases of spins, which leads to the generation of a spin echo at $t=TE$. At TE the magnitude of \vec{M}_{xy} is reduced relative to its initial value due to the T_2 dependent irreversible loss of spin phase coherence.

The time constants T_1 and T_2 depend on the chemical and physical properties of the investigated materials and substances (density, viscosity, temperature, chemical environment etc.). Due to this fact, the measured NMR signal magnitudes can be weighted by manipulating the saturation of longitudinal magnetisation (T_1 weighting by adjusting TR) or by manipulating the spin echo magnitudes (T_2 weighting by adjusting the TE). These signal weightings can be utilised to discriminate sample compounds with different relaxation properties. For example, in the NMR based imaging of biological samples T_1

and T_2 weighting provides additional intensity contrasts between different tissue types (brain matter, cerebrospinal fluid, lipids, muscles, blood, bones etc.).

2.1.5 NMR signal detection

After rf excitation, the transverse magnetization \vec{M}_{xy} rotates in the transverse plane with the Larmor frequency and decays exponentially due to T_2^* relaxation. In an electroconductive circuit (coil), which is placed orthogonal to the transverse plane, the rotating transverse magnetisation induces a voltage, whose strength is proportional to the magnitude as well as to the angular frequency of the rotating \vec{M}_{xy} vector. In order to discriminate both x and y components of the $|\vec{M}_{xy}|$ decay, two receive coils aligned along the x and y axes are used (see Fig. 2.4a). The measured, periodically oscillating, exponentially decaying voltages $u_x(t)$ and $u_y(t)$ are given by:

$$u_x(t) = \hat{u}(0) \cdot e^{-\frac{t}{T_2^*}} \cdot \cos(\omega_0 \cdot t + \varphi) \quad (2.22)$$

$$u_y(t) = \hat{u}(0) \cdot e^{-\frac{t}{T_2^*}} \cdot \sin(\omega_0 \cdot t + \varphi) \quad (2.23)$$

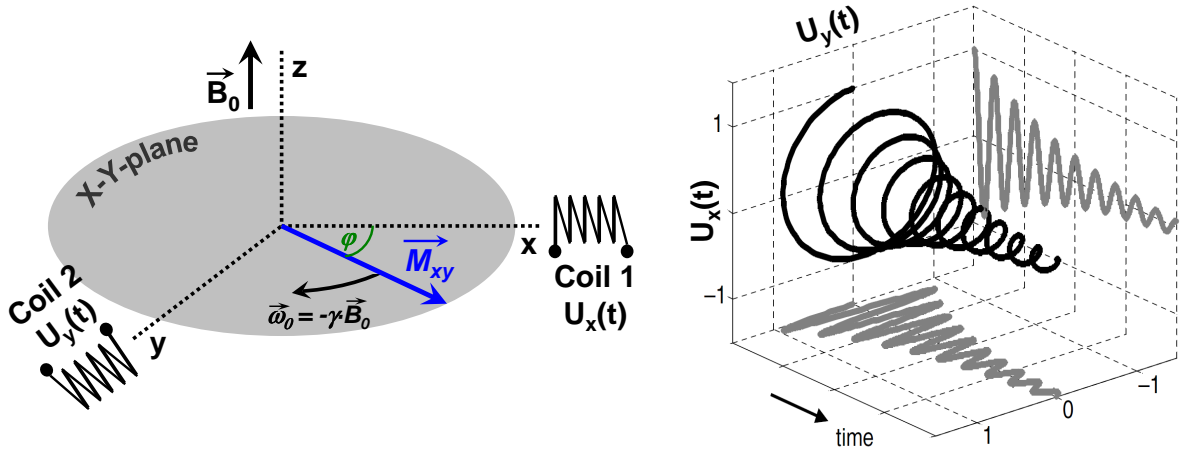


Figure 2.4: Principle of NMR signal detection with two 90° phase shifted receive coils, which are placed along the x and y axes of the transverse plane. The \vec{M}_{xy} vector rotates in the transverse plane with a nucleus specific Larmor frequency $\vec{\omega}_0$ and induces in both coils alternating currents with same magnitudes but a 90° phase shift. The magnitude of detected voltages decays with a time constant T_2^* . Right subplot is adapted from de Graaf [2007].

The signal's phase φ characterises the phase angle offset between the \vec{M}_{xy} vector and the receive coil at the time point $t = 0$. The full representation of the \vec{M}_{xy} vector rotating in the transverse plane by means of detected voltages $u_x(t)$ and $u_y(t)$ is facilitated by

using complex notation, which is referred to as the *Free Induction Decay* (FID):

$$\begin{aligned}
 u(t) &= u_x(t) + j \cdot u_y(t) = \\
 &= \hat{u}(0) \cdot e^{-\frac{t}{T_2^*}} \cdot [\cos(\omega_0 \cdot t + \varphi) + j \cdot \sin(\omega_0 \cdot t + \varphi)] \\
 &= \hat{u}(0) \cdot e^{-\frac{t}{T_2^*}} \cdot e^{j \cdot (\omega_0 \cdot t + \varphi)}
 \end{aligned} \tag{2.24}$$

Although the time domain FID contains all the relevant information about the nuclear spins, such as resonance frequency ω_0 and relative abundance (proportional to $\hat{u}(0)$), it is rarely used directly. Usually, the complex FID is converted to a complex valued frequency spectrum $U(\omega)$ by means of the Fourier transformation (*FT*):

$$U(\omega) = \int_{-\infty}^{\infty} u(t) \cdot e^{-j \cdot \omega \cdot t} \cdot dt \tag{2.25}$$

The spectral equivalent of an exponentially decaying sinusoid is the complex Lorentzian function, whose real and imaginary parts are referred in NMR as so-called absorption and dispersion components, respectively (see Fig. 2.5).

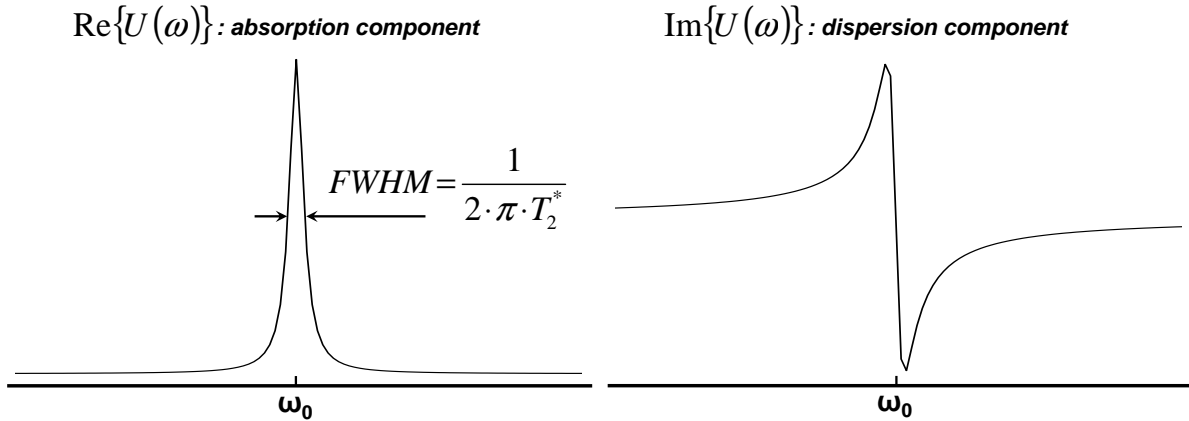


Figure 2.5: Representation of a complex FID time signal in the frequency domain. The real and imaginary parts of NMR spectrum are referred as the so-called absorption and dispersion components. The frequency domain description of a NMR signal is given by its Larmor frequency ω_0 as well as by intensity (area under the spectrum) and line-width *FWHM* of its absorption component.

The resonance signal of a spin ensemble experiencing the same local B_0 is characterised by its particular Larmor frequency (ω_0 in MHz) as well as by the intensity (area under the spectrum) and by the full line-width at half maximum (*FWHM*, in Hz) of the absorption component:

$$FWHM = (2\pi \cdot T_2^*)^{-1} \tag{2.26}$$

The dispersive component is substantially broader and has an intensity of zero (see

Fig. 2.5). Therefore, it is rarely used to describe the resonance peaks in NMR spectra.

Since the actually measured FID is a finite array (vector) of N_{samp} complex, discrete voltage values, sampled at equal time intervals Δt (*dwell time*):

$$u(n) = \hat{u} \cdot \sum_{n=0}^{N_{\text{samp}}-1} \left[e^{-\left(\frac{n \cdot \Delta t}{T_2}\right)} \cdot e^{j \cdot (\omega \cdot n \cdot \Delta t + \varphi)} \right] \quad , n = 0, 1, \dots, N_{\text{samp}} - 1 \quad (2.27)$$

its discrete spectrum can be calculated by applying the Discrete Fourier Transformation [Bronstein et al., 2001]. The frequency resolution of the spectrum is determined by the total acquisition time T_{acq} :

$$\Delta\omega = (N_{\text{samp}} \cdot \Delta t)^{-1}. \quad (2.28)$$

2.2 Magnetic resonance imaging (MRI)

The magnitude of transverse magnetisation \vec{M}_{xy} is proportional to the density of spins, whose nuclear magnetic moments are contributing to the macroscopic magnetisation. Therefore, the induced voltage $u(t)$ in a NMR receive coil can be used for the quantitative assessment of the amount of nuclei within the sample. In a sample with a heterogeneous spin density distribution, the magnitude of \vec{M}_{xy} vector as well as the Larmor frequencies and relaxation properties fluctuate spatially (i.e, they are functions of position vector \vec{r}). Therefore, the measured NMR signal $u(t)$ is proportional to:

$$u(t) \sim \int_V |\vec{M}_{\text{xy}}(\vec{r}, t = 0)| \cdot e^{-\frac{t}{T_2^*(\vec{r})}} \cdot e^{-j \cdot \omega_2(\vec{r}) \cdot t} \cdot d\vec{r} \quad (2.29)$$

To simplify the following description, spatially constant ω_0 and T_2^* as well as no T_2^* related signal attenuation during the signal acquisition should be assumed. Then, the expression given in Eq. 2.29 can be simplified to:

$$u(t) \sim \int_V |\vec{M}_{\text{xy}}(\vec{r})| \cdot e^{-j \cdot \omega_0 \cdot t} \cdot d\vec{r} \quad (2.30)$$

The fundamental principle underlying all NMR approaches for spatially resolved spin density imaging (MRI, magnetic resonance imaging) is based on the linear relation between the spins' Larmor frequency ω_0 and the \vec{B}_0 field strength (see Eq. 2.8). As first proposed by Lauterbur and by Mansfield and Grannell, the spatial discrimination of spin ensembles at different locations can be achieved by superposing the spatially constant \vec{B}_0 with additional magnetic fields, which possess the same orientation as \vec{B}_0 , but whose magnitudes vary linearly along one of three spatial directions (e.g. along the z -direction)

[Lauterbur, 1973; Mansfield and Grannell, 1973]:

$$\vec{B}(x, y, z) = \vec{B}_0 + [0 \cdot \vec{e}_x + 0 \cdot \vec{e}_y + (G_x \cdot x + G_y \cdot y + G_z \cdot z) \cdot \vec{e}_z]^T \quad (2.31)$$

with: $G_x = \frac{\partial B_z(x, y, z)}{\partial x}$, $G_y = \frac{\partial B_z(x, y, z)}{\partial y}$, $G_z = \frac{\partial B_z(x, y, z)}{\partial z}$

The magnitudes of applied linear field gradients G_x , G_y and G_z define the induced spatial variation of the z -component of the \vec{B} -field. This variation implies that spins at different locations can be distinguished by means of their characteristic Larmor frequencies:

$$\vec{\omega}(x, y, z) = \vec{\omega}_0 + \gamma \cdot [0 \cdot \vec{e}_x + 0 \cdot \vec{e}_y + (G_x \cdot x + G_y \cdot y + G_z \cdot z) \cdot \vec{e}_z]^T \quad (2.32)$$

2.2.1 Slice selection

Applying an rf pulse with limited bandwidth $\Delta\omega_{\text{rf}}$ while switching on simultaneously a linear field gradient in z -direction allows selective excitation of spins within a slice of thickness Δz (see Fig. 2.6) Δz :

$$\Delta z = \Delta\omega_{\text{rf}} \cdot (\gamma \cdot G_z)^{-1} \quad (2.33)$$

Spins, which are adjacent to the selected slice and whose Larmor frequencies do not match the bandwidth of the rf pulse, are not excited and do not contribute to the NMR signal. According to Eq. 2.33, the slice thickness can be adjusted by varying the G_z strength or the bandwidth $\Delta\omega_{\text{rf}}$ of the rf pulse. A nearly homogeneous excitation of all spins within a rectangular slice can be achieved by rf pulses, whose envelope is characterised by a *sinc* function (see Fig. 2.6) [de Graaf, 2007].

2.2.2 Frequency encoding

The so-called frequency encoding – a spatial encoding approach, which was first introduced by Lauterbur and by Mansfield and Grannell – also uses a linear field gradient (e.g., G_x , see Fig. 2.7a), which is switched on during signal acquisition [Lauterbur, 1973; Mansfield and Grannell, 1973]. The presence of this gradient implies that spin ensembles, which are located along the gradient direction, experience different magnetic field strengths and therefore rotate with different Larmor frequencies. The frequency encoded NMR signal is then proportional to:

$$u(t) \sim \int_x |\vec{M}_{\text{xy}}(x)| \cdot e^{-j\omega_0 t} \cdot e^{-j\gamma G_x x t} \cdot dx \quad (2.34)$$

2.2.3 Phase encoding

The third spatial encoding approach – the so called phase encoding – also uses a linear field gradient (e.g., G_y) to encode the NMR signal along the remaining spatial direction,

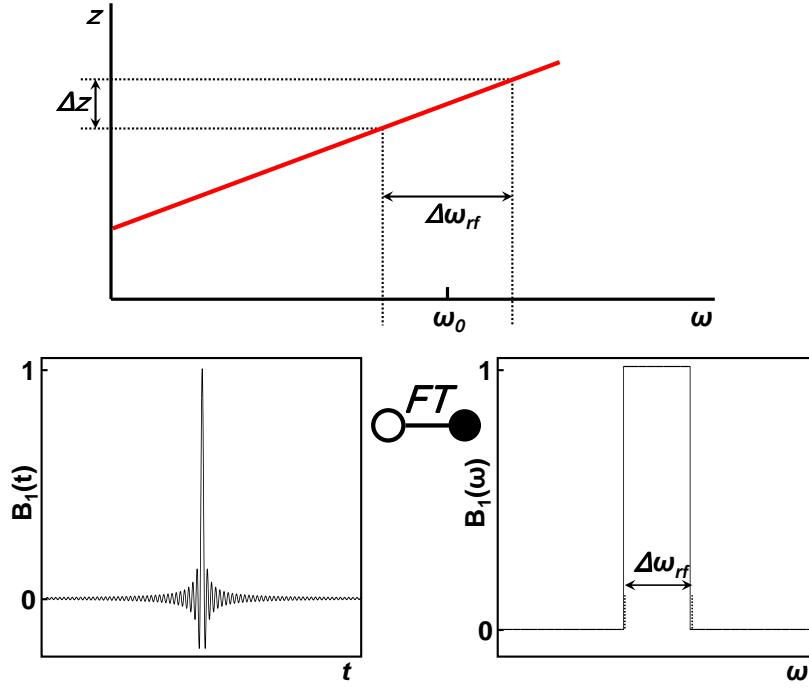


Figure 2.6: Principle of the slice selective excitation of spins by means of a *sinc* rf pulse in combination with linear magnetic field gradients. The slice thickness can be adjusted by the gradient strength or by the bandwidth $\Delta\omega_{rf}$ of the *sinc* rf pulse.

e.g., along the y -axis of the selected slice. This method approach was first introduced by [Kumar et al., 1975]. Contrary to frequency encoding the gradient is switched on for a short time interval t_φ with a certain gradient strength prior to signal acquisition (see Fig. 2.7a) to impart a phase variation of the transverse magnetisation along the gradient direction. Consequently, during signal acquisition spins rotate with identical Larmor frequency but spatially dependent phase angles $\varphi(y)$:

$$\varphi(y) = \gamma \cdot G_y \cdot y \cdot t_\varphi \quad (2.35)$$

The signal can not be spatially resolved by simply one phase encoding step, because the superimposed signal will contain no different frequencies in y -direction. To overcome this, the phase encoding has to be repeated successively with an incrementally varied G_y gradient magnitude (see Fig. 2.7a). The phase encoded signal is then proportional to:

$$u(G_y) \sim \int_y |\vec{M}_{xy}(y)| \cdot e^{-j\omega_0 t} \cdot e^{-j\gamma \cdot G_y \cdot y \cdot t_\varphi} \cdot dy \quad (2.36)$$

2.2.4 Two dimensional spatial encoding

A complete spatial signal encoding along the x and y axes of a selected slice is achieved by including the frequency and phase encoding steps within the time scheme of an NMR

sequence (e.g., a spin echo experiment, see Fig. 2.7a). Acquired data are then arranged in a two dimensional array, consisting of multiple, complex NMR signals:

$$u(t, G_y) \sim \int_x \int_y |\vec{M}_{xy}(x, y)| \cdot e^{-j \cdot \omega_0 \cdot t} \cdot e^{-j \cdot (\gamma \cdot G_x \cdot x + \gamma \cdot G_y \cdot y \cdot t_\varphi)} \cdot dy \cdot dx \quad (2.37)$$

By using the notations:

$$k_x = -\gamma \cdot G_x \cdot t \quad \text{and} \quad k_y = -\gamma \cdot G_y \cdot t_\varphi \quad (2.38)$$

equation 2.37 can be rewritten:

$$u(k_x, k_y) \sim \int_x \int_y |\vec{M}_{xy}(x, y)| \cdot e^{-j \cdot \omega_0 \cdot t} \cdot e^{j \cdot (k_x \cdot x + k_y \cdot y)} \cdot dy \cdot dx \quad (2.39)$$

This expression represents the transverse magnetization distribution $\vec{M}_{xy}(x, y)$ in a sample slice in spatial frequency space or so-called k -space. A corresponding representation of the transverse magnetization distribution in image space is obtained by applying a two dimensional inverse Fourier transformation to the k -space data (see Fig. 2.7b):

$$|\vec{M}_{xy}(x, y)| \cdot e^{-j \cdot \omega_0 \cdot t} \sim \int_{k_x} \int_{k_y} u(k_x, k_y) \cdot e^{-j \cdot (k_x \cdot x + k_y \cdot y)} \cdot dk_y \cdot dk_x \quad (2.40)$$

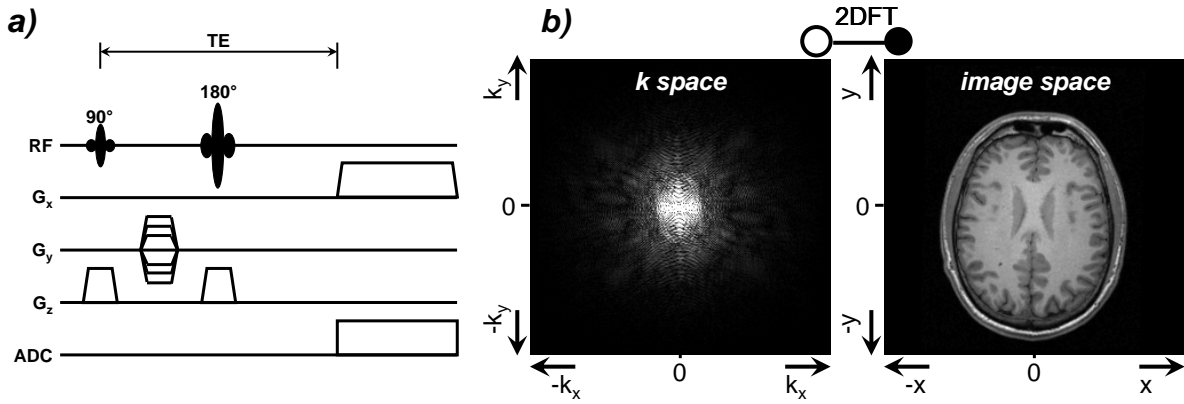


Figure 2.7: The principle of the spatial encoding of a two dimensional slice by the combined application of linear field gradient based frequency and phase encoding in two orthogonal directions during a spin echo experiment (a). The slice selection is usually performed along the third spatial direction (e.g. along the z -axis) by the combined application of *sinc* rf pulses and a linear field gradient G_z . The subplot (b) shows the k -space and image space representation of a spatially encoded brain slice, which was acquired in a healthy volunteer at 3 T with a T_1 weighted spin-echo sequence.

In a real experiment, frequency encoded NMR signals are finite data vectors containing N_{samp} equidistantly sampled discrete data points. Here the *dwell time* Δt denotes the distance between two k -space points in k_x direction, Δk_x . The incremental variation of

the phase encoding gradient G_y in steps of ΔG_y steps implies discrete sampling of the k -space in the phase encoding direction. The distance between two k -space points in k_y direction, Δk_y , is defined by ΔG_y .

$$\Delta k_x = \gamma \cdot G_x \cdot \Delta t \quad \Delta k_y = \gamma \cdot \Delta G_y \cdot t_\varphi \quad (2.41)$$

Both, Δk_x and Δk_y determine the edge size of an MR image (FoV: *Field of View*) in x and in y directions:

$$FoV_x = \frac{1}{\Delta k_x}, \quad FoV_y = \frac{1}{\Delta k_y} \quad (2.42)$$

The distance between two points in the image space (spatial resolution) in x and in y directions is determined by the number of sampled FID time points (N_{Samp}) and by number of performed phase encoding steps (N_φ), respectively:

$$\Delta x = \frac{1}{\Delta k_x \cdot N_{\text{Samp}}} \quad \Delta y = \frac{1}{\Delta k_y \cdot N_\varphi} \quad (2.43)$$

2.3 Magnetic resonance spectroscopy (MRS)

Similar to MRI, magnetic resonance spectroscopy (MRS) is based on the spectral analysis of NMR signals. In contrast to MRI, which uses the experimentally imparted Larmor frequency variation in NMR signals for spatial encoding, MRS utilises the molecule specific frequency information to identify chemical species [Dickinson, 1950; Proctor and Yu, 1950]. Since molecules possess an individual structure, which comprises atomic groups with different electronic environments and different numbers of constituting atoms, MR spectra consist of unique constellations of single or multiple resonance signals (peaks). Consequently, molecules can be identified by means of these unique spectral patterns (*spectroscopic fingerprint*) in a MR spectrum of a multi-compound sample. This can be used for qualitative as well as quantitative analysis of the chemical composition of samples.

In the frequency domain the following three parameters, which are described in detail below, are commonly used to characterise spectral patterns:

- signal intensity, which depends on the number of nuclei contributing to a peak
- resonance frequency or chemical shift value, which depends on the electronic environment of nuclei contributing to a peak
- Peak splitting, which arise due to the interactions between the nuclei via electronic boundaries.

The most frequently explored nuclei in *in vivo* MRS are hydrogen (^1H), phosphorus (^{31}P), carbon (^{13}C) and sodium (^{23}Na) (see Tab. 2.1). Proton MR spectroscopy (^1H -

MRS) dominates clinical spectroscopic examinations and research studies due to several advantageous properties of protons. The proton is the most sensitive nucleus for NMR due to its largest gyromagnetic ratio (γ). It has a natural isotopic abundance of 99.98 % and one of the highest abundances in biological tissues. Finally, the long T_2 time constants of protons (>50 ms, [Mlynárik et al., 2001]) *in vivo* facilitate spin echo based signal detection with echo times of several ten milliseconds.

2.3.1 Identification of chemical compounds

2.3.1.1 Chemical shift and peak intensity

For molecules consisting of different nuclei, the Larmor frequency not only depends on the gyromagnetic ratio and $|\vec{B}_0|$, but is also highly sensitive to the electronic environment of the nucleus under investigation. This individual variation of Larmor frequencies – the so called *chemical shift* – is associated with the magnetic shielding of nuclei by the surrounding electrons, which interact with the external magnetic field \vec{B}_0 . The resulting effective local magnetic field, sensed by the nucleus and defining the local Larmor frequency, can be described by:

$$B_{\text{loc}} = B_0 \cdot (1 - \sigma) \quad \text{or} \quad (2.44)$$

$$\omega_{\text{loc}} = \gamma \cdot B_0 \cdot (1 - \sigma) \quad (2.45)$$

The shielding constant σ depends on the density and distribution of the electrons surrounding the nucleus. The electron density is determined by the electronegativity of adjacent atoms, which are bounded to the nucleus under consideration. The electronegativity characterises the tendency of an atom to attract electrons. In Fig. 2.8 the relationship between shielding and resonance frequencies is demonstrated by means of a simulated ^1H -MR spectrum of acetaldehyde (or ethanal) molecule, which has three protons in the CH_3 -group and one proton in the CHO -group. The electron density around the protons in CH_3 -group is higher than around the proton in CHO -group, since the oxygen in the CHO -group has a higher electronegativity compared to protons. Therefore, CH_3 -group protons are more shielded and reveal a smaller resonance frequency than that of the CHO -group proton.

Usually, chemical shift values are represented as differences (δ) between the Larmor frequencies of the target (ω_{loc}) and a reference substance (ω_{ref}). Since these differences depend on the \vec{B}_0 strength (see Eq. 2.44), they are usually normalised to the rf frequency of the NMR spectrometer (ω_0) and given in relative units *ppm* (parts per million):

$$\delta = \frac{\omega_{\text{loc}} - \omega_{\text{ref}}}{\omega_0} \quad (2.46)$$

A widely accepted reference substance for *in vitro* ^1H -MR spectroscopic examinations

in organic solvents is tetramethylsilane (TMS), which has a higher magnetic shielding constant than most other molecules. Additionally, the resonance frequency of TMS is rather insensitive to temperature variations and ionic strength (pH). The ^1H -MR spectrum of TMS comprises an isolated singlet, whose chemical shift value is assigned to 0 ppm. However, since biological tissues do not contain TMS, other resonances are used for referencing frequencies *in vivo* (e.g., CH_3 -resonance of N-acetyl aspartate at 2.01 ppm or CH_3 -resonance of creatine at 3.01 ppm, see Fig. 1.3).

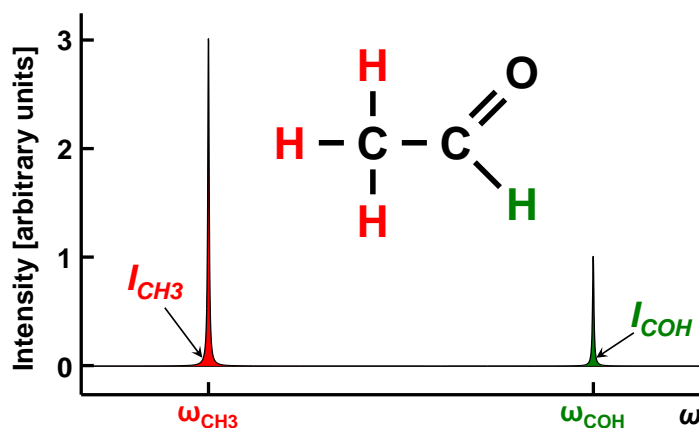


Figure 2.8: Simulated ^1H -MR spectrum ($\text{TE}=0\text{ ms}$) of acetaldehyde, whose molecule consists of a CH_3 and a CHO group. Due to differences in their chemical environment the protons in the CH_3 group and the proton in the CHO group give rise to two separate spectral peaks (singlets) at different resonance frequencies. Due to higher proton shielding in the CH_3 group than in the CHO group, the proton resonance frequency in the CH_3 group is lower than in the CHO group. The intensity ratio $I_{\text{CH}_3}:I_{\text{COH}}$ is 3:1 and corresponds to the ratio of the proton numbers in the CH_3 and CHO group.

Another important property, which can be demonstrated by using the example of acetaldehyde, is the relation between the number of nuclei with equal chemical environment and the intensity of the corresponding peak in the spectrum. The ^1H -MR spectrum of acetaldehyde contains two peaks, which correspond to the single proton in the CHO -group and to the three protons in the CH_3 -group, respectively. Thus, if all other conditions contributing to the measurement sensitivity are equal, the ratio of the peak intensities I_{CH_3} and I_{COH} is 3:1 and corresponds exactly to the ratio of number of nuclei contributing to the peaks.

2.3.1.2 Spin-spin coupling and peak splitting

Another feature of NMR spectra is the occurrence of peak splitting due to couplings between different nuclei in a molecule. This phenomenon arises from nuclear interactions either directly through space (dipolar coupling) or indirectly via electrons in chemical bonds (scalar coupling or J-coupling) [Ramsey and Purcell, 1952]. The scalar coupling can occur between neighbouring nuclei as well as through multiple chemical bonds within

a molecule. In NMR spectra of liquids, peak splitting is dominated by indirect scalar coupling, since the dipolar interactions average to zero due to rapid molecular motion (Brownian motion).

Peak splitting associated with scalar coupling can be described by using an example of a spin-spin-system containing two nuclei A and X with strongly different chemical environments (I for A and X nuclei is assumed to be $1/2$). With respect to the four possible spin orientation combinations, four different energy levels, E_1 , E_2 , E_3 and E_4 , can be distinguished (see Fig. 2.9a):

$$\begin{aligned} E_1 &= -\frac{h}{4 \cdot \pi} \cdot (\omega_A + \omega_X) & E_4 &= +\frac{h}{4 \cdot \pi} \cdot (\omega_A + \omega_X) \\ E_2 &= -\frac{h}{4 \cdot \pi} \cdot (\omega_A - \omega_X) & E_3 &= +\frac{h}{4 \cdot \pi} \cdot (\omega_A - \omega_X) \end{aligned} \quad (2.47)$$

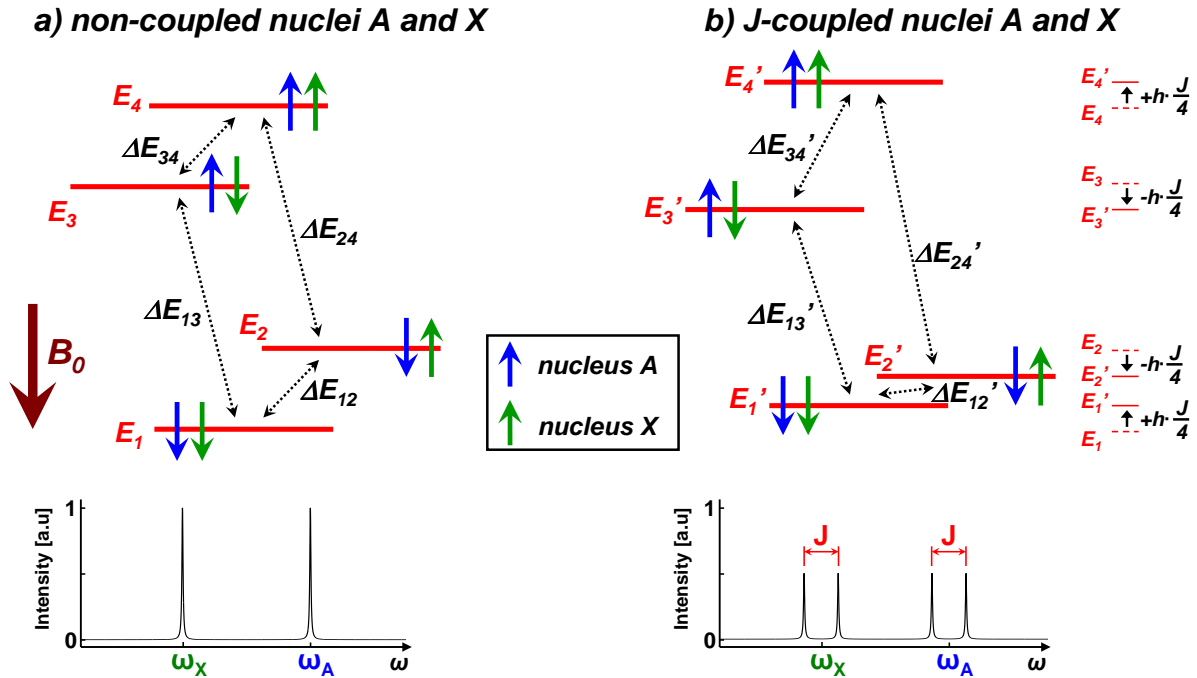


Figure 2.9: Energy level diagrams and simulated corresponding NMR spectra for two isolated (a) and two coupled (b) spins A and X . The diagram in (a) describes two energy level transitions for A and X nuclei with corresponding resonance frequencies ω_A and ω_X . In case of J-coupling between A and X nuclei (b), the nuclear A and X spins affect each other through the bonding electrons. According to the Fermi contact interaction the E_1' and E_4' spin states become energetically less favourable than E_1 and E_4 as one of the two nuclear-electronic spin orientations is forced to be parallel. Contrary, in the energetically more favourable E_2' and E_3' spin states all spin orientations can be anti-parallel. These energy level shifts and give rise to two nucleus A transitions with different frequencies, $\omega_A + J/2$ and $\omega_A - J/2$ and two nucleus X transitions with different frequencies, $\omega_X + J/2$ and $\omega_X - J/2$, which will lead to the splitting of A and X resonance signals into two separate lines.

The scalar coupling is based on the interaction between the magnetic moments of bonding electrons and nuclei, which is governed by the *Fermi contact* interaction [Fermi, 1930]. According to this interaction opposite orientations of the nuclear spin and the spins of the bonding electrons (s-orbital electrons) interacting with the nucleus are energetically favoured. Due to the *Pauli exclusion principle* coupling electrons have different spin quantum numbers and are orientated oppositely to each other. Therefore, when both nuclear spins of the coupled nuclei A and X are parallel (energy level E_1) or anti-parallel (energy level E_4) to the external magnetic field, the two electrons in the bond can not be both anti-parallel to the corresponding nuclear spin. This fact leads to increased E'_1 and E'_4 energy levels compared to the E_1 and E_4 levels in the uncoupled state. On the other hand, E_2 and E_3 levels become energetically more favourable ($E'_2 < E_2$ and $E'_3 < E_3$), since anti-parallel electron-nucleus spin orientations are compatible for both nuclei in these two states. The change of energy levels due to the scalar coupling is expressed by a coupling constant J , which varies for different molecules according to the number of chemical bonds between the interacting nuclei:

$$\begin{aligned} E'_1 &= E_1 + \frac{h}{4} \cdot J & E'_4 &= E_4 + \frac{h}{4} \cdot J \\ E'_2 &= E_2 - \frac{h}{4} \cdot J & E'_3 &= E_3 - \frac{h}{4} \cdot J \end{aligned} \quad (2.48)$$

The modified energy levels mean that four energy level transitions become different with respect to their inter-level distance and therefore give rise to two absorption peaks at $\omega_A \pm J/2$ for nucleus A and two absorption peaks at $\omega_X \pm J/2$ for nucleus X . In other words, the two resonance peaks, which appear at ω_A and ω_X in the uncoupled system, are each split into two peaks (see Fig. 2.9b). The spectral difference between the splitted resonance peaks equals the value of the coupling constant J . In contrast to the chemical shift value, J does not depend on \vec{B}_0 strength and is always given absolutely in Hz. The scalar coupling can occur over more than one bond. Thereby, the coupling strength (expressed by the value of J) decreases with an increasing number of bonds. Typical J values for scalar coupled protons (coupling over two or three bonds) are between 1 Hz and 15 Hz [Govindaraju et al., 2000].

Since each additional coupling spin leads to an additional split of all energy levels, the number of splittings is equal to $N-1$, where N denotes the number of interacting partners. However, if a nucleus interacts with multiple chemically equivalent nuclei, i.e. nuclei with identical chemical environment, particular couplings give rise to resonance peak splits with identical J constants and therefore lead to peak overlay. Here, the multiplet intensity ratios can be described by a binomial distribution given by the Pascal triangle [de Graaf, 2007].

Performing a spin-echo experiment, another J -coupling related feature also occurs - the periodical phase angle variation of splitted peaks as a function of echo time TE . This

effect is associated with the fact that the resonance frequencies of these peaks are shifted by $J/2$ relative to the nominal resonance frequency of the nucleus. Therefore, the 180° rf pulse refocuses the two particular magnetisation components with a phase shift $\varphi_J(TE)$ relative to each other:

$$\varphi_J(TE) = TE \cdot J \quad (2.49)$$

By performing multiple spin echo experiments with incrementally varied TE it is possible to determinate the J coupling constant by analysing the periodicity of peak phase changes [Muller et al., 1977].

2.3.2 *In vivo* MRS

Since MR spectroscopic experiments can be performed in conjunction with localisation approaches (see Chap. 2.2.1), MRS provides a unique tool for localised, non-invasive and quantitative assessment of metabolic processes in the living tissue (*in vivo*). *In vivo* MRS examinations can be performed with the same MR equipment (MR scanner) as is used for MR imaging. This equipment includes essentially the following components:

- Superconducting coil for generation of the static \vec{B}_0 field with typical clinical field strengths between 1 and 3 T.
- Pairs of non-superconducting coils for generation of linear field gradients G_x , G_y and G_z in three spatial directions. As described in Chap. 2.2, these gradients are used for the spatial encoding. Typically, the gradient magnitudes are up to 50 mT/m for whole-body systems.
- Additional non-superconducting coil pairs for generation of linear and quadratic field gradients, which are required for active local adjustment of \vec{B}_0 homogeneity within a probe (shimming, see following description in Chap. 2.3.2.2).
- Non-superconducting coils for spin excitation with oscillating magnetic $\vec{B}_1(t)$ fields (transmission mode) as well as for the detection of NMR signals (receive mode). Commonly, rf transmission and signal detection are performed with two separate rf coil systems. There are several rf receive coil designs, which are individually adapted to the body part of interest (head coils, spine coils, extremity coils etc.).

2.3.2.1 Localisation of target volume

Localised MRS is usually performed as single voxel spectroscopy (SVS), i.e., the spectrum is acquired from a single defined volume, or as chemical shift imaging (CSI, [Brown et al., 1982]), which provides simultaneous acquisition of multiple spectra from multiple voxels within a single (2D CSI) or multiple tissue slices (3D CSI).

Single voxel spectroscopy (SVS) Localisation of spectra from single sub-volumes within a sample is typically based on the successive selection of three orthogonal slices by means of frequency-selective rf pulses in conjunction with linear magnetic field gradients (see Chap. 2.2.1). With this arrangement, only spins in the intersection volume of all three slices contribute to the acquired NMR signal (see Fig. 2.10a). The size of the MRS voxel edges can be adjusted by the magnitude of the applied slice selective gradients and the bandwidth of the rf pulses.

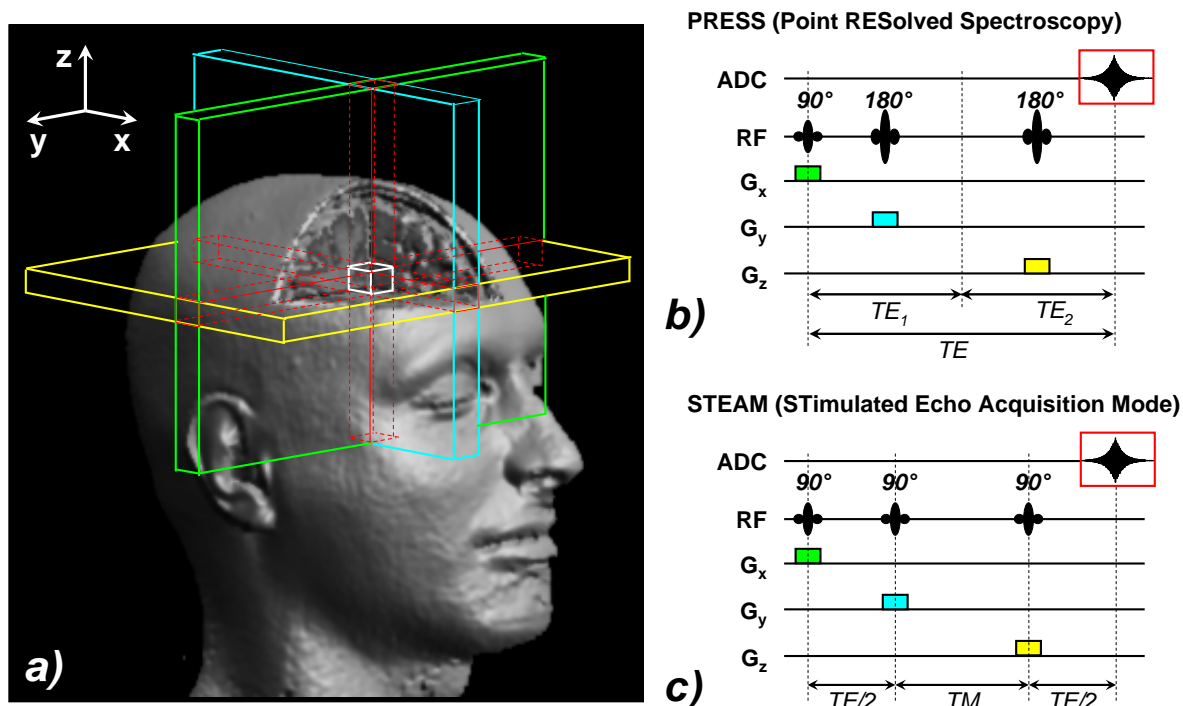


Figure 2.10: Volume localisation based on the successive selection of three orthogonal slices (blue, green and yellow) by means of three frequency-selective rf pulses in conjunction with three orthogonal linear magnetic field gradients G_x , G_y and G_z , which vary the \vec{B}_0 along three orthogonal directions (a). The PRESS approach (b) uses the *SE* principle, by applying two instead of one 180° refocusing slice selective pulses and detecting the second SE. The effective echo time TE is given by the sum of the particular echo times TE_1 and TE_2 . The STEAM method (c) generates a stimulated echo by successive application of three 90° rf pulses (see description in Chap. 2.3.2.1).

Two common MRS volume localisation approaches are based on the generation of spin echoes (PRESS - *Point RESolved Spectroscopy*) or stimulated echoes (STEAM - *STimulated Echo Acquisition Mode*). The PRESS approach utilises the principle of a simple spin echo experiment by applying two instead of one 180° refocusing slice selective pulses (see Fig. 2.10b) [Bottomley, 1987]. Whereas the first spin echo is generated by spins along the intersection column of the slices selected by the 90° excitation and the first 180° refocusing pulse, the second spin echo originates from the spins in the intersection volume of all three slices and is used for data sampling.

The STEAM sequence consists of three successive slice selective 90° rf pulses (see Fig. 2.10c) [Frahm et al., 1989]. The first pulse excites the spins in the selected slice. During the time period $TE/2$ spins will dephase with T_2^* in the transverse plane (xy -plane). Conceptually, the dephased spin vectors can then be fractioned into four macroscopic magnetisation components \vec{M}_{+x} , \vec{M}_{-x} , \vec{M}_{+y} and \vec{M}_{-y} , which are oriented in $+x$, $-x$, $+y$, $-y$ directions, respectively. Application of a second rf pulse after $TE/2$ along the $+x$ direction turns the \vec{M}_{+y} component into a negative and the \vec{M}_{-y} component into a positive longitudinal magnetisation, whereas \vec{M}_{-x} and \vec{M}_{+x} remain in the transverse plane. In the time period between the second and the third rf pulse (so-called 'mixing time' TM) the transverse magnetisation (\vec{M}_{-x} and \vec{M}_{+x} components) decays due to T_2^* relaxation whereas all components parallel to the z -direction (former \vec{M}_{+y} and \vec{M}_{-y}) are conserved and are solely affected by T_1 relaxation. The third rf pulse tilts the former \vec{M}_{+y} and \vec{M}_{-y} components, oriented now along the longitudinal direction, back into the transverse plane, where they form again the magnetisation vectors \vec{M}_{+y} and \vec{M}_{-y} . Since the spins, which contribute to the \vec{M}_{+y} and \vec{M}_{-y} components, have inverted phase shifts compared to the situation at time point $TE/2$, they will rephase during the $TE/2$ period after the third rf pulse and generate a stimulated echo at time point $TE+TM$.

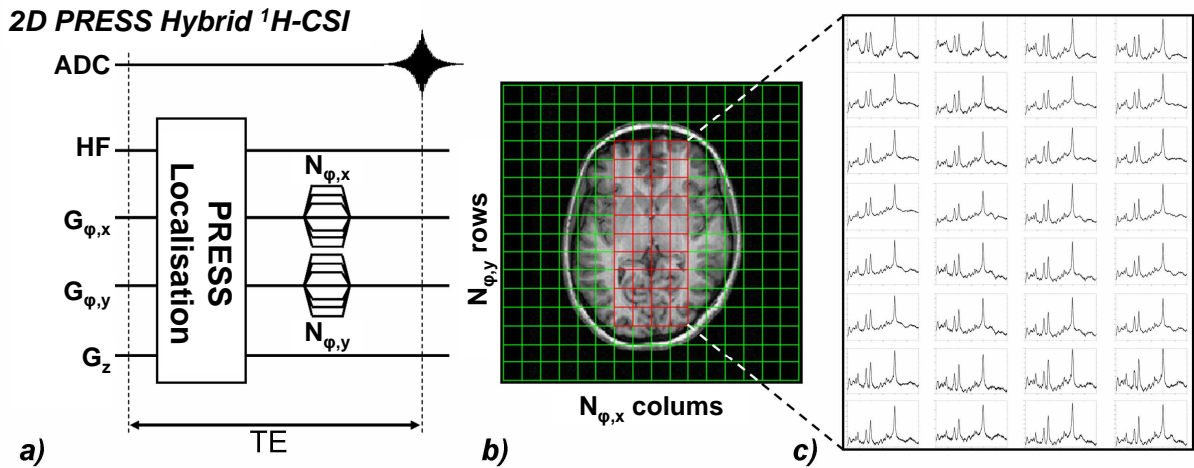


Figure 2.11: Scheme for a PRESS volume selection based two dimensional *in vivo* ^1H -CSI sequence (a), which allows acquisition and spatial encoding of ^1H -MR spectra in a single brain slice (c). The PRESS approach pre-selects a volume of interest (red rectangle in (b)) in order to suppress the signal contributions from outside the brain. The CSI field of view is separated into $N_{\varphi,y}$ rows and $N_{\varphi,x}$ columns by means of phase encoding. Presented *in vivo* spectra were acquired in the brain of a healthy volunteer at 3T with a $TE=30$ ms.

Chemical shift imaging (CSI) *Chemical shift imaging* (CSI) offers the possibility to simultaneously measure MR spectra from multiple voxels within one or multiple slices (see Fig. 2.11b and c) [Brown et al., 1982]. This approach is highly advantageous for a comparison of metabolic profiles in normal and pathological tissue or for the evaluation of

multifocal pathologies. Conventional CSI techniques use phase encoding in two or three spatial directions (2D-CSI and 3D-CSI) for the spatial discrimination of acquired signals (see Chap. 2.2.3). Frequency encoding can not be applied, since the spectral information contained in the FID or spin echo is required for chemical shift related separation of particular metabolites. Therefore, CSI examinations require usually a long acquisition time (TA), which in the case of 3D CSI is given by:

$$TA = N_{\varphi,x} \cdot N_{\varphi,y} \cdot N_{\varphi,z} \cdot NAS \cdot TR. \quad (2.50)$$

$N_{\varphi,x}$, $N_{\varphi,y}$ and $N_{\varphi,z}$ denote the numbers of phase encoding gradient increments in the particular spatial direction, and NAS and TR are the number of averaged single acquisitions and the repetition time, respectively. The usual restriction of $N_{\varphi,x}$, $N_{\varphi,y}$ and $N_{\varphi,z}$ to maximally 16 or 32 increments leads to spatial resolutions, which are several orders lower than in typical MRI applications. This limited k -space sampling causes signal contamination of a particular CSI voxel due to contributions from adjacent voxels (voxel bleeding). This is especially crucial for ^1H -CSI in the brain, where extracranial lipids are present with concentrations several orders of magnitude higher compared to other metabolites [de Graaf, 2007]. To avoid the lipid contamination, *in vivo* ^1H -CSI is usually performed in combination with volume selection techniques as applied for single voxel spectroscopy (an example for a 2D ^1H -PRESS-CSI sequence is shown in Fig. 2.11a). By using such a hybrid approach, lipid signals do not contribute to the measured signal, if voxels containing the extracranial tissue are located outside the PRESS selected volume.

2.3.2.2 Preparation of *in vivo* MRS examination

Besides volume selection, each MRS examination also requires several adjustments to achieve sufficient spectrum quality and thus to increase the accuracy of metabolite signal detection. In general, these adjustments comprise the following steps:

- Compensation of \vec{B}_0 inhomogeneities within the MRS volume (shimming)
- Tuning the water suppression (only for ^1H -MRS)
- Adjustment of experimental parameters (voxel volume, TR , TE) with respect to the desired SNR as well as to the T_1 and T_2 weightings of the acquired signal.

Shimming Since biological samples consist of several tissue types with different magnetic susceptibilities (tissue, bones, blood vessels, air etc.), the external magnetic field \vec{B}_0 is usually not homogeneous throughout the sample. These inhomogeneities lead to an increased effective transverse relaxation rate (T_2^* -relaxation) and cause broadening of resonance lines (see Eq. 2.26). Broad peaks, in turn, cause stronger overlapping of adjacent spectral patterns, thus impeding reliable separation of metabolite resonances. Compensation of \vec{B}_0 inhomogeneities within a target volume is usually performed by overlaying

the external \vec{B}_0 field with additional linear or higher order field gradients (shim gradients, see Fig. 2.12). Their strengths have to be adjusted individually with respect to the initial $|\vec{B}_0|$ field distribution within the volume of interest [de Graaf, 2007].

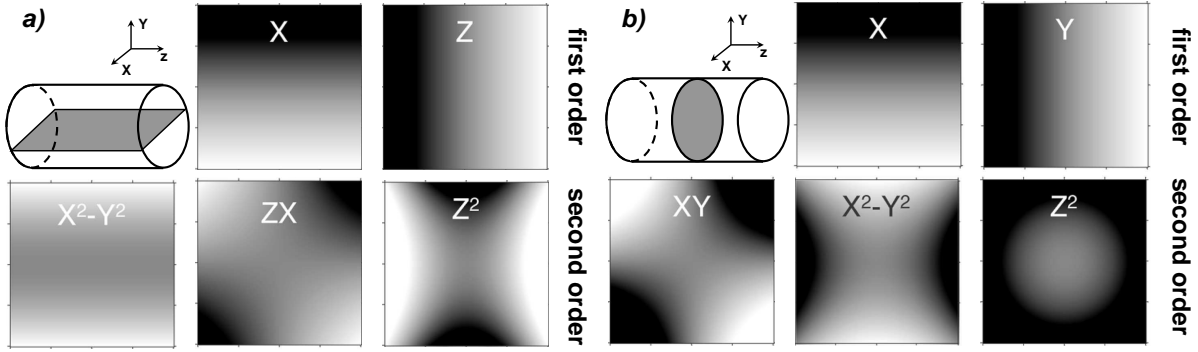


Figure 2.12: Coronal (a) and transverse (b) 2D representations of magnetic field magnitude distributions, which are generated by first and second order shim field gradients. Adapted from [de Graaf, 2007].

Water suppression In biological tissue the water signal intensity is several orders higher than the signals associated with low concentrated metabolites of interest (concentrations of major brain metabolites are in the range between 1 – 15 mmol/l [Govindaraju et al., 2000], brain water concentrations higher than 35.000 mmol/l [Ernst et al., 1993]). This makes metabolite detection from ¹H-MR spectra difficult and ambiguous (see Fig. 2.13). Therefore, selective suppression of the water signal has to be performed prior to volume selection. A widely used water suppression approach is the so called CHESS technique (*CHEMical Shift Selective water suppression*), which performs a selective excitation of water molecule spins with a frequency selective rf pulse followed by the switching of a dephasing gradient [Haase et al., 1985]. In this way, water spins are rephased at the time point of volume selection. A major advantage of CHESS is that it can precede any spectroscopic pulse sequence, since it leaves the metabolite resonances outside the spectral range of water signal unperturbed. In order to achieve optimal saturation of water signal, the bandwidth and the amplitude of CHESS pulses have to be individually adjusted.

Adjustment of experimental parameters Reliable identification of metabolic patterns in a MR spectrum requires sufficient *signal to noise ratio* (SNR) of metabolite signals [Kreis, 2004]. Though *SNR* depends on the concentrations of metabolites under investigation (C_M), it can also be increased by an appropriate setting of experimental parameters (e.g., MRS voxel size V_{Vox} ; *NAS*):

$$SNR \sim C_M \cdot V_{\text{Vox}} \cdot \sqrt{NAS} \quad (2.51)$$

However, *SNR* enhancement always represents a compromise between scan time (de-

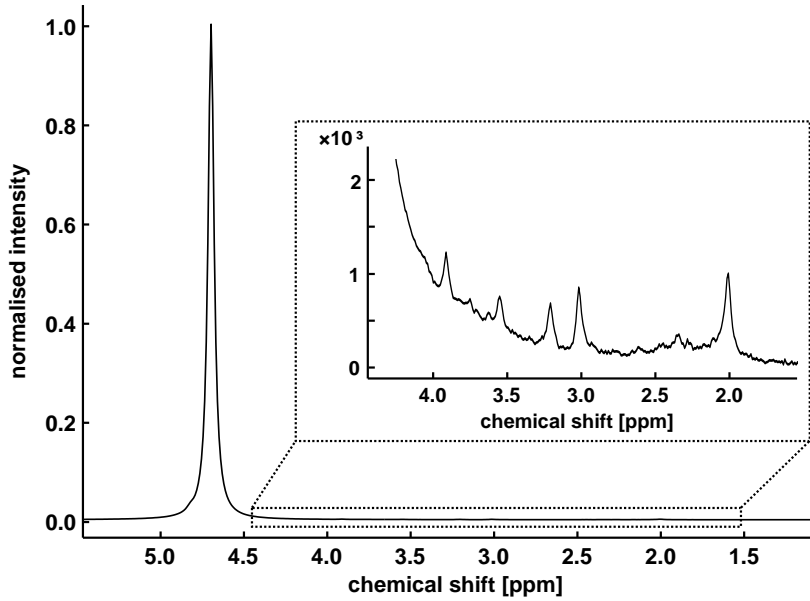


Figure 2.13: ^1H -MR brain spectrum ($B_0 = 3\text{ T}$, $TE = 30\text{ ms}$) acquired without water suppression shows the large magnitude difference between the water signal at 4.7 ppm and the signals of the low concentrated metabolite in the spectral range between 1.5 ppm and 4.5 ppm (see the resonances in the dashed box).

pending on NAS) and spatial specificity (depending on V_{Vox}) of the results. Additionally, since the magnetisation depends on \vec{B}_0 strength, SNR can also be increased with higher static magnet fields (see Chap. 2.1.2).

Adjustments of repetition time (TR) and echo time (TE) are crucial, since they determine the T_1 and T_2 weightings of the metabolite signals. For example, in clinical *in vivo* MRS applications T_2 weighting is often used to suppress undesired signals. Due to their short T_2 relaxation times, lipid signals are almost completely suppressed when using longer TE s. Signals of other metabolites with longer T_2 s than lipids are still present, though with substantial attenuation [Kreis, 2004].

An appropriate TE adjustment can also be used to highlight spectroscopic patterns of coupled metabolites, which normally overlap with adjacent signals of other substances. Utilising the TE related variation of peak phase of J -coupled metabolites (see Chap. 2.3.1.2), their signals can be separated from adjacent resonances by manipulating the peak phase at properly adjusted TE s [de Graaf, 2007; Schubert et al., 2004].

T_1 weighting of metabolite signals is always undesired, although it can never be completely avoided because it depends on TR , which has to be kept as short as possible to reduce the acquisition time (see Eq. 2.50).

2.3.3 Absolute quantitation of MR spectra

2.3.3.1 Importance and method description

Figure 2.14a shows the real part (absorption component) of a water suppressed *in vivo* ^1H -MR spectrum from the brain of a healthy volunteer. The particular peaks with different chemical shift values correspond to several metabolites, including the neuron density marker *N-acetyl aspartate* (NAA), excitatory neurotransmitter compounds *glutamate* (Glu) and *glutamine* (Gln), mitochondrial energy turnover marker *creatine* (Cr), cell membrane turnover marker total *choline* (tCho) as well as astroglial cell density marker *myo-Inositol* (mI) (see also Fig. 1.3). Alterations of these metabolites in biological tissue are often associated with various pathological processes at the cellular level and can therefore be used as clinical markers for diagnosis of different diseases.

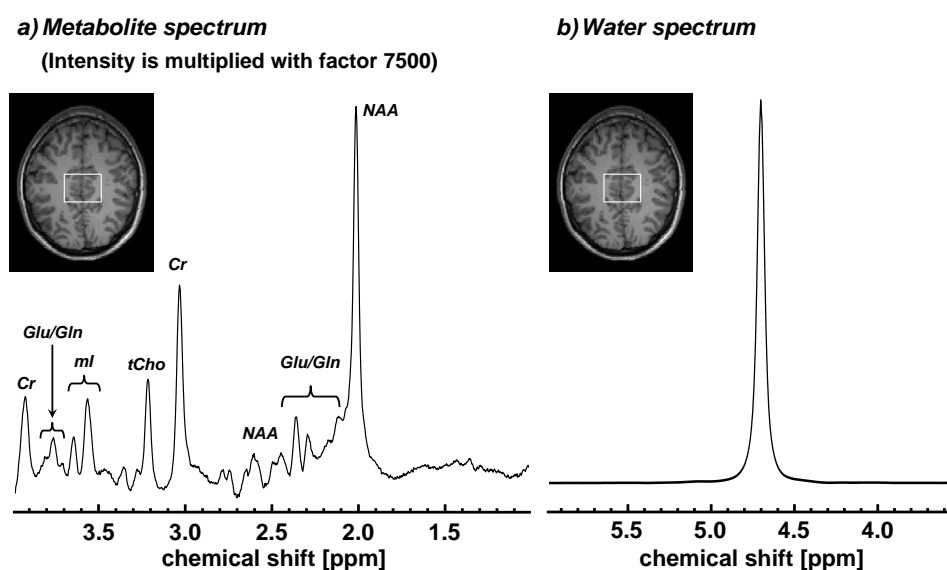


Figure 2.14: Water suppressed (a) and water non-suppressed (b) ^1H -MR spectra from a voxel placed in brain of a healthy volunteer (B_0 : 3 T, TE : 30 ms, PRESS-localisation). The metabolite spectrum (a) contains particular peaks of major ^1H -MR spectroscopically detectable brain metabolites NAA, Glu/Gln, Cr, tCho and mI. In this plot the intensity scale of metabolite spectrum (a) was multiplied with the factor 5000.

Even more important than the identification of metabolites in a spectrum is to determine of their tissue concentrations, which are in principle proportional to the peak intensities (areas under the peaks). However, the measured signal intensity is also affected by numerous technical factors, e.g., spatial homogeneity of rf excitation, sensitivity and gain of receive coils or signal modulations due to the applied RF pulse sequence. Due to these aspects direct quantitation of peak intensity is unreliable for inter- and intra-individual comparisons between different spectroscopic examinations that are performed with varying experimental conditions.

There is clearly a need for transforming metabolite intensities into quantitative units, for

example in absolute concentrations (given in *mmol/l*). Usually, the calculation of absolute metabolic concentrations (C_M) is done by relating estimated metabolite intensities (I_M) to the intensity of a reference substance (I_{ref}) with known concentration C_{ref} [Jansen et al., 2006]:

$$C_M = \frac{I_M}{I_{\text{ref}}} \cdot \frac{N_{\text{nucl,ref}}}{N_{\text{nucl,M}}} \cdot C_{\text{ref}} \cdot f_{\text{cor}} \quad (2.52)$$

The terms $N_{\text{nucl,M}}$ and $N_{\text{nucl,ref}}$ denote the numbers of nuclei within the molecule (stoichiometric factor) that contribute to the signals of the metabolite and the reference, respectively. The correction factor f_{cor} takes into account different experimental settings (e.g., homogeneity of rf excitation, receive coil gain, spatial position of MRS voxel relative to the receive coil, V_{Vox} , TR and TE) that were used for measurements of metabolite and reference signals.

2.3.3.2 External and internal referencing

In general, two referencing strategies exist, depending on whether the reference signal is acquired in the same tissue volume as the metabolite signals (*internal referencing*) or whether it is measured in an aqueous solution phantom (*external referencing*) [Jansen et al., 2006].

The advantage of external referencing is that the reference concentration is exactly known and does not depend on physiological conditions (age, gender, disease etc.). However, this method also implies consideration of all differences in the experimental conditions between acquisitions of metabolite and reference signals (see the factor f_{cor} in Eq. 2.52). This can be very time consuming and is also prone to numerous pitfalls.

Internal referencing does not require any parameter considerations, since reference and metabolite signals are measured in the same volume and with identical experimental settings. One potential uncertainty of this method, however, is that the reference concentration in tissue may depend on physiological factors, such as tissue type, age, gender or disease. In clinical *in vivo* ^1H -MRS examinations the intensity of the CH_3 -singlet of Cr at 3.01 ppm is often used for internal referencing of metabolite intensities (see Fig. 2.14a), since the concentration of creatine is relatively insensitive with respect to pathologic changes [Jansen et al., 2006]. Thereby, metabolite quantities are presented in the form of intensity ratios, e.g. NAA/Cr or tCho/Cr.

The intensity of the tissue water signal (I_W) is another commonly used internal reference for the absolute quantitation of metabolic concentrations. Contrary to the Cr intensity, referencing with tissue water requires an additional measurement of the unsuppressed water signal in the same volume as the metabolite spectrum. One apparent advantage of using tissue water is that its signal is several orders of magnitude larger than the metabolite signals (up to factor 10.000). Therefore, overlaps between the sig-

nals of water and metabolites can be neglected when quantifying the water intensity (see Fig. 2.14b). Considering the two hydrogen nuclei, which are contributing to the water signal ($N_{\text{nucl,W}} = 2$), the absolute metabolite concentrations can be calculated by:

$$C_M = \frac{I_M}{I_W} \cdot \frac{2}{N_{\text{nucl,M}}} \cdot C_W \cdot \alpha_W \quad (2.53)$$

Since the water concentration varies between different biological tissue types and depends on the presence of other substances (e.g. lipids or macromolecules), the assumption of a free water concentration ($C_W = 55.6 \text{ mol/l}$) is not fully adequate for biological tissue [Jansen et al., 2006]. The reduced water concentration in tissue can be taken into account by the tissue type specific relative water content α_W , which reflects the reduced water concentration in tissue relative to the concentration of free water and thus varies between 0 and 1. For example, as estimated by [Ernst et al., 1993], the relative water contents in the three major brain tissue types, *grey matter* (GM, reveal high density of neuronal, astroglial and other cells), *white matter* (WM, consists of neuron cell axons) and *cerebrospinal fluid* (CSF), amount to 0.78, 0.65 and 0.97, respectively.

2.3.3.3 Data pre-processing

In general, several pre-processing steps have to be performed on *in vivo* measured MR spectroscopic data to enhance the precision of metabolite quantitation. Pre-processing is often performed off-line after data acquisition and includes always correction of peak line shape distortions due to signal phase errors, compensation of the spectrum's baseline and estimation of metabolite intensities.

Phase correction. As described in Chap. 2.1.5, complex NMR signals (FID) are characterised by a phase angle φ (see Eq. 2.24). In a real NMR experiment this phase contains Larmor frequency independent and dependent time invariant phase errors (φ_0 and φ_1) as well as time variant, frequency independent phase shifts ($\varphi_{\text{ec}}(t)$), which have different origins and which will be corrected by means of different approaches [de Brouwer, 2009].

The time invariant, frequency independent zeroth-order phase error φ_0 originates from the initial spatial phase shift between the \vec{M}_{xy} vector and receive coil at the beginning of the signal acquisition (see Fig. 2.15a). This error has to be corrected by multiplying the acquired signal $u(n)$ with the term $e_c^{-\varphi}$ where $\varphi_c = \varphi_0$. A simple approach for an automatic φ_0 -correction, which was implemented and used for the pre-processing of all spectra in this work, is to maximise the ratio between the intensities of the real and imaginary parts ($R_{R/I}(\varphi_c)$) of the spectrum $U(n, \varphi_c)$ by incremental adaptation of the φ_c

between $-\pi$ and π (see Fig. 2.15b and c):

$$U(n, \varphi_c) = FT(u(n) \cdot e_c^{-j\varphi})$$

$$R_{R/I}(\varphi_c) = \frac{\text{Re}\{U(n, \varphi_c)\}}{\left|\text{Im}\{U(n, \varphi_c)\}\right|} \quad (2.54)$$

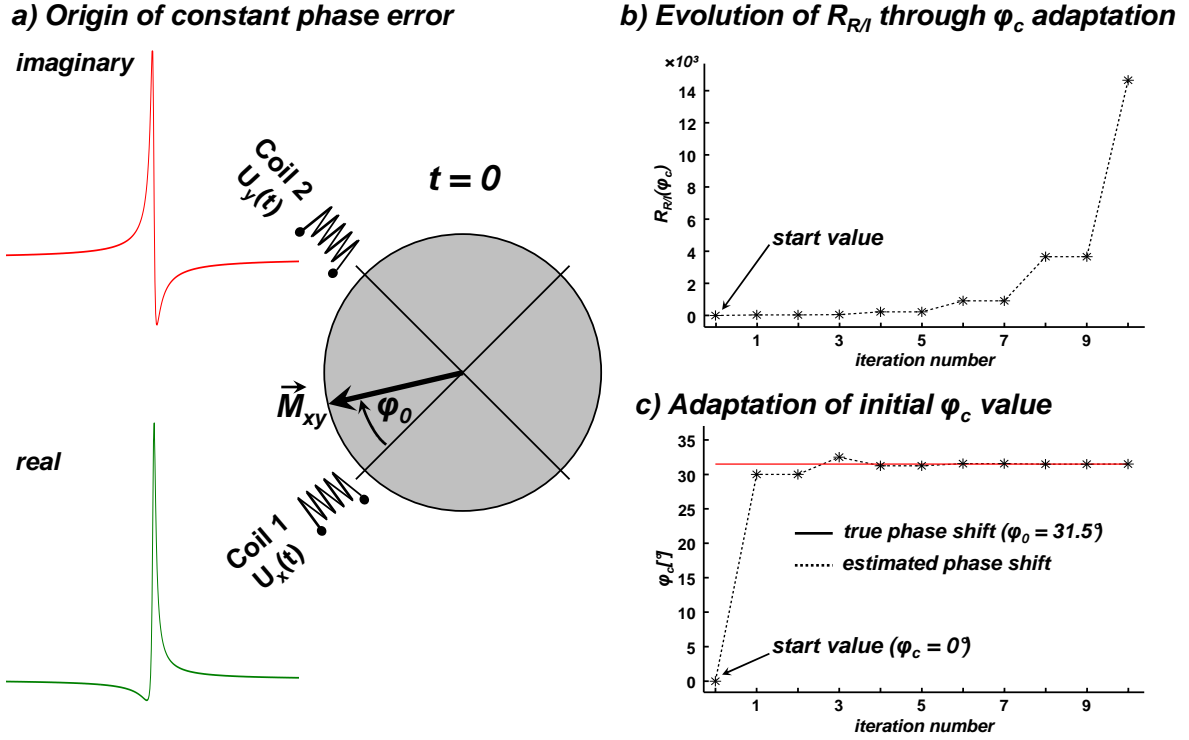


Figure 2.15: Arising of constant phase errors due to different directions of magnetisation vector \vec{M}_{xy} and receive coils at the beginning of signal acquisition (a). The correction of constant phase error is realised by multiplying the measured FID with a term $\exp(-j \cdot \varphi_c)$, which will be iteratively adapted by maximising the ratio between the spectrum's real and imaginary part integrals ($R_{R/I}(\varphi_c)$ see subplot b). Through the $R_{R/I}(\varphi_c)$ adaptation the difference between the estimated and initial (true) constant phase errors decreases (c). The presented demonstration of φ_0 -correction is based on simulated data.

A Larmor frequency dependent, first order phase error $\varphi_1(\omega)$ occurs if the FID or spin echo acquisition begins with a time delay t_D after the rf excitation or the spin echo. During this delay spin ensembles with different chemical environments and thus different Larmor frequencies develop different phase shifts with respect to the initial condition immediately after the rf excitation or at the spin echo maximum:

$$\varphi_1(\omega) = \omega \cdot t_D \quad (2.55)$$

The $\varphi_1(\omega)$ -correction is often realised by shifting the time signal vector along the time axis by successively adding zeros prior to the first signal data point. Ideally, the length of the added zero signal vector (number of added zeros times the sampling interval used for signal acquisition) should be equal to t_D .

Time dependent phase errors $\varphi_{ec}(t)$ are mostly the result of applying the field gradients (G_x, G_y, G_z) during the spin preparation period in a NMR sequence (e.g., in case of volume selective MRS, see Chap. 2.3.2.1). Rapid gradient switching generates time-varying magnetic fields and induces so-called *eddy currents* (EC) in all nearby conducting structures (e.g., main magnet and shim coils). These currents induce time variant magnetic fields, which superpose the \vec{B}_0 field and decay during the FID acquisition. The magnitude decay of these induced magnetic fields causes a dynamic variation of the spin phase during NMR signal acquisition (see Fig. 2.16b), which again is observable in a less predictable line shape distortions of peaks in the spectrum (see Fig. 2.16a and c).

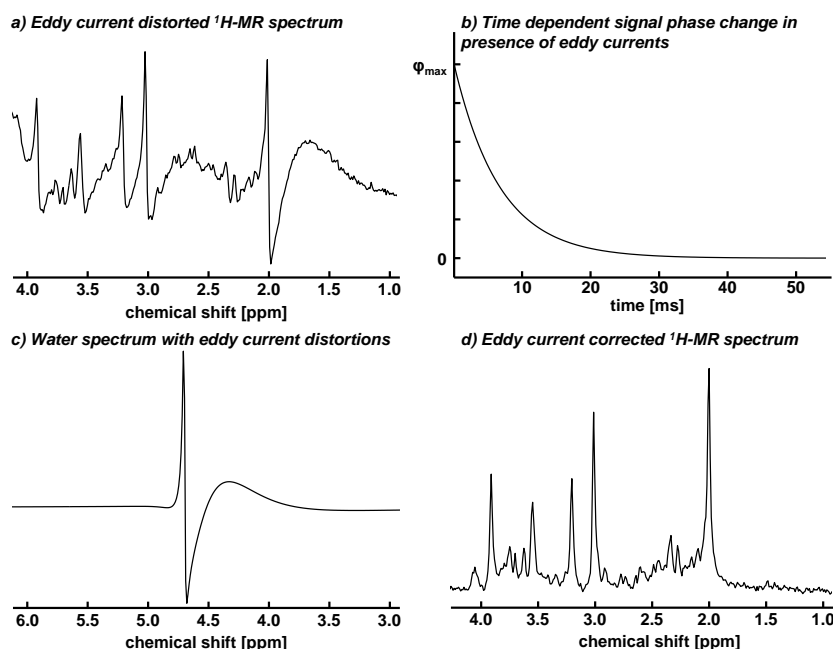


Figure 2.16: Distortions of peak line shapes in metabolite (a) and water (c) ¹H-MR spectra from the same spectroscopic volume due to eddy current induced temporal variation of signal phase ($\varphi(t)$) during the signal acquisition (b). The correction of time variant phase errors can be performed by modulating the metabolite signal with the opposite phase of reference water signal [Klose, 1990]. The corrected metabolite spectrum is shown in subplot (d). Presented spectra were acquired in the brain of a healthy volunteer at 3 T with a PRESS based single voxel MRS sequence ($TR/TE = 5000/30$ ms).

Klose [1990] introduced a simple but highly efficient approach for the correction of EC related line shape distortions by using the non-suppressed water signal, which is acquired with identical parameters and in the same MRS volume as the metabolite FID (see Fig. 2.16). Since both, metabolite and non-suppressed water signals comprise iden-

tical phase errors $\varphi_{ec}(t)$, the line shape correction can be performed by modulating the metabolite signal with the opposite phase of the water signal ($\varphi_W(t)$):

$$u_{\text{met,cor}} = \sum_{n=0}^{N_{\text{Samp}}-1} u_M(n) \cdot e^{-j \cdot \varphi_W(n)} \quad (2.56)$$

Baseline correction. Usually, distortions in the baseline of an *in vivo* ^1H -MR spectrum are related to broad resonances of large, fast relaxing macromolecules (MM) as well as to water signal residuals, which may remain due to less efficient water suppression. In general, the baseline shape can be fitted by high order polynomial functions or cubic splines and then subtracted from the original spectrum. However, a more reliable baseline correction approach comprises modelling of known baseline components (e.g. MM resonances, see the blue graph in Fig. 2.17a) and additional consideration of these *a priori* models through the fitting of metabolites within the spectrum [Kanowski et al., 2004; Seeger et al., 2003].

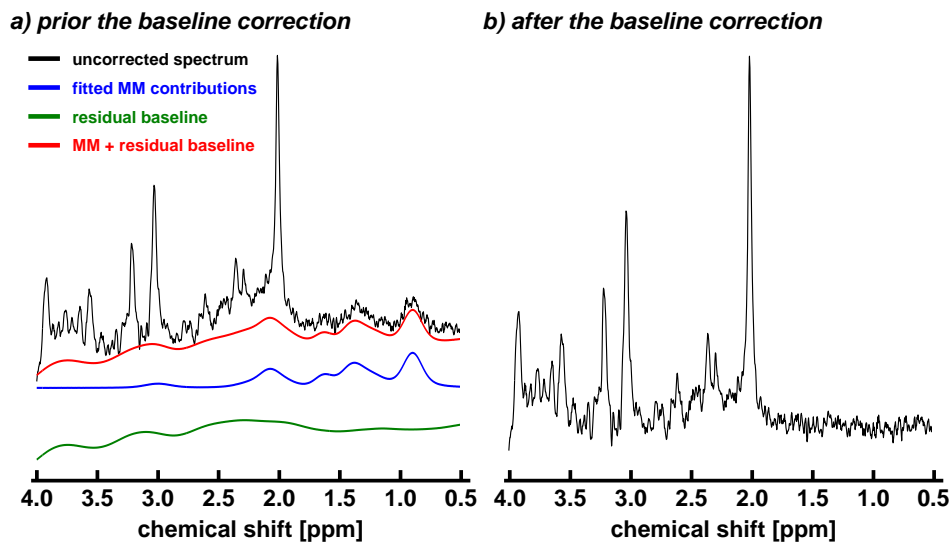
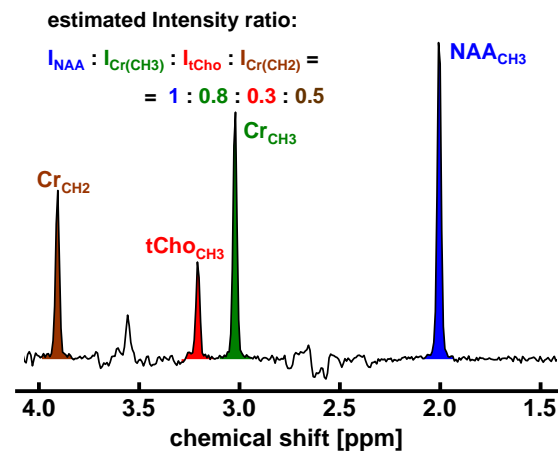


Figure 2.17: Principle of baseline correction in a ^1H -MR spectrum with broad MM contributions, which are modelled by separate Lorentzian functions (blue graph in subplot a). The residual baseline (green graph in subplot a) can be approximated by high order polynomial functions or cubic splines. Presented ^1H -MR spectrum was acquired in the brain of a healthy volunteer (B_0 : 3 T, TR/TE : 5000/30 ms, PRESS-localisation).

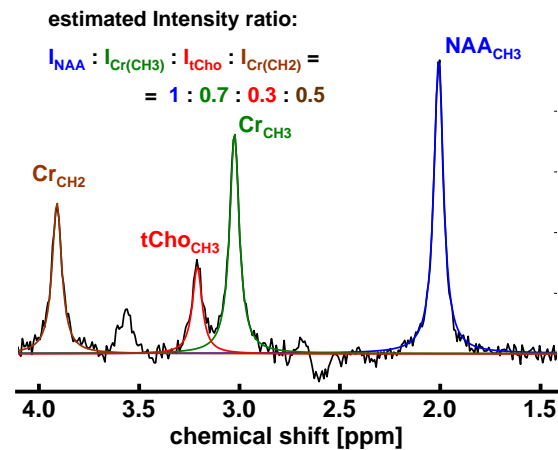
Estimation of metabolite intensities. Estimation of metabolite intensities from the MR spectrum represents the final and the most essential pre-processing step. For MR spectra with few, clearly separated metabolites peaks, metabolite intensities can be determined by a simple integration of the spectrum within pre-defined chemical shift ranges containing particular metabolite peaks (see Fig. 2.18a).

However, unambiguous adjustment of spectral ranges is often complicated by overlaps between particular peaks due to low spectral resolution in case of insufficient \vec{B}_0 homo-

a) quantitation via a simple integration of spectrum's intervals



b) AMARES quantitation via a spectrum's component fitting with Lorentzian functions



c) LCModel quantitation via a spectrum's fitting with *in vitro* metabolite spectra

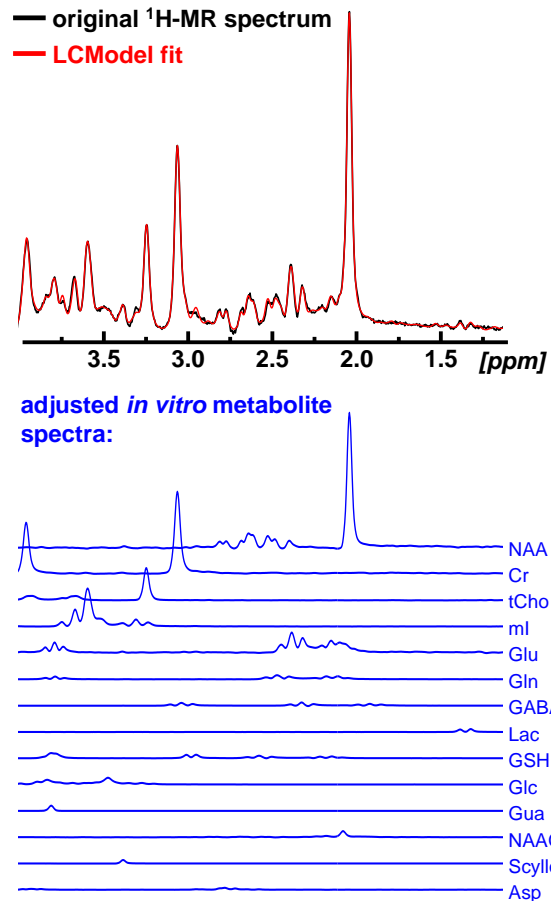


Figure 2.18: Integration of spectral intensities in selected frequency ranges (a) represents the most simple approach for the quantitation of metabolite intensities. However in case of spectral overlaps between metabolite peaks (b) the quantitation requires fitting of individual compounds by pre-defined mathematical models (Lorentzian or Gaussian functions). Both spectra in (a) and (b) were simulated based on real *in vitro* ¹H-MR spectra of Cr, tCho and NAA (B_0 : 3 T, TE : 135 ms), which were linearly combined by using identical metabolite magnitude weightings but with different damping factors ($T_{2,a}^* > T_{2,b}^*$). The quantitation of the spectrum in (a) performed with a simple integration approach and quantitation of the spectrum in (b) performed with a mathematical model based AMARES method [Vanhamme et al., 1997] provided approximately identical ratios between the intensities of the included compounds. The LCModel approach (c) is based on fitting the measured metabolite spectrum with a weighted linear combination of several metabolite models each comprising a complete metabolite fingerprint [Provencher, 1993]. In order to fit the measured spectrum adequately the LCModel approach requires basis data sets containing all metabolic compounds contributing to the real spectrum.

generality (see Fig. 2.18b) or due to a high number of metabolite signals, which contribute to the MR spectra, particularly at short TEs (see Fig. 2.18c). In these cases reliable peak intensity estimation requires a more sophisticated fitting of measured time signals ($u_{\text{meas}}(t)$) or spectra by means of a weighted linear combination of multiple (N_M) compounds:

$$u_{\text{meas}}(t) = \sum_{n=1}^{N_M} w_M \cdot u_{M,n}(t) \quad (2.57)$$

Here w_M denotes the compound intensity weighting factor, which has to be adjusted through the fit algorithm. The intensity time courses ($u_M(t)$) or spectra of particular metabolic compounds can be approximated by adequate mathematical model functions (e.g. Lorentzian or Gaussian functions, as they are used in AMARES (*Advanced Method for Accurate, Robust and Efficient Spectral fitting*) [Vanhamme et al., 1997], see Fig. 2.18b) or modelled by complete metabolite signal time courses or spectra (e.g. *in vitro* metabolite spectra models as they are used in the LCMoel suite (*Linear Combination Model*) [Provencher, 1993], see Fig. 2.18c).

The fit algorithm performs an iterative adjustment of all initialised model parameters (e.g. resonance frequency, magnitude, line width, phase, polynomial order for baseline fitting etc.) until the linear combination of selected compounds matches the measured spectrum as close as possible. Obviously, the convergence of the fit performance can be substantially improved by restricting the variation range of model parameters and including some *a priori* knowledge constraints with respect to known relations between particular parameters (e.g., nominal metabolite resonance frequencies, number and magnitude as well as phase relations of multiple peaks relative to each other). However, this procedure increases the dependence of quantitation results on user interaction and may make them less comparable with results achieved with another *a priori* knowledge set. Therefore, a more objective approach, implemented for example in the LCMoel suite of [Provencher, 1993] implies fitting of the multicomponent spectra by means of weighted linear combination of isolated metabolite spectra (models), which consider all chemical shifts, magnitude and phase relations among the resonances of several molecular groups. However, since the metabolite signal patterns often depend on adjusted measurement parameters (\vec{B}_0 strength, signal phase relations), an appropriate application of this method requires acquisition of multiple basis sets of metabolite model spectra for each individual experimental setting. The fit accuracy (quantitation accuracy) can be judged by means of the so-called *Cramer-Rao-Lower-Bounds* (CRLB) values, which are calculated separately for each fitted parameter within a used model function and which reflect the lowest standard deviation level for the corresponding parameter [Cavassila et al., 2001].

3 Quantitation of brain metabolites with respect to heterogeneous tissue compositions in spectroscopic voxels

3.1 Introduction

This chapter describes post-processing method combining the analysis of the MR spectroscopic and high resolution MR imaging data to determine the absolute concentrations of metabolites while considering heterogeneous tissue compositions in the spectroscopic voxels. Assuming the investigator induced variation of tissue volume fractions throughout the measurements performed in different persons, this method should correct the intra-individual biases of calculated metabolic values.

3.1.1 Theoretical aspects

Besides accurate acquisition and post-processing of MR spectroscopic data, quantitative estimation of metabolic concentrations (metabolite quantitation) represents another essential step to make results reliable and independent on experimental conditions. As described in Chap.2.3.3, metabolite quantitation requires normalization of estimated metabolic intensities to the intensity of an internal reference substance contained in the tissue or an external reference substance with known concentration. In the brain tissue water is often used as an internal concentration reference (see Eq.2.53). It has, however, to be assured that metabolite and water signals are originating from the same tissue type and that the water concentration in the considered tissue type is known. However, these assumptions are mostly not fulfilled in the case of *in vivo* ^1H -MRS examinations, where spectroscopic voxels commonly contain a mixture of different tissue types with different contents of metabolites and water [Ernst et al., 1993]. Consequently, *in vivo* measured metabolite and water signals (I_M^{vox} , I_W^{vox}) represent a weighted linear combination of signal contributions ($I_{M,n}$, $I_{W,n}$) from N_{tis} tissue types with different water amounts:

$$I_M^{\text{vox}} = \sum_{n=1}^{N_{\text{tis}}} f_n \cdot I_{M,n}, \quad I_W^{\text{vox}} = \sum_{n=1}^{N_{\text{tis}}} f_n \cdot I_{W,n}, \quad n = 1, 2, \dots, N_{\text{tis}} \quad (3.1)$$

The factors f_n denote volume fractions of the tissue compartments with particular volumes V_n , which are embedded in the MRS voxel with volume V_{vox} :

$$f_n = \frac{V_n}{V_{\text{vox}}}, \quad 0 \leq f_n \leq 1 \quad (3.2)$$

As described in Chap. 2.3.3, the variation of water signal intensities between different tissue types ($I_{W,1} \neq I_{W,2} \neq \dots \neq I_{W,N_{\text{tis}}}$) is related to the different water contents in these tissues. In general, the water concentration in tissue is clearly lower than the water concentration of an aqueous solution (free water concentration: $C_{W,0} = 55.6 \text{ mol/l}$). The relation between the signal intensity or concentration of tissue water ($I_{W,n}$ and $C_{W,n}$) and free water (I_W^0 and C_W^0) can thus be expressed by introducing a tissue specific factor α_n :

$$I_{W,n} = \alpha_n \cdot I_W^0, \quad C_{W,n} = \alpha_n \cdot C_W^0, \quad 0 \leq \alpha_n \leq 1 \quad (3.3)$$

Besides their specific water concentrations, different tissue types also differ with respect to their physical and chemical properties (density, diffusion capability, magnetic susceptibility, pH, etc.) and reveal different T_1 and T_2 time constants for the $|\vec{M}_z|$ recovery and $|\vec{M}_{xy}|$ decay for metabolites and water [Mlynárik et al., 2001; Stanisiz et al., 2005]. In a spin echo based MR spectroscopic experiment, tissue specific metabolite and water signal attenuations due to T_1 and T_2 processes can be taken into account by an attenuation factor $R_{\text{substance}}^{\text{tisX}}$:

$$R_{\text{substance}}^{\text{tisX}}(TR, TE) = \left(1 - e^{-\frac{TR}{T_1^{\text{tisX}}}}\right) \cdot e^{-\frac{TE}{T_2^{\text{tisX}}}} \quad (3.4)$$

Considering all factors affecting the measured intensities of metabolites (I_M^{vox}) and water (I_W^{vox}), the following equations can be formulated:

$$I_M^{\text{vox}} = \sum_{n=1}^{N_{\text{tis}}} f_n \cdot R_M^n \cdot I_{M,n}^0 \quad (3.5)$$

$$I_W^{\text{vox}} = I_W^0 \cdot \sum_{n=1}^{N_{\text{tis}}} f_n \cdot R_W^n \cdot \alpha_n \quad (3.6)$$

The term $I_{M,n}^0$ represents the metabolite intensity, which is measured in a voxel containing only tissue type n without relaxation associated attenuations.

In contrast to the known tissue specific water concentrations [Ernst et al., 1993], the relation between metabolite concentrations in particular tissue compartments is unknown. As indicated by Eq. 3.1, the measured signal from a heterogeneously composed voxel is given by the linear combination of particular signal intensities ($I_{M,n}^0$), each of which is weighted by the tissue volume fraction in the MRS voxel (f_{tisX}), as well as by the tissue specific attenuation factor $R_{M,n}$. In order to determine the pure metabolite concentrations

in N_{tis} different tissue types one has to solve an equation system with at least N_{tis} linearly independent equations, where each equation comprises an individually weighted linear combination of signal intensities from N_{tis} tissue compartments [Wang and Li, 1998]:

$$\begin{bmatrix} I_M^{\text{vox1}} \\ I_M^{\text{vox2}} \\ \vdots \\ I_M^{\text{voxN}} \end{bmatrix} = \begin{bmatrix} f_{\text{tis1}}^{\text{vox1}} \cdot R_M^{\text{tis1}} & f_{\text{tis2}}^{\text{vox1}} \cdot R_M^{\text{tis2}} & \cdots & f_{\text{tisN}}^{\text{vox1}} \cdot R_M^{\text{tisN}} \\ f_{\text{tis1}}^{\text{vox2}} \cdot R_M^{\text{tis1}} & f_{\text{tis2}}^{\text{vox2}} \cdot R_M^{\text{tis2}} & \cdots & f_{\text{tisN}}^{\text{vox2}} \cdot R_M^{\text{tisN}} \\ \vdots & \vdots & \ddots & \vdots \\ f_{\text{tis1}}^{\text{voxN}} \cdot R_M^{\text{tis1}} & f_{\text{tis2}}^{\text{voxN}} \cdot R_M^{\text{tis2}} & \cdots & f_{\text{tisN}}^{\text{voxN}} \cdot R_M^{\text{tisN}} \end{bmatrix} \cdot \begin{bmatrix} I_{M,\text{tis1}}^0 \\ I_{M,\text{tis2}}^0 \\ \vdots \\ I_{M,\text{tisN}}^0 \end{bmatrix} \quad (3.7)$$

This approach, however, is very time consuming, since it requires multiple spectroscopic experiments. Clinical examinations are frequently restricted to the measurement of a single metabolite spectrum in a single voxel and do not allow direct determination of metabolic intensities in particular tissue types within this voxel. Therefore, the calculation of absolute metabolite concentrations in this case is based on the assumption of identical metabolic quantities in all tissue types ($C_{M,1} = C_{M,2} = \dots = C_{M,N_{\text{tis}}}$). The measured metabolite intensity (I_M^{vox}) can then be represented as the weighted sum of identical intensities I_M^0 , which are differently attenuated according to the tissue type specific T_1 and T_2 constants:

$$I_M^{\text{vox}} = I_M^0 \cdot \sum_{n=1}^{N_{\text{tis}}} f_n \cdot R_M^n \quad (3.8)$$

Considering Eq. 2.53, the metabolite concentrations (C_M) can be calculated by solving Eqs. 3.6 and 3.8 for I_W^0 and I_M^0 , followed by multiplication of the ratio I_M^0/I_W^0 with the free water concentration C_W^0 :

$$\begin{aligned} C_M &= \frac{I_M^0}{I_W^0} \cdot \frac{2}{N_{\text{prot},M}} \cdot C_W^0 = \\ &= \frac{I_M^{\text{vox}}}{I_W^{\text{vox}}} \cdot \frac{2}{N_{\text{prot},M}} \cdot C_W^0 \cdot \frac{\sum_{n=1}^{N_{\text{tis}}} f_n \cdot R_{W,n} \cdot \alpha_n}{\sum_{n=1}^{N_{\text{tis}}} f_n \cdot R_{M,n}} \end{aligned} \quad (3.9)$$

Again, f_n denotes the volume fraction of the n^{th} tissue type within the MRS voxel volume, $N_{\text{prot},M}$ is the number of protons in the metabolite molecule, R represents the relaxation related attenuations of water and metabolite signals according to the tissue specific T_1 and T_2 constants and α_n gives the relative water content in the tissue. In fact, a data set containing the metabolite and water spectra from one single voxel provides the determination does not allow to discriminate between metabolic concentrations in different tissue types. Instead, the calculated concentration reflects moreover an average over all contributing tissue types. However, the determined tissue volume fractions can be used to consider the potential variation of results when comparing data from the differently

composed voxels.

3.1.2 Determination of the tissue volume fractions in the brain

Apparently, one of the most crucial premises to quantify metabolites in heterogeneously composed spectroscopic volumes is the reliable determination of tissue volume fractions (f_n). For example, estimation of brain metabolite concentrations from *in vivo* ^1H -MR spectra requires at least discrimination between *grey matter* (GM), *white matter* (WM) and *cerebrospinal fluid* (CSF), since these compartments substantially differ with respect to their water concentrations ($\alpha_{\text{GM}}=0.78$, $\alpha_{\text{WM}}=0.65$ and $\alpha_{\text{CSF}}=0.97$ [Ernst et al., 1993]) and also with respect to the T_1 and T_2 time constants for metabolites and water (see Tabs. 3.1 and 3.2). Additionally, vanishing metabolite concentrations in CSF mean, that metabolite signals are originating only from GM and WM, whereas water signal arise from all the compartments. Therefore, metabolite concentrations calculated without taking into account tissue composition in the voxels, will be substantially biased by the amount of CSF present in these voxels (CSF partial volume effect).

Table 3.1: *In vivo* T_1 and T_2 relaxation times of several brain metabolites in GM and WM at $B_0 = 3\text{ T}$.

	T_1 [s]		T_2 [s]	
	GM	WM	GM	WM
NAA	1.470 ¹	1.350 ¹	0.226 ²	0.264 ²
Cr	1.460 ¹	1.240 ¹	0.137 ²	0.155 ²
tCho	1.300 ¹	1.080 ¹	0.207 ²	0.202 ²
mI	1.230 ¹	1.010 ¹	0.167 ³	0.199 ³
Glu	1.270 ¹	1.170 ¹	0.161 ³	0.169 ³

¹ [Mlynárik et al., 2001]

² [Zaaraoui et al., 2007]

³ [Choi et al., 2010]

Considering the distinctly shorter T_2 of water in GM and WM compared to CSF (see Tab. 3.2), the volume fractions of brain matter ($f_{\text{BM}} = f_{\text{GM}} + f_{\text{WM}}$) and CSF (f_{CSF}) can be determined by bi-exponential fitting of the water intensity decay, sampled in a measurements series with incrementally increasing TE s (see Fig. 3.1) [Ernst et al., 1993]:

$$I_{\text{W}}(TE) = I_{\text{W,BM}}^0 \cdot e^{-\frac{TE}{T_2^{\text{BM}}}} + I_{\text{W,CSF}}^0 \cdot e^{-\frac{TE}{T_2^{\text{CSF}}}} \quad (3.10)$$

$$f_{\text{BM}} = \frac{I_{\text{W,BM}}^0}{I_{\text{W,BM}}^0 + I_{\text{W,CSF}}^0}, \quad f_{\text{CSF}} = \frac{I_{\text{W,CSF}}^0}{I_{\text{W,BM}}^0 + I_{\text{W,CSF}}^0} \quad (3.11)$$

In this formula T_2^{BM} denotes the mean value between the T_2 of water in GM and WM. This

Table 3.2: *In vivo* T_1 and T_2 relaxation times of water in GM, WM and CSF at $B_0 = 3$ T. Presented T_2 values in WM and GM represent the average values, which were obtained by analysing multi-exponential T_2 decays water decays in these tissue types [Stanisz et al., 2005]. The T_1 constants of WM and GM are determined by Stanisz et al. [2005] by assuming a monoexponential recovery of the longitudinal magnetisation.

	GM	WM	CSF
T_1 [s]	1.820 ¹	1.084 ¹	4.163 ²
T_2 [s]	0.099 ¹	0.069 ¹	0.503 ³

¹ [Stanisz et al., 2005]

² [Lin et al., 2001]

³ [Piechnik et al., 2009]

approach provides a reliable determination of the volume fractions of the brain matter and CSF in voxels, however, without unambiguous discrimination between the GM and WM fractions with very similar T_2 constants (see Tab. 3.2). One substantial disadvantage of this method is that the sampling of the water intensity decay extends the measurement time, which make it less applicable, for example, for CSI studies.

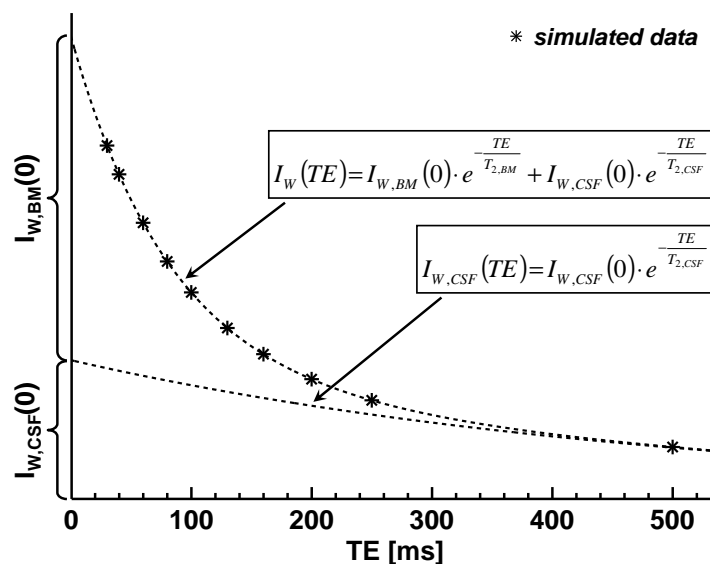


Figure 3.1: Bi-exponential fit of a T_2 decay of the brain water signal, which was calculated by using simulated data with TE in the range between 30 ms and 500 ms. For the simulation two brain compartments (BM and CSF) with different intensities were assumed. T_2 values for BM and CSF were adapted from the literature (see Tab. 3.2). The T_2 value of BM is the mean value of the T_2 's of GM and WM. Estimated fit function parameters $I_{W,BM}(0)$ and $I_{W,CSF}(0)$ can be used to determine brain matter and CSF volume fractions within a voxel (see Eq. 3.10).

Alternatively, tissue volume fractions can be obtained from high-resolution MR images, which have to be segmented into GM, WM and CSF compartments and co-aligned (co-registered) with the position and orientation of the MRS voxel (see Fig. 3.2). GM, WM and CSF volume fractions are then calculated as the ratios between the number of MR

3 Absolute quantitation of brain metabolites

image voxels assigned to a particular tissue class ($N_{\text{vox}}^{\text{GM}}$, $N_{\text{vox}}^{\text{WM}}$, $N_{\text{vox}}^{\text{CSF}}$) and the number of all MR image voxels in the MRS voxel:

$$\begin{aligned} f_{\text{GM}} &= \frac{N_{\text{vox}}^{\text{GM}}}{N_{\text{vox}}^{\text{GM}} + N_{\text{vox}}^{\text{WM}} + N_{\text{vox}}^{\text{CSF}}} \\ f_{\text{WM}} &= \frac{N_{\text{vox}}^{\text{WM}}}{N_{\text{vox}}^{\text{GM}} + N_{\text{vox}}^{\text{WM}} + N_{\text{vox}}^{\text{CSF}}} \\ f_{\text{CSF}} &= \frac{N_{\text{vox}}^{\text{CSF}}}{N_{\text{vox}}^{\text{GM}} + N_{\text{vox}}^{\text{WM}} + N_{\text{vox}}^{\text{CSF}}} \end{aligned} \quad (3.12)$$

With these volume fractions, concentrations of brain metabolites can be calculated by using the following formula:

$$\begin{aligned} C_{\text{met}} &= \frac{I_{\text{M}}^{\text{vox}}}{I_{\text{W}}^{\text{vox}}} \cdot \frac{2}{N_{\text{prot,M}}} \cdot C_{\text{W}}^0 \cdot \\ &\cdot \frac{f_{\text{GM}} \cdot R_{\text{W}}^{\text{GM}} \cdot \alpha_{\text{GM}} + f_{\text{WM}} \cdot R_{\text{W}}^{\text{WM}} \cdot \alpha_{\text{WM}} + f_{\text{CSF}} \cdot R_{\text{W}}^{\text{CSF}} \cdot \alpha_{\text{CSF}}}{f_{\text{GM}} \cdot R_{\text{M}}^{\text{GM}} + f_{\text{WM}} \cdot R_{\text{M}}^{\text{WM}}} \end{aligned} \quad (3.13)$$

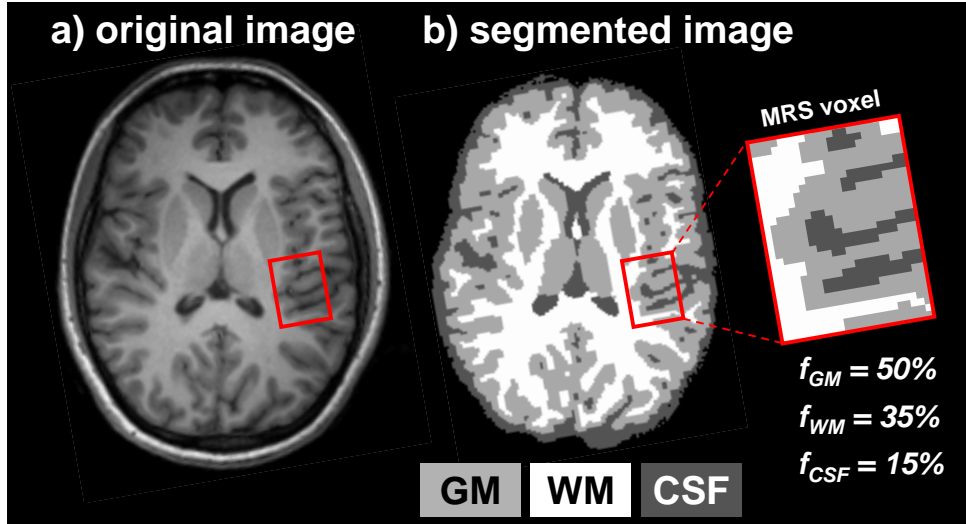


Figure 3.2: Estimation of GM, WM and CSF volume fractions within a MRS voxel (red) by using T_1 -weighted anatomic 3D MRI data (a), which were segmented into GM, WM and CSF compartments (b). The MRI slice shown in (a) was measured in the brain of a healthy volunteer with a *MP-RAGE* sequence at 3T (see detailed sequence description below and in [Brant-Zawadzki et al., 1992]). Tissue segmentation was performed by using the *FreeSurfer* brain image processing package (<http://surfer.nmr.mgh.harvard.edu/>, [Dale et al., 1999; Fischl et al., 1999]).

The latter approach has been preferred in most recent MR spectroscopic studies, since it provides the volume fractions of all major brain tissue compartments and allows to consider tissue composition in individual MRS voxels [Gasparovic et al., 2006; Wang and Li, 1998; Weber-Fahr et al., 2002]. The disadvantage is that this approach requires an additional anatomic MRI scan. On the other hand, MRI scans have to be performed for

the adjustment of MRS voxel position in any event and are therefore a routine part of clinical MRS protocols.

3.2 Combined processing of MRI and MRS data

3.2.1 Description of the data processing stream

The brain volume fractions determined from high resolution anatomical 3D MRI data sets were used to evaluate all *in vivo* ^1H -MR spectroscopic data processed in this thesis. The data processing stream, which was implemented as a fully automatic routine in MATLAB, is presented in Fig. 3.3 [Erdtel, 2009]. This stream contains the following steps:

1. **Segmentation of the high resolution whole-head 3D MRI data set.** This step is based on a fully automatic routines included in the image analysis suite *FreeSurfer* (Version 4.5.0, freely available under <http://surfer.nmr.mgh.harvard.edu/>, [Dale et al., 1999; Fischl et al., 1999]). After applying these routines, all voxels in the extracted brain volume are labelled according their assignment to certain subcortical areas (subcortical segmentation, [Fischl et al., 2002]). Using additional *a priori* information, these areas would be classified as GM, WM and CSF segments.
2. **Co-registration** of the segmented brain volume with the MR spectroscopic volume. This step is performed by using meta information from the MRI and MRS data file headers, which comprise MRI and MRS volume sizes as well as translational shifts and rotations of the volumes with respect to the MR scanner's coordinate system.
3. **Estimation of GM, WM and CSF volume fractions in the MRS voxel** (see Eq. 3.12).
4. **Loading tables with metabolite and water intensities.** Values are extracted from water suppressed and non-suppressed ^1H -MR spectra by using a fully automatic fitting routine included in the commercial software package *LCModel* [Provencher, 1993].
5. **Calculation of metabolite concentrations.**

The following subsections of this chapter describe these steps of the processing stream in more detail and present the *in vitro* and *in vivo* ^1H -MRS experiments that were performed to validate the effect of heterogeneous tissue composition on the accuracy of metabolite quantitation.

3.2.2 Tissue segmentation of brain MRI data

Segmentation of MRI brain volumes into GM, WM and CSF fractions typically uses T_1 -weighted, 3D MRI whole head data due to the enhanced contrast between these tissue

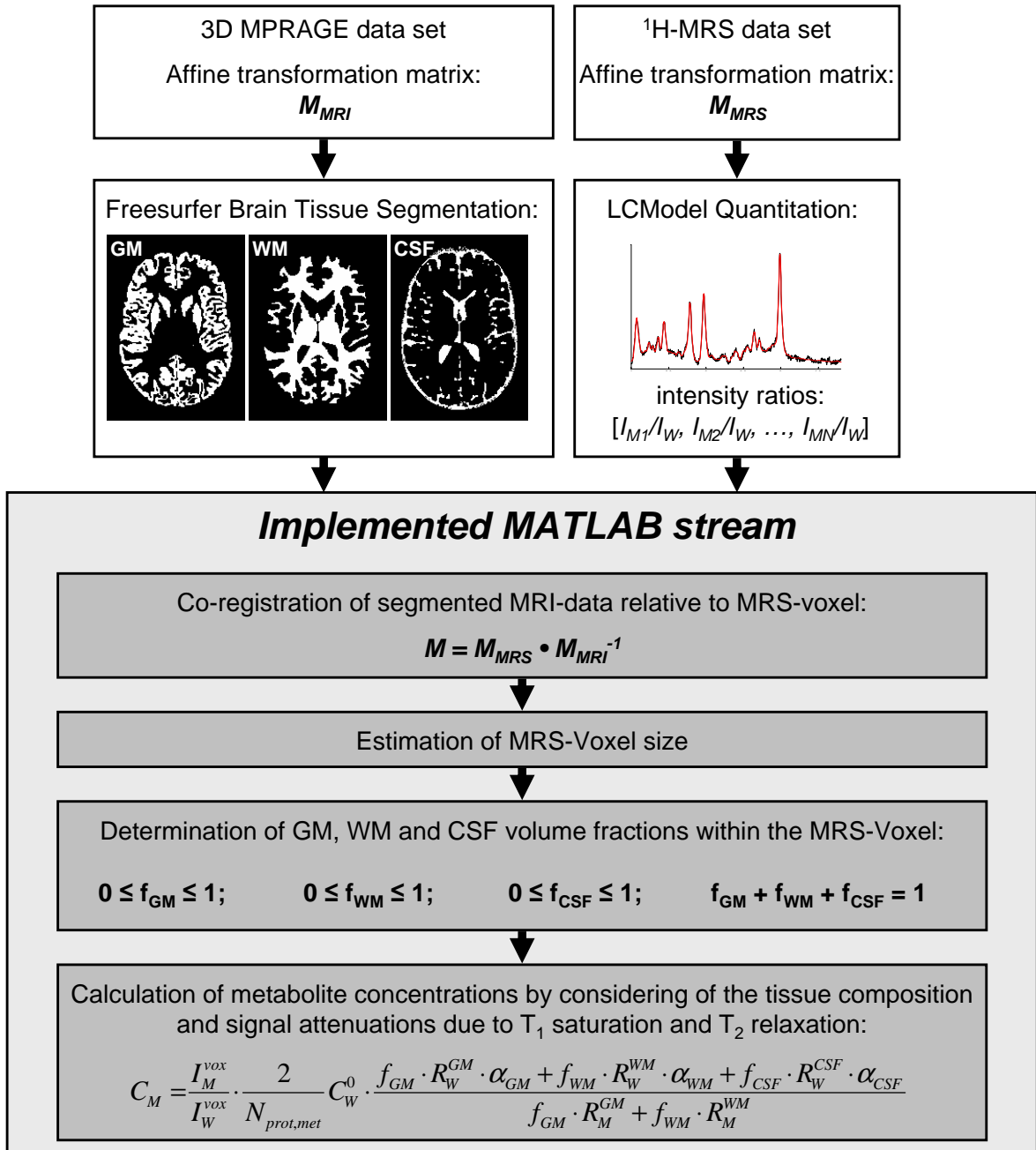


Figure 3.3: Implemented fully automatic workflow, which enables calculation of absolute metabolite concentrations with respect to heterogeneous tissue compositions within MRS voxels. The calculation is based on combined processing of tissue segmented high resolution brain volume data and spectroscopically detected signal intensities of brain metabolites and brain water. In order to determine GM, WM and CSF fractions within MRS voxels this tool performs co-registration of the MRI volume with respect to the MRS voxel. The estimation of the spatial shifts and rotations of MRI volume is based on the extraction of meta file information contained in the MRI and MRS data file headers.

types. A common MR sequence is the so-called *Magnetization Prepared Rapid Gradient Echo* (MP-RAGE) sequence [Brant-Zawadzki et al., 1992] with the following typical sequence parameters at 3T: $TE=3$ ms, $TR=2300$ ms, $TI=900$ ms, flip angle: 9° . The acquired volume usually contains 192 slices of 1 mm thickness in the sagittal orientation with an in-plane matrix of 256×256 pixels and isotropic pixel edge size of 1×1 mm². Depending on the use of additional accelerating techniques (e.g., the *Gene-Ralized Auto-calibrating Partially Parallel Acquisition* (GRAPPA) technique, [Griswold et al., 2002]), the acquisition time (TA) varies between 4 and 10 minutes.

The gold standard to segment brain MR images into brain tissue classes is still manual analysis by an experienced observer. However, this procedure is rather time consuming and calls for automatic approaches. In the present work all MRI brain volumes were processed by using a fully automatic stream, included in the image analysis suite *FreeSurfer* (Version 4.5.0, freely available under <http://surfer.nmr.mgh.harvard.edu/>, [Dale et al., 1999; Fischl et al., 1999]). This stream includes removal of non-brain tissue (see Fig. 3.4b), intensity normalization, transformation to Talairach-like space and subcortical segmentation, i.e., labelling of the brain volume segments according their assignment to particular cortical areas by using the *a priori* information from an anatomical brain atlas [Desikan et al., 2006; Fischl et al., 2002].

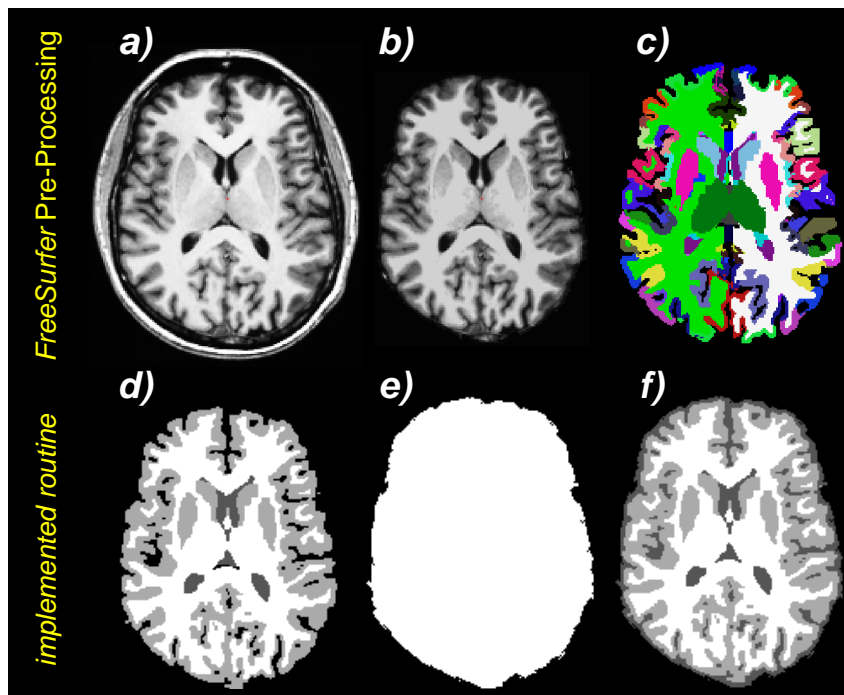


Figure 3.4: Steps during the segmentation process using a 3D high resolution T_1 weighted whole brain MRI data set: (a) transverse slice of an T_1 weighted MRI volume, (b) removal of non-brain structures, (c) segmentation of brain volume into separated cortical areas (represented by different RGB values), (d) classification of segmented cortical areas with respect to their assignment to GM, WM and CSF, (f) additional assignment of non classified CSF areas by using a brain mask (e).

The first step in the own processing stream is the segmentation of the brain volume into the GM, WM and CSF compartments. During subcortical segmentation, *FreeSurfer* identifies all MRI volume pixels by unique IDs, which correspond to particular cortical areas and can be used to visualise the segmented areas in an RGB image by assigning the extracted IDs to RGB values (see Fig. 3.4c). In the current *FreeSurfer* version, overall 256 subcortical areas are distinguished. By means of an *a priori* knowledge-based encoding table these IDs of subcortical areas are condensed into a smaller number of IDs, corresponding to GM, WM or CSF [Güllmar, 2008]. These new IDs can be assigned to characteristic grey scale values to visualise GM-WM-CSF segmented MRI volumes (see Fig. 3.4d). The encoding table used in the present work is shown in Table A.1.

Some pixels in the ventricles or in the sulci are not assigned to a specific subcortical area and are therefore not classified (black 'holes' in Fig. 3.4d). However, depending on whether these pixels are located inside or outside the brain volume, they can be subsequently relabelled as CSF or non-brain structures (skin, skull, air), respectively. Whether these non-classified pixels do belong to the brain volume or not is determined by using the 3D mask (see Fig. 3.4e), which defines the borders of the brain volume.

3.2.3 Co-alignment of MRI and MRS data

Following segmentation, co-registration has to be performed to realign the brain volume with respect to the position and orientation of the MRS volume. As demonstrated in Fig. 3.5, spatial co-registration uses affine transformations to perform translational shifts between the two volumes (translation) as well as re-orientations of both volumes relative to each other (rotation). Further operations, such as scaling or shearing could be omitted, since the *FreeSurfer* pre-processing stream re-grids the MRI volume into an isotropic spatial grid with 1 mm^3 large cubic voxels.

The complete representation of each volume element within the total MRI volume is defined by its intensity value (i.e., grey scale value) as well as by the position vector $\vec{v} = [v_x, v_y, v_z]^T$, which describes the coordinates of the volume element in a frame of reference $[x, y, z]^T$. To map the initial frame of reference to a target frame of reference ($[x, y, z]^T$ vs. $[x', y', z']^T$), a linear transformation of coordinates of the volume element has to be performed, which is described by a 3×3 transformation matrix \mathbf{A} [Bronstein et al., 2001]:

$$\mathbf{A} = \begin{bmatrix} a_{xx} & a_{xy} & a_{xz} \\ a_{yx} & a_{yy} & a_{yz} \\ a_{zx} & a_{zy} & a_{zz} \end{bmatrix} \quad (3.14)$$

Consequently, the position of a volume element in the target frame of reference (defined by the new vector \vec{v}') can be determined by multiplication of vector \vec{v} with the linear

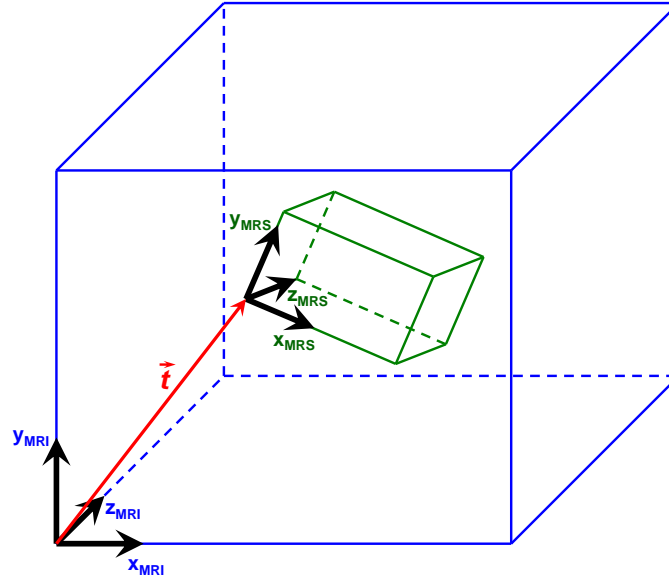


Figure 3.5: Co-registration of the MRI volume (blue box) with the MRS volume (green box) requires application of affine transformations, which brings the frame of reference of the MRI volume $([x_{\text{MRI}}, y_{\text{MRI}}, z_{\text{MRI}}]^T)$ into agreement with the frame of reference of the MRS volume $([x_{\text{MRS}}, y_{\text{MRS}}, z_{\text{MRS}}]^T)$. The transformation considers first the spatial shift between the MRI and MRS volume origins (translation component, characterised by the vector \vec{t}) following by rotations of the MRI volume relative to the MRS volume (rotation component).

transformation matrix \mathbf{A} :

$$\vec{v}' = \mathbf{A} \cdot \vec{v} \quad (3.15)$$

In the specific case of co-registration of the MRI volume with the MRS voxel the different orientations of the MRI and MRS frames of reference have to be considered first. This is done by applying three rotation matrices \mathbf{R}_x , \mathbf{R}_y and \mathbf{R}_z , which describe the rotations of the MRI volume around the x' , y' and z' axes of the MRS frame of reference by the angles α_x , α_y and α_z , respectively:

$$\begin{aligned} \mathbf{R}_x &= \begin{bmatrix} 1 & 0 & 0 \\ 0 & \cos \alpha_x & -\sin \alpha_x \\ 0 & \sin \alpha_x & \cos \alpha_x \end{bmatrix} \\ \mathbf{R}_y &= \begin{bmatrix} \cos \alpha_y & 0 & \sin \alpha_y \\ 0 & 1 & 0 \\ -\sin \alpha_y & 0 & \cos \alpha_y \end{bmatrix} \\ \mathbf{R}_z &= \begin{bmatrix} \cos \alpha_z & -\sin \alpha_z & 0 \\ \sin \alpha_z & \cos \alpha_z & 0 \\ 0 & 0 & 1 \end{bmatrix} \end{aligned} \quad (3.16)$$

A combination of rotations is summarised in the rotation matrix \mathbf{R} , which is the matrix

product of the particular rotation components \mathbf{R}_x , \mathbf{R}_y and \mathbf{R}_z .

In a second step, co-registration has to take into account the spatial shift between the two coordinate frames (translation). This shift is described by a translation vector $\vec{t} = [t_x, t_y, t_z]^T$ (see red arrow in Fig. 3.5). Considering both, rotation and translation components, the representation of a vector \vec{v}' in the MRS frame of reference is given by:

$$\begin{bmatrix} v_x' \\ v_y' \\ v_z' \end{bmatrix} = \begin{bmatrix} r_{xx} & r_{xy} & r_{xz} \\ r_{yx} & r_{yy} & r_{yz} \\ r_{zx} & r_{zy} & r_{zz} \end{bmatrix} \cdot \begin{bmatrix} v_x \\ v_y \\ v_z \end{bmatrix} + \begin{bmatrix} t_x \\ t_y \\ t_z \end{bmatrix} \quad (3.17)$$

In order to reduce the calculation complexity due to the combination of matrix multiplication and addition, it is favourable to define the complete transformation by a single matrix by using so-called homogeneous coordinates [Bronstein et al., 2001]. This means to represent a 3D vector $\vec{v} = [v_x, v_y, v_z]^T$ as a 4D vector $\vec{v}_{\text{hom}} = [v_x, v_y, v_z, 1]^T$. By using homogeneous coordinate space, translations and rotations can be performed in one step by multiplying the vector \vec{v}_{hom} with the transformation matrix \mathbf{M}_{hom} , which is formed by the product of the translation matrix \mathbf{T}_{hom} and rotation matrix \mathbf{R}_{hom} :

$$\mathbf{T}_{\text{hom}} = \begin{bmatrix} 0 & 0 & 0 & t_x \\ 0 & 0 & 0 & t_y \\ 0 & 0 & 0 & t_z \\ 0 & 0 & 0 & 1 \end{bmatrix} \quad \mathbf{R}_{\text{hom}} = \begin{bmatrix} r_{xx} & r_{xy} & r_{xz} & 1 \\ r_{yx} & r_{yy} & r_{yz} & 1 \\ r_{zx} & r_{zy} & r_{zz} & 1 \\ 0 & 0 & 0 & 1 \end{bmatrix} \quad (3.18)$$

In the current data processing work flow (see Fig. 3.3) the complete transformation matrix \mathbf{M}_{hom} was calculated by a product of two matrices, $(\mathbf{M}_{\text{MRI,hom}})^{-1}$ and $\mathbf{M}_{\text{MRS,hom}}$, describing first the re-alignment of the frame of references of the MRI volume into the frame of reference of the MR scanner and, second the transformation of the scanner's coordinate system into the coordinate system of the MRS voxel [Erdtel, 2009]:

$$\vec{v}_{\text{hom}}' = \mathbf{M}_{\text{hom}} \cdot \vec{v}_{\text{hom}} = \mathbf{M}_{\text{MRS,hom}} \cdot (\mathbf{M}_{\text{MRI,hom}})^{-1} \cdot \vec{v}_{\text{hom}} \quad (3.19)$$

Matrices $\mathbf{M}_{\text{MRI,hom}}$ and $\mathbf{M}_{\text{MRS,hom}}$ were formed by using the spatial information in the headers of the MRI and MRS data files, respectively (MRI file in NifTI format (NifTI: *Neuroimaging Informatics Technology Initiative* [NifTI, 2009]); MRS file in RDA format (RDA: *Raw DATA*, Siemens Medical Solutions, Erlangen, Germany).

3.3 Experimental validation

The implemented method was validated by means of two separate ^1H -MR spectroscopic studies. The first study was performed with a specially constructed phantom containing NAA aqueous solutions to evaluate the accuracy of metabolite quantitation. In the second study concentrations of three brain metabolites, NAA, Cr and total choline (tCho)

were estimated from brain ^1H -MR spectra of healthy controls with different experimental parameters (MRS voxel size and repetition time). The aim of this second study was to evaluate whether the implemented quantitation algorithm is able to compensate biases of calculated concentrations due to variation of experimental settings.

3.3.1 General experimental conditions

Both studies were performed on a clinical whole-body 3 T MR scanner (Magnetom Trio, Siemens Medical Solutions, Erlangen, Germany). A double-resonance ($^1\text{H}/^{31}\text{P}$) *transmit/receive* volume head coil operating at 123.3 MHz and 50.0 MHz, respectively (Biomedical Rapid GmbH, Würzburg, Germany) was used for the phantom study. *In vivo* data were measured using a 12-channel *receive only* multiple channel head coil (head matrix coil, Siemens Medical Solutions, Erlangen, Germany).

In both studies, the location of the MRS voxels was selected based on T_1 -weighted images acquired with a 3D MP-RAGE sequence (see Chap. 3.2.2 for detailed description of parameter settings).

A PRESS sequence with single volume localisation was used for all ^1H -MR spectroscopic measurements (TE : 30 ms, N_{Sample} : 4096, BW : 4 kHz ($BW = \Delta t^{-1}$, Δt is the sampling dwell time, see Chap. 2.1.5), sequence scheme is shown in Fig. 2.10b). NAS and TR differed between the *in vitro* and *in vivo* studies (see Chaps. 3.3.3.2 and 3.3.4.1). To ensure sufficient B_0 field homogeneity in the spectroscopic volumes, automatic first and second order MR shimming was performed, followed by manual fine-tuning of the shim gradients using the linewidth of the unsaturated water signal as a control parameter.

In each single experiment spectra were measured with and without the water suppression to quantitate the intensities of metabolites ($I_{\text{M}}^{\text{vox}}$) and water ($I_{\text{W}}^{\text{vox}}$). The water non-suppressed spectrum was used to correct the line shape distortions due to the eddy currents (see the phase correction subsection in Chap. 2.3.3.3).

3.3.2 Post-processing of MR spectra

Metabolite and water spectra were phase and eddy current corrected by using a self written MATLAB function. Baseline correction of spectra and quantitation of metabolite and water intensities ($I_{\text{M}}^{\text{vox}}$ and $I_{\text{W}}^{\text{vox}}$) was performed with the LCModel package (V 2.5, [Provencher, 1993]). *In vivo* metabolite spectra were fitted by using an imported basis data set, containing 15 *in vitro* metabolite model spectra (NAA, Cr, *glycerophosphorylcholine* (GPC), *phosphorylcholine* (PCh), Glu, Gln, GABA, mI, *scyllo-Inositol* (Scyllo), *lactate*, *alanine*, *aspartate*, *taurine*, *glucose* and *guanidoacetate*). Metabolite intensities were fitted in the chemical shift range between 0.5 and 4.2 ppm to take into account baseline distortions caused by macromolecules (MM) (see Fig. 2.17). The corresponding broad resonances were included in the model spectra basis set as simulated singlets at 0.9, 1.2, 1.4, 1.7 and 2.0 ppm [Provencher, 1993]. *In vitro* NAA spectra were analysed with the

same basis set by excluding all metabolite model spectra except the NAA spectrum. *In vitro* and *in vivo* measured water intensities (I_W^{vox}) were automatically quantitated with the LCModel by fitting the first 20 points of water FID with a mono exponential decay function.

SNR and spectral linewidth of the NAA CH_3 -group singlet at 2.01 ppm were determined by LCModel and monitored for all extracted spectra. SNR_{NAA} was calculated by taking the ratio between the baseline corrected NAA peak amplitude and twice the standard deviation of the spectrum's residuals that remained after subtraction of the fitted results from the original spectrum [Provencher, 1993]. The spectral linewidth was determined from the *FWHM* value (full width at half maximum) of the NAA singlet.

3.3.3 *In vitro* study

3.3.3.1 Description of phantom

The aim of the *in vitro* study was to simulate the quantitation of metabolite ^1H -MR spectra in voxels, which were composed of brain tissue analogous compartments with different water concentrations. Furthermore, these compartments should contain different NAA levels and simulate partial volume effects of CSF, which often occur in *in vivo* brain ^1H -MRS measurements due to the vanishing metabolite content in CSF. Considering these requirements, the phantom was made up of a plastic box (205 mm long, 104 mm wide and 53 mm high) with 18 impermeable chambers (chamber volume: $33 \times 33 \times 53 \text{ mm}^3$, chamber wall thickness: 1.0–1.5 mm), which were separately filled via reclosable ports (see Fig. 3.6a). The prepared phantom was immersed into a plastic tank, filled with distilled water to reduce magnetic susceptibility inhomogeneities around the phantom chambers. For the measurements this tank was placed in the centre of the head coil.

The phantom chambers were filled with three kinds of aqueous solutions with different concentrations of water (C_W) and NAA (C_{nom}). The first solution represented white matter of the brain (*white matter solution*, WMS) with 50 mmol/l NAA and 33.3 mol/l water ($\alpha_{\text{WMS}} = 0.6$). The second solution represented grey matter (*grey matter solution*, GMS) and contained 25 mmol/l NAA and 44.4 mol/l water ($\alpha_{\text{GMS}} = 0.8$). The third solution represented the cerebral spinal fluid (*cerebral spinal fluid solution*, CSFS) and contained only free distilled water ($C_W^{\text{CSFS}} = 55.6 \text{ mol/l}$, $\alpha_{\text{CSFS}} = 1.0$, $C_{\text{nom}}^{\text{CSFS}} = 0 \text{ mmol/l}$). Concentration of the water in the solutions was adjusted by adding deuterium oxide (D_2O), whose molecular structure and physical properties are similar to water. However, since deuterium has a different magnetic moment and spin, it does not contribute to the NMR signal of water. NAA levels in WMS and GMS were adjusted by dilution of a commercially available NAA concentrate (Sigma Aldrich GmbH, Germany) in a buffer solution, containing 72 mmol/l *dipotassium phosphate* (K_2HPO_4) and 28 mmol/l *monopotassium phosphate* (KH_2PO_4). In order to adjust the pH to 7.2, *sodium hydroxide* (NaOH) was successively added to WMS and GMS.

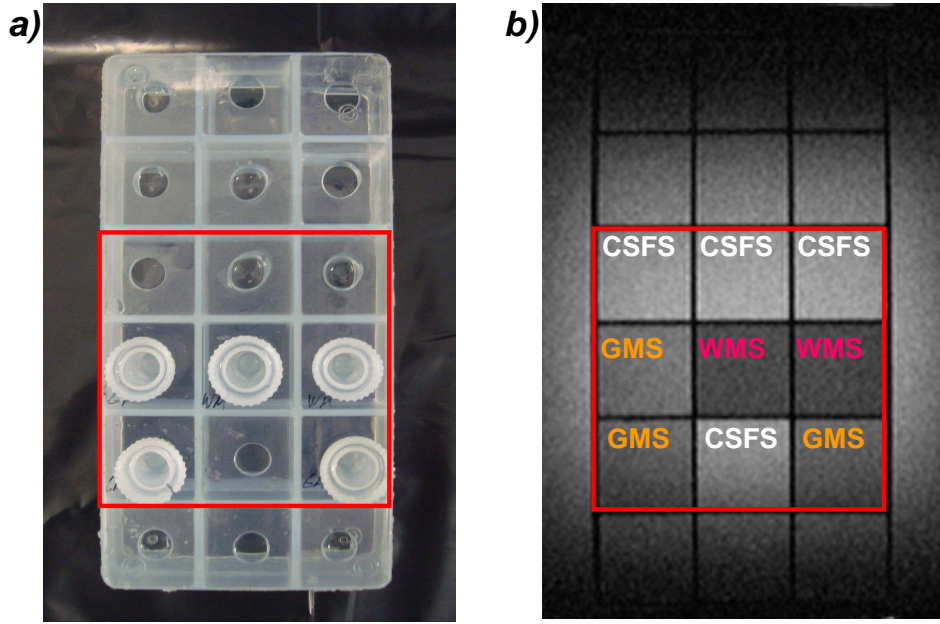


Figure 3.6: Photograph of the phantom containing 18 impermeable refillable chambers (a). Chambers closed by plugs were filled with GM and WM representing solutions (GMS, WMS). Non-closed chambers contain a CSF representing solution (CSFS). Variation of MR water signal intensities due to different contents of free water in GMS, WMS and CSFS solutions on a coronal slice (b), which was reconstructed from a 3D MP-RAGE data set.

Two, three and thirteen of the eighteen phantom chambers were filled with WMS, GMS and CSFS, respectively. The distribution of the phantom chambers with the particular solutions is demonstrated in Fig. 3.6b. In this figure, the different solutions can be distinguished by their image intensity, which depends on the water concentration.

3.3.3.2 Performed measurements

The evaluation of the partial volume effect correction was based on two *in vitro* series, which consisted of five and eight single MR spectroscopic experiments at different voxel locations, respectively (see Fig. 3.7). As mentioned, in each experiment spectra were acquired with and without the water suppression ($TR_M/TR_W = 15000$ ms; $NAS_M/NAS_W = 32/16$, $V_{Vox} = 15 \times 15 \times 15$ mm³). In the first series, five different MRS voxel positions were selected to sample different volume fractions of WMS and CSFS, thus simulating tissue heterogeneity in a two compartment system (see Fig. 3.7a). In the second series, eight MRS voxel positions were aligned along a diagonal line connecting the centres of the phantom chambers with WMS and GMS (see Fig. 3.7b). In this way, the voxel compositions varied with respect to volume fractions of all three compartments.

Volume fractions of the three solutions in the MRS voxels were determined by manual segmentation of MP-RAGE data, which was co-registered with the spectroscopic volumes. All extracted volume fractions are summarised in Tab. 3.3.

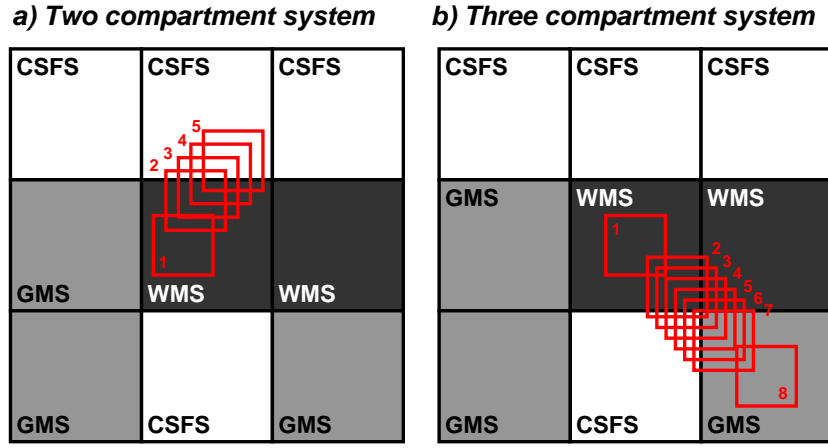


Figure 3.7: Selected locations of MRS voxels (red) in the two compartment experiment (a) and in the three compartment experiment (b).

Table 3.3: Volume fractions of GMS, WMS and CSFS (f_{GMS} , f_{WMS} and f_{CSFS} in %) in the 5 and 8 MRS voxels of the first and second phantom series.

<i>First series</i>				<i>Second series</i>			
Nr.	f_{GMS}	f_{WMS}	f_{CSFS}	Nr.	f_{GMS}	f_{WMS}	f_{CSFS}
1	0.0	100.0	0.0	1	0.0	100.0	0.0
2	0.0	85.2	14.8	2	1.0	905	08.5
3	0.0	62.8	37.2	3	5.7	761	18.2
4	0.0	40.3	59.7	4	15.0	613	23.7
5	0.0	17.8	82.2	5	26.3	506	23.1
				6	50.9	276	21.5
				7	74.1	14.1	11.8
				8	100.0	0.0	0.0

The T_1 and T_2 relaxation time constants of NAA and water in GMS, WMS and CSFS (see Tab. 3.4) were estimated from additional ^1H -MR spectroscopic measurements with different TR and TE adjustments [Erdtel, 2009]. The extracted signal courses were fitted by mono-exponential functions to describe T_1 recovery (see Eq. 2.19) and T_2 decay (see Eq. 2.21). The estimated T_1 and T_2 values were used to correct the calculated NAA concentrations, according to Eq. 3.13.

NAA concentrations were calculated by assuming homogeneously composed MRS voxels containing only WMS ($C_{\text{hom}}^{\text{WMS}}$) or only GMS ($C_{\text{hom}}^{\text{GMS}}$) and alternatively by considering the individual volume fractions of GMS, WMS and CSFS in the voxels (C_{het}). In the first series (crossing from WMS to CSFS), differences between the calculated NAA concentrations and the nominal NAA level in WMS ($C_{\text{nom}}^{\text{WMS}} = 50 \text{ mmol/l}$) were used to evaluate the compensation of error occurring due to the increased CSFS partial volume effect. In the

Table 3.4: Estimated *in vitro* T_1 and T_2 relaxation times for NAA and water in GMS, WMS and CSFS [Erdtel, 2009].

	T_1 [s]			T_2 [s]		
	GMS	WMS	CSFS	GMS	WMS	CSFS
NAA	1.62±0.39	1.68±0.23	-	1.20±0.30	0.99±0.26	-
Water	3.22±0.77	4.14±0.11	2.94±0.03	2.46±0.61	2.51±0.62	2.03±0.33

second series (crossing from WMS to GMS chamber with a variation of CSFS content), differences between the experimentally determined NAA levels and the nominal NAA concentrations (C_{nom}) were used to evaluate the CSFS partial volume effect compensation as well as to verify whether the calculated metabolic levels may reproduce the initially adjusted difference of the NAA concentrations between the GMS and WMS solution. In the second series, the nominal NAA change was approximated by a linear decline of the NAA concentration between the WMS and GMS ($C_{nom}^{WMS} = 50$ mmol/l; $C_{nom}^{GMS} = 25$ mmol/l).

3.3.4 *In vivo* study

The aim of the *in vivo* study was to evaluate whether the combined analysis of spectroscopic and imaging data improves the estimations of brain metabolite concentrations. The insular cortex was selected as the region of interest for the spectroscopic experiments for two reasons. Firstly, assessment of metabolic information from this brain area is important for numerous psychiatric research applications, since it is known to be involved in the regulation of many cognitive brain functions (e.g. self awareness, anxiety, affective pain processing and interpersonal experience [Apkarian et al., 2005; Phan et al., 2002]). Secondly, since the insular cortex is located close to the brain ventricles, spectroscopic voxels may contain substantial CSF fractions, which makes consideration of partial volume effects necessary. Furthermore, the short T_2 and long T_1 relaxation time constants *in vivo* (see Tabs. 3.1 and 3.2) lead to non-negligible attenuations of metabolite and water signals. Especially the large differences of water's T_1 and T_2 between brain matter and CSF (see Tab. 3.2) may cause substantial errors when using water signal as a tissue internal concentration reference without considering signal attenuation.

Two different experimental settings (voxel sizes, TRs) were used to acquire two sets of spectroscopic data. It was hypothesised that considering the tissue specific relaxation parameters would reduce inter-individual variations. It was also assumed that consideration of the CSF contents in the MRS voxels results in more precise calculation of metabolic concentration indicated by a better correlation between metabolic concentrations and tissue compositions in the spectroscopic volume.

3.3.4.1 Performed measurements

Overall 14 male healthy volunteers (mean age: 25 ± 3 years) participated in the *in vivo* study. The subjects were divided into two groups (GI, GII), each consisting of seven volunteers. ^1H -MR spectroscopic examinations were performed in the left anterior insular cortex (selected voxel position is showed in Fig. 3.8a). Metabolite spectra were calculated by averaging 64 and 128 water suppressed single acquisitions for the volunteer groups GI and GII, respectively ($NAS_M^{GI}/NAS_M^{GII} = 64/128$). Water spectra were reconstructed in both groups by averaging 16 single water non-suppressed acquisitions ($NAS_W = 16$). Experimental protocols also differed between GI and GII regarding the adjusted voxel sizes (GI: $V_{Vox}^{GI} = 2.5$ ml; GII: $V_{Vox}^{GII} = 3.0$ ml) as well as repetition times (GI: $TR_M^{GI}/TR_W^{GI} = 5.0$ s/5.0 s; GII: $TR_M^{GII}/TR_W^{GII} = 2.0$ s/10.0 s).

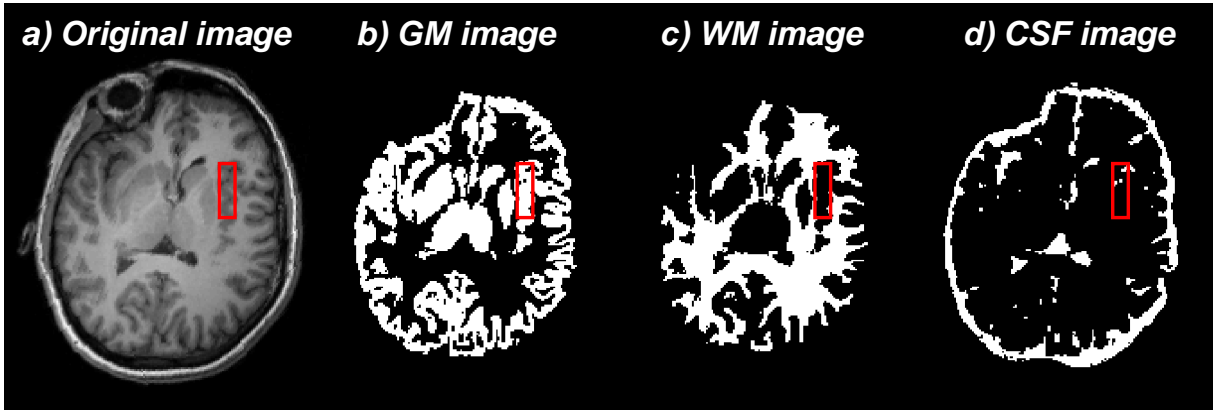


Figure 3.8: Position of the MRS voxel (red box) in the left insular cortex of a healthy volunteer (GII) on a transverse slice of the 3D T_1 -weighted MRI data set (a), which was co-registered with the MRS voxel. Corresponding GM (b), WM (c) and CSF (d) masks, generated by *FreeSurfer*, were used to determine the brain tissue fractions (f_{GM} , f_{WM} and f_{CSF}) within the MRS voxel.

3.3.4.2 Post processing of MRI and MRS data

High resolution, whole head MR volumes (MP-RAGE data) were pre-processed and automatically segmented into GM, WM and CSF compartments (as described in Chap. 3.2.2). Segmented images were co-registered with the spectroscopic volumes to determine the relative tissue volume fractions (f_{GM} , f_{WM} and f_{CSF}) in the MRS voxels (see Fig. 3.8b, c and d).

Absolute concentrations of NAA, Cr and tCho were calculated with two different assumptions. First, homogeneous GM MRS voxels were assumed without any WM and CSF contents. Estimated concentration values are referred to as $C_{M_x,uncor}^{GI}$ and $C_{M_x,uncor}^{GII}$ for GI and GII, respectively. Secondly, metabolic concentrations were estimated by considering the determined GM, WM and CSF volume fractions in the voxels ($C_{M_x,cor}^{GI}$ and $C_{M_x,cor}^{GII}$). In both approaches, attenuation of metabolite and water signals due to relaxation was taken into account.

3.3.4.3 Statistical data evaluation

Extracted relative volumes of the GM, WM and CSF compartments were compared between GI and GII with an unpaired *t-test*. With the known volume fractions of CSF, the influence of partial volume effects on the calculated metabolite concentrations was evaluated.

A *t-test* was also used to compare the metabolite concentrations in both groups calculated by assuming homogeneous as well as heterogeneous MRS voxels ($C_{M_x, \text{uncor}}^{\text{GI}}$ vs. $C_{M_x, \text{cor}}^{\text{GI}}$ and $C_{M_x, \text{uncor}}^{\text{GII}}$ vs. $C_{M_x, \text{cor}}^{\text{GII}}$).

Uncorrected and corrected concentrations were also compared between GI and GII ($C_{M_x, \text{uncor}}^{\text{GI}}$ vs. $C_{M_x, \text{uncor}}^{\text{GII}}$) and ($C_{M_x, \text{cor}}^{\text{GI}}$ vs. $C_{M_x, \text{cor}}^{\text{GII}}$) to decide, whether the potential metabolic level differences are originating:

- from a variation of the CSF volume due to the voxel size or
- from differences in GM and WM volume fractions between GI and GII.

Finally, the relation between the corrected concentrations ($C_{M_x, \text{cor}}^{\text{GI}}$ and $C_{M_x, \text{cor}}^{\text{GII}}$) and the corresponding GM content was assessed by means of the coefficient of determination (R^2). Analogous analysis was also performed to assess the correlation between the uncorrected metabolic levels ($C_{M_x, \text{uncor}}^{\text{GI}}$ and $C_{M_x, \text{uncor}}^{\text{GII}}$) and the corresponding CSF content.

3.4 Results

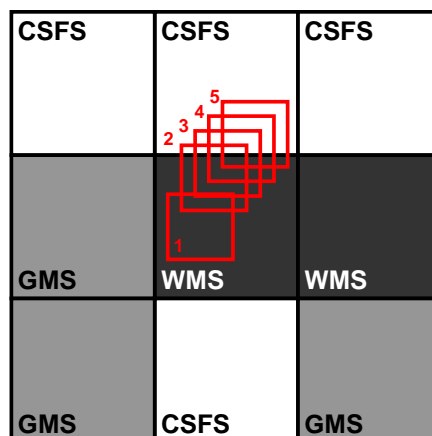
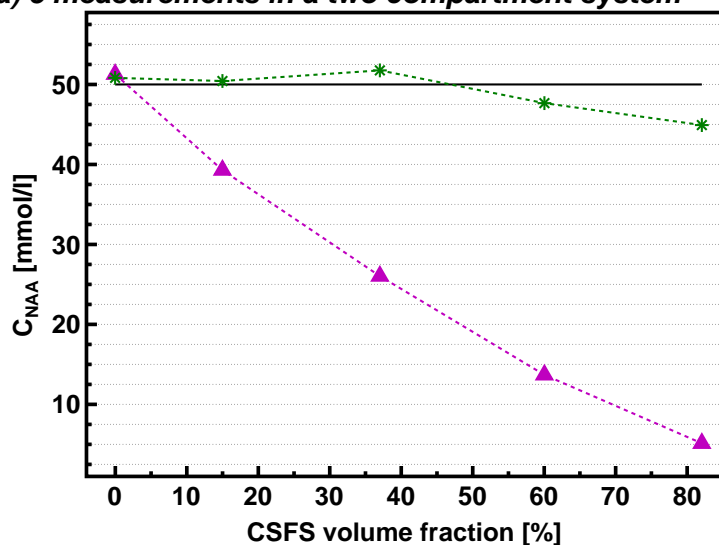
3.4.1 *In vitro* study

All *in vitro* ^1H -MR spectra revealed sufficient spectral resolution ($FWHM < 1.5$ Hz). Depending on the CSFS content, SNR_{NAA} varied between 20 and 290. With *Cramer Rao Lower Bound* (CRLB) values below 2%, data quality was sufficiently high to accurately quantitate NAA intensities.

Fig. 3.9 shows plots of the NAA concentration as a function of volume fraction, which were obtained from the two compartment experiment (Fig. 3.9a) and from the three compartment experiment (Fig. 3.9b). In the two compartment system, the magenta graph (filled triangles) represents the NAA levels calculated by assuming homogeneous MRS voxels containing only WMS ($C_{\text{hom}}^{\text{WMS}}$), whereas the green graph (asterisks) shows the NAA values calculated by considering the WMS and CSFS volume fractions in the MRS voxels (C_{het}). In the Fig. 3.9b, the magenta (filled triangles) and brown (filled circles) graphs depict the NAA concentrations estimated by assuming homogeneous WMS ($C_{\text{hom}}^{\text{WMS}}$) and GMS voxels ($C_{\text{hom}}^{\text{GMS}}$), respectively. The green graph (asterisks) illustrates the NAA levels calculated for heterogeneous GMS-WMS-CSFS voxels. The black solid lines in Figs. 3.9a and b indicate nominal NAA concentrations (C_{nom}).

In the first series, uncorrected NAA concentrations ($C_{\text{hom}}^{\text{WMS}}$) revealed an approximately linear decline with increasing CSFS volume fraction (see magenta graph in Fig. 3.9a). In

a) 5 measurements in a two compartment system



b) 8 measurements in a three compartment system

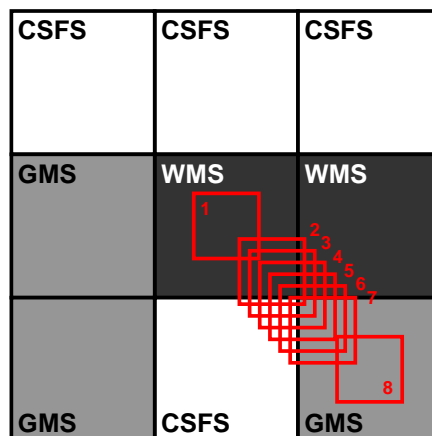
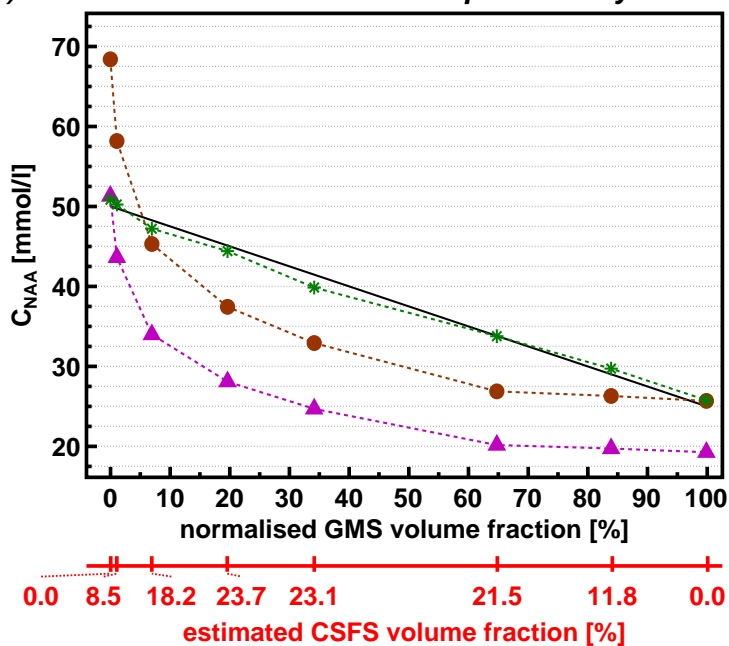


Figure 3.9: Plots of NAA concentrations, which were obtained in the *in vitro* experiment series in MRS voxels containing two compartments (a) and three compartments (b). Magenta and brown graphs show NAA concentration courses, which were calculated by assuming homogeneous MRS voxels containing only WMS (magenta) or only GMS (brown). Green graphs represent NAA concentrations, which were calculated by considering the heterogeneous composition within MRS voxels. Black graphs show nominal NAA concentrations. In (a) NAA concentrations are plotted against increasing CSFS volume fractions (f_{CSFS}), whereas in (b) NAA concentrations are plotted against the normalised GMS fraction ($f'_{GMS} = f_{GMS}/(1 - f_{CSFS})$). The corresponding CSFS fractions are presented on the additional red axis below (b).

the voxel with maximum CSFS content (82%), the calculated NAA concentration was approximately 90% lower compared to the nominal NAA level. In contrast, corrected NAA concentrations revealed much better agreement with the nominal values (see the green graph in Fig. 3.9a). In contrast to the highly underestimated $C_{\text{hom}}^{\text{WMS}}$ values, the maximum difference between corrected and nominal NAA concentrations was 5%, except for the voxel with a highest CSFS content, in which the calculated NAA concentration was 10% lower than the nominal value (see the last point of the green graph in Fig. 3.9a).

Results obtained with the three solution compartments (second series) reproduced the observations of the first series. The magenta and brown graphs in Fig. 3.9b show the increasing underestimation of the uncorrected NAA concentrations with increasing CSFS fractions. The offset between the magenta and brown curves in Fig. 3.9b can be attributed to different amounts of water concentrations, which were assumed for the calculation of $C_{\text{hom}}^{\text{WMS}}$ ($\alpha_{\text{WMS}} = 0.6$, magenta graph) and $C_{\text{hom}}^{\text{GMS}}$ ($\alpha_{\text{GMS}} = 0.8$, brown graph). This also explains why the first point of the $C_{\text{hom,WMS}}$ plot (corresponding to the MRS voxel containing only WMS) and the last point of the $C_{\text{hom,GMS}}$ plot (corresponding to the MRS voxel containing only GMS) are in a good agreement with the nominal NAA levels. Mean relative differences between calculated and nominal NAA concentrations were $27.3 \pm 13.8\%$ for $C_{\text{hom}}^{\text{WMS}}$ and $16.3 \pm 10.6\%$ for $C_{\text{hom}}^{\text{GMS}}$.

Contrary to $C_{\text{hom}}^{\text{GMS}}$ and $C_{\text{hom}}^{\text{WMS}}$, corrected NAA concentrations, which were calculated by considering the heterogeneous voxel composition (C_{het} , green graph in Fig. 3.9b), closely followed the linear decline of nominal NAA levels (black line in Fig. 3.9b). The largest difference between the C_{het} level and the nominal value was 4% and observed for MRS voxels with the largest CSFS content. The mean relative difference between the calculated C_{het} levels and the nominal NAA concentrations was $2.0 \pm 1.2\%$.

3.4.2 *In vivo* study

As demonstrated by the representative *in vivo* metabolite ^1H -MR spectrum in Fig. 3.10d, all spectroscopic data showed high spectral resolution. Averaged over all metabolite spectra, the mean $FWHM_{\text{NAA}}$ was 3.9 ± 0.7 Hz. Due to the twofold higher NAS_{M} in the GII protocol, the metabolite spectra had the expected ($\sim \sqrt{2}$) larger SNR_{NAA} compared to GI group ($SNR_{\text{NAA}}^{\text{GI}} = 11.3 \pm 1.7$ vs. $SNR_{\text{NAA}}^{\text{GII}} = 16.7 \pm 0.8$, $p < 0.001$). In both groups SNR was large enough to provide sufficient accuracy for quantitation of NAA, Cr and tCho ($CRLB < 6\%$).

Mean volume fractions (f_{GM} , f_{WM} and f_{CSF}) are presented in Tab. 3.5 for both groups. Tab. 3.5 also contains mean values of normalised GM and WM volume fractions ($f'_{\text{GM}} = f_{\text{GM}}/(1 - f_{\text{CSF}})$ and $f'_{\text{WM}} = f_{\text{WM}}/(1 - f_{\text{CSF}})$), which were used for the CSF fraction independent evaluation of grey and white matter volume fraction variation between GI and GII. The normalised GM content (f'_{GM}) in GII was 20% higher than in GI ($p = 0.001$). Correspondingly, the f'_{WM} value was 35% lower in GII than in GI ($p = 0.001$). Compared

to GI, voxels in GII contained an approximately twofold higher CSF content ($p = 0.014$).

Table 3.5: Mean values and standard deviations (SD) of extracted GM, WM and CSF fractions (f_{GM} , f_{WM} , f_{CSF}) in GI and GII. The f'_{GM} and f'_{WM} values indicate the CSF corrected GM and WM fractions ($f'_{GM} = f_{GM}/(1 - f_{CSF})$). The p -values reflect the results of a t -test based mean value comparison of tissue fractions between GI and GII.

	f_{GM}		f_{WM}		f_{CSF}		f'_{GM}		f'_{WM}	
	GI	GII	GI	GII	GI	GII	GI	GII	GI	GII
Mean	0.61	0.69	0.34	0.21	0.05	0.10	0.64	0.77	0.36	0.23
SD	0.04	0.06	0.06	0.06	0.04	0.02	0.05	0.06	0.05	0.06
p (t -test)	0.009		0.001		0.014		0.001		0.001	

Fig. 3.10 shows the distributions of uncorrected and corrected NAA, Cr and tCho concentrations in GI and GII ($C_{M_x,uncor}$: black stars in blue boxes; $C_{M_x,cor}$: black stars in green boxes). Bold red lines indicate the median values of absolute concentration for the corresponding group, whereas the lower and upper box plot limits indicate the 25th and 75th percentiles, respectively. Tab. 3.6 summarises the mean $C_{M_x,uncor}$ and $C_{M_x,cor}$ values and corresponding standard deviations (SD) for NAA, Cr and tCho for both groups. The p -values of the t -test comparisons are also presented in Tab. 3.6. Uncorrected Cr and tCho concentrations were significantly lower in GII than in GI (up to -11% , $p < 0.08$). In contrast, NAA concentrations indicated only an apparent, but not significant decrease in GII compared to GI (-3% , $p = 0.29$).

Considering the CSF contamination in the MRS voxels led to significant increases of concentrations for all metabolites in GII (between 6% and 9% , $p < 0.06$) but not in GI ($p > 0.2$). In contrast to the NAA values calculated by assuming homogeneous voxels, CSF-corrected NAA concentrations were higher in GII than in GI ($+8\%$, $p = 0.04$). No significant group differences were observed for corrected Cr and tCho concentrations ($p > 0.25$).

Positive correlations were detected between the tissue corrected NAA and Cr concentrations and GM contents in the voxels ($R_{NAA,cor}^2 = 0.86$, $p_{NAA,cor} = 0.0001$, $R_{Cr,cor}^2 = 0.51$, $p_{Cr,cor} = 0.06$, see Figs. 3.11a and b). No significant relationship could be estimated between tissue corrected tCho concentrations and GM content ($R_{tCho,cor}^2 = 0.01$, $p_{tCho,cor} = 0.97$, see Fig. 3.11c).

Highly significant, negative correlations were observed between the CSF volume fraction and relative differences between uncorrected and corrected NAA, Cr and tCho levels (f_{CSF} vs. $100 \cdot (C_{M_x,uncor}/C_{M_x,cor}) - 100$; $R^2 < -0.85$, $p < 0.001$; see Fig. 3.11d). In GI the inter-individual variance of calculated differences between the uncorrected and corrected concentrations was apparently larger in GI (see asterisks in Fig. 3.11d) than in GII (see filled triangles in Fig. 3.11d). This can be ascribed to a lower quantitation accuracy achieved for the GI data with a lower SNR .

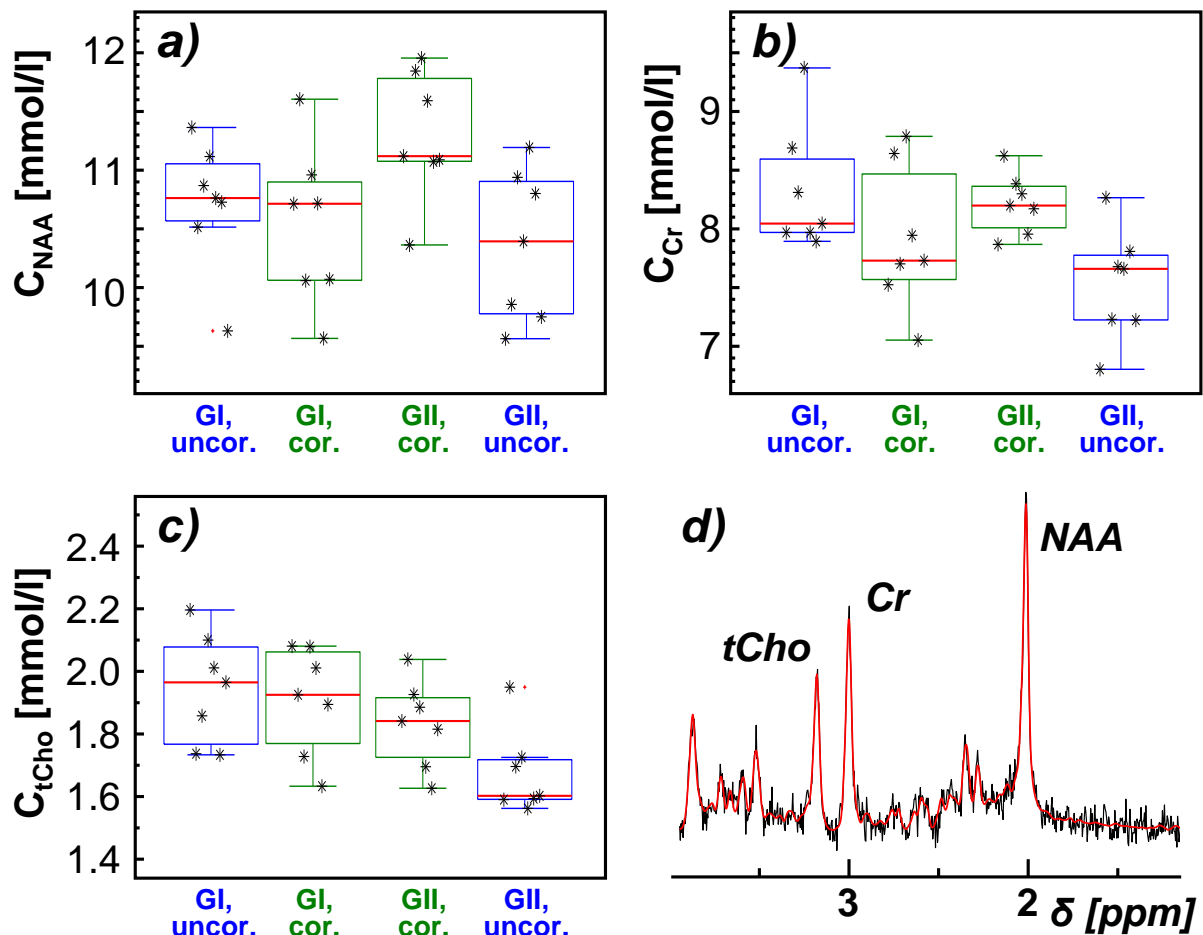


Figure 3.10: *In vivo* NAA (a), Cr (b) and tCho (c) concentrations for both control groups (GI: two left distributions; GII: two right distributions). Concentrations calculated by assuming homogeneously and heterogeneously composed MRS voxels, are presented within blue and green boxes, respectively. Red lines in the boxes represent median values, the upper and lower box limits correspond to the 75th and 25th percentile, respectively. Subplot (d) shows a representative phase- and baseline- corrected ¹H-MR spectrum (black) and the corresponding LCMoDel fit (red) from the insular cortex of a volunteer (GII).

3.5 Discussion

This chapter presented the implementation and validation of a fully automatic approach to correct brain metabolite concentrations with respect to CSF partial volume effects. The discrimination between the GM, WM and CSF volume fractions in the MRS voxel make it also possible to take into account the tissue specific signal attenuations due to T_1 saturation and T_2 relaxation. The presented method minimises the influence of experimental settings (MRS voxel size and position, TR and TE) on the results. By integrating pre-processing steps provided by external software tools, such as *LCMoDel* and *FreeSurfer*, the data processing stream uses the advantages of these widely established and extensively evaluated packages for the quantitative analysis of MRI and MRS data.

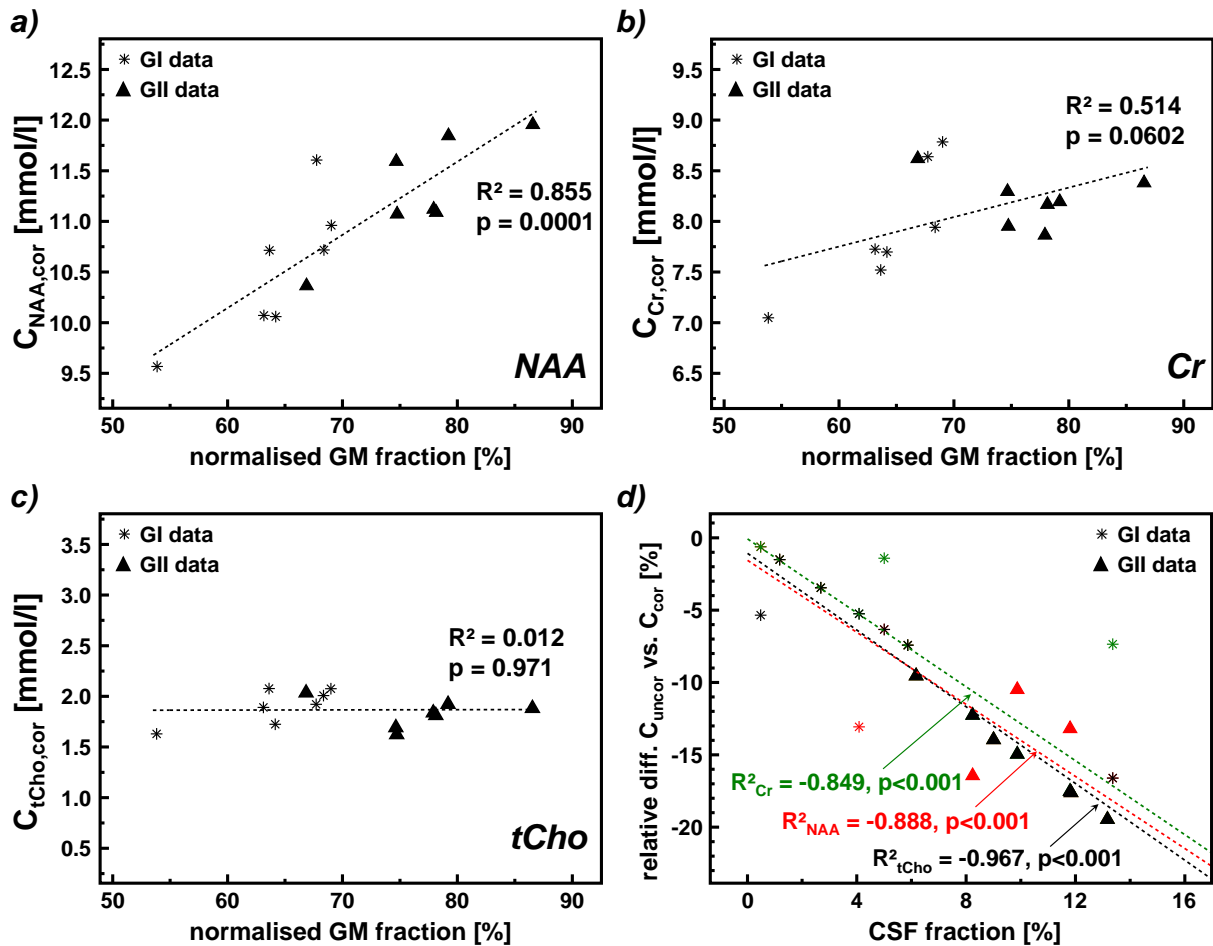


Figure 3.11: Distributions of tissue corrected NAA (a), Cr (b) and tCho (c) concentrations estimated for GI (stars) and GII (triangles) with respect to normalised GM contents within MRS voxels. Dashed graphs represent the regression lines (with corresponding R^2 and p -values), which were calculated in order to evaluate the relationships between calculated metabolic levels and GM content in voxels. Subplot (d) shows relative differences between tissue uncorrected and corrected NAA (red), Cr (green) and tCho (black) concentrations with respect to the CSF fractions in the MRS voxels. Dashed graphs in subplot (d) represent the regression lines (with corresponding R^2 and p -values) for NAA, Cr and tCho, which were calculated to show the effect of increased CSF fraction on the underestimation of tissue uncorrected concentrations.

Table 3.6: Absolute NAA, Cr and tCho concentrations ($MEAN \pm SD$, in mmol/l) calculated for GI and GII by assuming homogeneously (uncorrected concentrations C_{uncor}) and heterogeneously (corrected concentrations C_{cor}) composed MRS voxels. The Δ^* values indicate the relative differences of calculated concentrations between GI and GII, whereas the Δ^{**} values indicate the relative differences between uncorrected and corrected concentration values within GI and within GII. Finally, p^* and p^{**} indicate the t -test based significance level of calculated differences Δ^* and Δ^{**} .

			GI	GI	Δ^* [%]	p^*
NAA	C_{uncor}	[mmol/l]	10.7±0.6	10.4±0.6	-2.8±0.2	0.289
	C_{cor}	[mmol/l]	10.5±0.7	11.3±0.6	7.6±1.3	0.040
	Δ^{**}	[%]	-1.9±1.1	8.7±0.5		
	p^{**}		0.587	0.013		
Cr	C_{uncor}	[mmol/l]	8.3±0.5	7.5±0.5	-9.6±0.7	0.013
	C_{cor}	[mmol/l]	7.9±0.6	8.2±0.3	3.8±3.8	0.253
	Δ^{**}	[%]	-4.8±1.7	9.3±2.8		
	p^{**}		0.210	0.006		
tCho	C_{uncor}	[mmol/l]	1.9±0.2	1.7±0.1	-10.5±5.2	0.077
	C_{cor}	[mmol/l]	1.9±0.2	1.8±0.1	-5.3±5.3	0.389
	Δ^{**}	[%]	0.0±0.0	5.9±0.3		
	p^{**}		0.709	0.052		

3.5.1 *In vitro* study

The phantom study demonstrated the importance of CSF partial volume effects, which are often not negligible *in vivo*. Fig. 3.9a indicates that a CSF fraction of 15 %, which is realistic for *in vivo* conditions, may lead to substantial underestimation of the calculated metabolite concentrations (approximately 20 %). By assuming an *in vivo* NAA concentration of approximately 10 mmol/l in the brain [Govindaraju et al., 2000], this error corresponds to a reduction of 2 mmol/l and may therefore cause misinterpretation of *in vivo* data. After correction the difference between actual and nominal NAA concentration was below 1 % in the same voxel. With higher CSFS fractions the corrected NAA values were underestimated by up to 10 % (see the last point in the green graph in Fig. 3.9a).

This relatively large error may be ascribed to the limited accuracy to determine the volume fractions, which depends on the spatial resolution of the segmented MRI data. In this study, MRI voxels were assigned to one of the compartments by using their grey value intensity. However, for the MRI voxels containing the boundary layer between two compartments (e.g. between WMS and CSFS), the blurring of the grey value may lead to

an uncertainty of the assignment. Currently, the MP-RAGE volume was measured with an isotropic resolution of 1 mm implying that the shift between the true and estimated positions of the boundary layer can be up to 0.5 mm. Considering the special case of a two compartment experiment where the $15 \times 15 \times 15 \text{ mm}^3$ large MRS voxel contains only WMS and CSFS solutions, this shift means that a $0.5 \times 15 \times 15 \text{ mm}^3$ large volume fraction of the MRS voxel can not be unambiguously assigned to one of the included compartments. The influence of this uncertainty is negligible for MRS voxels with low CSFS contents, where the measured metabolite and water signals are dominated by contributions from WMS. However, as demonstrated in Fig. 3.12, the quantitation error due to an incorrectly estimated position of a boundary layer between WMS and CSFS grows dramatically when the CSFS fraction increases. This figure shows simulated evolutions of quantitation error with increasing CSFS fraction for five different shifts between the true and wrongly assigned positions of the boundary layer between WMS and CSFS (simulated shifts: $\Delta x = 0.1, 0.2, 0.3, 0.4, 0.5 \text{ mm}$) within a $15 \times 15 \times 15 \text{ mm}^3$ MRS voxel. As can be seen, the increase of quantitation error depends on the shift between true and estimated boundary layers. By considering the quantitation error of 10 %, which occurred *in vitro* for a CSFS content of 82 % (see the last point on green graph in Fig. 3.9a) and by comparing this error with the evolutions shown in Fig. 3.12, it can be assumed that the shift between true and estimated WMS and CSFS boundaries *in vitro* was approximately -0.3 mm .

Enhanced accuracy for voxels with CSF fractions more than 60 % requires increased MR image resolution, which on the other hand contradicts the need for short measurement times. However, since placement of MRS voxels in cortical areas with such high CSF contents is less reasonable from a practical point of view, these errors are more an aspect of a theoretical discussion than a real problem occurring in practice.

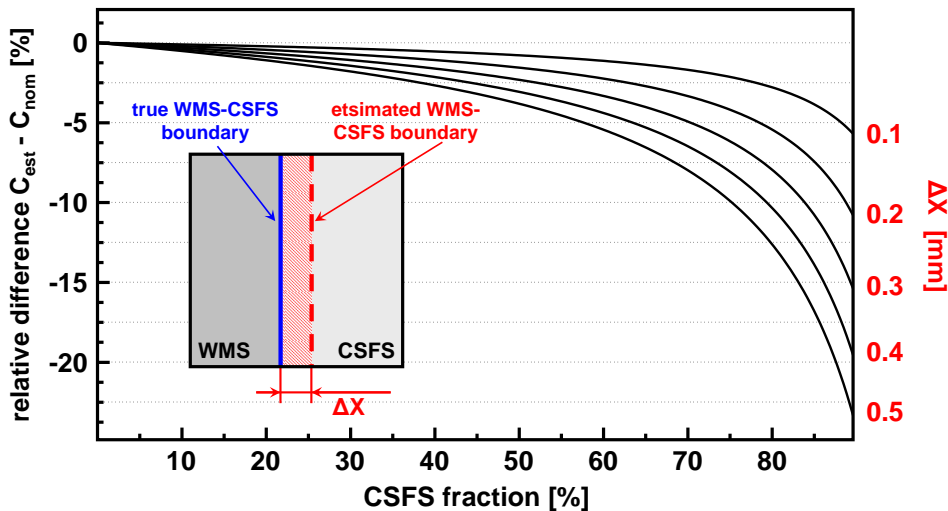


Figure 3.12: Simulated evolution of quantitation error due to incorrectly determined WMS-CSFS boundary with respect to increasing CSFS fraction in a $15 \times 15 \times 15 \text{ mm}^3$ large MRS voxel. Δx denotes the spatial shift between nominal and determined WMS-CSFS boundaries.

In order to reduce the number of parameters, which are affecting signal intensity, short echo times ($TE = 30$ ms) and long repetition times ($TR = 15$ s) were selected for the acquisition of *in vitro* spectroscopic data. The overall signal attenuations due to T_1 saturation and T_2 relaxation were below 3% for NAA and below 4% for water (Tab. 3.4) and did not vary substantially between GMS, WMS and CSFS. Thus, the variation of uncorrected NAA concentrations between differently located MRS voxels can not be ascribed to relaxation and saturation, but is exclusively related to different fractions of CSFS, GMS and WMS in the voxels.

Another aspect, which should be considered when comparing *in vitro* and the *in vivo* data, is the large difference between adjusted NAA concentrations in WMS and GMS of the phantom ($C_{\text{nom}}^{\text{WMS}} = 2 \cdot C_{\text{nom}}^{\text{GMS}}$), which unless realistic for *in vivo* conditions. As shown in Fig. 3.12, reliable quantitation of metabolite concentrations requires precisely determined volume fractions. To avoid misinterpretation of NAA level variations due to segmentation errors pronounced potentially differently for particular voxels, a high difference of nominal NAA concentrations was adjusted between WMS and GMS. In the phantom study the analysis of quantitation errors due to erroneously determined volumes of GMS and WMS fractions was omitted, since it was assumed, that these errors should evolve in a analogous manner as the already analysed and previously discussed errors due to incorrectly determined CSFS fraction volume.

3.5.2 *In vivo* study

The results of *in vivo* examinations are in line with conclusions drawn from the *in vitro* study. Similar to the two compartment phantom experiments (see Fig. 3.9a), *in vivo* NAA, Cr and tCho levels revealed a significant, negative correlation with increasing CSF volume, when calculated with homogeneously composed MRS voxels ($p < 0.001$, see Fig. 3.11d). Due to the significantly larger CSF fraction in GII (see Tab. 3.5), underestimation of metabolic levels should be more prominent in GII than in GI. This assumption is supported by the up to 13% lower, uncorrected NAA, Cr and tCho concentrations in GII compared to GI (significant for Cr and tCho, $p < 0.08$, see Fig. 3.10 and Tab. 3.6). The increase of NAA, Cr and tCho levels after correction was significant only for GII ($p < 0.08$), whereas the corrected concentrations in GI did not significantly differ from the uncorrected values ($p > 0.2$).

Another aspect, which was only observed when evaluating the corrected metabolite concentrations, is the relationship between metabolic levels and GM content in spectroscopic volumes. The graphs in Fig. 3.11a and b demonstrate a linear increase of NAA and Cr concentrations with increasing GM content ($R^2 > 0.5$, $p < 0.061$), suggesting that NAA and Cr levels are higher in pure GM than in pure WM. This conclusion is in line with findings of several recent ^1H -MR spectroscopic studies, whose results also indicate higher NAA and Cr concentrations in GM than in WM [Gasparovic et al., 2006; Malucelli et al.,

2009; Wang and Li, 1998]. In general, the higher GM concentration of NAA is related to a higher density of neuron cells. The Cr singlet at 3.01 ppm is the sum of signal contributions from *creatine* and *phosphocreatine* (PCr), whose concentrations ratio in brain tissue or even in other tissue types is approximately one [Govindaraju et al., 2000]. In biological cells PCr, together with *adenosine triphosphate* (ATP), plays a crucial role in the energy metabolism, which takes place in the mitochondria. Consequently, PCr concentration increases with increasing number of mitochondria. Since GM contains more cell bodies (e.g. neurons and glia cells) than WM, it consequently contains more mitochondria and thus reveals higher PCr and Cr concentrations. The Cr intensity is often used as an internal reference for metabolite intensity normalisation [Jansen et al., 2006] and a constant Cr concentration is usually assumed in GM and WM. However, the lower amounts of Cr in WM observed in the present study as well as in other recently published studies [Malucelli et al., 2009; Wang and Li, 1998] imply that the ratio between GM and WM in the voxels has to be taken into account when using Cr to calculate normalised metabolite intensities.

The corrected NAA concentrations revealed a larger difference between WM and GM than the corrected Cr concentrations (compare Fig. 3.11a and b). These different dependencies of NAA and Cr levels on GM volume fraction may explain, why mean corrected NAA concentrations were significantly higher in voxels with higher mean GM content in GII than in GI, whereas corrected Cr concentrations revealed an apparent but not significant increase between GI and GII ($p > 0.3$, see Tab. 3.6).

In contrast to NAA and Cr, the evaluation of corrected tCho concentrations did neither reveal any significant correlations between tCho and GM content (Fig. 3.11c), nor significant differences in tCho levels between GI and GII ($p > 0.3$, see Tab. 3.6). However, the mean tCho concentration of 1.9 ± 0.2 mmol/l for GI and 1.8 ± 0.1 mmol/l for GII suggests lower tCho levels in GM than in WM, which is in agreement with findings of other ^1H -MR spectroscopic studies, which reported tCho ratios between WM and GM of up to 1.3 [Brief et al., 2009; Natt et al., 2005; Noworolski et al., 1999]. Reasons for higher tCho concentrations in WM are not clear yet. As a possible explanation some authors suggested high amounts of choline containing compounds in the myelin sheaths of neuron axons, whose density is higher in WM than in GM [Cohen et al., 1995; Michaelis et al., 1993].

The accuracy of metabolite quantitation depends on correctly determined water concentrations in WM, GM and CSF and relaxation constants. Contrary to *in vitro* examinations, where these values are known, *in vivo* metabolite quantitation was based on values taken from the literature (see Tabs. 3.1 and 3.2). Possible inaccuracies in estimated concentrations may therefore arise from variations of tissue relaxation properties and water contents due to biological variance across the brain volume (relaxation differences up to 5% [Tofts and du Boulay, 1990]). As shown by [Gasparovic et al., 2009] a more accurate determination of water concentrations in different brain tissues can be obtained by using high resolution proton density weighted MR images, which cover the spectroscopic volume

of interest. Instead of using constant values for α_{GM} , α_{WM} and α_{CSF} as reported by [Ernst et al., 1993], the former approach allows an individually adapted consideration of water content variation in the brain. Unfortunately, it also prolongs the examination time due to the additional MRI scan.

To summarise, the results of both phantom and volunteer examinations demonstrated the clear need to consider tissue composition in spectroscopic volumes to minimise underestimation of metabolic concentrations caused by CSF partial volume effect. It was shown that *in vivo* concentrations of NAA and Cr vary in different brain tissue types. Therefore, considering the tissue composition can be crucial to avoid misinterpretations when comparing results of measurements performed with the individually adjusted voxel sizes or with the different measurement settings.

4 *In vivo* detection of cerebral glutamate changes induced by heat pain with functional ^1H -MRS.

4.1 Introduction

This chapter describes *in vivo* experiments in volunteers that were conducted to perform time resolved ^1H -MRS in the brain while simultaneously applying external pain stimuli. The goal was to investigate whether acute pain stimulus related changes of glutamate - a metabolite, which provides the excitatory neurotransmission between neurons - are reliably detectable. In order to highlight the impact of functional spectroscopic experiments, a short overview is given on the state-of-the-art of functional neuroimaging techniques used to explore physiological processes associated with neuronal activity.

4.1.1 Functional neuroimaging

Neuronal activity typically entails a number of physiological events that include action potentials, which are generated and forwarded in an activated neuron and lead to neurotransmission and post-synaptic receptor interactions with other neurons. Synchronous propagation of action potentials in multiple neurons results in temporally varying distributions of electrical potentials on the surface of the brain or scalp that can be detected by an appropriately arranged electrode array. This principle is used in *electroencephalography* (EEG) - a neuroimaging technique, which is characterised by high temporal resolution on the order of several milliseconds [Nunez, 1989].

The essential feature, which is exploited by other neuroimaging methods, is that the locally enhanced neurotransmission is associated with an increased energy production in the activated brain region [Shulman and Rothman, 1998]. Since oxidation of glucose is the primary energy source in the brain, increased neurotransmitter activity is related to elevated metabolic rates of glucose (CMR_{Gluc}) and oxygen (CMR_{O_2}). Spatial distributions of CMR_{Gluc} alterations can be detected by tracing externally administered, radioactively labelled glucose in the brain, as it used with *Positron Emission Tomography* (PET) [Shulman and Rothman, 1998].

Since both glucose and oxygen are supplied to the cells by the blood, a local increase in brain energy demand leads to a local increase in *cerebral blood flow* (CBF) and *cere-*

bral blood volume (CBV). Direct detection of CBF changes is possible by applying MR based *arterial spin labelling* (ASL) techniques, which trace the perfusion of pre-saturated (labelled) blood water spins in brain tissue [Williams et al., 1992].

Another neuronal activity related feature, utilised by most NMR-based functional imaging studies (fMRI studies) today, is the so called BOLD contrast (BOLD: *Blood Oxygen Level Dependent* contrast), which is based on the different magnetic susceptibilities of paramagnetic deoxyhemoglobin (i.e. hemoglobin with no oxygen bound to it) and diamagnetic oxyhemoglobin. In the 'low' neuronal activity state (resting state), the magnetic susceptibility difference between diamagnetic tissue and paramagnetic deoxyhemoglobin leads to local field inhomogeneities around the blood vessels, which are carrying deoxyhemoglobin. Enhanced neuronal activity (active state) is related to an increase of CBF and CBV, which again is associated with a decreased amount of deoxyhemoglobin inside red blood cells and consequently with a local reduction of the \vec{B}_0 disturbances. This change in susceptibility differences is reflected in a local increase of the effective transverse relaxation time constant T_2^* and can be detected by using T_2^* sensitive MR imaging techniques (*BOLD-fMRI* [Belliveau et al., 1991]).

4.1.2 Functional MR spectroscopy (fMRS)

As already mentioned in Chap. 1.3, MR spectroscopy makes it possible to selectively detect different metabolites, which are directly involved in neurotransmission (Glu, GABA, Gln) or associated with the energy metabolism on the cellular level (lactate, glucose). Functional MR spectroscopy (fMRS) relates measured metabolic levels to defined external events (e.g., stimulation) and provides, therefore, information about metabolic processes that support the dynamic regulation and adaptation of neuronal networks with respect to changes of environmental conditions.

4.1.2.1 *In vivo* ^{13}C -fMRS

The most recent *in vivo* fMRS applications on animals and humans are related to tracing labelled *carbon-13* isotopes (^{13}C) along their way through the metabolic pathways (dynamic ^{13}C -MR spectroscopy). Contrary to the hydrogen isotope (^1H), however, which has a natural abundance of 99.99%, the natural abundance of the MR detectable carbon isotope ^{13}C is only 1.11% (see Tab. 2.1). Consequently, the sensitivity of ^{13}C -MRS measurements is substantially lower compared to ^1H -MRS. The ^{13}C signal sensitivity can be enhanced by the administration of labelled physiological substances enriched with ^{13}C nuclei. Frequently, such MRS experiments are based on the administration of ^{13}C -labelled glucose, which enters the brain cells from the blood and is metabolised in cells to other metabolites, for example in neurotransmitters Glu, Gln and GABA [Rothman et al., 2003; Shulman and Rothman, 1998]. The stimulus induced alterations of neurotransmission activity can be assessed for each neurotransmitter separately by observing

the dynamic changes of intensities of corresponding peaks in ^{13}C -MR spectra. However, despite their apparent advantages in direct detection of event related neurotransmission changes, functional ^{13}C -MRS experiments require sophisticated equipment for well defined dynamic administration and monitoring of labeled glucose as well as ^{13}C compatible MR hardware. Moreover, the expensive ^{13}C enriched metabolic compounds make ^{13}C -fMRS examinations less favourable for clinical applications.

4.1.2.2 *In vivo* ^1H -fMRS

Contrary to ^{13}C -fMRS, detection of event related metabolic changes by means of ^1H -MRS is more applicable in clinical praxis, since it does neither require external administration of labelled substrates nor specially designed MR coil systems. On the other hand, since ^1H -MRS does not use labelled substrates, the assignment of observed event related metabolic changes to metabolic pathways becomes more ambiguous. One example for this problem is the interpretation of spectroscopically detected stimulus related changes of glutamate (Glu) in the human brain that have been reported in recent functional ^1H -MRS (^1H -fMRS) studies [Giove et al., 2006; Mangia et al., 2007; Mullins et al., 2005]. It is well known that cortical Glu is compartmentalised in both intercellular (neuronal and astroglial cells) and sub-cellular (cytosolic, mitochondrial and vesicular) pools. These pools are in permanent exchange with each other and are all involved in excitatory glutamatergic neurotransmission, but also in other metabolic processes like aerobic energy production in the *tricarboxylic acid cycle* (TCA) or GABA production in GABAergic neurons [Hertz, 2006]. However, since the ^1H -MR spectroscopically measured Glu level reflects the sum of all these compartments, it is more challenging to assign the detected Glu changes to task related glutamatergic neurotransmission changes or to other cellular processes.

During the last two decades only a few *in vivo* human studies have been published, which reported on ^1H -MR spectroscopically detected metabolic changes in the brain due to visual or painful stimulation or in consequence of performing motor tasks (for an overview of studies see Tab. 4.1). The first of these studies reported detection of lactate changes in activated brain regions during prolonged stimulation (longer than 20 min). The authors ascribed the observed lactate increase to the transient onset of anaerobic glycolysis caused by the increased energy demand [Giove et al., 2003].

Spectroscopic *in vivo* detection of event related changes of neurotransmitters Glu, Gln or GABA is more challenging due to the complex spectral multiplet structure of these metabolites as well as spectral overlap with further signals of similar chemical shifts. However, more recent studies demonstrated the feasibility of direct ^1H -MR spectroscopic detection of stimulus related neurotransmitter changes *in vivo* [Giove et al., 2006; Kupers et al., 2009; Mangia et al., 2007; Mullins et al., 2005; Peca et al., 2010]. The increasing number of such studies may be ascribed to the improved availability of high field MR scanners ($B_0 \geq 3\text{ T}$), which enable enhanced spectral resolution and more reliable sepa-

Table 4.1: Summary of recently *in vivo* ^1H -fMRS studies, which reported on changes of several brain metabolites (Lactate, Glu, Gln, GABA, Glucose and Glx (sum of Glu, Gln and GABA)) in different cortical regions (oC: *occipital cortex*, Thal: *thalamus*; aCC: *anterior cingulate cortex*) during visual or painful stimulation or during performing motor tasks. Symbols ' \uparrow ', ' \downarrow ' and '-' indicate significant increase, significant decrease and no changes of regarded metabolites, respectively. The abbreviation '*n/a*' denotes that the regarded metabolites were not specified in the particular study.

	Stimulus	Reg.	B_0 [T]	Lac	Glx	Glu	Gln	GABA	Gluc
Prichard et al. [1991]	Visual	oC	2.0	\uparrow	n/a	n/a	n/a	n/a	n/a
Sappey-Marinier et al. [1992]	Visual	oC	2.0	\uparrow	n/a	n/a	n/a	n/a	n/a
Kuwabara et al. [1995]	Motor task	Thal	1.5	\uparrow	n/a	n/a	n/a	n/a	n/a
Chiappa et al. [1999]	Visual	oC	1.5	\uparrow	n/a	n/a	n/a	n/a	n/a
Mangia et al. [2003]	Visual	oC	1.5	\uparrow	n/a	n/a	n/a	n/a	n/a
Mullins et al. [2005]	Cold pain	aCC	4.0	n/a	\uparrow	\uparrow	\uparrow	n/a	n/a
Giove et al. [2006]	Visual	oC	1.5	n/a	\uparrow	-	n/a	n/a	n/a
Mangia et al. [2007]	Visual	oC	7.0	\uparrow	\uparrow	n/a	n/a	n/a	\downarrow
Kupers et al. [2009]	Heat pain	aCC	3.0	n/a	\uparrow	\uparrow	n/a	\uparrow	n/a
Peca et al. [2010]	Visual	oC	3.0	n/a	\uparrow	\uparrow	\uparrow	n/a	n/a

ration of overlapping metabolite signals compared to 1.5 T scanners (see Eq. 2.44). The effect of higher field strength on *in vivo* spectra quality and especially on the accuracy of Glu detection was evaluated in an own recent study [Gussew et al., 2008]. There, it was shown that SNR increased up to 40% for all metabolite peaks and that overlap of adjacent metabolite peaks was reduced due to the increased frequency differences between particular peaks when going from 1.5 T to 3 T (see Fig. 4.1). As a consequence, quantitation accuracy for metabolites with complex spectral patterns (e.g. Glu) was distinctly improved.

In contrast to other recent ^1H -fMRS studies that investigated metabolite changes between a resting state and a continuously applied visual or painful stimulus [Giove et al., 2006; Kupers et al., 2009; Mangia et al., 2007; Mullins et al., 2005; Peca et al., 2010], the experiments described in this chapter comprise cyclic application of short heat pain stimuli. It was assumed that this stimulation scheme ensures reduced adaptation of the pain processing network due to receptor saturation, which may affect metabolic changes during prolonged stimulation [Giove et al., 2003]. Furthermore, synchronisation between stimulation and spectra acquisitions allows precise assignment of acquired spectra to defined stimulation states (i.e., the time point prior to the start of stimulation, the time point at maximum stimulus and one or more time points during the post stimulus state).

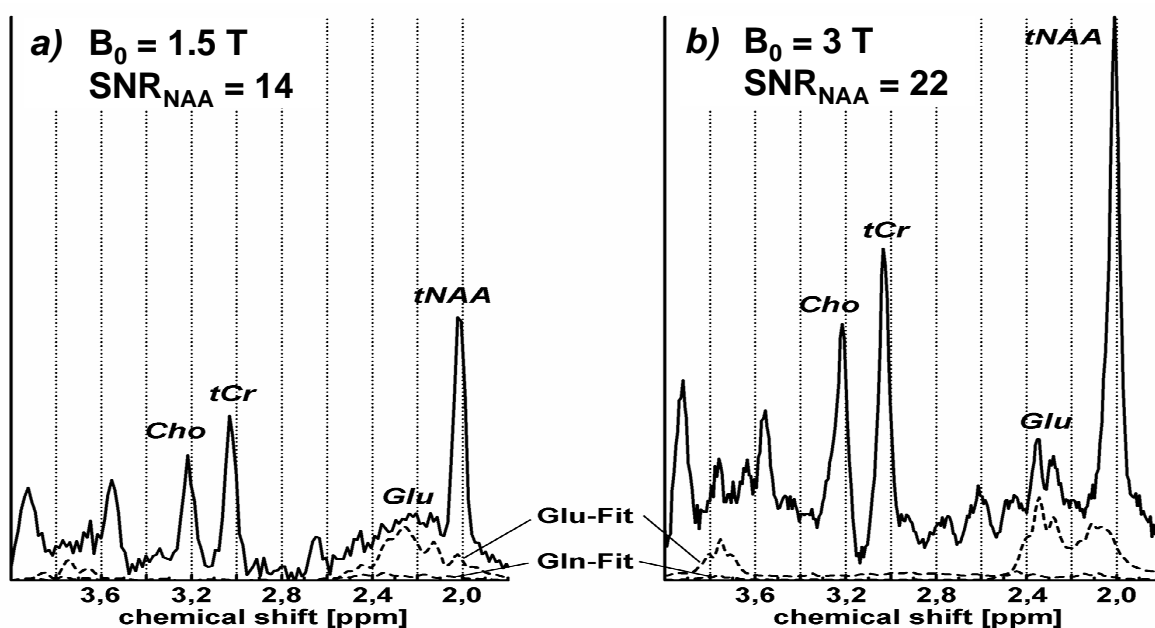


Figure 4.1: *In vivo* ¹H-MR spectra from the insular cortex of a healthy volunteer at 1.5 T (a) and 3 T (b) (¹H-PRESS-CSI sequence, $TE/TR = 30/5000$ ms). Signal intensities of the plotted spectra are normalised to the corresponding noise levels (twice the standard deviation in a signal-free spectral range between -1 and 0 ppm). Besides enhanced SNR , the 3 T spectrum also reveals higher spectral resolution, leading to a better separation of overlapping multiplets (e.g. signals of *Glu* and *Gln*, see dashed lines in both plots). The presented data is adapted from [Gussew et al., 2008].

4.2 Time resolved fMRS experiments during pain stimulation

4.2.1 Application of painful heat stimuli

Stimulation of pain receptors (nociceptors) on the skin surface of volunteers was performed by means of painful heat stimuli, which were applied to the forearm with an MR compatible *Peltier element* thermode (surface: 30×30 mm², see the box labelled β in Fig. 4.2a). A *Peltier element* thermode consists of two conjuncted elements (usually semiconductors) with different electrical properties, which generate a temperature gradient between each other as a consequence of the passage of electric current [Lindner et al., 2001]. The temperature on the thermode surface can be regulated by the voltage in the thermode circuit. Depending on the polarity of the voltage the thermode is capable of heating and cooling. The used thermode (Neuro Sensory Analyzer TSA-II, MEDOC Ltd., Ramat Yishay, Israel) allows temperature changes in the range between 0°C and 50°C with a maximum slope of 8°C per second. Except for the thermode all control units of the stimulation device (see the parts labelled 1 and 2 in Fig. 4.2a) were placed outside the high-frequency shielded MR scanner cabin to avoid any electromagnetic influences.

As shown schematically in Fig. 4.2b, the time course of the applied stimulation sequence consisted of a temperature increase from baseline ($T_{\text{baseline}} : 32^\circ\text{C}$) up to the beforehand

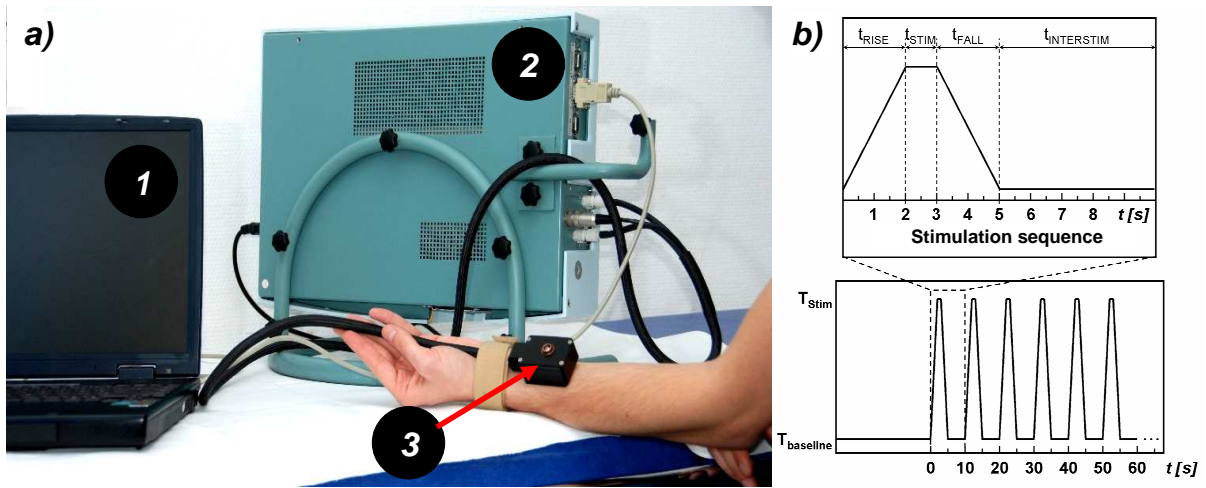


Figure 4.2: Set-up used to apply heat stimuli (a): stimulation PC (1), control device (2), and *Peltier element* thermode (3). Time course applied for heat pain stimulation (b) with cyclic temperature alterations between baseline (T_{baseline}) and stimulus levels (T_{Stim}). One complete stimulation sequence consists of an increase from T_{baseline} to T_{Stim} , stimulus period (t_{Stim} : 1 s) followed by a return to T_{baseline} and an inter-stimulus resting period ($t_{\text{INTERSTIM}}$: 5 s). The rise and fall times (t_{RISE} , t_{FALL}) are 2 s each.

individually determined painful temperature level T_{Stim} (see below), which was then held constant for 1 s (t_{Stim}), followed by the return to the baseline temperature. Rise and decay times (t_{RISE} , t_{FALL}) were 2 s each. This sequence was repeated periodically with a resting period of 5 s between two subsequent repetitions ($t_{\text{INTERSTIM}}$) in order to sample multiple FIDs at different time points of the stimulation sequence.

4.2.2 Spectroscopic data sampling

In order to assign the measured MR spectra to predefined stimulation conditions, the timing of the applied MR sequence (magnetisation preparation, volume localisation and start of acquisition) had to be controlled by external electrical trigger signals. These trigger pulses were generated by the control unit of the stimulation device (see Fig. 4.2a) and sent to the MR scanner via a coaxial cable. The 3 T whole body MR scanner (Magnetom Trio TIM, Siemens Medical Solutions, Erlangen, Germany) used in these experiments supports triggered data acquisition to synchronise measurements with physiological motion (e.g., cardiac or respiratory motion) to suppress artefacts. The system requires rectangular, TTL-like trigger pulses with a voltage magnitude between +2 V and +15 V and duration and inter-pulse interval of at least 10 ms each. The time lag between successively generated trigger pulses defines the time resolution of spectroscopic sampling of the stimulation time course. To guarantee equal T_1 weighting of the acquired spectra this trigger time lag has to be kept constant (equal to the adjusted repetition time TR in the applied MRS sequence).

Averaging of FID signals (NAS: *Number of Averaged Single acquisitions*) is typically

performed to increase the *SNR* of metabolite signals (see Eq. 2.51 in Chap. 2.3.2.2). In the experiment here, the stimulation sequence had to be successively repeated *NAS* times to accumulate a data pool with *NAS* separate FIDs for each sampled time point of the stimulation sequence. Fig. 4.3 shows schematically the data sampling protocol to collect ^1H -MR spectra with different stimulation conditions. Prior to the start of the stimulation, 128 water-suppressed and 16 non-suppressed measurements were performed to estimate the initial metabolic levels in the resting state and to determine the water signal intensity. Subsequently, four stimulation blocks including dynamic spectra acquisitions were acquired. Each stimulation block comprised three consecutive dynamic runs, each of which consisted of 32 single FID acquisitions. During the first and second dynamic run the stimulation sequence was repeated sixteen times. For each repetition in both runs two acquisitions were performed at different time points of the stimulation sequence. In the bottom part of Fig. 4.3 the data acquisition time points are represented by filled squares for the first run (P_1 and R_1) and by filled diamonds for the second run (P_2 and R_2). Acquisition of the first FID during the first run (P_1) was carried out at the time point when T_{stim} was reached. The second FID during the first run (R_1) was sampled two seconds after the temperature had returned to T_{baseline} . During the second run these acquisition time points were each delayed by one second relative to the first run (i.e., $P_2 = P_1 + 1\text{ s}$ and $R_2 = R_1 + 1\text{ s}$). The third run ('*DUMMY*') was performed without stimulation to avoid adaptation during the prolonged stimulation (filled triangle in the bottom part of Fig. 4.3).

This data sampling scheme led to five different FID groups during the four stimulation blocks. The first and second group consists of 4×16 single FID acquisitions each, corresponding to the stimulation time points P_1 and P_2 at the beginning and the end of the temperature plateau. The third and fourth group also includes 4×16 single acquisitions corresponding to time points R_1 and R_2 in the inter-stimulus interval $t_{\text{INTERSTIM}}$. The fifth group with 4×32 non-triggered single acquisitions corresponds to the third '*DUMMY*' run. To assign the successively acquired FIDs to the first, second, third and fourth data group the information in the log files of the stimulation device about all trigger events and corresponding temperature levels was used. After finishing the experiment, data were stored in the following five pools:

- **Pool '*REF*'**: 128 water suppressed FIDs acquired prior to the stimulations
- **Pool '*WATER*'**: 16 water non-suppressed FIDs acquired prior to the stimulations
- **Pool '*PAIN*'**: 128 water suppressed FIDs acquired at stimulation cycle time points P_1 and P_2 (sum of 4×16 FIDs at P_1 and 4×16 FIDs at P_2)
- **Pool '*REST*'**: 128 water suppressed FIDs acquired at stimulation cycle time points R_1 and R_2 (sum of 4×16 FIDs at R_1 and 4×16 FIDs at R_2)

- **Pool 'DUMMY'**: 128 water suppressed FIDs sampled during the third 'DUMMY' run

In principle, separate storage of single acquisition data allows an individual analysis of spectra at the time points P_1 , R_1 , P_2 and R_2 . However, in the current study these data at these points were condensed into the 'PAIN' and 'REST' pools to ensure a sufficient *SNR* of the calculated average spectra.

4.2.3 Reconstruction of MR spectra

Conventionally, spectroscopic data are stored as a mean signal calculated by averaging all successively performed single acquisitions in one experimental series. For example, the scanner software stores mean signals in the already mentioned 'RDA' files (see Chap. 3.2.3). This strategy, however, is not useful if an individual, event related ordering of single acquisitions is required. Alternatively, the software also supports data storage in so called 'RAW' files, which contain the non-averaged single acquisition data and are thus more suited for the fMRS experiment here. By using meta information from the 'RAW' file headers, the stored data can be reorganised in a three dimensional data array of size $NAS \times M \times N_{\text{Samp}}$. NAS denotes the number of successively performed single acquisitions in a measurement series, N_{Samp} gives the number of discretely sampled data points of a single FID, and M represents the number of receive channels of the used rf coil. For circular polarised volume coils with one single receive channel, M equals one. For this coil type, single acquisition data can be extracted from the stored data array without any additional processing steps. In contrast, for phased array receive coils with M separate receive channels, a summed FID signal has to be calculated by linearly combining signal contributions from each coil channel. This step was also included in the data reconstruction work flow, since the phased array head coil was used for sampling ^1H -MRS and MRI data in the current study.

The data sampling scheme described in Chap. 4.2.2 produces overall 14 'RAW' files with single acquisition, multi-channel data originating from the water suppressed and non-suppressed baseline measurements prior to the stimulation as well as from the four stimulation blocks each containing three 'RAW' files with data from the first, second and third dynamic run. With the 12 channel phased array head coil and 4096 sampled FID data points, the data in each of these 'RAW' files can be reorganised in a data array of size $NAS \times 12 \times 4096$. All of these separately stored data sets were passed through a fully automatic, self implemented data post-processing stream (see Fig. 4.4), which manages the reconstruction of single acquisition time signals from the multi-channel coil data sets as well as the individual assignment of reconstructed signals to the previously defined 'REF', 'WATER', 'PAIN', 'REST' and 'DUMMY' pools.

The first step in the processing stream includes processing of non-suppressed water data. For each of the 12 coil channels, mean water signals were calculated by averaging over the

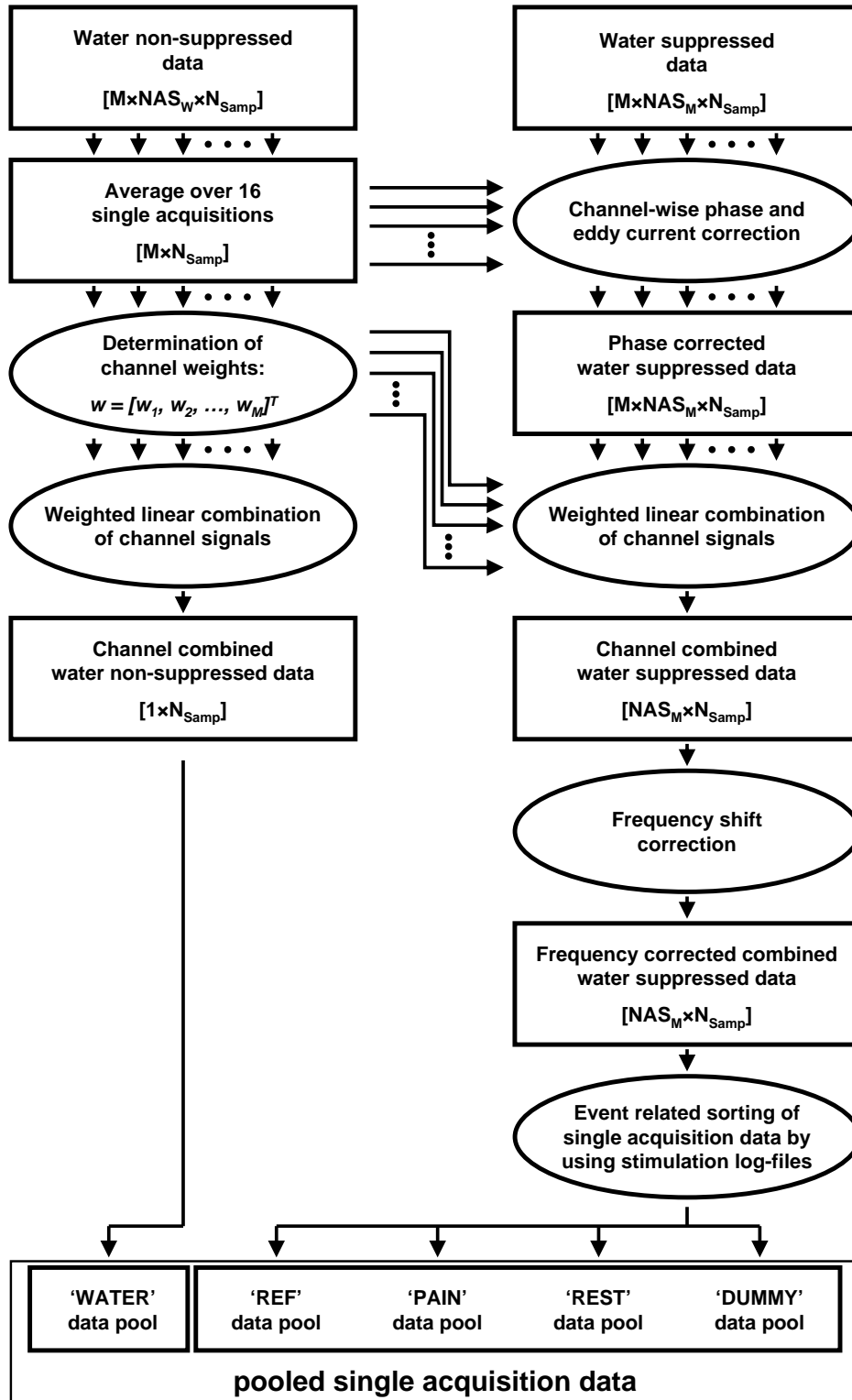


Figure 4.4: Implemented data processing stream, which manages the reconstruction of water suppressed and non-suppressed single acquisition time signals from the multi-channel coil data sets as well as the individual assignment of reconstructed signals to the previously defined 'REF', 'WATER', 'PAIN', 'REST' and 'DUMMY' pools. Multi-channel water non-suppressed data will be used to correct the phase and eddy current related line shape distortions in water suppressed data from corresponding coil channels as well as for the determination of channel weights. Prior the assignment of single acquisition data to separate data pools, these data set will be frequency corrected.

16 single acquisitions ($NAS_W = 16$). These mean signals were used for zero-order phase error and eddy current correction of all water suppressed data from the corresponding coil channel (see Chap. 2.3.3.3). The mean water signals were also used for the linear combination of signals from the coil channels. Coil channel signals were individually weighted with respect to their SNR prior to combination. The method applied for the determination of channel weighting factors is described in more detail in Chap. 4.2.4.

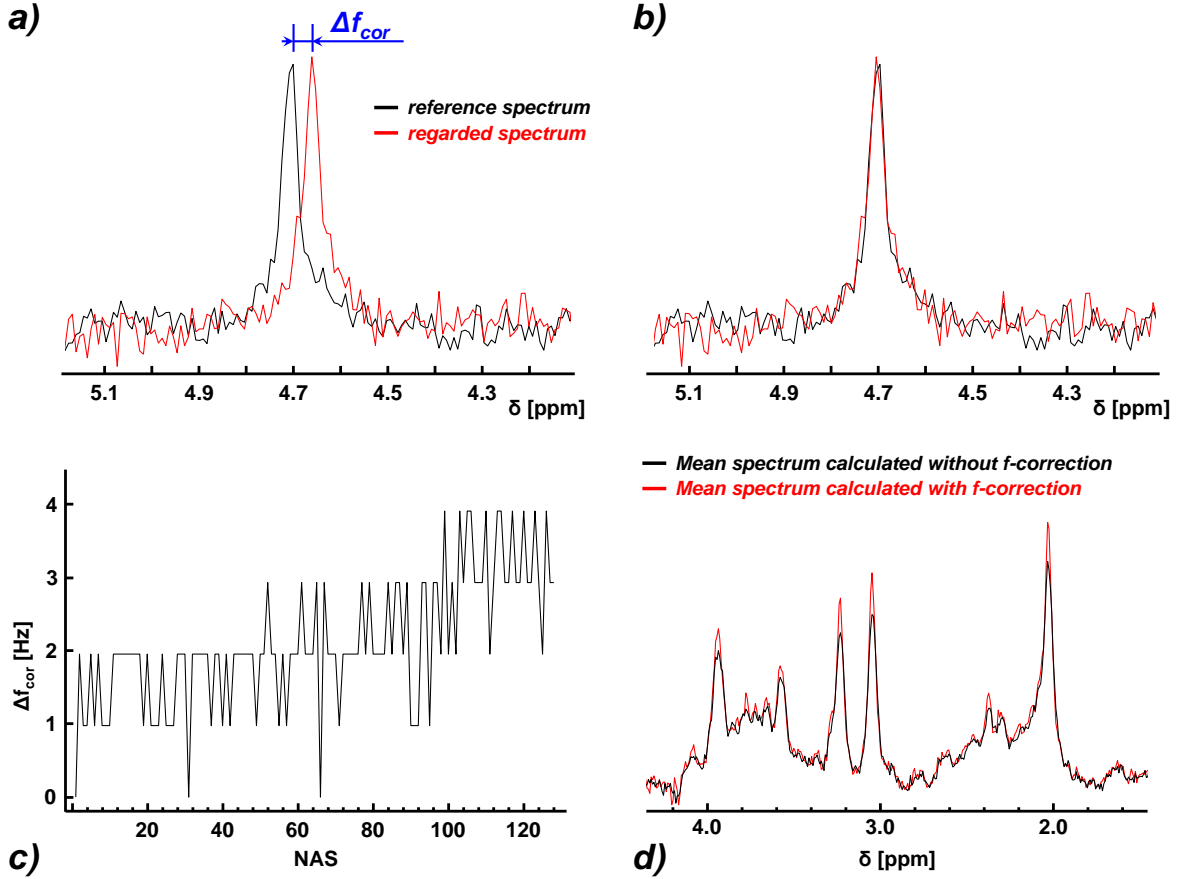


Figure 4.5: Principle of implemented frequency correction method, which was applied to all channel-combined single acquisition data. Frequency shifts Δf_{cor} are determined by comparing the frequency position of the residual water peak in the actual spectrum (red graph in subplots a and b) and the reference spectrum of a single FID (black graph in subplots a and b). The correction is based on multiplying the regarded time signal with a complex sinusoidal function with frequency offset Δf_{cor} . Subplot (c) shows a representative evolution of estimated frequency drifts of a series containing 128 ^1H -MRS single acquisitions, which were performed in the brain of a healthy volunteer by means of a PRESS sequence ($TE/TR = 30/5000$ ms; $B_0 = 3$ T). The impact of frequency correction on enhancement of the metabolite SNR becomes apparent when comparing the mean spectra, which were calculated by averaging 128 frequency corrected and un-corrected FIDs (d).

Following phase correction and channel combination, a set containing NAS one dimensional data arrays (size: N_{Samp}) was obtained for each processed 'RAW' file. Each of these 1D arrays represents a channel combined single acquisition time signal. To take

into account potential frequency drifts, which may occur during the long data acquisition period, all calculated sum signals were additionally frequency corrected by multiplication with a complex sinusoidal term:

$$y_{\text{cor}}(t) = y_{\text{uncor}}(t) \cdot e^{-j \cdot 2 \cdot \pi \cdot \Delta f_{\text{cor}} \cdot t} \quad (4.1)$$

The frequency shift Δf_{cor} was determined in the spectral domain by comparing the frequency position of the residual water peak at 4.7 ppm in the reference spectrum (spectrum of the FID acquired first during the baseline series) and in the actual considered single acquisition spectrum (see Fig. 4.5a). As shown in Fig. 4.5d, application of this frequency correction provided substantial *SNR* increase in the mean spectra calculated by averaging over a series of corrected single acquisition signals.

4.2.4 Weighted linear combination of multi-channel MRS data

The use of *receive* phased array rf coils in MR spectroscopy can substantially improve spectra quality due to a sensitivity advantage compared to single channel circular polarized coils [Brown, 2004; Natt et al., 2005]. In general, these multi-channel coils consist of an array of M surface coils surrounding the object (see Fig. 4.6a). Since surface coils have inhomogeneous and spatially dependent sensitivity profiles, the magnitude of the detected signal (\hat{u}_k) is inversely proportional to the distance between the surface coil centre and the source of the FID signal. The phase of the detected complex FID signal (φ_k) depends on the orientation of the surface coil axis relative to the direction of the macroscopic transverse magnetisation vector \vec{M}_{xy} at the time point of acquisition start. Finally, the magnitude of noise (ε_k) may also vary between the coil channels due to hardware specific differences between surface coils. Considering all these aspects, the FID signal from M coil channels can be described by the following equation:

$$u_k(t) = \hat{u}_k \cdot e^{-j \cdot (\omega \cdot t + \varphi_k)} + \varepsilon_k, \quad k = 1, 2, \dots, M \quad (4.2)$$

Simple linear combination of channel signals $u_k(t)$, as it given by:

$$u_{\text{sum}}(t) = \frac{1}{M} \cdot \sum_{k=1}^M u_k(t), \quad (4.3)$$

may, however, lead to cancellation and therefore to a reduced intensity of the combined signal $u_{\text{sum}}(t)$ due to variation of signal amplitude \hat{u}_k , phase φ_k and noise level ε_k between the coil channels (see the blue plot in Fig. 4.6b).

As demonstrated by the green plot in Fig. 4.6b, the intensity of the combined signal can be substantially increased by performing phase correction prior to linear combination. However, in this case individual magnitude and noise levels in the time signals from particular coil channels are not taken into account. This means that the intensity advantage

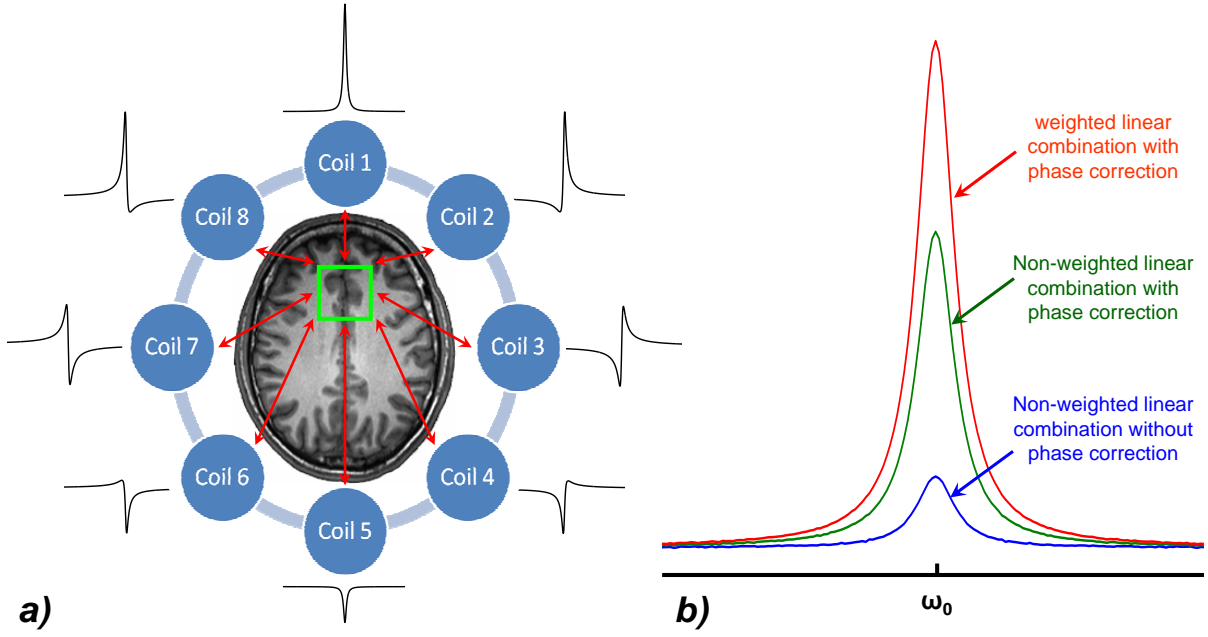


Figure 4.6: Schematic representation of eight surface coils (channels), which are arranged equidistantly on the perimeter of a phased array *receive* coil (a). The magnitudes and phases of measured FID signals (black graphs) are varying between the channels due to different distances between coil centres and MRS voxel (green box) and different orientations of the coil axes relative to \vec{M}_{xy} at $t = 0$ s. Subplot (b) shows the intensity enhancements of the combined signals calculated by non-weighted (green graph) and weighted (red graph) linear combination of phase corrected channel signals compared to the summed signal calculated by non-weighted linear combination of non phase corrected channel signals (blue graph). Presented graphs are based on simulated 8-channel spectroscopic data.

of coil elements with a shorter distance to the signal source (MRS voxel) is not exploited to enhance SNR of the combined signal. Alternatively, channel signals can be weighted with respect to their individual *SNR* prior to the combination:

$$u_{\text{sum}}(t) = \sum_{k=1}^M w_k \cdot u_k(t)$$

$$\text{Channel weighting factors: } 0 \leq w_k \leq 1, \quad \sum_{k=1}^M w_k = 1 \quad (4.4)$$

Compared to a *non-weighted linear combination* (nLC), a *weighted linear combination* method (wLC) provides further substantial intensity improvement in the combined signal (see the red plot in Fig. 4.6b). Recently proposed methods to adjust the channel weighting factors are based on the determination of single channel *SNR* in the time or frequency domain [Brown, 2004; Maril and Lenkinski, 2005; Natt et al., 2005]. By assuming an exponentially decaying time signal (FID), the *SNR* can be expressed in the time domain as the ratio between the first sampled intensity value and the noise magnitude, which can be derived from the root mean square value calculated over an appropriate number of

sampled points in the final part of the FID:

$$SNR_k = \frac{u_k(1)}{\sqrt{\frac{1}{N_{\text{Samp}} - N_1} \cdot \sum_{n=N_1}^{N_{\text{Samp}}} u_k(n)^2}} \quad (4.5)$$

The index N_1 denotes the start point of the final FID part, which contains essentially noise and which can be chosen empirically by considering the T_2^* relaxation time constant. In order to obtain weighting factors in the range between 0 and 1, the SNR_k values are normalised to their maximum:

$$w_k = \frac{SNR_k}{\max(SNR)_M} \quad (4.6)$$

There are certain advantages to perform the adjustment of channel weighting factors based on SNR , since this approach works fast and is computationally not expensive. However, especially for data with low SNR , the weighting factors become increasingly erroneous and may produce unpredictable amplifications of noise-dominated channels, which again leads to SNR reduction in combined signals.

Alternatively, Sandgren et al. [2005] presented a more robust approach for weight determination, which is based on *Singular Value Decomposition* (SVD) of the multi channel data matrix \mathbf{U} [Bronstein et al., 2001]. This matrix comprises M rows (the M channels), which contain the measured channel signals each with a length N_{Samp} :

$$\mathbf{U} = \begin{bmatrix} u_{1,1} & u_{1,2} & \cdots & u_{1,N_{\text{Samp}}} \\ u_{2,1} & u_{2,2} & \cdots & u_{2,N_{\text{Samp}}} \\ \vdots & \vdots & \ddots & \vdots \\ u_{M,1} & u_{M,2} & \cdots & u_{M,N_{\text{Samp}}} \end{bmatrix} \quad (4.7)$$

With SVD the matrix \mathbf{U} is factorized into the product of three matrices \mathbf{W} , $\mathbf{\Sigma}$ and \mathbf{V}^* ,

where \mathbf{W} and \mathbf{V} are unitary matrices of size $M \times M$ and $N_{\text{Samp}} \times N_{\text{Samp}}$, respectively:

$$\begin{aligned}
 \mathbf{U} &= \mathbf{W} \cdot \mathbf{\Sigma} \cdot \mathbf{V}^* = \\
 &= \begin{bmatrix} w_{1,1} & w_{1,2} & \cdots & w_{1,M} \\ w_{2,1} & w_{2,2} & \cdots & w_{2,M} \\ \vdots & \vdots & \ddots & \vdots \\ w_{M,1} & w_{M,2} & \cdots & w_{M,M} \end{bmatrix} \cdot \begin{bmatrix} \sigma_{1,1} & 0 & \cdots & 0 \\ 0 & \sigma_{2,2} & \cdots & 0 \\ \vdots & \vdots & \ddots & \vdots \\ 0 & 0 & \cdots & \sigma_{M,N_{\text{Samp}}} \end{bmatrix} \cdot \\
 &\quad \cdot \begin{bmatrix} v_{1,1} & v_{1,2} & \cdots & v_{1,N_{\text{Samp}}} \\ v_{2,1} & v_{2,2} & \cdots & v_{2,N_{\text{Samp}}} \\ \vdots & \vdots & \ddots & \vdots \\ v_{N_{\text{Samp}},1} & v_{N_{\text{Samp}},2} & \cdots & v_{N_{\text{Samp}},N_{\text{Samp}}} \end{bmatrix}^* \quad (4.8)
 \end{aligned}$$

The star of the \mathbf{V} matrix denotes the conjugate transpose operator. Matrix $\mathbf{\Sigma}$ is an $M \times N_{\text{Samp}}$ diagonal matrix with so-called singular values σ_k , which are arranged in descending order on the main diagonal ($\sigma_{1,1} > \sigma_{2,2} > \sigma_{3,3} > \dots > \sigma_{M,N_{\text{Samp}}} > 0$).

The SVD factorisation is often used for the rank estimation of matrices where the rank is equal to the number of non-zero singular values. By assuming that the rows of \mathbf{U} represent the same, but differently weighted FID signal $u(t)$ contaminated by normally distributed noise, the rank of \mathbf{U} is equal to one and only the first singular value in $\mathbf{\Sigma}$ is non-zero. Therefore, only the first column of \mathbf{W} and the first row of \mathbf{V}^* contribute to \mathbf{U} and represent the column vector with weight values (w_k) and a row vector with the product $\sigma_{1,1} \cdot u(t)$, respectively.

In order to ensure an accurate combination of multi-channel data in the current fMRS study, both SNR and SVD based channel weights determination methods were implemented. The robustness of these two approaches was evaluated by means of simulated multi-channel MRS data sets. Simulations were done with a self-written MATLAB program, which performs a fully automatic data generation and processing. The base signal $u(n)$, which was underlying the simulated data in several channels, was a mono-exponential intensity decay simulating the time course of a water signal with $\omega_0 = 0$ Hz and $T_2^* = 125$ ms:

$$u(n) = e^{-\frac{n}{T_2^* \cdot N_{\text{Samp}}}}, \quad n = 0, 2, \dots, N_{\text{Samp}} - 1 \quad (4.9)$$

As is shown in Fig. 4.6a, an arrangement of eight coil channels ($M = 8$) was simulated, which were configured equidistantly on the perimeter of a phase array receive coil. Consequently, signals in eight rows of the generated two dimensional data matrix \mathbf{U} represented the individually weighted and phased base signal $u(n)$ (see the Eq. 4.9). The nominal channel weighting factors $w_{k,\text{nom}}$ were adjusted as inverse distances (d_k) between the particular coils and the MRS voxel. These initialised weights were additionally normalised to their

sum in order to scale them within the interval between 0 and 1:

$$w_k^0 = \frac{(d_k)^{-1}}{\sum_{k=1}^M (d_k)^{-1}} \quad (4.10)$$

Signal phase values were adjusted between 0 and $2 \cdot \pi$ with respect to individual channel coil orientations relative to the direction of the simulated \vec{M}_{xy} vector at time point $t = 0$ s. Thereby, the phase value for the first channel (Coil 1 in Fig. 4.6a) was set to zero. Normally distributed noise signals with zero mean were generated separately for each single channel and then added to generated channel signals. In order to evaluate the influence of noise magnitude on the robustness of SNR and SVD based weights determination, overall eight multi-channel data sets were generated with SNR levels ($N_{\text{noise}} = 8$): 10, 20, 30, 40, 50, 75, 100, 150. The *SNR* level was defined in the time domain as the ratio between the first point of the real part of the base signal $u(n)$ (see Eq. 4.9) and twice the noise signal's standard deviation, which was varied with respect to the target *SNR*. For each adjusted *SNR* level simulations were repeated sixteen times ($N_{\text{set}} = 16$) in order to compare the noise level related evolution of variation of channel weights w_k^{SNR} and w_k^{SVD} , which were calculated with SNR and SVD approaches, respectively. The variations of w_k^{SNR} and w_k^{SVD} were assessed for each single channel and for each adjusted *SNR* level by means of variation coefficients cv_k^{method} :

$$cv_k^{\text{method}} = 100 \cdot \frac{\text{std}(w_k^{\text{method}})_{N_{\text{set}}=16}}{\text{mean}(w_k^{\text{method}})_{N_{\text{set}}=16}} \quad (4.11)$$

Additionally, the mean relative differences (Δ_k^{method}) between the calculated (w_k^{method}) and nominal (w_k^0) channel weights were estimated over 16 performed repetitions for each adjusted *SNR* level and used for the quantitative assessment of accuracy of SNR and SVD based weight determination methods:

$$\Delta_k^{\text{method}} = \text{mean} \left[100 \cdot \text{abs} \left(\frac{w_k^{\text{method}} - w_k^0}{w_k^0} \right) \right]_{N_{\text{set}}=16} \quad (4.12)$$

Fig. 4.7 shows surface plots of SNR related distributions of calculated cv_k^{method} (a and b) and Δ_k^{method} (c and d) values for the channel weights w_k^{SNR} and w_k^{SVD} . By considering these plots it can be concluded that the SVD based approach provides a substantially higher robustness (cv_k^{SVD} up to 20 % vs. cv_k^{SNR} up to 85 %) and provides a higher accuracy of channel weight estimation (Δ_k^{SVD} up to 20 % vs. Δ_k^{SNR} up to 85 %) than the SNR based method. Especially for simulated data with a high noise magnitude the variation of SVD calculated weights as well as the corresponding estimation error remains below 10 % for all channels, whereas for the SNR based method these values increase dramatically (up to 85 %).

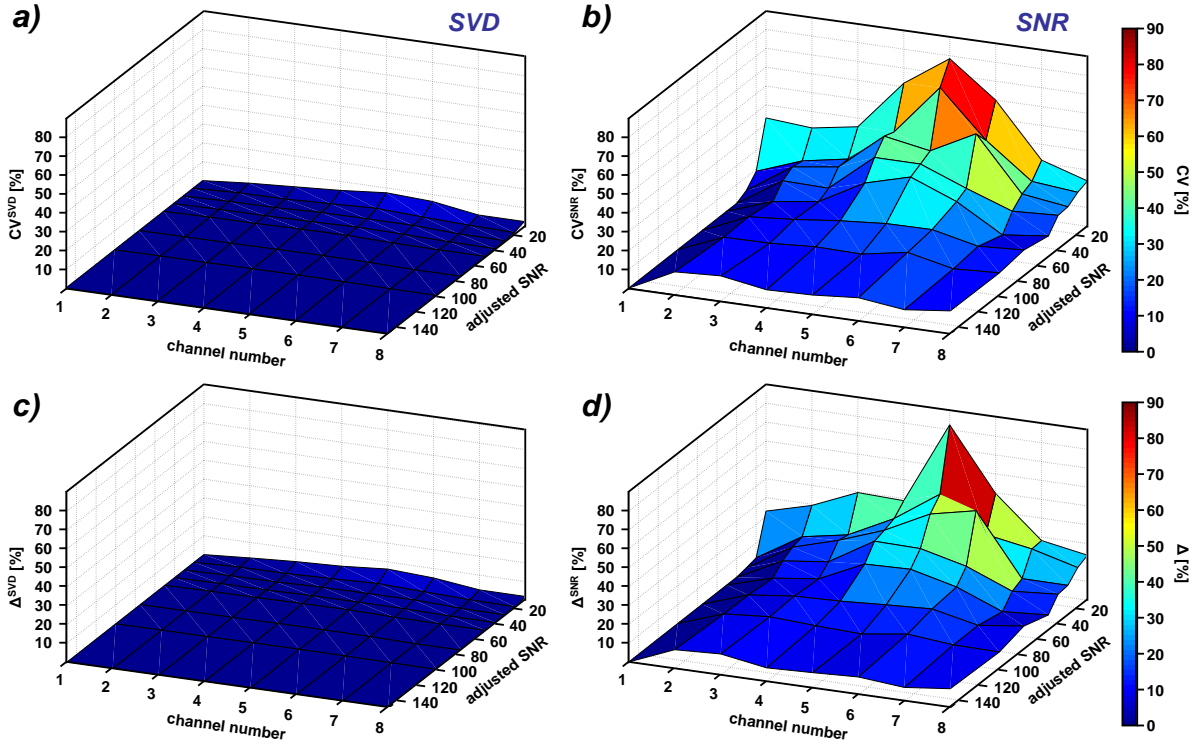


Figure 4.7: Distributions of channel weighting factors variation coefficients (cv_k^{method} : a and b) and mean determination errors (Δ_k^{method} : c and d), which were calculated through analysing of 16 simulated eight-channel data sets. Simulations were performed by changing the initially adjusted *SNR* level from 10 to 150. Left plots show the analysed parameter for weighting factors determined with SVD approach (w_k^{SVD}) whereas in right plots the same parameter are presented for weights calculated with SNR based method (w_k^{SNR}).

By regarding the results of the performed simulations, the SVD based approach was integrated into the automatic stream for the post-processing of *in vivo* multi-channel data in the actual fMRS study (see Fig. 4.4). One limitation of the SVD based method is associated with the higher computation time demand compared to the SNR method. However, since the data processing was performed off-line, this aspect can be neglected. In further studies, which may comprise online channel combination parallel to the data acquisition, the computation time may for example be reduced by using the parallel data processing techniques on computers with multiple kernels.

4.3 *In vivo* examinations on healthy volunteers

4.3.1 Subject population

Six healthy, right-handed male subjects (mean age 31.1 ± 11.1 years) were recruited within the own institution. Prior to the experiments volunteers were informed by a radiologist about all procedures and their possible risks and signed an informed consent.

4.3.2 Adjustment of stimulus temperature

Painful heat stimuli were applied to the inner skin area of the left forearm by using the technique described in Chap. 4.2.1 (see Fig. 4.2). To ensure comparable pain intensities among all participating volunteers the stimulation temperature level, T_{Stim} , was adjusted individually prior to the MR experiments. For this purpose subjects were instructed to rate the perceived pain intensity for incrementally increased temperatures (T_{Stim} values between 45°C and 49°C) using the *Visual-Analogue pain Scale* (VAS). The VAS is a generally accepted scale for quantitative pain intensity rating, which ranges from one (corresponding to "no pain") to ten (corresponding to "worst pain imaginable") [Korff et al., 2000]. The T_{Stim} value corresponding to the VAS interval between six and seven was chosen for the stimulation in the MR-spectroscopic experiments. To monitor possible habituation effects during the experiments subjects were asked to rate the perceived pain intensity again immediately after the MR examinations.

4.3.3 Acquisition of MRI and MRS data

All measurements were performed on a 3T whole-body MR scanner (Magnetom TIM Trio, Siemens Medical Solutions, Erlangen, Germany) using a twelve channel phased array receive-only head matrix coil for signal detection. ^1H -MR spectra were acquired with a conventional PRESS sequence and single volume selection ($TR/TE = 2500/30$ ms; $N_{\text{Samp}} = 4096$, $BW = 4$ kHz). Prior to the spectroscopic scans, T_1 -weighted, 3D whole-head MRI data sets were acquired with the MP-RAGE sequence (see Chap. 3.3.1 for detailed parameter settings) to select spectroscopic voxels in the left *anterior insula* (aI, see Fig. 4.8). This region was selected in the current study, since previous BOLD-fMRI and PET studies have confirmed that it is directly involved in the pain processing [Baliki et al., 2006; Casey, 1999; Craig et al., 2000]. Zero-, first- and second-order shim gradients were adjusted with an automatic B_0 -field 3D mapping technique, followed by manual fine-tuning of the first-order shim gradients to optimize B_0 homogeneity in the MRS volume. This procedure resulted in mean water linewidths of 15.1 ± 0.8 Hz (14.0 – 15.8 Hz). Following frequency adjustment, the water-selective suppression pulse (suppressed spectral bandwidth: 80 Hz) was similarly calibrated manually. During the acquisition of water-suppressed spectra, the transmitter rf frequency was set to the chemical shift value of the $^4\text{CH}_2$ signal group of Glu (-2.35 ppm relative to the water resonance at 4.7 ppm). Spectra without water suppression were acquired with the non-shifted transmitter rf frequency. This ensured nearly equally located volumes for the Glu and water signals due to reduced chemical shift misregistration effects.

The spectroscopic data sampling and reconstruction of mean 'REF', 'WATER', 'PAIN', 'REST' and 'DUMMY' spectra was performed with the technique described in Chaps. 4.2.2 and 4.2.3. Additionally, 'MEAN-REF' and 'MEAN-PAIN' spectra were generated by averaging the channel combined data from the 'REF' and 'PAIN' pools over all volunteers

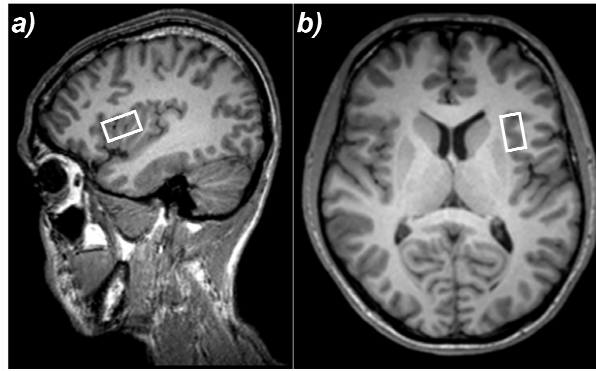


Figure 4.8: Sagittal (a) and transverse (b) MP-RAGE slices on which the location of the 2.5 ml MRS voxel is indicated in the left aI.

($NAS_{\text{sum}} = 6 \times 128 = 768$). To account for the coil load variation among the volunteers, data sets of different subjects were normalized to the intensities of the corresponding water signals prior to the averaging.

4.3.4 Calculation of absolute metabolic concentrations

Quantification of metabolic intensities in the mean '*REF*', '*PAIN*', '*REST*' and '*DUMMY*' spectra was performed by using the *LCModel* V 2.5 [Provencher, 1993] with an imported basis set consisting of fifteen single *in vitro* metabolite model spectra (see the detailed list of particular metabolite models in Chap. 3.3.2). The following five metabolites were included in the quantitative analysis since their CRLB values were lower than 20% in all spectra: NAA, Cr, tCho, Glu and mI. Absolute concentrations of these metabolites were calculated by using the water intensity as a tissue internal concentration reference and by taking into account the heterogeneous tissue composition in MRS voxels (see Eq. 3.13 in Chap. 3.1.2). In order to quantify the pain stimulation related changes of Glu, NAA, Cr, tCho and mI in aI, their mean levels were calculated for '*PAIN*', '*REST*' and '*DUMMY*' states by averaging over all volunteers and then compared with the corresponding values in the '*REF*' condition by a paired two-tailed *t*-test.

4.4 Results of *in vivo* ^1H -fMRS study

4.4.1 Evaluation of subjectively perceived pain intensity

Prior to the start of the MR examinations volunteers reported VAS values between six and seven which, however, decreased during the course of stimulation to values between two and four as revealed by the volunteers' rating immediately after finishing the experiments. Some, but not all subjects noticed a painful afterburning sensation effect that lasted during the resting phase ('*DUMMY*' state) between two consecutive stimulation runs.

4.4.2 Evaluation of spectroscopic data quality

All reconstructed spectra showed high spectral resolution and sufficient SNR ($SNR_{\text{NAA}} > 11$, see Tab. 4.2). As revealed by the low CRLB values for the five analysed metabolites, the quality of spectra allowed metabolite intensity quantitation with sufficient accuracy (see Tab. 4.2).

Table 4.2: Mean SNR_{NAA} and $FWHM_{\text{NAA}}$ (in Hz) as well as mean CRLB values (in %) for the five analysed metabolites (value: $MEAN \pm SD$) in reconstructed 'REF', 'PAIN', 'REST' and 'DUMMY' spectra.

		REF	PAIN	REST	DUMMY
SNR_{NAA}		11.8±2.1	13.2±2.8	12.0±2.3	11.8±2.8
$FWHM_{\text{NAA}}$	[Hz]	4.7±1.2	4.6±1.0	4.4±0.6	4.8±1.2
$CRLB_{\text{Glu}}$	[%]	9.7±0.8	8.3±1.1	10.8±2.2	9.2±0.9
$CRLB_{\text{NAA}}$	[%]	3.8±0.7	3.8±0.9	4.0±0.8	3.8±1.1
$CRLB_{\text{Cr}}$	[%]	3.7±0.5	3.3±0.5	3.8±0.7	3.5±0.5
$CRLB_{\text{tCho}}$	[%]	4.8±0.7	4.2±0.7	4.8±0.7	4.7±0.8
$CRLB_{\text{mI}}$	[%]	7.7±2.0	6.7±1.5	7.2±1.1	7.2±1.3

4.4.3 Evaluation of pain related metabolite level changes

Intra-individual absolute concentrations of Glu, NAA, Cr, total Choline and mI are plotted in Figs. 4.9 and 4.10 for the stimulation states 'REF', 'PAIN', 'REST' and 'DUMMY'. The differently coloured stars represent the concentration values of the six volunteers. The bold red lines within the boxes indicate the median values of metabolite concentrations over all volunteers, whereas the upper and lower box plot limits show the 75th and 25th percentiles, respectively. Tab. 4.3 summarizes mean Glu and NAA concentrations corresponding to different stimulation states as well as mean relative Glu and NAA percentage changes in 'PAIN', 'REST' and 'DUMMY' states relative to the 'REF'-condition (all values are presented as averages over all volunteers). Similarly to Tab. 4.3, Tab. 4.4 contains the mean concentrations of Cr, tCho and mI for the corresponding stimulation states as well as percentage changes during the 'PAIN', 'REST' and 'DUMMY' states relative to the 'REF'-condition.

During the 'PAIN' state, Glu concentrations were substantially increased with a mean value of $18.1 \pm 8.3\%$ ($p = 0.003$) above the initial 'REF' level. Following stimulation, Glu concentrations revealed a decreasing trend in the 'REST' and 'DUMMY' states back to the baseline value prior to stimulation, except for one volunteer (see Glu course of the brown stars in Fig. 4.9a). For this volunteer Glu concentrations remained increased during 'REST' and 'DUMMY' conditions, with values close to the 'PAIN' state level. Mean Glu concentrations obtained for 'REST' and 'DUMMY' were apparently, but not

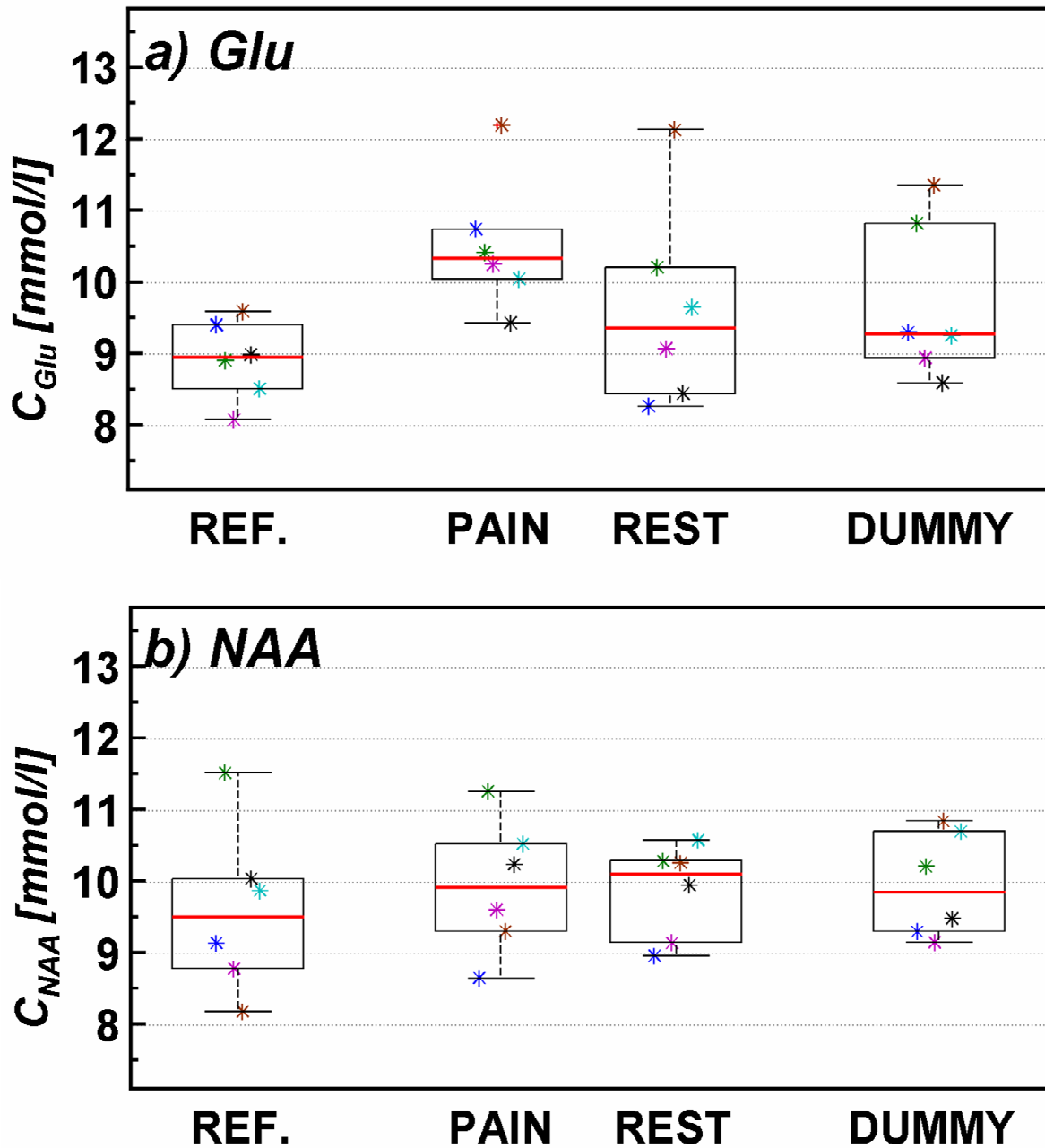


Figure 4.9: Absolute concentrations of Glu (a) and NAA (b) in *mmol/l* for the stimulation states: 'REF', 'PAIN', 'REST' and 'DUMMY'. The different colours of the diagram symbols represent the six single subjects. Bold red lines within the boxes indicate the median values of metabolite concentrations over all 10 volunteers whereas the upper and lower box plot limits show the 75th and 25th percentiles, respectively.

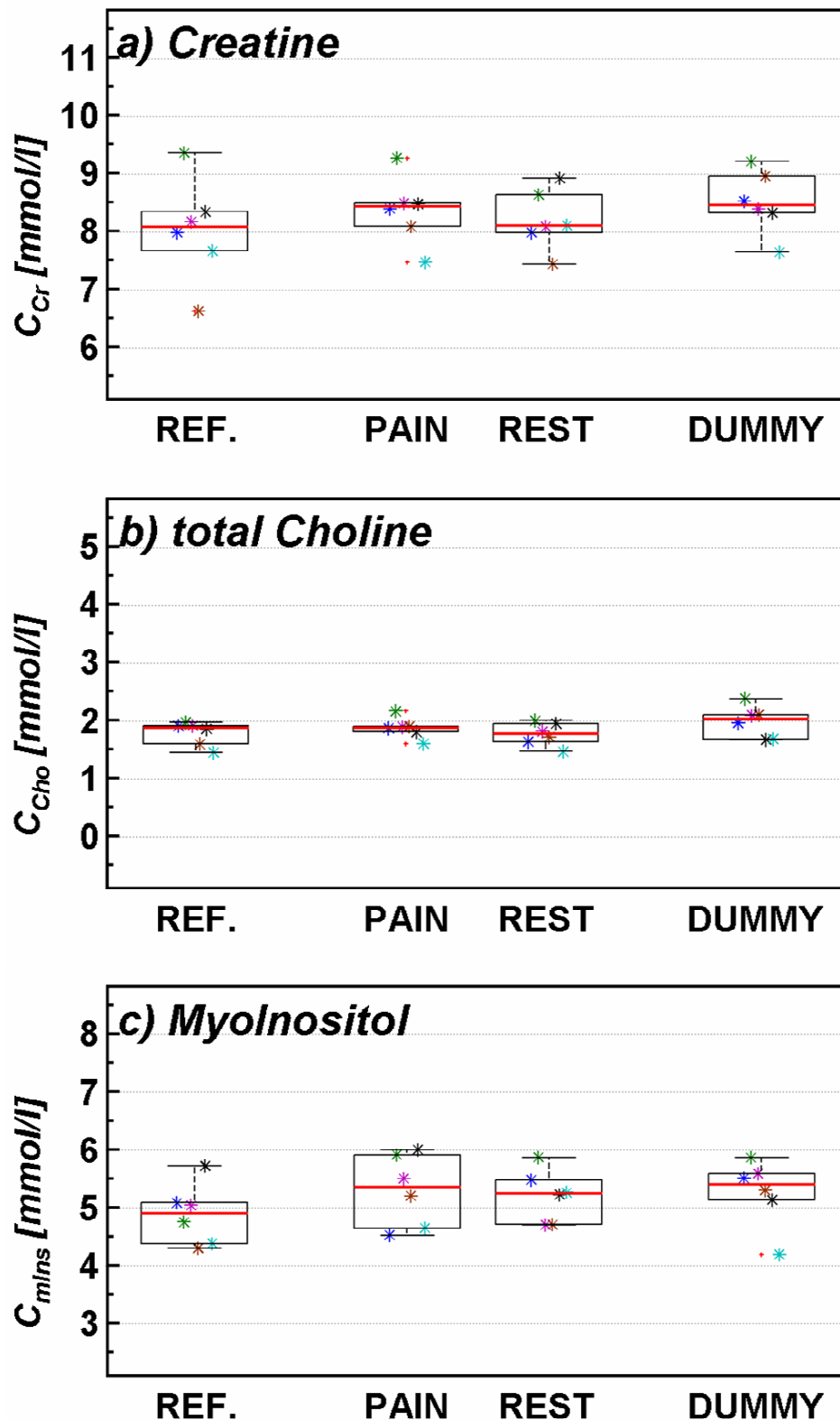


Figure 4.10: Absolute concentrations of Cr (a), tCho (b) and mI (c) in $mmol/l$ for the stimulation states: 'REF', 'PAIN', 'REST' and 'DUMMY'. The different colours of the diagram symbols represent the six single subjects. Bold red lines within the boxes indicate the median values of metabolite concentrations over all volunteers; the upper and lower box plot limits show the 75th and 25th percentiles, respectively.

Table 4.3: Mean absolute concentrations of Glu and NAA (C_x : $MEAN \pm SD$ in mmol/l) for the different stimulation states '*REF*', '*PAIN*', '*REST*' and '*DUMMY*'. The p_x -values represent the results of a paired two-tailed t -test for comparison of mean Glu and NAA concentrations between the '*REF*' condition and different stimulation sequence states. ΔC_x denotes changes of metabolite concentrations (in %) for different stimulation sequence states relative to the '*REF*' condition.

		REF	PAIN	REST	DUMMY
<i>Glu:</i>					
C_{Glu}	[mmol/l]	8.9±0.6	10.5±0.9	9.6±1.4	9.7±1.1
Δ_{Glu}	[%]		18.1±8.3	8.1±14.4	9.0±10.3
p_{Glu}			0.003	0.248	0.092
C_{Glu}^*	[mmol/l]	8.7±0.6	10.1±0.6	8.9±0.6	9.0±0.3
Δ_{Glu}^*	[%]		16.1±9.1	1.9±12.9	3.5±7.4
p_{Glu}^*			0.010	0.856	0.436
<i>NAA:</i>					
C_{NAA}	[mmol/l]	9.6±1.2	9.9±0.9	9.9±0.7	10.0±0.7
Δ_{NAA}	[%]		4.0±7.2	3.8±12.2	5.0±15.2
p_{NAA}			0.244	0.568	0.545
C_{NAA}^*	[mmol/l]	9.5±0.6	9.8±0.8	9.7±0.8	9.7±0.7
Δ_{NAA}^*	[%]		3.2±6.4	2.1±4.3	2.2±5.8
p_{NAA}^*			0.385	0.403	0.535

* Mean C_{Glu} , Δ_{Glu} , C_{NAA} , Δ_{NAA} and corresponding p values calculated for five volunteers, excluding the volunteer with NAA-concentration change of up to 32% during the stimulation time course (see brown stars in Fig. 4.9b).

significantly increased relative to '*REF*' (up to 9% increase, $p > 0.090$). Overall, there was a rather large variability of Glu levels extracted for '*PAIN*', '*REST*' and '*DUMMY*' states compared to the '*REF*' condition (see Tab. 4.3).

NAA concentrations remained rather constant throughout the experiments with variances in the range of up to $\pm 10\%$ except for the same single volunteer, whose spectra had also revealed the aberrant Glu course and who showed a monotonous strong NAA increase during the stimulation cycle (see brown stars in Fig. 4.9b). A similar behaviour was also observed for the Cr and mI time courses in this volunteer (see Figs. 4.10a and c). Overall, however, Cr, tCho and mI revealed no significant concentration changes between '*PAIN*', '*REST*' and '*DUMMY*' states and '*REF*' for all volunteers ($p > 0.1$, see Tab. 4.4).

All analyses were additionally repeated while excluding the data of the volunteer with aberrant Glu and NAA time courses. Modified concentrations of Glu and NAA are also presented in Tab. 4.3 (see data marked by a star). Excluding the high '*PAIN*' state Glu-concentration of the volunteer marked with brown stars led to a smaller, but still

Table 4.4: Mean absolute concentrations of Cr, tCho and mI (C_x : $MEAN \pm SD$ in mmol/l) for the different stimulation states 'REF', 'PAIN', 'REST' and 'DUMMY'. The p_x -values represent the results of a paired two-tailed t -test for comparison of mean Glu and NAA concentrations between the 'REF' condition and different stimulation sequence states. ΔC_x denotes changes of metabolite concentrations (in %) for different stimulation sequence states relative to the 'REF' condition.

		REF	PAIN	REST	DUMMY
Cr:					
C_{Cr}	[mmol/l]	8.0±0.9	8.4±0.6	8.2±0.5	8.5±0.5
Δ_{Cr}	[%]		4.8±8.8	2.7±7.0	7.1±14.0
p_{Cr}			0.220	0.483	0.261
tCho:					
C_{tCho}	[mmol/l]	1.8±0.2	1.9±0.2	1.8±0.2	2.0±0.3
Δ_{tCho}	[%]		5.6±8.9	-0.6±8.0	11.8±14.5
p_{tCho}			0.198	0.781	0.110
mI:					
C_{mI}	[mmol/l]	4.9±0.5	5.3±0.6	5.2±0.5	5.3±0.6
Δ_{mI}	[%]		9.1±12.7	7.6±13.3	8.5±13.9
p_{mI}			0.147	0.267	0.216

significant increase of Glu in the 'PAIN' state compared to the 'REF' state ($16.1 \pm 9.1\%$, $p_{PAIN}^* = 0.01$). Furthermore, the mean Glu concentrations in the 'REST' and 'DUMMY' states were much closer to the initial 'REF' values as indicated by the increased p -values ($p_{REST}^* = 0.856$ vs. $p_{REST} = 0.248$; $p_{DUMMY}^* = 0.436$ vs. $p_{DUMMY} = 0.092$).

Finally, Fig. 4.11 shows the 'MEAN-REF' and 'MEAN-PAIN' spectra calculated by averaging all volunteer data measured in the 'REF' and 'PAIN' states, respectively. The upper part of Fig. 4.11 represents the difference spectrum obtained by subtracting the 'MEAN-REF' from the 'MEAN-PAIN' spectrum. The amplitudes of the Glu- $^4\text{CH}_2$ multiplet at 2.35 ppm and the Glu- ^2CH multiplet at 3.75 ppm are clearly increased in the 'MEAN-PAIN' spectrum compared to the 'MEAN-REF' spectrum.

4.5 Discussion

4.5.1 Technical aspects of implemented method

The present chapter described the implemented MRS data sampling method, which comprises a trigger based synchronisation of data acquisition with the application of short painful heat stimuli. First of all, triggering provides precise assignment of acquired spectra to defined conditions within the applied stimulation sequence and enables tracing of

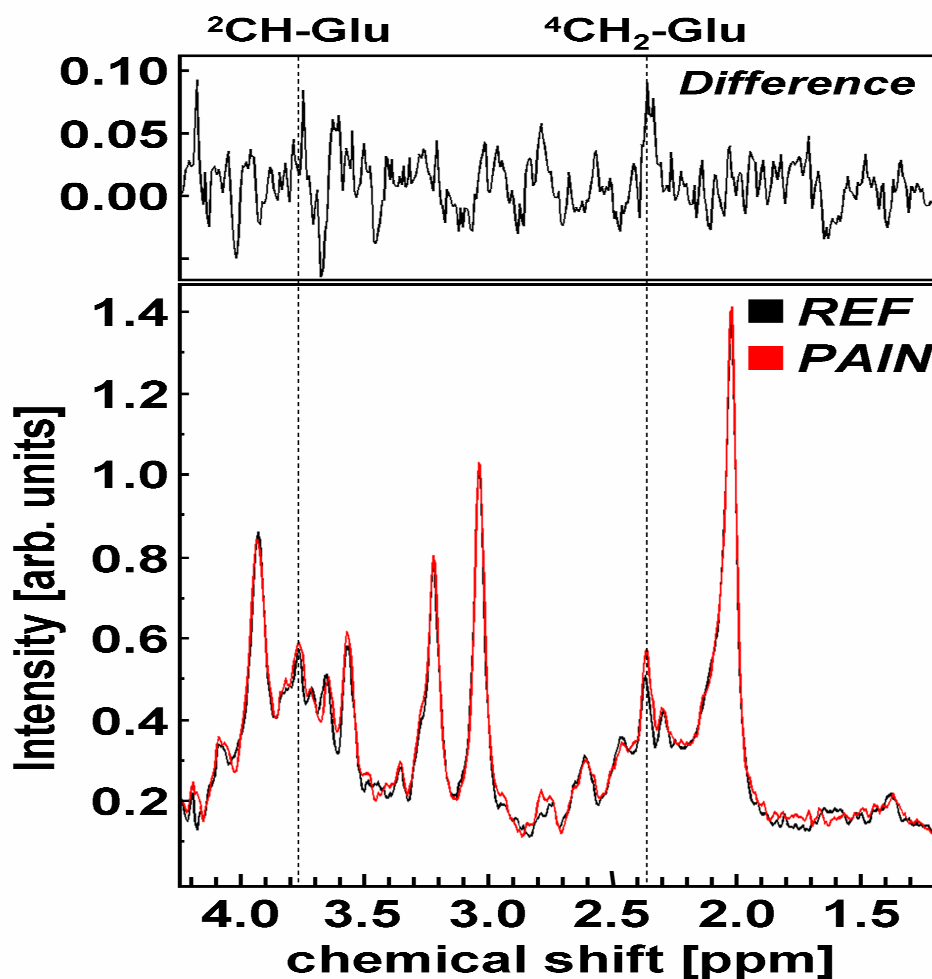


Figure 4.11: The 'MEAN-REF' (black) and 'MEAN-PAIN' (red) spectra obtained by averaging the 'REF'- and 'PAIN' single acquisition data from all subjects. The upper graph shows the difference spectrum extracted by subtraction of the 'MEAN-REF' from the 'MEAN-PAIN' spectrum. Of note are the apparently increased amplitudes of the Glu- ${}^4\text{CH}_2$ and Glu- ${}^2\text{CH}$ signals at 2.35 ppm and 3.75 ppm, respectively, in the 'MEAN-PAIN' spectrum compared to the reference state (marked by dashed lines).

event related metabolic changes with a time resolution of several seconds. This approach appears to be superior to the 'block design' ${}^1\text{H-fMRS}$ concept, which is based on averaging single acquisition data during several minutes of resting and stimulus state periods [Mangia et al., 2007; Mullins et al., 2005]. Authors of these recent studies proposed that the detected metabolic changes reflect long-time metabolic level shifts between two steady state like conditions (*Baseline* and *Stimulation*). In contrast, the presented 'event related' approach may potentially make it possible to discriminate between different neurophysiological processes, which occur dynamically during a short time period and are responsible for an adaptation of neuronal activity state to environmental conditions.

However, an essential premise for the separate evaluation of dynamical metabolic processes is sufficient sensitivity of the measurement method. For example, in order to de-

rive any unambiguous conclusions regarding neurotransmission changes during the pain processing, it is necessary to consider event related changes of both excitatory and inhibitory neurotransmitters (Glu, GABA) as well as to detect the alterations of metabolites, which are involved in brain energy consumption (e.g., lactate or glucose). These aspects can, however, not be assessed yet with the data of the present study, which was performed at a relatively low magnetic field strength ($B_0 = 3\text{T}$) and by using a conventional PRESS sequence for acquisition. Spectral resolution and *SNR* were sufficient only for Glu intensities (see the relatively low quantitation errors (CRLB-values) for Glu in Tab. 4.2), whereas other target metabolites could not be quantitated with sufficient accuracy ($CRLB_{\text{GABA, Gluc}} > 30\%$). In order to assess the time courses of these other metabolites more sensitive spectroscopic techniques have to be implemented and adapted. Some promising approaches include the use of higher magnetic fields [Tkáč and Gruetter, 2005] or J-editing techniques (e.g. detection of GABA with a *MEGA-PRESS* method [Rothman et al., 1984]).

Further attention should focus on the optimisation of the stimulation sequence in order to improve reproducibility and specificity of results. As revealed by the generally decreasing VAS values during the session, habituation effects could not be completely avoided with the applied design. A randomized order of stimulations may potentially help to overcome this limitation.

Furthermore, the time points of spectral acquisition were currently adjusted to the stimulation sequence timing but not to the temporal dynamics of brain activation. A more accurate metabolic time course extraction may become possible by simultaneous acquisition of EEG data that provide temporally highly resolved information of electrophysiological brain activity.

Finally, movements of the volunteers and corresponding voxel displacements between different measurements can not be excluded completely given the relatively long data acquisition period. This undesired motion may explain, for instance, the high variation of NAA, Cr, and mI concentrations in one single volunteer (see data marked with a brown star in Fig. 4.9 and Fig. 4.10a/c). The inter-individual differences in the Glu time courses between all volunteers may thus be ascribed to partial volume effects associated with voxel displacements. Therefore, improved motion control by means of additional short MRI scans may facilitate identification of potential influences of voxel displacements on metabolic changes.

4.5.2 Detection of heat pain associated glutamate changes

Several published fMRI and PET studies have demonstrated that neuronal activations in the *anterior insula* (aI) are strongly associated with cognitive processing of acute pain in the human brain [Brooks et al., 2002; Casey, 1999; Craig et al., 2000]. The detected Glu changes during thermal pain stimulation may thus reflect a modified glutamatergic

neurotransmission in this brain region. Since no evidence of strong lateralization has been reported in the literature with respect to pain related activation patterns in the aI [Casey, 1999], this cortical region appears to be well suited for *in vivo* single-voxel ^1H -MR spectroscopic investigations that usually require *a priori* information about the spatial location of the expected metabolic changes.

Glutamate is the major excitatory neurotransmitter within the nervous system with strong effects on neurons. Moreover, it is also involved in many other metabolic processes [Hertz, 2006; Rothman et al., 2003]. The importance of Glu for neurotransmission can be inferred by its abundance, the presence of the corresponding receptors and transporters in brain tissue as well as by the fact that 60 – 80 % of the brain's oxidative energy production is associated with glutamatergic neuronal activity [Rothman et al., 2003]. During neurotransmission Glu circulates between the neurons and astroglial cells with an interim conversion into Gln and an efflux rate which depends linearly on the activation state [Rothman et al., 2003; Shulman and Rothman, 1998]. In a related ^1H -MRS pain study, Mullins et al. [2005] observed a strong correlation between significant Glu and Gln increases in the anterior cingulate cortex of healthy volunteers and the subjectively perceived pain intensity during application of painful cold stimuli. Their hypothesis was that increased neurotransmission induces Glu changes by an increased efflux rate through the neuroglial Glu/Gln-cycle. On the other hand, Mangia et al. [2007] ascribed Glu changes in the human occipital cortex after visual stimulation to an increase of oxidative metabolism in the TCA cycle during neuron activation.

However, despite these two hypotheses that relate the increased Glu levels to altered neuronal activity the origin of the spectroscopically detected Glu changes remains unresolved as long as the observed changes cannot be unambiguously assigned to particular cellular Glu compartments (see the mentioned limitations in Chap. 4.1.2.2). Combined ^1H - and ^{13}C -MR spectroscopy including metabolic labelling techniques may be one possibility to extract the neuronal Glu fraction that is directly involved in the Glu/Gln neurotransmission cycle. The pain induced increase of Glu concentration is clearly seen when comparing the '*MEAN-REF*' and '*MEAN-PAIN*' spectra in Fig. 4.11. It is also reflected in the estimated concentration levels for individual volunteers and the increase of the mean Glu concentration (see Fig. 4.9a and Tab. 4.4). However, this increase of $18.1 \pm 8.3\%$ in the '*PAIN*' state is approximately twice as large compared to the increase of $9.3 \pm 6.1\%$ detected by Mullins et al. [2005] in the anterior cingulate cortex (aCC) during continuous cold pain stimulation of the left foot. Possible explanations for these differences may be smaller partial volume effects in this current study due to smaller voxel volumes (2.5 ml in own study vs. 8.0 ml in the study by Mullins et al. [2005]) as well as different influences of adaptation processes. Since periodic short stimuli were applied, nociceptor saturation on the skin surface and hence pain adaptation may have been significantly reduced compared to the method of Mullins et al. [2005], who applied the stimulus for ten minutes. Mangia et al. [2007] described a much lower increase of Glu (up to 4 %) in the occipital

cortex during visual stimulation. Potentially, such a large difference between the values reported by Mangia et al. [2007] and the current values may be caused by the different stimulation paradigms (acute pain vs. visual stimulation), which reflect different changes of glutamatergic metabolism. On the other hand, the studies by Mullins et al. [2005] and Mangia et al. [2007] were both performed on scanners with magnetic fields of 4 T and 7 T, respectively, as well as by using shorter echo times than in the experiments described here ($TE = 30$ ms vs. $TE_{\text{Mullins}} = 20$ ms and $TE_{\text{Mangia}} = 6$ ms). Therefore, Glu quantitation may be affected by several sensitive factors, such as lower spectrum *SNR*, higher overlap with signals of other metabolites due to lower spectral resolution or by the more advanced phase evolution within the Glu multiplets due the J-coupling at $TE = 30$ ms.

The strong inter-individual Glu variability observed in the '*REST*' state and the fact that only a single time point was sampled in the inter-stimuli resting period make drawing conclusions on the Glu time course during the complete stimulation cycle difficult and ambiguous. Considering the afterburning effects reported by some volunteers, high Glu variations in the '*REST*' state may be due to differently prolonged perceptions of pain intensity. However, assuming a direct relationship between neuronal activity and ^1H -MR spectroscopically detected Glu concentration, the observed decreasing trend between the '*PAIN*' and '*REST*' state may possibly reflect the return of Glu to its resting level. On the other hand, the slightly but insignificantly increased Glu concentration in the '*REST*' state relative to the '*REF*' state may also support the hypothesis of Glu increase during neuronal stimulation with accelerated oxidative metabolism followed by a delayed decrease of the oxidative metabolism in the resting state [Mangia et al., 2007].

In summary, the described *in vivo* study represents the first report of a pain stimulus related response of glutamergic activity in the anterior insula investigated with functional ^1H -MRS. Despite the mentioned difficulties and limitations in determining Glu concentration, the initial question whether changes of cortical Glu levels in the cerebral pain processing regions induced by acute pain are traceable with ^1H -MRS can be positively answered in light of the results.

5 *In vivo* detection of chronic pain induced metabolic changes in brain by means of ¹H-MRS

5.1 Introduction

This chapter describes a clinical study on patients with *non-specific chronic low back pain* (nCLBP) and healthy controls aiming to evaluate whether ¹H-MR spectroscopy is feasible to detect metabolic changes in the brain occurring during the manifestation of chronic pain. Measurements were performed in three different, pain processing cortical regions - *anterior insula* (aI), *anterior cingulate cortex* (aCC) and *thalamus* (Th). Both aCC and aI belong to the human limbic system. They are less involved in the encoding of pain location or pain intensity, but are strongly involved in the affective assessment of peripheral nociceptive stimuli with respect to their interpretation as being painful or not (*'suffering component'* of pain) [Apkarian et al., 2005; Peyron et al., 2000]. Thus, aCC and aI appear to be well suited for localized ¹H-MR spectroscopic investigations of potential metabolic changes induced by chronic pain with unknown pain origin. Contrary to aI and aCC, the Th is generally responsible for the forwarding of stimuli from nociceptive and other peripheral receptors to the appropriate cortical structures [Brooks and Tracey, 2005]. However, since recent ¹H-MR spectroscopic studies reported on chronic pain related metabolic changes in Th [Fukui et al., 2006; Pattany et al., 2002], metabolic concentrations in Th were also compared between patients and controls in this investigation.

5.2 Material and Methods

5.2.1 Patient population

Two groups of persons were examined, the first consisting of two male and eight female nCLBP patients (right-handed, age: 22 – 52 years, weight: 52 – 83 kg, body height: 160 – 180 cm), and the second comprising ten right-handed healthy controls that were pairwise matched to the patients with respect to gender, age, body weight and height. Patients underwent detailed clinical history evaluation conducted by a pain physiologist to unravel potential origins of their disorders. Pain was classified as *'non-specific'* if it could not be linked to defined disorders, like muscle, nerve or vertebral disc injuries, as

assessed by means of conventional structural MRI data of the low back area. At the time of examination, patients had suffered from permanent pain in the low back area for at least one year (range: 1 – 5 years). Patients were also asked to rate pain intensity during four weeks prior to the examination by using the VAS scale (see Chap. 4.3.2, [Korff et al., 2000]). VAS values in the patient group ranged from two to six (4.1 ± 1.1). At the time of examination patients had stopped medication for at least one day.

5.2.2 MR imaging and ^1H -MR spectroscopy

All measurements were performed on a 3T whole-body MR scanner (Magnetom TIM Trio, Siemens Medical Solutions, Erlangen, Germany) using a twelve channel phased array receive-only head matrix coil for signal detection. MR spectra were acquired with a conventional PRESS sequence and single volume selection ($TR/TE = 2500/30$ ms; $N_{\text{Samp}} = 4096$, $BW = 4$ kHz). Prior to the spectroscopic scans, T_1 -weighted, 3D whole-head MRI data sets were acquired with the MP-RAGE sequence (see Chap. 3.3.1 for detailed parameter settings) in order to adjust spectroscopic voxel positions in the left aI ($V_{\text{aI}} = 3.0$ ml; see Fig. 5.1a), aCC ($V_{\text{aCC}} = 3.9$ ml; see Fig. 5.1b) and left Th ($V_{\text{Th}} = 3.5$ ml; see Fig. 5.1c). Zero-, first- and second-order shim gradients were adjusted with an automatic B_0 -field 3D mapping technique, followed by manual fine-tuning of the first-order shim gradients to optimize B_0 homogeneity in the MRS volume. This procedure resulted in mean water linewidths of 16.5 ± 2.7 Hz, 14.9 ± 1.9 Hz and 21.0 ± 2.3 Hz for aI, aCC and Th, respectively. Following frequency adjustment, the water-selective suppression pulse (suppressed spectral bandwidth: 80 Hz) was similarly calibrated manually. For each spectroscopic voxel two MR spectra were acquired - the first spectrum with water suppression ($NAS_{\text{aI}}/NAS_{\text{aCC}} = 128$, $NAS_{\text{Th}} = 256$), the second spectrum without water suppression ($NAS = 16$). Spectra recorded with water suppression were corrected for zero-order phase errors and eddy current distortions by using the non-suppressed water signal phase as a reference (see the description of the applied method in Chap. 2.3.3.3). Overall examination time was approximately 60 minutes.

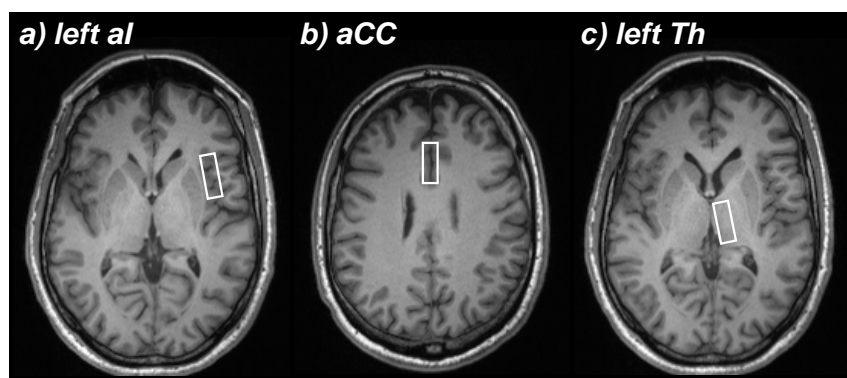


Figure 5.1: Transverse, T_1 -weighted MRI slices illustrating the selected MRS voxel positions in the left aI (a), aCC (b) and left Th (c).

5.2.3 Quantitation of ^1H -MRS data

Quantitation of metabolic and water signal intensities from water suppressed and non-suppressed spectra was performed by using the *LCModel* V 2.5 [Provencher, 1993] with an imported basis set that consisted of fifteen single *in vitro* metabolite model spectra (see the detailed list of particular metabolite models in Chap. 3.3.2). Absolute metabolite concentrations (in *mmol/l*) were calculated for NAA, Cr, tCho, mI, Glu and Gln by taking into account individual GM, WM and CSF volume fractions f_{GM} , f_{WM} and f_{CSF} within the MRS voxels (see the method description in Chap. 3). The determination of f_{GM} , f_{WM} and f_{CSF} values was based on combined analysis of MRS data and high resolution T_1 weighted MRI data (MP-RAGE data set).

5.2.4 Evaluation of structural MRI data

Since recent studies reported morphologic changes in the brain during the time course of chronic pain manifestation (see the overview by Borsook et al. [2007]), morphological evaluation of the acquired MP-RAGE data was also included in the analysis. To first approximation morphological changes were assessed by comparing the GM, WM and CSF volume fractions (f_{GM} , f_{WM} and f_{CSF}) in the MRS voxels in aI, aCC and Th of CLBP patients and healthy controls. However, inter-individual comparison of volume fractions may be affected by investigator dependent MRS voxel placement as well as by inter-individual differences in the size of the cortical structures. To overcome this problem, the software *FreeSurfer* can be used to determine mean cortical thickness (in *mm*) in certain cortical areas. The cortical thickness is computed by finding the shortest distance between a given point on the estimated pial surface and the GM-WM-boundary [Fischl and Dale, 2000]. Since cortical thickness values are estimated by regarding the whole MRI volume, they are more user independent than brain tissue fractions in MRS voxels and are therefore more adequate for an objective evaluation of morphological changes due to CLBP.

5.2.5 Statistical analysis

Mean values of absolute NAA, Cr, tCho, mI, Glu, Gln and Glx concentrations and relative GM, WM and CSF volume fractions were calculated by averaging separately over all nCLBP patients and all controls. Mean cortical thickness of selected anatomical structures within the adjusted aI and aCC MRS voxels were also evaluated to assess potential neuroanatomical alterations due to chronic pain manifestation. Since the *FreeSurfer* routine does not provide the cortical thickness of the thalamus, which consists of different nuclear groups without clear tissue boundaries, the assessment of potential morphological changes in thalamus was performed by comparing relative thalamus volumes. The latter were calculated as the ratio between the number of pixels assigned by *FreeSurfer* to the thalamus, and the number of pixels in the whole brain.

All calculated values (metabolite concentrations, GM, WM and CSF fractions as well as cortical thicknesses and relative Th volumes) were compared between the control and nCLBP patient groups by a paired two-tailed t -test. Prior to the statistical analysis all spectra were visually inspected for the presence of artefacts. For the corresponding pairs of MR spectra (*'Patient - Control'*), a maximum linewidth of 10 Hz of the NAA-singlet at 2.01 ppm (calculated by the *LCModel*) was chosen as a threshold criterion for including the quantitative metabolite results into the statistical analysis. Applying this criterion, all ten data pairs from the left aI and aCC ($N_{\text{aI}} = N_{\text{aCC}} = 10$) and six data pairs from the left Th ($N_{\text{Th}} = 6$) were included. Quantitative results for Gln and Glx were only included, if the corresponding CRLB values, calculated by the *LCModel* for the Gln fit, were below 30%. Consequently, comparison of Gln and Glx concentrations between patients and controls was only performed for five MR spectra pairs of the aI and aCC.

5.3 Results

5.3.1 Spectroscopic data quality

All spectra showed high spectral resolution and sufficient SNR (see Tab. 5.1). As revealed by the low CRLB values for all metabolites listed in Tab. 5.1, the quality of spectra allowed metabolite intensity quantitation with sufficient accuracy.

Table 5.1: Mean SNR_{NAA} , $FWHM_{\text{NAA}}$ and metabolite CRLB values estimated by the *LCModel* ($MEAN \pm SD$), averaged over all selected spectroscopic data sets (2×10 spectra for the aI and aCC; 2×6 spectra for the Th).

		aI	aCC	Thalamus
SNR_{NAA}		14.1±2.0	16.1±2.3	13.2±2.7
$FWHM_{\text{NAA}}$	[Hz]	4.8±1.0	4.5±0.7	7.1±1.0
$CRLB_{\text{NAA}}$	[%]	4.0±0.9	3.4±0.5	4.2±1.0
$CRLB_{\text{Cr}}$	[%]	3.6±0.5	3.1±0.2	4.2±0.4
$CRLB_{\text{tCho}}$	[%]	4.5±0.6	3.5±0.5	4.3±0.6
$CRLB_{\text{mI}}$	[%]	7.0±1.4	5.5±0.9	9.0±2.7
$CRLB_{\text{Glu}}$	[%]	9.4±2.4	7.7±1.3	10.6±2.1
$CRLB_{\text{Gln}}$	[%]	25.3±6.1*	20.2±1.6*	-

* based on five data pairs (nCLBP patient vs. control) with $CRLB_{\text{Gln}}$ values below 30%.

5.3.2 CLBP related metabolic changes

Fig. 5.2 summarizes the distributions of absolute NAA, Cr, tCho, mI, Glu, Gln and Glx concentrations in the aI (Fig. 5.2a), aCC (Fig. 5.2b) and left Th (Fig. 5.2c) of nCLBP

patients (black stars within blue box plots) and corresponding healthy controls (black stars within green box plots). Mean phase- and baseline-corrected spectra from aI, aCC and Th are presented in Fig. 5.3 (top row), together with the corresponding mean *LCModel* fit graphs for Gln, Glu and Glx. These spectra and graphs were obtained by averaging over all selected data sets of nCLBP patients (red graphs) and healthy controls (black graphs). Prior to averaging, spectra and fit graphs were individually normalized to the maximum of phase and baseline corrected CH_3 -singlet of creatine (Cr) at 3.0 ppm to take into account inter-individually variable coil loadings and intensity scaling factors. Mean NAA, Cr, tCho, mI, Glu, Gln and Glx concentrations as well as metabolite levels differences between patients and healthy controls are presented in Tab. 5.2. These values were obtained by averaging over all patient and healthy control data sets, which fulfilled the inclusion criteria ($FWHM_{\text{NAA}} < 10$ Hz in general and $CRLB_{\text{Gln}} < 30\%$ for Gln and Glx concentrations). Concentration differences between patients and controls are also presented in Tab. 5.2.

As can be seen from the Gln fit graphs (see the plots in the second row of Figs. 5.3a and b) and the corresponding absolute Gln concentration distributions (see Figs. 5.2a and b and Tab. 5.2), Gln decreased by up to 15% in aI and aCC of nCLBP patients, although without reaching statistical significance due to high inter-individual concentration variations ($p < 0.310$). This decrease is also observed as a slight intensity reduction of the $^4\text{CH}_2$ -Gln-multiplet at 2.45 ppm in patient spectra of aI and aCC (see upper subplots in Figs. 5.3a and b).

Significantly decreased Glu concentrations were observed in the aCC of patients ($-10.2 \pm 11.8\%$; $p = 0.027$), whereas the Glu concentration in aI was not significantly different between patients and controls ($p = 0.950$). Due to the simultaneously decreased Gln and Glu concentrations in aCC, the Glx intensity reduction between 2.2–2.5 ppm and between 3.7–3.8 ppm is clearly seen in the patients' aCC spectrum and the corresponding Glx fit graph (see upper and bottom subplots in Fig. 5.3b). The Glx concentration decrease in patients was $12.9 \pm 10.1\%$ ($p = 0.01$).

In the Th, quantitation of Gln suffered from low spectral resolution and limited SNR (see Tab. 5.1), and the results were excluded from the final quantitative analysis. Nevertheless, as can be seen in the middle and bottom subplots of Fig. 5.3c, Glu and Gln intensities also indicate a decrease in the Th in patients, similar to aCC.

Patients had significantly lower NAA concentrations in aI ($p = 0.024$); a decreasing, though non-significant trend with a similar range as for aI (up to 4.5%) was also observed in the aCC and Th (see Tab. 5.2).

Compared with controls, mean spectra from aI, aCC and Th in the patient group show a clear intensity drop between 3.6 ppm and 3.7 ppm (see upper subplots in Fig. 5.3), which may be related to decreased mI levels, as indicated by the evidently decreased, but statistically non-significant different mI concentrations ($p > 0.16$, see Tab. 5.2).

Finally, patients indicated lower tCho concentrations, especially in aI and aCC (tCho

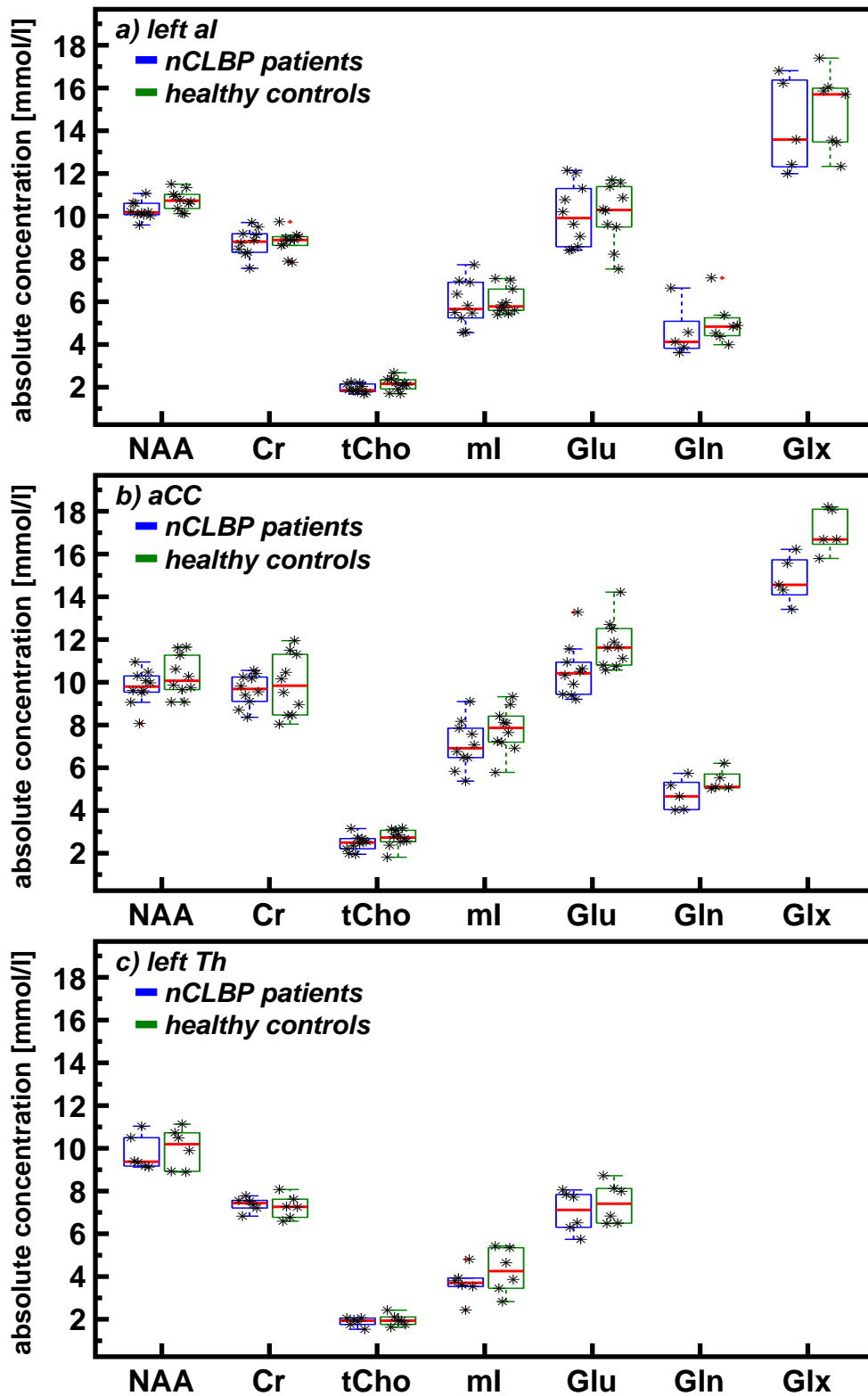


Figure 5.2: Distributions of absolute NAA, Cr, tCho, mI, Glu, Gln and Glx concentrations in mmol/l in left aI (a), aCC (b) and left Th (c) of nCLBP patients (black stars in blue boxes) and corresponding healthy controls (black stars in green boxes). Gln and Glx values were only included, if the corresponding CRLB values for Gln were below 30%. Therefore, no Gln and Glx distributions are shown for the left Th. Bold red lines within the boxes indicate the median values for the patient or control group, whereas the lower and upper box limits show the 25th and 75th percentiles, respectively. Outliers are marked by red crosses.

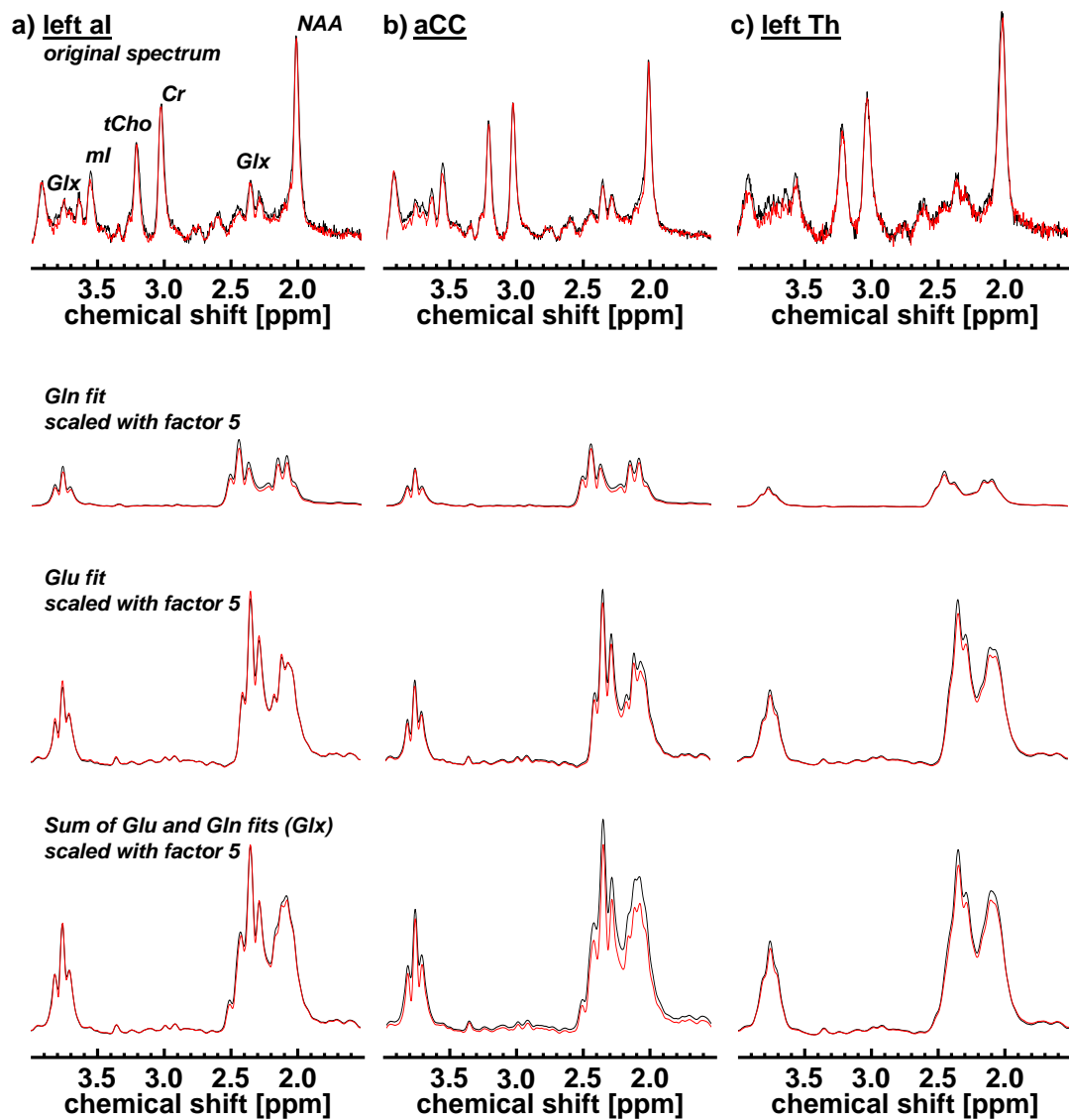


Figure 5.3: Phase and baseline corrected mean ^1H -MR spectra (top row) and mean *LCModel* fits of Gln, Glu and Glx (scaled with a factor 5), obtained by averaging over all data of nCLBP patients (red graphs) and controls (black graphs) from left aI (a), aCC (b) and left Th (c). Prior to averaging all graphs were normalized to the corresponding Cr intensities to obtain inter-individually comparable intensities.

Table 5.2: Mean absolute concentrations (C_M : $MEAN \pm SD$ in mmol/l) of NAA, Cr, tCho, mI, Glu, Gln and Glx in aI, aCC and Th of patients and controls. Mean relative concentration differences between patients and controls are listed as Δ -values (in %) together with the corresponding p -values (two-tailed t -test).

	C_M [mmol/l]		Δ [%]	p -value
	nCLBP patients	Controls		
aI ($N_{aI} = 10$):				
NAA	10.3±0.4	10.7±0.5	-4.4±3.9	0.024
Cr	8.8±0.6	8.8±0.6	0.5±11.1	0.996
tCho	1.9±0.2	2.1±0.3	-7.5±17.5	0.108
mI	5.9±1.1	6.0±0.6	-0.7±21.9	0.781
Glu	10.0±1.5	10.1±1.4	1.6±20.7	0.950
Gln	4.5±1.2*	5.3±1.0*	-15.3±8.0*	0.305*
Glx	14.2±2.2*	15.0±2.0*	-4.2±16.6*	0.580*
aCC ($N_{aCC} = 10$):				
NAA	9.8±0.8	10.3±1.0	-4.4±10.5	0.211
Cr	9.6±0.8	9.9±1.4	-1.2±12.1	0.629
tCho	2.4±0.4	2.7±0.4	-7.5±15.4	0.188
mI	7.1±1.2	7.8±1.0	-8.3±13.8	0.167
Glu	10.5±1.2	11.8±1.2	-10.2±11.8	0.027
Gln	4.7±0.7*	5.4±0.5*	-11.0±20.2*	0.143*
Glx	14.8±1.1*	17.1±1.0*	-12.9±10.1*	0.010*
Th ($N_{Th} = 6$):				
NAA	9.8±0.8	10.0±0.9	-1.9±11.3	0.636
Cr	7.4±0.3	7.3±0.5	1.9±6.6	0.681
tCho	1.9±0.2	2.0±0.3	-3.6±9.7	0.565
mI	3.7±0.8	4.3±1.1	-9.1±27.5	0.308
Glu	7.0±1.0	7.5±1.0	-4.6±15.8	0.475

* based on five data pairs (nCLBP patient vs. control) with $CRLB_{Gln}$ values below 30 %.

decline up to 8.5%, $p < 0.200$, see Tab. 5.2). However, since the calculated metabolic concentrations represent averaged values between WM and GM tissue fractions, the observed tCho decline in aI and aCC may be ascribed to the lower WM content in the corresponding MRS volumes of patients (see Tab. 5.3).

No differences in Cr concentrations were found between both groups in all investigated regions of interest ($p > 0.6$).

5.3.3 CLBP related morphological changes

To investigate morphological changes in pain processing brain areas (see the summary of studies in Borsook et al. [2007]), mean WM, GM and CSF volume fractions of the MRS voxels in aI, aCC and Th were also compared between nCLBP patients and healthy controls (see Tab. 5.3). Patients revealed up to 21% lower WM content and up to 10% higher GM content. However, the WM decrease was significant only in the aI of patients ($p = 0.046$). No apparent CSF fraction differences were observed between patients and controls.

Table 5.3: Mean relative GM, WM and CSF volume fractions (f_{GM} , f_{WM} and f_{CSF} ; $MEAN \pm SD$ in %) within the aI, aCC and Th spectroscopic voxels in patients and controls. Relative differences of determined brain tissue fractions between patients and controls are listed as Δ -values (in %) together with corresponding p -values (two-tailed t -test).

	f_{tissue} [%]		Δ [%]	p -value
	nCLBP patients	Controls		
aI ($N_{aI} = 10$):				
WM	16.3±2.5	20.5±4.6	-17.0±23.5	0.046
GM	70.0±3.8	66.4±5.3	6.1±8.5	0.131
CSF	13.6±3.6	13.1±3.7	11.6±45.5	0.810
aCC ($N_{aCC} = 10$):				
WM	6.1±2.1	7.4±2.6	-13.8±21.4	0.258
GM	68.9±6.0	64.3±8.0	8.8±17.6	0.187
CSF	25.0±6.6	28.3±7.6	-1.7±55.1	0.338
Th ($N_{Th} = 6$):				
WM	17.0±8.7	23.7±11.0	-21.2±32.5	0.317
GM	83.0±8.7	76.3±11.0	10.1±17.2	0.322
CSF	0.1±0.1	0.0±0.0	-	0.179

Tab. 5.4 summarises the cortical thicknesses for several anatomical structures, which were enclosed by MRS voxels in the left aI and aCC. The aI voxels comprised four anatomical structures: *anterior circular sulcus of insula* (aCSI, orange coloured in Fig. 5.4a), *superior circular sulcus of insula* (sCSI, green coloured in Fig. 5.4a), *short gyri of insula* (SGI,

violet coloured in Fig. 5.4a), and *sulcus lateralis anterior* (aSL, blue coloured in Fig. 5.4a). Cortical thickness was increased significantly in patients for aSCI ($\Delta = 11.1 \pm 10.5\%$, $p = 0.031$), whereas the remaining insular structures only revealed a trend towards thickness increase (see Tab. 5.4) without reaching statistical significance ($p > 0.3$). Averaged over all insular substructures an increase of cortical thickness of approximately 6% ($p > 0.3$) was evident, but not significant for nCLBP patients. This supports the finding of the increased relative GM volume fraction in aI of patients (see Tab. 5.3). However, both the cortical thickness and volume fraction reveal high inter-individual variation.

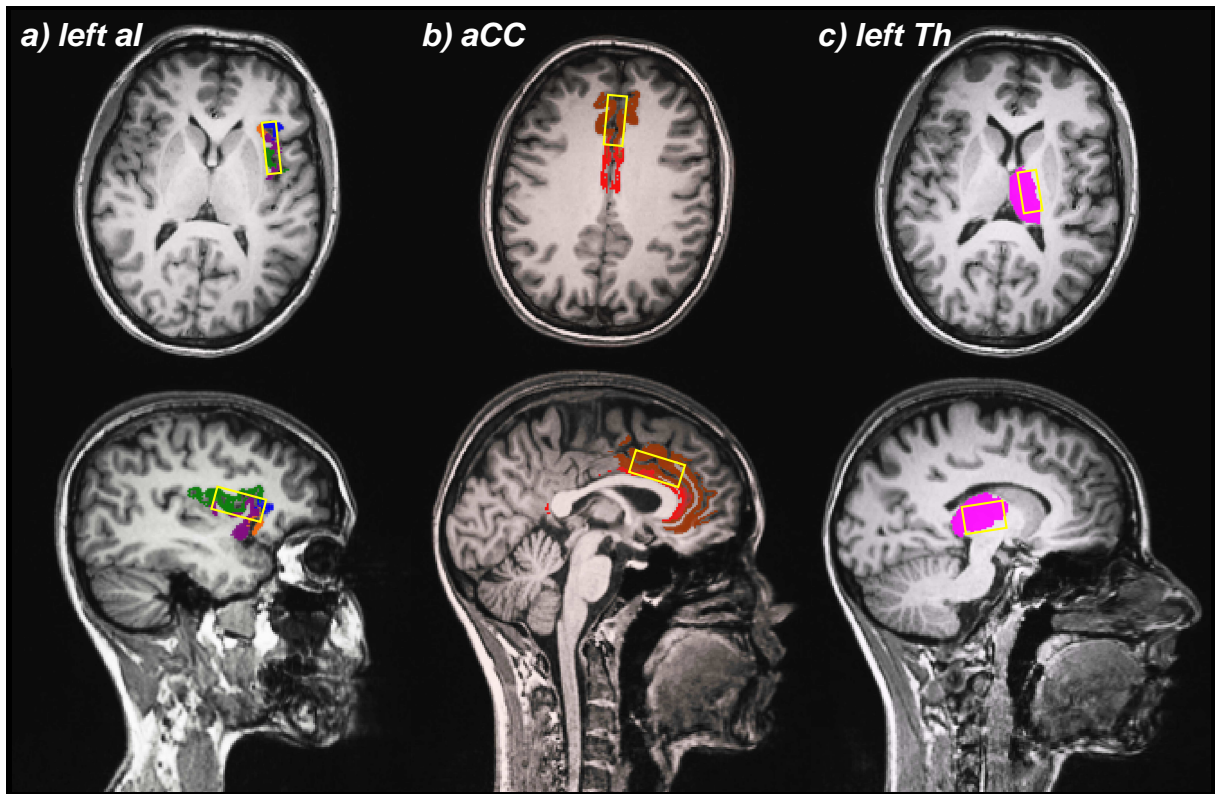


Figure 5.4: Transverse (upper row) and sagittal (lower row) projections of 3D MP-RAGE head data sets showing the locations of the MRS voxels (marked in yellow) in aI (a), aCC (b) and Th (c). Different colours indicate anatomical structures, which are enclosed by the MRS-voxels: *anterior circular sulcus of insula* (orange), *superior circular sulcus of insula* (green), *short gyri of insula* (violet), *sulcus lateralis anterior* (blue), *anterior cingulate gyri and sulci* (brown), *pericallosal sulci* (red) and *thalamus* (magenta). Cortical thickness values of these structures (except for thalamus) were calculated by *FreeSurfer* and compared between patients and controls. For the thalamus only relative volumes were compared.

The aCC voxels comprised two anatomical structures: *anterior cingulate gyrus and sulcus* (aCGS, brown coloured in Fig. 5.4b) and *pericallosal sulcus* (PS, red coloured in Fig. 5.4b). Neither aCGS nor PS were significantly different between patients and controls ($p > 0.7$).

Finally, the relative volumes of *thalamus* (magenta coloured in Fig. 5.4c) did not significantly differ between patients and controls (mean relative Th volume in patients:

$0.46 \pm 0.04\%$; mean relative Th volume in controls: $0.48 \pm 0.07\%$; $p > 0.6$).

Table 5.4: Mean cortical thicknesses ($MEAN \pm SD$ in mm) of subcortical structures (calculated by *FreeSurfer*) within the aI and aCC spectroscopic voxels selected for patients and healthy controls. Relative cortical thickness differences between the nCLBP patients and controls are listed as Δ -values (in %) together with corresponding p -values (two-tailed t -test). Used abbreviations: *anterior circular sulcus of insula* (aCSI), *superior circular sulcus of insula* (sCSI), *short gyri of insula* (SGI), *sulcus lateralis anterior* (aSL), *anterior cingulate gyrus and sulcus* (aCGS), *pericallosal sulcus* (PS).

	Cortical thickness [mm]		Δ [%]	p -value
	nCLBP patients	Controls		
<i>MRS voxel located in aI ($N_{aI} = 10$):</i>				
aCSI	3.0 ± 0.3	2.7 ± 0.3	11.1 ± 10.5	0.031
sCSI	2.6 ± 0.1	2.6 ± 0.1	1.1 ± 3.3	0.453
SGI	3.7 ± 0.2	3.6 ± 0.2	3.0 ± 7.9	0.307
aSL	2.3 ± 0.4	2.1 ± 0.3	8.0 ± 18.5	0.369
average*	2.9 ± 0.6	2.8 ± 0.6	5.8 ± 12.3	0.330
<i>MRS voxel located in aCC ($N_{aCC} = 10$):</i>				
aCGS	2.7 ± 0.2	2.7 ± 0.3	0.3 ± 10.0	0.799
PS	2.4 ± 0.3	2.4 ± 0.4	2.3 ± 16.3	0.919
average*	2.5 ± 0.3	2.5 ± 0.4	1.0 ± 13.4	0.946

* Values were calculated by averaging over all particular anatomical structures in aI and aCC, respectively.

5.4 Discussion

The major aim of the current clinical study was to investigate whether *in vivo* ^1H -MRS allows quantification of chronic pain related metabolic changes in human brain areas that are known to be involved in cortical pain processing. Single-voxel (SVS) ^1H -MRS was used, which is less affected by mislocalisation artefacts compared to CSI techniques that may suffer, for example, from signal contaminations of adjacent voxels due to k -space undersampling (see the CSI section in Chap. 2.3.2.1). On the other hand, SVS measurements are quite time consuming and require *a priori* knowledge about the spatial location of the expected metabolic changes. Therefore, findings of recent fMRI, PET and EEG studies were utilized to select three specific cortical areas - aI, aCC and Th, which are known to be relevant for the assessment of peripheral nociceptive stimuli [Apkarian et al., 2005; Peyron et al., 2000]. In the present study, spectra acquisition was restricted to the left aI and left Th to keep the scan time for the participants within reasonable limits. Furthermore, as no evidence of strong lateralization has been reported in the literature with respect to pain related neuronal activity enhancement in these regions [Peyron et al.,

2000], it was presumed that the achieved results are representative for both left and right parts of aI and Th.

The decreased Gln levels in all investigated pain processing regions of patients and the significantly reduced Glu concentration in aCC may represent the most interesting findings of this study. With respect to the role of Glu as a major excitatory neurotransmitter [Hertz, 2006], its significant decrease in aCC of patients may be explained by modified excitatory neurotransmission due to prolonged pain perception or other affective consequences of chronic pain. This hypothesis is supported by the observed trend of decreased Gln (see Tab. 5.2), which acts as an intermediate product in the glutamatergic neurotransmission cycle. Because spectrally resolved detection of Glu and Gln *in vivo* is limited by the strong overlap of these resonances at $B_0 = 3\text{T}$, concentrations of Glx concentrations (sum of Glu and Gln) were also compared between patients and controls. Similar to Glu and Gln, the Glx concentration was significantly decreased by approximately 13% in the aCC ($p = 0.01$) and only slightly decreased by approximately 4% ($p = 0.580$) in the aI of the patient group.

Due to the limited *SNR* and restricted spectral resolution of the Th spectra, results of Gln quantitation in Th were excluded from the final analysis. As Glu concentration did not differ between patients and healthy volunteers ($p > 0.45$), it was thus not possible to draw any unambiguous conclusions with respect to neurotransmitter changes in the Th. Nevertheless, due to the apparent Gln, Glu and Glx intensity decreases in the fit graphs of patients (see Fig. 5.3c), an analogous behaviour as in the aCC may be assumed for the Th.

Cortical changes of Gln and Glu in the presence of chronic pain and their relation to neurotransmitter cycle dysfunction have been described recently in ^1H -MRS studies conducted on patients suffering from chronic migraine [Dichgans et al., 2005; Prescott et al., 2009], chronic neuropathic pain [Siddall et al., 2006; Stanwell et al., 2010]. According to these studies, Gln seems to be a more specific marker for chronic pain associated neurotransmission changes, since it participates mostly in neurotransmission metabolism processes, such as Glu or GABA reuptake [Hertz, 2006]. In contrast, the question about interpretation of detected Glu changes remains open as long as the observed changes cannot be unambiguously assigned to an extra-cellular Glu fraction in the synaptic clefts or to particular intra-cellular Glu compartments, which are all involved in neurotransmission, but also in other metabolic processes (see the discussion in Chap. 4.1.2.2).

Since excitatory glutamatergic neurotransmission is usually interacting with the corresponding inhibitory neurotransmission, changes of the major neuronal inhibitory neurotransmitter GABA are also expected to occur as a consequence of chronic pain and may thus be used for a more comprehensive exploration of neurotransmission associated origins of chronic pain manifestation. Unfortunately, due to the strong overlap of GABA resonances with signals of other metabolites and the low cortical GABA concentrations ($< 2\text{mmol/l}$ [Govindaraju et al., 2000]), the accuracy of GABA detection *in vivo* by

means of conventional ^1H -MRS techniques is quite low at 3 T. In the present study the CRLB values of GABA, calculated with the *LCModel*, were larger than 30 % for all spectra and, thus, did not allow any reliable evaluation of GABA changes. However, since the investigation of GABA is quite important in the context of chronic pain, further studies at higher static magnetic field strengths or with sophisticated measurement techniques, which were already mentioned in the discussion part of Chap. 4.5.1, are required.

Of note is also the finding of chronic pain related Glx reduction in aI in conjunction with the observed reduced WM volume fraction (up to 17 %) and the slight, non-significant GM volume fraction increase (see Tab. 5.3). Since the absolute metabolite concentrations calculated in the present study represent mean values between GM and WM compartments, and Glu and Gln concentrations are typically lower in WM than in GM [Choi et al., 2006a, b], a higher Glx level would be normally assumed for patients. Within this context, chronic pain related reduction of Glx concentration, as observed here, may then indicate reduced activity of glutamatergic neurons.

Besides changes of Glu and Gln, nCLBP patients also revealed significantly lower NAA concentrations in aI ($p = 0.024$) and a decreasing, though not significant, trend in Th and aCC (see Tab. 5.2). The reduction of NAA - a metabolite, which is commonly proposed as a neuronal density marker [Govindaraju et al., 2000] - is in agreement with recent studies of Fukui et al. [2006] and Pattany et al. [2002], who observed NAA decreases in the Th of patients with chronic neuropathic pain after spinal cord injury. Grachev et al. [2002], who reported decreased NAA concentrations in dorsolateral prefrontal brain matter of chronic low back pain patients, ascribed this decrease to neurodegenerative processes due to the permanently enhanced neuronal activity in the pain processing brain regions. Along similar lines, Mullins et al. [2005] hypothesized that the prolonged enhanced glutamatergic activity associated with chronic pain may lead to excitotoxic neuronal damage, which should be reflected in NAA decrease. This hypothesis may support by the observed increased Glu concentrations during stimulation with acute heat pain (see Chap. 4). However, it can not be unambiguously verified by means of the results of the present study, since an increase of Glu was not observed in chronic pain patients. It can be assumed that the enhanced Glu activity occurs in an earlier state of chronic pain manifestation so that the currently detected NAA decrease in patients reflects already the consequence of excitotoxic neuronal damage.

Compared to healthy controls, aI, aCC and Th patient spectra show a clear intensity drop between 3.6 ppm and 3.7 ppm (see upper subplots in Fig. 5.3), which may be related to decreased mI. As summarized in Tab. 5.2 patients revealed evidently decreased, though statistically non-significant mI concentrations in aCC and Th ($p < 0.310$). Since mI has been proposed as a marker for the density of astroglial cells [Govindaraju et al., 2000], this decrease may be ascribed to a loss of astroglial cells due to prolonged increased glutamatergic activity during an earlier state of chronic pain manifestation (see the discussion about decreased NAA above). Interestingly, the mI decrease observed here contradicts the

findings of Grachev et al. [2002] and Pattany et al. [2002], who described non-significant evidence of a mI increase in the orbitofrontal cortex and thalamus of chronic pain patients. However, since these studies were performed on MR scanners operating at 1.5 T, this discrepancy may be due to reduced accuracy with respect to mI quantitation achievable at the lower field strength. Alternatively, the intensity drop between 3.6 ppm and 3.7 ppm observed in the own current study for patients' spectra (see upper subplots in Fig. 5.3), may also be associated with negative glucose changes due to reduced neurotransmission activity. However, since the fitting errors of glucose intensity were rather large in regarded spectra ($CRLB_{\text{Gluc}} > 60\%$), this interpretation remains highly vague and requires further studies.

Finally, when comparing brain matter fractions between nCLBP patients and healthy controls, a significant WM decrease was detected in the aI of patients ($-17.0 \pm 23.5\%$, $p < 0.05$, see Tab. 5.3). Since a similar behaviour was observed for aCC and Th, it would stand to reason that these changes indicate morphological rearrangements occurring during chronic pain manifestation in pain processing areas. This hypothesis is also supported by recent findings of diffusion tensor imaging and voxel based morphometric studies, which reported chronic pain related WM volume decreases in pain processing cerebral regions (mostly WM areas close to aCC and prefrontal cortex) as a consequence of reorganisation of white matter tracts and progressive demyelination [Buckalew et al., 2008; Geha et al., 2008]. However, since in the present study WM and CSF changes were determined only by comparing tissue compositions in single MRS voxels, the results may be contaminated by inter-individual variations of manually adjusted MRS voxel positions and are therefore not adequate for comprehensive and objective comparison with results of other morphological whole brain investigations.

The cortical thickness analysis allows a more objective assessment of morphological GM alterations. A significant increase of cortical thickness was observed only for the patients' *anterior circular sulcus of insula* (see Tab. 5.4), which, however, is a structure that occupies only a relative small volume fraction within the adjusted aI MRS voxels (see the orange coloured structure Fig. 5.4a). Neither the remaining insular substructures nor the substructures in the aCC voxel revealed significant cortical thickness changes. This observation may explain why no statistically significant GM volume fraction changes were observed in aI and aCC of patients. (see Tab. 5.3).

On the other hand, the reduced concentrations of the neuronal marker NAA in aI and aCC as well as the decrease of astroglial marker mI in aCC of patients indicate cell loss, which should rather lead to GM reduction. Recent morphological studies reported a GM increase in several pain processing areas in the presence of chronic back pain [Schmidt-Wilcke et al., 2006], fibromyalgia [Schmidt-Wilcke et al., 2007] or chronic vulvar pain [Schweinhardt et al., 2008]. The authors of these reports discussed cell size or synaptic bulk size changes as well as enhanced angiogenesis as possible causes for the GM increase. Thus, it may be assumed that the chronic pain related neuron and glial cell loss, indicated

by the NAA and mI decrease, does not cause GM volume reduction because of possible increases of cell size or synaptic bulk size. This statement remains hypothetical, since it can only be proved by histological analysis, which however were not reported in the literature up to now.

In conclusion, the results of this present study indicate a role of ^1H -MRS measurements to assess nCLBP induced metabolic changes in the human central nervous system (CNS) to explore mechanisms underlying the manifestation of chronic pain. Despite the relatively small sample size and different durations and intensities of pain perception in the patient group, changes of several brain metabolites were observed, which again may potentially be used as diagnostic markers for assessment of chronic pain disease. Especially, the decreased Gln and Glu concentrations in patients indicate disordered glutamatergic neurotransmission due to prolonged pain perception. Future studies should thus concentrate on applying more sophisticated experimental approaches, which allow improved separation of Glu, Gln and GABA resonances *in vivo* in order to explore the dysfunctions of both excitatory and inhibitory neurotransmitter systems, which are underlying or occurring during the manifestation of chronic pain. More specific conclusions regarding the chronic pain related neurotransmitter dysfunctions may potentially be derived in the future by stimulus related detection of neurotransmitter changes in chronic pain patients and healthy controls during acute pain stimulation as it was described in Chap. 4. Finally, morphological changes observed in the present study for patients in conjunction with observed alterations of metabolic cell density markers (NAA and mI) indicate reorganisation processes on the cellular level, which may also be used for the more objective diagnostic assessment of chronic pain related changes in CNS.

6 Conclusions and Outlook

The major aim of this thesis was to explore whether pain associated changes of metabolites in the human brain are detectable with ^1H -MRS *in vivo*. This question can be positively answered in light of the results obtained during the acute pain stimulation of healthy volunteers (fMRS study) as well as by comparing the metabolic levels in different pain processing regions of chronic pain patients and healthy volunteers (clinical study). In the fMRS study, the stimulus triggered data acquisition allowed time resolved detection of metabolites with a temporal resolution of a few seconds and thus enabled to quantitate metabolic concentrations in different conditions within a short stimulation sequence. It was shown that the concentration of the excitatory neurotransmitter glutamate significantly increases during the application of a transient pain stimulus and returns back to its initial level within few seconds. These dynamic changes may reflect the regulation of glutamatergic neurotransmission in the brain with respect to the enhanced neuronal activity due to the sensation of pain. Application of this method offers opportunities to investigate, whether the *in vivo* MR spectroscopy is also able to detect changes in neurotransmission depending on the altering conditions such as the intensity and duration of pain sensation or the adaptation to pain stimulus or the pain inhibition based on medication. This, in turn, can be utilised to explore biochemical mechanisms associated with the neuronal hypersensitisation, which is assumed to underlay the manifestation of the chronic pain. Considering the pain associated enhanced release of glutamate in the extracellular space, the decreased concentrations of the cellular density markers mI and NAA, as they were observed in patients, may reflect the excitotoxic cellular damage induced by the more or less permanent sensation of pain in this disease. Detection of changes of these metabolic markers in the time course of the chronic pain disease may therefore be important for the diagnostic assessment of the tissue damage. Unfortunately, the results of the clinical study do not allow unambiguous conclusions about the neurotransmitter disordering in chronic pain state. Decreased glutamate and glutamine concentrations observed in the several brain regions of chronic pain patients may reflect both, the disordered neurotransmission as well as the cellular loss due to excitotoxic damage in an earlier state of the disease. To prove these hypotheses, functional MRS experiments have to be performed on patients and healthy controls to compare the time courses of dynamic glutamate changes, associated with the application of acute pain stimuli.

In the present work, detecting of glutamate changes associated acute pain with was restricted to the insular cortex. Consequently, in order to paint the full picture further in-

vestigations including measurements in other cerebral pain processing regions are certainly necessary to monitor all pain induced metabolic changes in the brain. Some further limitations turned out during the progression of described studies that should be considered in following investigations to improve reproducibility and specificity of results. Firstly, as revealed by the decrease in the pain intensity during the pain stimulation, habituation effects could not be completely avoided with applied stimulation design. A randomized order of stimulations as well as varying the intensity of pain stimulus may potentially help to overcome this limitation. Furthermore, LASER based stimulation techniques using short light pulses of a few nanoseconds are most likely more effective to reduce adaptations that cannot be excluded by the relatively slow thermal stimuli. Secondly, the time points of spectral acquisition were adjusted to the stimulation time course but not to the temporal dynamics of brain activation. A more accurate metabolic time course extraction may become possible by simultaneous acquisition of electroencephalography (EEG) data that provide temporally highly resolved information of electrophysiological activity in the brain. Thirdly, the specificity of results may be improved by acquiring more than only two spectra within a stimulation sequence. However, since it will extend the total scan time, the number of averaged single acquisitions has to be reduced, which in turn will decrease the SNR and impair the quantitation accuracy. This can, however, be compensated by experiments at higher magnetic fields, for example at 7 T. Finally, since excitatory glutamatergic activity is usually interacting with the corresponding inhibitory neurotransmission, changes of GABA - the major inhibitory neurotransmitter - are also expected to occur during the pain sensation. Future efforts should thus concentrate on applying more sophisticated experimental approaches, which allow reliable *in vivo* detection of glutamate and GABA.

Bibliography

- Andersson, G. B. (1999). Epidemiological features of chronic low-back pain. *Lancet*, 354(9178):581–585.
- Apkarian, A. V., Bushnell, M. C., Treede, R.-D., and Zubieta, J.-K. (2005). Human brain mechanisms of pain perception and regulation in health and disease. *Eur J Pain*, 9(4):463–484.
- Baliki, M. N., Chialvo, D. R., Geha, P. Y., Levy, R. M., Harden, R. N., Parrish, T. B., and Apkarian, A. V. (2006). Chronic pain and the emotional brain: specific brain activity associated with spontaneous fluctuations of intensity of chronic back pain. *J Neurosci*, 26(47):12165–12173.
- Banaschak, S., Rzanny, R., Reichenbach, J. R., Kaiser, W. A., and Klein, A. (2005). Estimation of postmortem metabolic changes in porcine brain tissue using ^1H -MR spectroscopy—preliminary results. *Int J Legal Med*, 119(2):77–79.
- Belliveau, J. W., Kennedy, D. N., McKinstry, R. C., Buchbinder, B. R., Weisskoff, R. M., Cohen, M. S., Vevea, J. M., Brady, T. J., and Rosen, B. R. (1991). Functional mapping of the human visual cortex by magnetic resonance imaging. *Science*, 254(5032):716–719.
- Bloch, F., Hansen, W., and Packard, M. (1946). The nuclear induction experiment. *Phys Rev*, 70:474–485.
- Borsook, D., Moulton, E. A., Schmidt, K. F., and Becerra, L. R. (2007). Neuroimaging revolutionizes therapeutic approaches to chronic pain. *Mol Pain*, 3:25–33.
- Bottomley, P. (1987). Spatial localization in NMR spectroscopy *in vivo*. *Ann. N. Y. Acad. Sci.*, 508:333–348.
- Brant-Zawadzki, M., Gillan, G. D., and Nitz, W. R. (1992). MP RAGE: a three-dimensional, T_1 -weighted, gradient-echo sequence—initial experience in the brain. *Radiology*, 182(3):769–775.
- Brief, E. E., Moll, R., Li, D. K. B., and Mackay, A. L. (2009). Absolute metabolite concentrations calibrated using the total water signal in brain ^1H -MRS. *NMR Biomed*, 22(3):349–354.
- Bronstein, I., Semendjajew, K., Musiol, G., and Mühlig, H. (2001). *Taschenbuch der Mathematik*. Verlag Harri Deutsch, Frankfurt am Main.

- Brooks, J. and Tracey, I. (2005). From nociception to pain perception: imaging the spinal and supraspinal pathways. *J Anat*, 207(1):19–33.
- Brooks, J. C. W., Nurmikko, T. J., Bimson, W. E., Singh, K. D., and Roberts, N. (2002). fMRI of thermal pain: effects of stimulus laterality and attention. *Neuroimage*, 15(2):293–301.
- Brown, M. A. (2004). Time-domain combination of MR spectroscopy data acquired using phased-array coils. *Magn Reson Med*, 52(5):1207–1213.
- Brown, T. R., Kincaid, B. M., and Ugurbil, K. (1982). NMR chemical shift imaging in three dimensions. *Proc Natl Acad Sci U S A*, 79(11):3523–3526.
- Buckalew, N., Haut, M. W., Morrow, L., and Weiner, D. (2008). Chronic pain is associated with brain volume loss in older adults: preliminary evidence. *Pain Med*, 9(2):240–248.
- Burtscher, I. M. and Holtås, S. (2001). Proton MR spectroscopy in clinical routine. *J Magn Reson Imaging*, 13(4):560–567.
- Casey, K. L. (1999). Forebrain mechanisms of nociception and pain: analysis through imaging. *Proc Natl Acad Sci U S A*, 96(14):7668–7674.
- Cavassila, S., Deval, S., Huegen, C., van Ormondt, D., and Graveron-Demilly, D. (2001). Cramér-Rao bounds: an evaluation tool for quantitation. *NMR Biomed*, 14(4):278–283.
- Chiappa, K. H., Hill, R. A., Huang-Hellinger, F., and Jenkins, B. G. (1999). Photosensitive epilepsy studied by functional magnetic resonance imaging and magnetic resonance spectroscopy. *Epilepsia*, 40 Suppl 4:3–7.
- Choi, C., Coupland, N. J., Bhardwaj, P. P., Kalra, S., Casault, C. A., Reid, K., and Allen, P. S. (2006a). T₂ measurement and quantification of glutamate in human brain in vivo. *Magn Reson Med*, 56(5):971–977.
- Choi, C., Coupland, N. J., Bhardwaj, P. P., Malykhin, N., Gheorghiu, D., and Allen, P. S. (2006b). Measurement of brain glutamate and glutamine by spectrally-selective refocusing at 3 Tesla. *Magn Reson Med*, 55(5):997–1005.
- Choi, C., Patel, A., Douglas, D., and Dimitrov, I. (2010). Measurement of proton T₂ of coupled-spin metabolites in gray and white matter in human brain at 3 T. In *In Proc. Intl. Soc. Mag. Reson. Med. 18. ISMRM*.
- Cohen, B. M., Renshaw, P. F., Stoll, A. L., Wurtman, R. J., Yurgelun-Todd, D., and Babb, S. M. (1995). Decreased brain choline uptake in older adults. an in vivo proton magnetic resonance spectroscopy study. *JAMA*, 274(11):902–907.
- Craig, A. D., Chen, K., Bandy, D., and Reiman, E. M. (2000). Thermosensory activation of insular cortex. *Nat Neurosci*, 3(2):184–190.

- Dagenais, S., Caro, J., and Haldeman, S. (2008). A systematic review of low back pain cost of illness studies in the united states and internationally. *Spine J*, 8(1):8–20.
- Dale, A. M., Fischl, B., and Sereno, M. I. (1999). Cortical surface-based analysis. I. segmentation and surface reconstruction. *Neuroimage*, 9(2):179–194.
- de Brouwer, H. (2009). Evaluation of algorithms for automated phase correction of NMR spectra. *J Magn Reson*, 201(2):230–238.
- de Graaf, R. A. (2007). *In Vivo NMR Spectroscopy, Principles and Techniques (2nd Edition)*. John Wiley and Sons Ltd., Chichester, England.
- Deistung, A., Rauscher, A., Sedlacik, J., Stadler, J., Witoszynskyj, S., and Reichenbach, J. R. (2008). Susceptibility weighted imaging at ultra high magnetic field strengths: theoretical considerations and experimental results. *Magn Reson Med*, 60(5):1155–1168.
- Desikan, R. S., Segonne, F., Fischl, B., Quinn, B. T., Dickerson, B. C., Blacker, D., Buckner, R. L., Dale, A. M., Maguire, R. P., Hyman, B. T., Albert, M. S., and Killiany, R. J. (2006). An automated labeling system for subdividing the human cerebral cortex on mri scans into gyral based regions of interest. *Neuroimage*, 31(3):968–980.
- Dichgans, M., Herzog, J., Freilinger, T., Wilke, M., and Auer, D. P. (2005). ^1H -MRS alterations in the cerebellum of patients with familial hemiplegic migraine type 1. *Neurology*, 64(4):608–613.
- Dickinson, W. (1950). Dependence of the ^1F nuclear resonance position on chemical compound. *Phys. Rev.*, 77:736.
- Erdtel, M. (2009). Entwicklung und Implementierung eines Visualisierungstools zur gewebespezifischen Analyse von ^1H -MR spektroskopisch gemessenen Metabolitenverteilungen im menschlichen Gehirn. Master’s thesis, Fachhochschule Jena.
- Ernst, T., Kreis, R., and Ross, B. (1993). Absolute quantitation of water and metabolites in the human brain, I. compartments and water. *J. Magn. Reson.*, B 102:1–8.
- Fermi, E. (1930). Über die magnetischen momente der atomkerne. *Z. Phys.*, 60:320.
- Fischl, B. and Dale, A. M. (2000). Measuring the thickness of the human cerebral cortex from magnetic resonance images. *Proc Natl Acad Sci U S A*, 97(20):11050–11055.
- Fischl, B., Salat, D. H., Busa, E., Albert, M., Dieterich, M., Haselgrove, C., van der Kouwe, A., Killiany, R., Kennedy, D., Klaveness, S., Montillo, A., Makris, N., Rosen, B., and Dale, A. M. (2002). Whole brain segmentation: automated labeling of neuroanatomical structures in the human brain. *Neuron*, 33(3):341–355.
- Fischl, B., Sereno, M. I., and Dale, A. M. (1999). Cortical surface-based analysis. II: Inflation, flattening, and a surface-based coordinate system. *Neuroimage*, 9(2):195–207.

- Frahm, J., Bruhn, H., Gyngell, M., Merboldt, K., Hänicke, W., and Sauter, R. (1989). Localized high-resolution proton NMR spectroscopy using stimulated echoes: initial applications to human brain in vivo. *Magn. Reson. Med.*, 9(1):79–93.
- Fukui, S., Matsuno, M., Inubushi, T., and Nosaka, S. (2006). N-acetylaspartate concentrations in the thalami of neuropathic pain patients and healthy comparison subjects measured with ^1H -MRS. *Magn Reson Imaging*, 24(1):75–79.
- Gasparovic, C., Neeb, H., Feis, D. L., Damaraju, E., Chen, H., Doty, M. J., South, D. M., Mullins, P. G., Bockholt, H. J., and Shah, N. J. (2009). Quantitative spectroscopic imaging with in situ measurements of tissue water T_1 , T_2 , and density. *Magn Reson Med*, 62(3):583–590.
- Gasparovic, C., Song, T., Devier, D., Bockholt, H. J., Caprihan, A., Mullins, P. G., Posse, S., Jung, R. E., and Morrison, L. A. (2006). Use of tissue water as a concentration reference for proton spectroscopic imaging. *Magn Reson Med*, 55(6):1219–1226.
- Geha, P. Y., Baliki, M. N., Harden, R. N., Bauer, W. R., Parrish, T. B., and Apkarian, A. V. (2008). The brain in chronic CRPS pain: abnormal gray-white matter interactions in emotional and autonomic regions. *Neuron*, 60(4):570–581.
- Giove, F., Garreffa, G., Peca, S., Carni, M., Macri, M. A., Bonaventura, C. D., Vaudano, A. E., Giallonardo, A. T., Prencipe, M., Bozzao, L., Pantano, P., Colonnese, C., and Maraviglia, B. (2006). Metabolic alteration transients during paroxysmal activity in an epileptic patient with fixation-off sensitivity: a case study. *Magn Reson Imaging*, 24(4):373–379.
- Giove, F., Mangia, S., Bianciardi, M., Garreffa, G., Salle, F. D., Morrone, R., and Maraviglia, B. (2003). The physiology and metabolism of neuronal activation: in vivo studies by NMR and other methods. *Magn Reson Imaging*, 21(10):1283–1293.
- Govindaraju, V., Young, K., and Maudsley, A. A. (2000). Proton NMR chemical shifts and coupling constants for brain metabolites. *NMR Biomed*, 13(3):129–153.
- Grachev, I. D., Thomas, P. S., and Ramachandran, T. S. (2002). Decreased levels of n-acetylaspartate in dorsolateral prefrontal cortex in a case of intractable severe sympathetically mediated chronic pain (complex regional pain syndrome, type I). *Brain Cogn*, 49(1):102–113.
- Griswold, M. A., Jakob, P. M., Heidemann, R. M., Nittka, M., Jellus, V., Wang, J., Kiefer, B., and Haase, A. (2002). Generalized autocalibrating partially parallel acquisitions (GRAPPA). *Magn Reson Med*, 47(6):1202–1210.
- Güllmar, D. (2008). *Anisotropic EEG/MEG volume conductor modeling based on Diffusion Tensor Imaging*. PhD thesis, Technische Universität Ilmenau.

- Gussev, A., Rzanny, R., Scholle, H.-C., Kaiser, W. A., and Reichenbach, J. R. (2008). [quantitation of glutamate in the brain by using mr proton spectroscopy at 1.5 T and 3 T]. *Rofo*, 180(8):722–732.
- Haase, A., Frahm, J., Hänicke, W., and Matthaei, D. (1985). ^1H NMR chemical shift selective (chess) imaging. *Phys Med Biol*, 30(4):341–344.
- Hahn, E. (1950). Spin echos. *Phys. Rev.*, 80:580–594.
- Harris, R. E., Sundgren, P. C., Craig, A. D., Kirshenbaum, E., Sen, A., Napadow, V., and Clauw, D. J. (2009). Elevated insular glutamate in fibromyalgia is associated with experimental pain. *Arthritis Rheum*, 60(10):3146–3152.
- Hertz, L. (2006). Glutamate, a neurotransmitter—and so much more. a synopsis of wierzba iii. *Neurochem Int*, 48(6-7):416–425.
- Heyne, J.-P., Rzanny, R., Hansch, A., Leder, U., Reichenbach, J. R., and Kaiser, W. A. (2006). ^{31}P -MR spectroscopic imaging in hypertensive heart disease. *Eur Radiol*, 16(8):1796–1802.
- Hiepe, P. (2009). Implementierung und Erprobung von Pulssequenzen für die diffusionsgewichtete MR-Bildgebung basierend auf stimulierten Echos. Master’s thesis, Fachhochschule Jena.
- Jansen, J. F. A., Backes, W. H., Nicolay, K., and Kooi, M. E. (2006). ^1H -MR spectroscopy of the brain: absolute quantification of metabolites. *Radiology*, 240(2):318–332.
- Kalender, W. (2006). *Computertomographie: Grundlagen, Gerätetechnologie, Bildqualität, Anwendungen. 2. Auflage*. Publicis Corporate Publishing, Erlangen, Deutschland. ISBN: 3895782157.
- Kanowski, M., Kaufmann, J., Braun, J., Bernarding, J., and Tempelmann, C. (2004). Quantitation of simulated short echo time ^1H human brain spectra by LCMoDel and AMARES. *Magn Reson Med*, 51(5):904–912.
- Klose, U. (1990). In vivo proton spectroscopy in presence of eddy currents. *Magn Reson Med*, 14(1):26–30.
- Korff, M. V., Jensen, M. P., and Karoly, P. (2000). Assessing global pain severity by self-report in clinical and health services research. *Spine (Phila Pa 1976)*, 25(24):3140–3151.
- Kreis, R. (2004). Issues of spectral quality in clinical ^1H -magnetic resonance spectroscopy and a gallery of artifacts. *NMR Biomed*, 17(6):361–381.
- Krismer, M. and Tulder., M. V. (2007). Low back pain (non-specific). *Best Pract. Res. Clin. Rheumatol.*, 21(1):77–91.

- Kumar, A., Welti, D., and Ernst, R. (1975). Imaging of macroscopic objects by NMR fourier zeugmatography. *Naturwissenschaften*, 62:34,, 62:34.
- Kupers, R., Danielsen, E. R., Kehlet, H., Christensen, R., and Thomsen, C. (2009). Painful tonic heat stimulation induces GABA accumulation in the prefrontal cortex in man. *Pain*, 142(1-2):89–93.
- Kuwabara, T., Watanabe, H., Tsuji, S., and Yuasa, T. (1995). Lactate rise in the basal ganglia accompanying finger movements: a localized ^1H -MRS study. *Brain Res*, 670(2):326–328.
- Lauterbur, P. C. (1973). Image formation by induced local interactions: Examples employing nuclear magnetic resonance. *Nature*, 242:190–191.
- Levitt, M. H. (2008). *Spin Dynamics. Basics of Nuclear Magnetic Resonance (2nd Edition)*. John Wiley and Sons Ltd, Chichester, England.
- Lin, C., Bernstein, M., Huston, J., and Fain, S. (2001). Measurements of T_1 relaxation times at 3.0 T: Implications for clinical MRA. In *In Proc. Intl. Soc. Mag. Reson. Med. 11, ISMRM, page 1391*.
- Lindner, H., Brauer, H., and Lehmann, C. (2001). *Taschenbuch der Elektrotechnik und Elektronik*. Fachbuchverlag Leipzig.
- Malucelli, E., Manners, D. N., Testa, C., Tonon, C., Lodi, R., Barbiroli, B., and Iotti, S. (2009). Pitfalls and advantages of different strategies for the absolute quantification of n-acetyl aspartate, creatine and choline in white and grey matter by ^1H -MRS. *NMR Biomed*, 22(10):1003–1013.
- Mangia, S., Garreffa, G., Bianciardi, M., Giove, F., Salle, F. D., and Maraviglia, B. (2003). The aerobic brain: lactate decrease at the onset of neural activity. *Neuroscience*, 118(1):7–10.
- Mangia, S., Tkáč, I., Gruetter, R., de Moortele, P.-F. V., Maraviglia, B., and Uğurbil, K. (2007). Sustained neuronal activation raises oxidative metabolism to a new steady-state level: evidence from ^1H NMR spectroscopy in the human visual cortex. *J Cereb Blood Flow Metab*, 27(5):1055–1063.
- Mansfield, P. and Grannell, P. (1973). NMR diffraction in solids? *J. Phys. C: Solid State Phys.*, 6:422–426.
- Maril, N. and Lenkinski, R. E. (2005). An automated algorithm for combining multivoxel MRS data acquired with phased-array coils. *J Magn Reson Imaging*, 21(3):317–322.
- Mark, L. P., Prost, R. W., Ulmer, J. L., Smith, M. M., Daniels, D. L., Strottmann, J. M., Brown, W. D., and Hacein-Bey, L. (2001). Pictorial review of glutamate excitotoxicity: fundamental concepts for neuroimaging. *AJNR Am J Neuroradiol*, 22(10):1813–1824.

- Mason, G. F. and Krystal, J. H. (2006). MR spectroscopy: its potential role for drug development for the treatment of psychiatric diseases. *NMR Biomed*, 19(6):690–701.
- Michaelis, T., Merboldt, K. D., Bruhn, H., Hännicke, W., and Frahm, J. (1993). Absolute concentrations of metabolites in the adult human brain in vivo: quantification of localized proton MR spectra. *Radiology*, 187(1):219–227.
- Mlynárik, V., Gruber, S., and Moser, E. (2001). Proton T_1 and T_2 relaxation times of human brain metabolites at 3 Tesla. *NMR Biomed*, 14(5):325–331.
- Mountford, C. E., Stanwell, P., Lin, A., Ramadan, S., and Ross, B. (2010). Neurospectroscopy: the past, present and future. *Chem Rev*, 110(5):3060–3086.
- Muller, L., Kumar, A., and Ernst, R. (1977). Two-dimensional carbon-13 spin-echo spectroscopy. *J. Magn. Reson.*, 25:383–390.
- Mullins, P. G., Rowland, L. M., Jung, R. E., and Sibbitt, W. L. (2005). A novel technique to study the brain’s response to pain: proton magnetic resonance spectroscopy. *Neuroimage*, 26(2):642–646.
- Natt, O., Bezkorovaynyy, V., Michaelis, T., and Frahm, J. (2005). Use of phased array coils for a determination of absolute metabolite concentrations. *Magn Reson Med*, 53(1):3–8.
- NifTI (2009). Neuroimaging Informatics Technology Initiative (NifTI). <http://nifti.nimh.nih.gov/>.
- Noworolski, S. M., Nelson, S. J., Henry, R. G., Day, M. R., Wald, L. L., Star-Lack, J., and Vigneron, D. B. (1999). High spatial resolution ^1H -MRSI and segmented MRI of cortical gray matter and subcortical white matter in three regions of the human brain. *Magn Reson Med*, 41(1):21–29.
- Nunez, P. L. (1989). Generation of human eeg by a combination of long and short range neocortical interactions. *Brain Topogr*, 1(3):199–215.
- Pattany, P. M., Yezierski, R. P., Widerström-Noga, E. G., Bowen, B. C., Martinez-Arizala, A., Garcia, B. R., and Quencer, R. M. (2002). Proton magnetic resonance spectroscopy of the thalamus in patients with chronic neuropathic pain after spinal cord injury. *AJNR Am J Neuroradiol*, 23(6):901–905.
- Peca, S., Carni, M., Bonaventura, C. D., Aprile, T., Hagberg, G. E., Giallonardo, A. T., Manfredi, M., Mangia, S., Garreffa, G., Maraviglia, B., and Giove, F. (2010). Metabolic correlates of brain activity in a FOS epilepsy patient. *NMR Biomed*, 23(2):170–178.
- Peyron, R., Laurent, B., and Garc a-Larrea, L. (2000). Functional imaging of brain responses to pain. a review and meta-analysis (2000). *Neurophysiol Clin*, 30(5):263–288.

- Phan, K. L., Wager, T., Taylor, S. F., and Liberzon, I. (2002). Functional neuroanatomy of emotion: a meta-analysis of emotion activation studies in PET and fMRI. *Neuroimage*, 16(2):331–348.
- Piechnik, S. K., Evans, J., Bary, L. H., Wise, R. G., and Jezzard, P. (2009). Functional changes in CSF volume estimated using measurement of water T₂ relaxation. *Magn Reson Med*, 61(3):579–586.
- Prescot, A., Becerra, L., Pendse, G., Tully, S., Jensen, E., Hargreaves, R., Renshaw, P., Burstein, R., and Borsook, D. (2009). Excitatory neurotransmitters in brain regions in interictal migraine patients. *Mol. Pain*, 5:34–45.
- Prichard, J., Rothman, D., Novotny, E., Petroff, O., Kuwabara, T., Avison, M., Howseman, A., Hanstock, C., and Shulman, R. (1991). Lactate rise detected by ¹H NMR in human visual cortex during physiologic stimulation. *Proc Natl Acad Sci U S A*, 88(13):5829–5831.
- Proctor, W. and Yu, F. (1950). The dependence of a nuclear magnetic resonance frequency upon chemical compound. *Phys. Rev.*, 77:717.
- Provencher, S. W. (1993). Estimation of metabolite concentrations from localized in vivo proton NMR spectra. *Magn Reson Med*, 30(6):672–679.
- Purcell, E. M., Torrey, H. C., and Pound, R. V. (1946). Resonance absorption by nuclear magnetic moments in a solid. *Phys. Rev.*, 69:37–38.
- Ramsey, N. F. and Purcell, E. M. (1952). Interactions between nuclear spins in molecules. *Phys. Rev.*, 85(1):143–144.
- Röntgen, W. (1895). Über eine neue Art von Strahlen. In *In: Sitzungsberichte der Würzburger Physik.-Medic.-Gesellschaft*.
- Rothman, D. L., Behar, K. L., Hetherington, H. P., and Shulman, R. G. (1984). Homonuclear ¹H double-resonance difference spectroscopy of the rat brain in vivo. *Proc Natl Acad Sci U S A*, 81(20):6330–6334.
- Rothman, D. L., Behar, K. L., Hyder, F., and Shulman, R. G. (2003). In vivo NMR studies of the glutamate neurotransmitter flux and neuroenergetics: implications for brain function. *Annu Rev Physiol*, 65:401–427.
- Rubinstein, S. M. and van Tulder, M. (2008). A best-evidence review of diagnostic procedures for neck and low-back pain. *Best Pract Res Clin Rheumatol*, 22(3):471–482.
- Rzanny, R., Grassme, R., Reichenbach, J. R., Scholle, H.-C., and Kaiser, W. A. (2006). Investigations of back muscle fatigue by simultaneous ³¹P-MRS and surface emg measurements. *Biomed Tech (Berl)*, 51(5-6):305–313.

- Rzanny, R., Klemm, S., Reichenbach, J. R., Pfeiderer, S. O. R., Schmidt, B., Volz, H.-P., Blanz, B., and Kaiser, W. A. (2003). ^{31}P -MR spectroscopy in children and adolescents with a familial risk of schizophrenia. *Eur Radiol*, 13(4):763–770.
- Sandgren, N., Stoica, P., Frigo, F. J., and Selén, Y. (2005). Spectral analysis of multi-channel MRS data. *J Magn Reson*, 175(1):79–91.
- Sappey-Marinier, D., Calabrese, G., Fein, G., Hugg, J. W., Biggins, C., and Weiner, M. W. (1992). Effect of photic stimulation on human visual cortex lactate and phosphates using ^1H and ^{31}P magnetic resonance spectroscopy. *J Cereb Blood Flow Metab*, 12(4):584–592.
- Schmidt-Wilcke, T., Leinisch, E., Gänssbauer, S., Draganski, B., Bogdahn, U., Altmep-pen, J., and May, A. (2006). Affective components and intensity of pain correlate with structural differences in gray matter in chronic back pain patients. *Pain*, 125(1-2):89–97.
- Schmidt-Wilcke, T., Luerding, R., Weigand, T., Jürgens, T., Schuierer, G., Leinisch, E., and Bogdahn, U. (2007). Striatal grey matter increase in patients suffering from fibromyalgia—a voxel-based morphometry study. *Pain*, 132 Suppl 1:S109–S116.
- Schubert, F., Gallinat, J., Seifert, F., and Rinneberg, H. (2004). Glutamate concentrations in human brain using single voxel proton magnetic resonance spectroscopy at 3 Tesla. *Neuroimage*, 21(4):1762–1771.
- Schweinhardt, P., Kuchinad, A., Pukall, C. F., and Bushnell, M. C. (2008). Increased gray matter density in young women with chronic vulvar pain. *Pain*, 140(3):411–419.
- Seeger, U., Klose, U., Mader, I., Grodd, W., and Nägele, T. (2003). Parameterized evaluation of macromolecules and lipids in proton MR spectroscopy of brain diseases. *Magn Reson Med*, 49(1):19–28.
- Shulman, R. G. and Rothman, D. L. (1998). Interpreting functional imaging studies in terms of neurotransmitter cycling. *Proc Natl Acad Sci U S A*, 95(20):11993–11998.
- Siddall, P. J., Stanwell, P., Woodhouse, A., Somorjai, R. L., Dolenko, B., Nikulin, A., Bourne, R., Himmelreich, U., Lean, C., Cousins, M. J., and Mountford, C. E. (2006). Magnetic resonance spectroscopy detects biochemical changes in the brain associated with chronic low back pain: a preliminary report. *Anesth Analg*, 102(4):1164–1168.
- Smesny, S., Rosburg, T., Nenadic, I., Fenk, K. P., Kunstmann, S., Rzanny, R., Volz, H.-P., and Sauer, H. (2007). Metabolic mapping using 2d ^{31}P -MR spectroscopy reveals frontal and thalamic metabolic abnormalities in schizophrenia. *Neuroimage*, 35(2):729–737.
- Staden, H. V. (1989). *Herophilus: the art of medicine in early Alexandria : edition, translation and essays*. Cambridge University Press.

- Stanisz, G. J., Odrobina, E. E., Pun, J., Escaravage, M., Graham, S. J., Bronskill, M. J., and Henkelman, R. M. (2005). T_1 , T_2 relaxation and magnetization transfer in tissue at 3T. *Magn Reson Med*, 54(3):507–512.
- Stanwell, P., Siddall, P., Keshava, N., Cocuzzo, D., Ramadan, S., Lin, A., Herbert, D., Craig, A., Tran, Y., Middleton, J., Gautam, S., Cousins, M., and Mountford, C. (2010). Neuro magnetic resonance spectroscopy using wavelet decomposition and statistical testing identifies biochemical changes in people with spinal cord injury and pain. *Neuroimage*, 53(2):544–552.
- Tkáč, I. and Gruetter, R. (2005). Methodology of ^1H NMR spectroscopy of the human brain at very high magnetic fields. *Appl Magn Reson*, 29(1):139–157.
- Tofts, P. S. and du Boulay, E. P. (1990). Towards quantitative measurements of relaxation times and other parameters in the brain. *Neuroradiology*, 32(5):407–415.
- Tracey, I. and Bushnell, M. C. (2009). How neuroimaging studies have challenged us to rethink: is chronic pain a disease? *J Pain*, 10(11):1113–1120.
- Vanhamme, van den Boogaart A, and S, V. H. (1997). Improved method for accurate and efficient quantification of MRS data with use of prior knowledge. *J Magn Reson*, 129(1):35–43.
- Wang, Y. and Li, S. J. (1998). Differentiation of metabolic concentrations between gray matter and white matter of human brain by in vivo ^1H magnetic resonance spectroscopy. *Magn Reson Med*, 39(1):28–33.
- Weber-Fahr, W., Ende, G., Braus, D. F., Bachert, P., Soher, B. J., Henn, F. A., and Büchel, C. (2002). A fully automated method for tissue segmentation and CSF-correction of proton MRSI metabolites corroborates abnormal hippocampal NAA in schizophrenia. *Neuroimage*, 16(1):49–60.
- Williams, D. S., Detre, J. A., Leigh, J. S., and Koretsky, A. P. (1992). Magnetic resonance imaging of perfusion using spin inversion of arterial water. *Proc Natl Acad Sci U S A*, 89(1):212–216.
- Zaaraoui, W., Fleysher, L., Fleysher, R., Liu, S., Soher, B. J., and Gonen, O. (2007). Human brain-structure resolved T_2 relaxation times of proton metabolites at 3 Tesla. *Magn Reson Med*, 57(6):983–989.

List of Figures

1.1	X-Ray applications in medicine	2
1.2	Different brain MRI contrasts	2
1.3	High field <i>in vivo</i> brain ^1H -MR spectrum	3
1.4	^1H -MR spectra of glutamate, glutamine and GABA	6
2.1	Visualisation of the trajectory of the magnetisation vector \vec{M}	13
2.2	Longitudinal and transverse relaxation	14
2.3	Spin echo experiment	15
2.4	NMR signal detection	16
2.5	Real and imaginary parts of an NMR spectrum	17
2.6	Slice selection with sinc rf pulses	20
2.7	MRI sequence diagram	21
2.8	Simulated ^1H -MR spectrum of acetaldehyde.	24
2.9	Representation of spectral peak splitting due to J-coupling in a A-X-system.	25
2.10	PRESS and STEAM approaches for the localised acquisition of ^1H -MR spectra.	28
2.11	Principle of PRESS localisation based 2D <i>in vivo</i> ^1H -CSI in brain	29
2.12	Spatial B_0 field distributions in presence of linear and second order shim gradients	31
2.13	Water signal contamination in the ^1H -MR brain spectrum	32
2.14	Water suppressed and non-suppressed <i>in vivo</i> ^1H -MR brain spectra	33
2.15	Origin and correction of zeroth order phase errors	36
2.16	Eddy current related peak line shape distortions in MR spectrum	37
2.17	Baseline correction in <i>in vivo</i> ^1H -MR spectrum	38
2.18	Basic principles of metabolite intensity quantitation	39
3.1	Determination of brain matter and CSF volume fractions by using the bi-exponential fit of T_2 water intensity decay.	45
3.2	Determination of GM, WM and CSF volume fractions by using segmented brain MRI data.	46
3.3	Implemented data processing work flow to calculate absolute metabolite concentrations.	48
3.4	Processing steps for segmentation of T_1 weighted whole brain MRI data	49

3.5	Co-registration of the MRI volume with the MRS volume.	51
3.6	Multi-chamber phantom	55
3.7	Selected MRS voxel positions in the <i>in vitro</i> study	56
3.8	Selected MRS voxel position in <i>in vivo</i> study	58
3.9	NAA changes determined by spectroscopic experiments in a two- and three-compartment system	60
3.10	Distributions of tissue corrected and uncorrected metabolite levels <i>in vivo</i> .	63
3.11	Distribution of <i>in vivo</i> metabolic concentrations with respect to the GM content	64
3.12	Simulation of the quantitation error due to incorrectly determined boundary between compartments	66
4.1	Advantage of using a higher B_0 strength for ^1H -MRS	75
4.2	Stimulation set-up	76
4.3	Examination protocol for stimulus related ^1H -MR spectra acquisition during cyclic heat pain stimulation.	79
4.4	Post-processing work flow for reconstruction of even-related spectra	80
4.5	Frequency correction of single ^1H -MR spectra	81
4.6	Principle of a phased array receive coils.	83
4.7	Evaluation of SNR and SVD based channel weights	87
4.8	Location of MRS voxel	89
4.9	Induced Glu and NAA concentration changes in ^1H -fMRS study.	91
4.10	Induced Cr, tCho and mI concentration changes in ^1H -fMRS study.	92
4.11	Mean spectra calculated over all volunteer data for ' <i>REF</i> '- and ' <i>PAIN</i> ' conditions	95
5.1	Locations of MRS voxels in aI, aCC and Th	100
5.2	Chronic pain associated metabolic changes	104
5.3	^1H -MR spectra of nCLBP patients and healthy controls	105
5.4	Anatomical structures underlying selected MRS voxels in aI, aCC and Th. .	108

List of Tables

2.1	NMR properties of common nuclei	10
3.1	<i>In vivo</i> T_1 and T_2 relaxation times of brain metabolites in GM and WM.	44
3.2	<i>In vivo</i> T_1 and T_2 relaxation times of water in GM, WM and CSF.	45
3.3	Volume fractions of GMS, WMS and CSFS in MRS voxels	56
3.4	Estimated <i>in vitro</i> T_1 and T_2 relaxation times for NAA and water in GMS, WMS and CSFS	57
3.5	Brain tissue volume fractions in GI and GII groups	62
3.6	Tissue corrected and uncorrected <i>in vivo</i> metabolic levels for GI and GII	65
4.1	Overview of recent <i>in vivo</i> ^1H -fMRS studies.	74
4.2	Quality and fit accuracy parameter estimated by <i>LCModel</i>	90
4.3	Mean Glu and NAA concentrations	93
4.4	Mean Cr, tCho and mI concentrations	94
5.1	Quality and fit accuracy parameter estimated by <i>LCModel</i>	102
5.2	Absolute concentrations of brain metabolites in aI, aCC and Th	106
5.3	GM, WM and CSF volume fractions estimated in aI, aCC and Th MRS voxels	107
5.4	Cortical thickness of subcortical structures in aI and aCC voxels	109
A.1	Look-up table for transforming <i>Freesurfer</i> subcortical region IDs into brain tissue class IDs.	131

Appendix

A.1 Look-up table for brain tissue class labeling of MRI data

Table A.1: Transformation of subcortical brain segment IDs used by *Freesurfer* to the reduced number of brain tissue class IDs (0=background, 6=WM, 7=GM, 8=CSF, 9=cortical ribbon (GM also)).

Cortical area label	Freesurfer ID	Brain tissue class
Unknown	0	0
Left-Cerebral-White-Matter	2	6
Left-Cerebral-Cortex	3	9
Left-Lateral-Ventricle	4	8
Left-Inf-Lat-Vent	5	8
Left-Cerebellum-White-Matter	7	6
Left-Cerebellum-Cortex	8	7
Left-Thalamus	9	7
Left-Thalamus-Proper	10	6
Left-Caudate	11	7
Left-Putamen	12	7
Left-Pallidum	13	7
3rd-Ventricle	14	8
4th-Ventricle	15	8
Brain-Stem	16	6
Left-Hippocampus	17	7
Left-Amygdala	18	7
Left-Insula	19	7
Left-Operculum	20	7
CSF	24	8
Left-Accumbens-area	26	6
Left-Substantia-Nigra	27	7
Left-VentralDC	28	6
Left-choroid-plexus	31	8
Right-Cerebral-White-Matter	41	6
Right-Cerebral-Cortex	42	9
Right-Lateral-Ventricle	43	8
Right-Inf-Lat-Vent	44	8
Right-Cerebellum-White-Matter	46	6
Right-Cerebellum-Cortex	47	7
Right-Thalamus	48	7
Right-Thalamus-Proper	49	6
Right-Caudate	50	7

Cortical area label	Freesurfer ID	Brain tissue class
Right-Putamen	51	7
Right-Pallidum	52	7
Right-Hippocampus	53	7
Right-Amygdala	54	7
Right-Insula	55	7
Right-Operculum	56	7
Right-Accumbens-area	58	6
Right-Substantia-Nigra	59	7
Right-VentralDC	60	6
Right-choroid-plexus	63	8
5th-Ventricle	72	8
Left-Lateral-Ventricles	75	8
Right-Lateral-Ventricles	76	8
WM-hypointensities	77	6
Left-WM-hypointensities	78	6
Right-WM-hypointensities	79	6
Left-non-WM-hypointensities	81	6
Right-non-WM-hypointensities	82	6
Optic-Chiasm	85	6
Corpus-Callosum	86	6
Left-Amygdala-Anterior	96	7
Right-Amygdala-Anterior	97	7
CSF-SA	122	8
Spinal-Cord	126	6
Left-Caudate/Putamen	136	7
Right-Caudate/Putamen	137	7
Left-Clastrum	138	7
Right-Clastrum	139	7
Left-IntCapsule-Ant	155	6
Right-IntCapsule-Ant	156	6
Left-IntCapsule-Pos	157	6
Right-IntCapsule-Ant	158	6
Left-hippocampal-fissure	193	7
Left-CADG-head	194	7
Left-subiculum	195	7
Left-fimbria	196	6
Right-hippocampal-fissure	197	7
Right-CADG-head	198	7
Right-subiculum	199	7
Right-fimbria	200	6
alveus	201	6
perforant-pathway	202	6
parasubiculum	203	7
presubiculum	204	7
subiculum	205	7
CA1	206	7
CA2	207	7

A.1 Look-up table for brain tissue class labeling of MRI data

Cortical area label	Freesurfer ID	Brain tissue class
CA3	208	7
CA4	209	7
fimbria	212	6
lateral-ventricle	213	8
entorhinal-cortex	216	7
Amygdala	218	7
Cerebral-White-Matter	219	6
Cerebral-Cortex	220	7
Inf-Lat-Vent	221	8
Fornix	250	6
CC-Posterior	251	6
CC-Mid-Posterior	252	6
CC-Central	253	6
CC-Mid-Anterior	254	6
CC-Anterior	255	6

Publications

Papers

- **A. Gussev**, R. Rzanny, D. Güllmar, H.-C. Scholle, J.R. Reichenbach: ^1H -MR spectroscopic detection of metabolic changes in pain processing brain regions in the presence of non-specific chronic low back pain. *Neuroimage*, 2011, 54(2):1315-1323.
- **A. Gussev**, R. Rzanny, M. Erdtel, H.-C. Scholle, W.A. Kaiser, H.-J. Mentzel, J.R. Reichenbach: Time-resolved functional ^1H -MR spectroscopic detection of glutamate concentration changes in the brain during acute heat pain stimulation. *Neuroimage*, 2010, 49(2):1895-1902.
- **A. Gussev**, R. Rzanny, H.-C. Scholle, W.A. Kaiser, J.R. Reichenbach: Quantitative Bestimmung von Glutamat im Hirn mithilfe der MR-Protonenspektroskopie bei 1,5 T und 3 T. *Rofo*, 2008, 180(8):722-732.

Book contributions

- **A. Gussev**, R. Rzanny, M. Erdtel, H.-C. Scholle, J.R. Reichenbach: ^1H -MR spektroskopischer Nachweis metabolischer Änderungen im Gehirn beim unspezifischen chronischen Rückenschmerz. 2010, Dokumentation der 16. Erfurter Tage - Jahrestagung der Berufsgenossenschaft für Gaststätten und Nahrungsmittel; Verlag Dr. Bussert & Stadeler, Jena, ISBN 9783942115049; p. 311-322.
- **A. Gussev**, R. Rzanny, H.-C. Scholle, W.A. Kaiser, J.R. Reichenbach: ^1H -MR-spektroskopischer Nachweis von Änderungen der Glutamat-Konzentration im Gehirn bei Stimulation mit akuten Schmerzreizen und bei unspezifischen chronischen Rückenschmerzen. 2009, Dokumentation der 15. Erfurter Tage - Jahrestagung der Berufsgenossenschaft für Gaststätten und Nahrungsmittel; Verlag Dr. Bussert & Stadeler, Jena, ISBN 9783932906947; p. 311-326.
- **A. Gussev**, R. Rzanny, P. Schmidt, W.A. Kaiser, H.-C. Scholle, J.R. Reichenbach: ^1H -MR-spektroskopischer Nachweis von Änderungen der Glutamat-Konzentrationen im Gehirn bei Stimulation mit akuten Schmerzreizen. 2008, Dokumentation der 14. Erfurter Tage - Jahrestagung der Berufsgenossenschaft für Gaststätten und Nahrungsmittel; Verlag Dr. Bussert & Stadeler, Jena, ISBN 9783932906909; p. 406-420.
- H. Wagner, C. Puta, C. Anders, R. Graßme, **A. Gussev**, F. Mörl, A. Petrovitch, J.R. Reichenbach, R. Rzanny, N. Schilling, S. Wisch, R. Blickhan, H.H.W. Gabriel, R. Grieshaber, H.-C. Scholle: Chronisch-unspezifischer Rückenschmerz - von der

Funktionsmorphologie zur Prävention - Grundlagen und Schlussfolgerungen für Diagnostik und Therapie. 2008, Dokumentation der 14. Erfurter Tage - Jahrestagung der Berufsgenossenschaft für Gaststätten und Nahrungsmittel; Verlag Dr. Bussert & Stadeler, Jena, ISBN 9783932906909; p. 181-205.

- R. Rzanny, R. Graßme, **A. Gussew**, W.A. Kaiser, H.-C. Scholle, J.R. Reichenbach: Eine Analyse der metabolischen und myoelektrischen Veränderungen im Rückenmuskel bei isometrischer Belastung. 2008, Dokumentation der 14. Erfurter Tage - Jahrestagung der Berufsgenossenschaft für Gaststätten und Nahrungsmittel; Verlag Dr. Bussert & Stadeler, Jena, ISBN 9783932906909; p. 387-396
- **A. Gussew**, R. Rzanny, H.-C. Scholle, W.A. Kaiser, J.R. Reichenbach: Untersuchungen zur Quantifizierungsgenauigkeit des Neurotransmitters Glutamat mittels ^1H -CSI-Messungen im menschlichen Gehirn bei 1,5 T und 3 T. 2007, Dokumentation der 13. Erfurter Tage - Jahrestagung der Berufsgenossenschaft für Gaststätten und Nahrungsmittel; Verlag Dr. Bussert & Stadeler, Jena, ISBN 9783932906824; p. 399-405.

Conference Abstracts

- **A. Gussew**, R. Rzanny, H.-C. Scholle, J.R. Reichenbach. ^1H -MR spektroskopischer Nachweis metabolischer Änderungen im Gehirn beim unspezifischen chronischen Rückenschmerz. In: Proc. 5. Arbeitstagung "Motodiagnostik - Mototherapie" der Deutschen Physiologischen Gesellschaft, Jena, Germany, 2010, p. 10.
- **A. Gussew**, R. Rzanny, H.-C. Scholle, J.R. Reichenbach. *in vivo* ^1H -MR spectroscopic investigations of metabolic changes in human brain associated with unspecific low back pain. In: Proc. 18th Annual Meeting ISMRM, Stockholm, Sweden, 2010. p. 956.
- **A. Gussew**, M. Erdtel, R. Rzanny, J.R. Reichenbach. *In vitro* and *in vivo* validation of absolute quantitation of brain proton MR spectra (^1H -MRS) with respect to heterogeneous tissue compositions. In: Proc. 18th Annual Meeting ISMRM, Stockholm, Sweden, 2010. p. 905.
- R. Rzanny, A. Hansch, A. Pfeil, **A. Gussew**, D. Drobnik, J.R. Reichenbach. The compatibility of temporary pacemaker leads with magnetic resonance imaging - an *ex vivo* tissue study. In: Proc. 18th Annual Meeting ISMRM, Stockholm, Sweden, 2010. p. 3890.
- **A. Gussew**, S. Smesny, B. Milleit, R. Rzanny, H. Sauer, J.R. Reichenbach. Concept for combined ^1H and ^{31}P MR spectroscopic investigations in patients with

schizophrenia In: Proc. of 2nd Biennial Conference SIRS, Florence, Italy, 2010. p. 2341.

- B. Milleit, **A. Gussew**, R. Rzanny, S. Thiel, C. Milleit, H. Sauer, J. R. Reichenbach, S. Smesny. Multi-regional ^1H magnetic resonance spectroscopy reveals local differences in concentrations of N-acetylaspartate (NAA) and glutamate in patients at Ultra High Risk (UHR) to develop psychosis. In: Proc. of 2nd Biennial Conference SIRS, Florence, Italy, 2010. p. 2341.
- M. Erdtel, **A. Gussew**, R. Rzanny, M. E. Bellemann, J.R. Reichenbach. Absolute Quantifizierung von ^1H -MR spektroskopisch detektierten Metaboliten im Gehirn unter Berücksichtigung von Partialvolumen- und Relaxationseffekten. In: Proc. 12. Jahrestagung DSISMRM, Basel, Switzerland, 2009, P09.
- **A. Gussew**, R. Rzanny, H.-C. Scholle, W.A. Kaiser, J.R. Reichenbach. ^1H -MR spektroskopischer Nachweis von Änderungen der Glutamat-Konzentration im Gehirn bei akuter Schmerzstimulation. In: Proc. 17. Tagung der Arbeitsgruppe AKP der Deutschen Physiologischen Gesellschaft, Jena, Germany, 2009, p.7.
- **A. Gussew**, M. Erdtel, R. Rzanny, J.R. Reichenbach. Absolute quantitation of brain metabolites with respect to the CSF fraction in ^1H -MR spectroscopic volumes. In: Proc. World Congress on Medical Physics and Biomedical Engineering, Munich, Germany, 2009; IFMBE Proceedings 25 (2), p. 489-492.
- **A. Gussew**, R. Rzanny, K.-H. Herrmann, S. Schmidt, O.W. Witte, J.R. Reichenbach. *In vivo* ^1H -MRS of the rat brain with a clinical 3 T whole-body MR scanner: Estimation of absolute metabolic concentrations and T_2 values. In: Proc. World Congress on Medical Physics and Biomedical Engineering, Munich, Germany, 2009; IFMBE Proceedings 25 (2), p. 500-502.
- R. Rzanny, N. Stutzig, **A. Gussew**, H. Burmeister, W.A. Kaiser, H-A. Thorhauer, J.R. Reichenbach. Monitoring training-induced metabolic adaptations in the M. gastrocnemius of volleyball players by ^{31}P -MRS. In: Proc. World Congress on Medical Physics and Biomedical Engineering, Munich, Germany, 2009; IFMBE Proceedings 25 (2).
- R. Rzanny, N. Stutzig, **A. Gussew**, W. A. Kaiser, H. A. Thorhauer, J. R. Reichenbach. ^{31}P -MR-spektroskopische Untersuchungen des Muskelstoffwechsels an Probanden mit unterschiedlicher Faserverteilung. In: Proc. 90. Jahrestagung der Deutschen Röntgen-Gesellschaft, Berlin, Germany, 2009. p. 273.
- **A. Gussew**, J. Orme, R. Rzanny, J.R. Reichenbach. Weighted Combination of Multichannel ^1H -MRS Data: Comparison of SNR- and SVD-based Methods by sim-

ulated, *in vitro* and *in vivo* data. In: Proc. 17th Annual Meeting ISMRM, Honolulu, Hawaii, USA, 2009. p. 2341.

- R. Rzanny, N. Stutzig, **A. Gussev**, W.A. Kaiser, H.-A. Thorhauer, J.R. Reichenbach. ^{31}P -MR investigations of training effects on resting state concentration of phosphor metabolites in the M. Gastrocnemius. In: Proc. 17th Annual Meeting ISMRM, Honolulu, Hawaii, USA, 2009. p. 2395.
- **A. Gussev**, R. Rzanny, H.P. Burmeister, H.-C. Scholle, W.A. Kaiser, J.R. Reichenbach. Time-resolved ^1H -MR spectroscopic investigations of cortical glutamate changes during painful heat stimulation. In: Proc. ECR, Vienna, Austria, 2009, Eur. Radiol. 19, Suppl. 1: C-699.
- R. Rzanny, N. Stutzig, **A. Gussev**, H.P. Burmeister, W.A. Kaiser, H.-A. Thorhauer, J.R. Reichenbach. Investigations of muscles with different fibre distribution by using ^{31}P -MRS. In: Proc. ECR, Vienna, Austria, 2009, Eur. Radiol. 19, Suppl. 1: C-639.
- P.A.T. Baltzer, R. Rzanny, **A. Gussev**, M. Dietzel, T. Vag, A.B. Herzog, J.R. Reichenbach, W.A. Kaiser. MR-spectroscopy (MRS) of the breast: Is there a link between choline compound amplitude and the contrast agent used? Initial results, comparing two contrast agents. In: Proc. ECR, Vienna, Austria, 2009, Eur. Radiol. 19, Suppl. 1: B-753.
- **A. Gussev**, R. Rzanny, H.-C. Scholle, W.A. Kaiser, J.R. Reichenbach. Time-resolved functional ^1H -MR spectroscopic investigations of cortical glutamate changes during painful heat stimulation. In: Proc. ISMRM Workshop 'MR Spectroscopy in Neuropsychiatric Disorders', Quebec City, Canada, 2008.
- R. Rzanny, **A. Gussev**, H.-C. Scholle, W.A. Kaiser, J.R. Reichenbach. The Impact of SNR and spectral Resolution on Glutamate Quantification: Results of *In vitro* and *in vivo* ^1H -MRS at 1.5 T and 3 T. In: Proc. ISMRM Workshop 'MR Spectroscopy in Neuropsychiatric Disorders', Quebec City, Canada, 2008.
- **A. Gussev**, R. Rzanny, H.-C. Scholle, W.A. Kaiser, J.R. Reichenbach. Untersuchungen der Änderung kortikaler Glutamat-Konzentrationen bei akuten schmerzhaften Hitzereizen mit zeitaufgelöster funktioneller ^1H -MR Spektroskopie. In: Proc. 11. Jahrestagung DSISMRM, Frankfurt/Main, Germany, 2008, V12.
- J. Orme, **A. Gussev**, R. Rzanny, J.R. Reichenbach. Weighted Combination of Multichannel ^1H -MRS Data: Comparison of SNR- and SVD-based Methods. In: Proc. 11. Jahrestagung DSISMRM, Frankfurt/Main, Germany, 2008, P4.
- **A. Gussev**, R. Rzanny, P. Schmidt, H.-C. Scholle, W.A. Kaiser, J.R. Reichenbach. Untersuchungen des kortikalen Glutamatstoffwechsels bei akuten ischämischen

Schmerzreizen mit ^1H -MR spektroskopischen Bildgebung In: Proc. 39. Jahrestagung DGMP, Oldenburg, Germany, 2008.

- **A. Gussew**, R. Rzanny, H.-C. Scholle, W.A. Kaiser, J.R. Reichenbach. Time resolved functional proton MR spectroscopic investigations of cortical glutamate changes during painful heat stimulation. In: Proc. 16th Annual Meeting ISMRM, Toronto, Canada, 2008. p. 1559.
- R. Rzanny, N. Stutzig, **A. Gussew**, W.A. Kaiser, H. Thorhauer, J. R. Reichenbach. Investigations of metabolic differences due to differences in the muscle fibre distribution by using ^{31}P -MRS at 3.0 T. In: Proc. 16th Annual Meeting ISMRM, Toronto, Canada, 2008. p. 2577.
- **A. Gussew**, R. Rzanny, P. Schmidt, H.-C. Scholle, W.A. Kaiser, J.R. Reichenbach. Zeitaufgelöste ^1H -MR spektroskopische Untersuchungen des kortikalen Glutamatstoffwechsels bei akutem Schmerzreiz durch Hitzestimulation. In: Proc. 90. Jahrestagung der Deutschen Röntgen-Gesellschaft, Berlin, Germany, 2008. RöFo 180 (Suppl. S1): p. 273.
- P. Schmidt, **A. Gussew**, R. Rzanny, J.R. Reichenbach, W.A. Kaiser. MR spektroskopische Evaluierung der zentralen Nozizeption von Männern und Frauen. In: Proc. 90. Jahrestagung der Deutschen Röntgen-Gesellschaft, Berlin, Germany, 2008. RöFo 180 (Suppl. S1): p. 297.
- R. Rzanny, R. Graßme, J.R. Reichenbach, **A. Gussew**, W.A. Kaiser, H.-C. Scholle. ^{31}P -MR spektroskopische Untersuchungen zur Ermüdung des Rückenmuskels bei abgestufter isometrischer Belastung. In: Proc. 90. Jahrestagung der Deutschen Röntgen-Gesellschaft, Berlin, Germany, 2008. RöFo 180 (Suppl. S1): p. 295.
- P. Schmidt, **A. Gussew**, R. Rzanny, J.R. Reichenbach, W.A. Kaiser. Nociception in men and women using 3 Tesla MR spectroscopy. In: Proc. ECR, Vienna, Austria, 2008, Eur. Radiol. 18(2), Suppl.1: p. 492.
- **A. Gussew**, R. Rzanny, P. Schmidt, W.A. Kaiser, H.-C. Scholle, J.R. Reichenbach. ^1H -MR spektroskopische Untersuchungen des kortikalen Neurotransmitterstoffwechsels bei akuten ischämischen Schmerzreizen. In: Proc. 10. Jahrestagung DSISMRM, Würzburg, Germany, 2007, ISSN 1863-6365, p.50.
- **A. Gussew**, R. Rzanny, H.-C. Scholle, W.A. Kaiser, J.R. Reichenbach. Quantitative Bestimmung von Glutamat im Hirn mit Hilfe der ^1H -CSI bei 1,5 T und 3 T. In: Proc. 10. Jahrestagung DSISMRM, Würzburg, Germany, 2007, ISSN 1863-6365, p. 47.
- **A. Gussew**, R. Rzanny, W.A. Kaiser, J.R. Reichenbach. Vergleich der Quantifizierungsgenauigkeiten von Glutamat im Hirn bei CSI-Untersuchungen bei 1,5 T

und 3 T. In: Proc. 88. Jahrestagung der Deutschen Röntgen-Gesellschaft, Berlin, Germany, 2008. RöFo 88 (Suppl. S1).

- R. Rzanny, F. Kalb, **A. Gussew**, W.A. Kaiser, J.R. Reichenbach. Investigations on absolute quantification of ^1H -MR spectroscopic measurements depending on the adjustment parameters. In: Proc. ECR, Vienna, Austria, 2007, Eur. Radiol. 17, Suppl.1: p. 782.
- R. Rzanny, F. Kalb, **A. Gussew**, W.A. Kaiser, J.R. Reichenbach. Absolute quantification of ^1H -MR spectra: Comparing water reference quantification with metabolic calibration. In: Proc. ECR, Vienna, Austria, 2007, Eur. Radiol. 17, Suppl.1: p. 781.
- **A. Gussew**, R. Rzanny, S. Banaschak, J.R. Reichenbach. ^1H -MR Spektroskopie postmortaler metabolischer Veränderungen in Folge von Zersetzungsprozessen im Schweinehirn. In: Proc. Gemeinsame Jahrestagung der Österreichischen, Deutschen und Schweizer Gesellschaften für Biomedizinische Technik, Salzburg, Austria, 2003, Biomed. Technik 48 (Suppl.1): p. 552-553.

Invited Talks

- ^1H -MR spektroskopischer Nachweis von Änderungen der Glutamat-Konzentrationen im Gehirn bei Stimulation mit akuten Schmerzreizen. Neurowissenschaftliches Seminar der Medical Physics Group und Klinik für Psychiatrie der Universitätsklinikum Jena, Jena, Germany, 11.06.2008.
- *In vivo* ^1H -MR Spektroskopie: Grundlagen und klinische Anwendungen. Fortbildungsveranstaltungsreihe am Institut für Diagnostische und Interventionelle Radiologie der Universitätsklinikum Jena, Jena, Germany, 07.04.2009.
- ^1H -MR spektroskopische Untersuchungen zur Nachweisbarkeit biochemischer Veränderungen im zentralen Nervensystem unter dem Einfluss von Schmerz. Forschungsseminar am Institut für Biomedizinische Technik und Informatik der TU-Ilmenau, Ilmenau, Germany, 24.11.2009.

Danksagung

Die vorliegende Arbeit wäre nicht zustande gekommen ohne Hilfe und Unterstützung seitens verschiedener Menschen. Mein herzlichster Dank gilt zuallererst meinen Betreuern Professor Jürgen R. Reichenbach und Doktor Reinhard Rzanny von der Medical Physics Group am Universitätsklinikum Jena (UKJ) sowie Professor Andreas Keller vom Institut für Biomedizinische Technik und Informatik an der Technischen Universität Ilmenau. Diese Menschen standen mir während der Gesamtzeit meiner Arbeit mit fachlichen Diskussionen und konstruktiven Anregungen stets zur Seite.

Meine Vorstellung über die klinische Relevanz der durchgeführten Arbeitsschritte konnte ich durch Diskussionen mit ärztlichen Kollegen vom UKJ vertiefen, denen ich ebenfalls von Herzen danken möchte. An dieser Stelle möchte ich besonders die Unterstützung durch Professor Hans-Christoph Scholle von der Klinik für Unfallchirurgie, Professor Hans-Georg Schaible vom Institut für Physiologie und Professor Karl-Jürgen Bär von der Klinik für Psychiatrie hervorheben.

Gedankt sei allen Diplomanden und Praktikanten die mit mir zusammenarbeiteten und deren Beiträge wesentlich zur dieser Arbeit beitrugen. Mein Dank gilt allen Kollegen der Medical Physics Group sowie dem medizinisch-technischen Personal, auf deren fachliche und freundschaftliche Unterstützung ich mich ebenfalls jederzeit verlassen konnte.

Des Weiteren möchte ich mich beim Kompetenzzentrum für Interdisziplinäre Prävention (KIP) Jena (Projekt 1.1.29) sowie bei der Bernstein Group for Computational Neuroscience Jena (BMBF 01GQ0703) für die finanzielle Unterstützung während der Anfertigung dieser Arbeit bedanken.

Auf keinen Fall möchte ich vergessen, meinen Eltern, Galina und Roland Laube, für ihren Rückhalt und ihre Liebe zu danken. Ein besonderer Dank gilt meiner Frau Ricarda und meinem Sohn Pavel für ihre Nähe.

